

# Modeling broad-spectrum light sources in vivo for applications in cancer treatment and diagnostics

A Thesis  
Submitted to the Faculty  
in partial fulfillment of the requirements for the  
degree of

Doctor of Philosophy

in

Engineering Sciences

by Ethan Phillip M. LaRochelle

Thayer School of Engineering  
Guarini School of Graduate and Advanced Studies  
Dartmouth College  
Hanover, New Hampshire

April 2020

Examining Committee:

Chair \_\_\_\_\_  
Kimberley S. Samkoe, Ph.D.

Member \_\_\_\_\_  
Brian W. Pogue, Ph.D.

Member \_\_\_\_\_  
Scott C. Davis, Ph.D.

Member \_\_\_\_\_  
Mark Niedre, Ph.D.

---

F. Jon Kull, Ph.D.

Dean of the Guarini School of Graduate and Advanced Studies



# **Modeling broad-spectrum light sources in vivo for applications in cancer treatment and diagnostics**

## **Abstract**

Electromagnetic photons in different forms, ranging from visible light to ionizing radiation, are used as the mechanism to trigger disruptive treatment pathways in cancer, and can simultaneously provide diagnostic information. The physical interactions these photons undergo is a complex stochastic process that is not easily simplified to analytical solutions. One approach for estimating clinically-actionable photon fluence is to develop Monte Carlo models of the system in question. The work presented in this thesis presents efficient methods to simulate these models and demonstrates applications in the fields of photodynamic therapy (PDT) and radiotherapy.

Dermatologic applications of PDT generally use the pro-drug aminolevulinic acid (ALA), which is selectively converted to the photosensitizer protoporphyrin IX (PpIX) within neoplastic cells. PpIX is commonly activated with both blue and red wavelengths of light in clinical treatment, but more recently broad-spectrum daylight has been investigated as an activation source. When broad-spectrum sunlight or lamps are used to activate PpIX, the dose planning becomes more complicated. Clinically, the effect of tissue optical properties is often overlooked. The first aim of this work presents a model-based method to estimate PDT dose at depth in tissue and proposes a simplified lookup table approach to improve clinical adoption of daylight or lamplight activation. The second aim

refines this model based on clinical applications of daylight-PDT, time-correlated spectroradiometer, and weather forecast data to have broader planning and dosimetric utility.

During radiotherapy electrons are generated with sufficient energy to create broad-spectrum optical Cherenkov emissions in tissue, which can then be used to excite luminescent compounds. The third aim of this work investigates how models of both Cherenkov emissions and Cherenkov-excited luminescence can be used to determine limiting factors in optical detection. With a Cherenkov-excited, oxygen-sensitive, phosphorescent compound the partial pressure of oxygen ( $pO_2$ ) in the tumor microenvironment can be recorded non-invasively. The final aim experimentally demonstrates measurements of *in vivo*  $pO_2$  at high temporal resolution during fractionated radiotherapy treatments.

## **Acknowledgments**

While writing my thesis and reflecting on the time I've spent as a student, from elementary school through my current endeavor at Dartmouth, I feel both privileged and dismayed to think I've spent over 20 years on this pursuit. At times, getting through each new academic year had challenges, from disciplinary issues in my earlier years, to gaps for medical leave in high school, and my parents' deaths during my PhD, I'm comforted to know I've always had a strong support system.

Even though I didn't always recognize it at the time, my parents had a strong influence on my path. As a child, we often went on family drives to check on the progress of construction sites my dad had designed, which frequently devolved into critiquing my dad's choice in speed-bump placement. Being raised in the presence of an engineer from a young age provided me the opportunity to observe the design choices of the world around me. While my dad skewed towards the absent-minded engineer, my mom demonstrated her selfless devotion to helping others every day, and while at times this resulted in higher levels of chaos, she used this to further convey the importance of adaptability and creativity.

My path to pursuing a PhD focused on developing tools for medical imaging was in many ways guided by the values set by my parents, to pursue education, observe the world around me, questioning what doesn't make sense and looking for ways to help, knowing someone is always behind the design. While the designers' intentions are not always clear, working to understand the constraints can provide valuable insight for future endeavors.

As part of my research, I spent many hours looking at raw data and images that most people would discard as useless noise. However, by continuously questioning how the data was collected and forming an understanding of the system constraints, valuable information can be extracted. This information, the optical signature of random photon and electron collisions, is seemingly plucked from the ether of the universe. Arriving at this point requires a combination of technical engineering and a splash of creativity.

I would like to thank my thesis committee for their guidance through this process. Brian Pogue has been a continued source of inspiration. He has always been supportive of trying crazy ideas, at least once, and continues to provide unbiased guidance to further my career. I am especially appreciative of his flexibility to allow me to take time to address my dad's medical care after my mom passed. Scott Davis has also acted as an indispensable mentor throughout my PhD candidacy and I am very grateful for his early involvement, pushing me to do my best work and dive deep into research. Kim Samkoe has always been incredibly helpful and approachable, getting the brunt of my most-basic questions about fluorescence and biochemistry. Mark Niedre has been very welcoming and open to sharing new ideas about future directions of *in vivo* imaging.

And of course, my wife, Kellie deserves the biggest thanks for putting up with my ever-increasing PhD-induced absent mindedness. Kellie has been my rock through this process, holding everything together through all the ups and downs. Thank you for reminding me to get away from the computer, go for walks with the dogs, and generally encouraging me to take time to enjoy life.

# Table of Contents

LIST OF TABLES .....	XIII
LIST OF FIGURES.....	XIV
<i>LIST OF ACRONYMS</i> .....	XXI
<b>1 PHOTON INTERACTIONS WITH MATTER.....</b>	<b>1</b>
1.1 INTRODUCTION.....	1
1.2 LIGHT INTERACTIONS WITH MATTER.....	3
1.2.1 <i>Jablonski Diagram</i> .....	3
1.2.2 <i>Interaction Cross sections</i> .....	5
1.2.3 <i>Index of refraction</i> .....	6
1.2.4 <i>Absorption</i> .....	6
1.2.5 <i>Scattering</i> .....	7
1.2.6 <i>Emissions</i> .....	8
1.3 IONIZING RADIATION INTERACTION WITH MATTER.....	9
1.3.1 <i>Photoelectric effect</i> .....	10
1.3.2 <i>Compton effect</i> .....	11
1.3.3 <i>Pair production</i> .....	12
1.4 BROAD SPECTRUM LIGHT SOURCES.....	12
1.4.1 <i>Sunlight</i> .....	12
1.4.2 <i>Lamps and LEDs</i> .....	13
1.4.3 <i>Cherenkov emissions</i> .....	14

1.5	TISSUE OPTICAL PROPERTIES.....	15
1.5.1	<i>Major chromophores</i> .....	15
1.5.2	<i>Autofluorescence</i> .....	16
1.6	OVERVIEW AND AIMS.....	17
1.6.1	<i>Summary of chapters</i> .....	18
1.7	REFERENCES.....	19
<b>2</b>	<b>MONTE CARLO MODELING PHOTON-TISSUE INTERACTION USING ON-DEMAND CLOUD INFRASTRUCTURE.....</b>	<b>21</b>
2.1	INTRODUCTION.....	21
2.2	MATERIALS AND METHODS.....	25
2.3	RESULTS.....	32
2.4	DISCUSSION.....	33
2.5	CONCLUSIONS.....	37
2.6	ACKNOWLEDGEMENTS.....	37
2.7	SUPPLEMENTARY MATERIAL.....	37
2.8	REFERENCES.....	38
<b>3</b>	<b>A MODEL OF PHOTODYNAMIC DOSE AT DEPTH IN TISSUE.....</b>	<b>42</b>
3.1	INTRODUCTION.....	42
3.2	MATERIALS AND METHODS.....	48
3.2.1	<i>Monte Carlo model</i> .....	48
3.2.2	<i>Light Fluence</i> .....	51

3.2.3	<i>PpIX production and photobleaching</i> .....	54
3.2.4	<i>Photodynamic Dose</i> .....	56
3.3	RESULTS .....	56
3.4	DISCUSSION.....	63
3.5	CONCLUSIONS.....	69
3.6	ACKNOWLEDGMENTS .....	70
3.7	SUPPLEMENTARY MATERIAL .....	70
3.8	REFERENCES.....	71
<b>4</b>	<b>WEATHER-BASED DOSE PLANNING FOR DAYLIGHT-PDT OF SKIN</b> .....	<b>76</b>
4.1	INTRODUCTION .....	76
4.2	MATERIALS AND METHODS.....	78
4.3	RESULTS.....	81
4.4	DISCUSSION.....	86
4.5	CONCLUSIONS.....	89
4.6	ACKNOWLEDGMENTS .....	90
4.7	REFERENCES.....	90
<b>5</b>	<b>ESTIMATING SIGNAL INTENSITY FOR <i>IN VIVO</i> IMAGING OF CHERENKOV AND EXCITED LUMINESCENCE</b> .....	<b>93</b>
5.1	INTRODUCTION .....	93
5.2	THEORY .....	95
5.2.1	<i>Signal Source</i> .....	95

5.2.2	<i>Tissue Optical Properties</i> .....	96
5.2.3	<i>Detection Hardware</i> .....	98
5.3	METHODS.....	99
5.3.1	<i>Cherenkov</i> .....	100
5.3.2	<i>Luminescence</i> .....	101
5.3.3	<i>Tissue Optics</i> .....	101
5.3.4	<i>System Configuration</i> .....	102
5.4	RESULTS AND DISCUSSION .....	107
5.4.1	<i>Cherenkov Emission</i> .....	109
5.4.2	<i>Cherenkov-excited Luminescence</i> .....	111
5.4.3	<i>Experimental validation</i> .....	114
5.5	CONCLUSIONS.....	123
5.5.1	<i>Imaging system</i> .....	123
5.5.2	<i>In vivo properties</i> .....	124
5.5.3	<i>Model</i> .....	125
5.6	ACKNOWLEDGMENTS .....	125
5.7	SUPPLEMENTARY MATERIAL .....	126
5.8	REFERENCES.....	126
<b>6</b>	<b>MODELS OF CHERENKOV SPREAD AND LIMITS OF DETECTION IN TISSUE</b> .....	<b>130</b>
6.1	INTRODUCTION .....	130
6.2	MATERIALS AND METHODS.....	131

6.2.1	<i>Cherenkov spread</i> .....	132
6.2.2	<i>Limits of detection</i> .....	133
6.3	RESULTS .....	136
6.3.1	<i>Cherenkov spread</i> .....	136
6.3.2	<i>Limits of detection</i> .....	139
6.4	DISCUSSION.....	145
6.4.1	<i>Cherenkov spread</i> .....	145
6.4.2	<i>Limits of detection</i> .....	146
6.5	CONCLUSIONS.....	148
6.6	REFERENCES.....	149
<b>7</b>	<b>CHERENKOV-EXCITED LUMINESCENCE AND LUMINESCENT COMPOUNDS FOR USE IN RADIOTHERAPY</b> .....	<b>151</b>
7.1	INTRODUCTION .....	151
7.1.1	<i>Oxygenation</i> .....	152
7.1.2	<i>Field Verification</i> .....	154
7.2	METHODS AND MATERIALS.....	156
7.2.1	<i>Oxygenation</i> .....	156
7.2.2	<i>Field Verification</i> .....	159
7.3	RESULTS .....	163
7.3.1	<i>Oxygenation</i> .....	163
7.3.2	<i>Field Verification</i> .....	170

7.4	DISCUSSION.....	176
7.4.1	<i>Oxygenation</i> .....	176
7.4.2	<i>Field Verification</i> .....	182
7.5	CONCLUSION.....	186
7.5.1	<i>Oxygenation</i> .....	186
7.5.2	<i>Field Verification</i> .....	186
7.6	ACKNOWLEDGMENTS .....	187
7.7	REFERENCES.....	187
<b>8</b>	<b>NEAR REAL-TIME NON-CONTACT <i>IN VIVO</i> PO<sub>2</sub> ESTIMATION DURING FRACTIONATED EXTERNAL BEAM RADIOTHERAPY .....</b>	<b>192</b>
8.1	INTRODUCTION .....	192
8.2	METHODS.....	196
8.2.1	<i>Imaging system</i> .....	196
8.2.2	<i>Luminescent pO<sub>2</sub> sensor</i> .....	197
8.2.3	<i>In vitro</i> .....	197
8.2.4	<i>In vivo</i> .....	198
8.2.5	<i>Image Analysis</i> .....	199
8.3	RESULTS.....	202
8.3.1	<i>In vitro</i> .....	203
8.3.2	<i>In vivo</i> .....	208
8.4	DISCUSSION.....	212

8.5	CONCLUSIONS.....	215
8.6	ACKNOWLEDGMENTS .....	216
8.7	REFERENCES.....	216
<b>9</b>	<b>CONCLUSIONS AND FUTURE WORK.....</b>	<b>219</b>
9.1	OVERVIEW .....	219
9.2	MODELING .....	219
9.2.1	<i>Code modifications.....</i>	<i>219</i>
9.2.2	<i>Infrastructure.....</i>	<i>221</i>
9.3	PHOTODYNAMIC THERAPY TRANSLATION.....	222
9.3.1	<i>Light Dose estimates.....</i>	<i>222</i>
9.3.2	<i>PDD estimates .....</i>	<i>224</i>
9.4	RADIATION THERAPY TRANSLATION .....	226
9.5	REFERENCES.....	227
<b>10</b>	<b>THESIS DEFENSE VIDEO RECORDING.....</b>	<b>229</b>

## List of Tables

Table 2.3-1: Execution times for GAMOS simulations with given source events .....	33
Table 3.1-1: Depths of Representative Skin Lesions from Figure 3.1-1.....	44
Table 3.2-1: Light dose distribution parameters used to calculate effective cytotoxic threshold.....	54
Table 3.3-1: Depth( $\mu\text{m}$ ) of threshold photodynamic dose for different treatment times after 30 min incubation.....	61
Table 3.3-2: Minimum treatment times needed for PpIX-induce cytotoxicity for various Sun irradiance (350nm-800nm) values based on uniformly scaled irradiance measurements taken with Apogee SS-110 and reported previously by Marra et. al.18 Yellow-highlighted cells indicate treatment times between 2-2.5 hours, whereas red is treatments over 2.5 hours. Additional data is provided in S463	
Table 5.4-1: Parameters considered in photon budget and typical range of quanta available at each stage.....	108
Table 5.8-1: Summary of photon budget parameters for different source depths in tissue, using optimal wavelength range.....	129
Table 7.4-1: Side-by-side comparison of phosphorescent oxygen sensors utilized for CEL .....	182
Table 8.2-1:Phosphorescence properties of PtG4 and Oxyphor 2P .....	202
Table 8.3-1:The measured in vivo minimum dose required for detection for 50uM PtG4 or Oxyphor 2P based SNR>1 for given delays .....	212

## List of Figures

Figure 1.2-1: An example of a Jablonski diagram showing how absorbed optical photons lead to state transitions, where the probability of absorption and emission is shown at the bottom. The inset at the bottom right is a representation of interactions which occur when the excited compound is a photosensitizer. ....	4
Figure 1.3-1: The relative areas of dominant contribution from the three types of interactions that occur, based upon the energy of the photon ( $\gamma$ ) and the atomic number ( $Z$ ) of the matter. Lines indicate where neighboring types of interaction have equal probability. Based on Figure 7.1 of Attix. <sup>6</sup> .....	10
Figure 2.1-1: GAMOS architecture relies on Geant4 and allows for user-defined plugins (A). GAMOS is installed with external dependencies, some of which are larger than the base program (B). The complexity of the Geant4 code-base is represented by the number .....	23
Figure 2.2-1: The relative size of GAMOS and the external packages are shown (A). The concept of how the GAMOS installation is deployed using a Virtual Machine (B) or Container (C) architecture. ....	28
Figure 2.2-2: A programmatically configured cloud-infrastructure can be used to send jobs to individual containers located on multiple servers, which send results to specific storage buckets.....	31
Figure 3.1-1: Representative skin lesions (H&E 40x). The black line represents the distance from the surface of the corneal layer to the surface of the lesion. The yellow line represents the distance from the surface of the corneal layer to the base of the lesion. An example of an actinic keratosis (A), basal cell carcinoma, superficial type (B), squamous cell carcinoma in situ (C), basal cell carcinoma, nodular type (D), invasive well-differentiated squamous cell carcinoma (E), and a hypertrophic actinic keratosis (F). ....	44
Figure 3.1-2: (A) Spectrum of 6 light sources. The simulation (dotted) is based on a theoretical uniform spectrum, whereas the other white light sources (solid) are of equal irradiance but based on measured spectral distributions. The narrow-band sources (dashed) are based on clinically-relevant irradiance used in conventional PDT and the spectrum is nearly equivalent to the FDA-approved Blue-U (Sun/DUSA) and the RhodaLED (Biofrontera) light sources. (B) PpIX-weighted spectrum showing wide variation in effective irradiance. ....	47
Figure 3.2-1: A representation of the GAMOS geometry is shown in the upper left. Tissue optical properties $\mu_s$ (middle) and $\mu_a$ (right) were defined between 350nm and 900nm for each of the 7 tissue layers. A constant refractive index ( $n$ ) and anisotropy ( $g$ ) were assumed for each layer and are provided in the table. ....	50

Figure 3.2-2: (A) Fluence rate at various depths in 7-layer tissue model, based on a simulated spectrally uniform light source. (B) The PpIX-weighted effective fluence rate in the same model. (C) Geometry of 7-layer skin model, where arrows indicate depths used in A and B..... 52

Figure 3.3-1: A comparison of the fluence rate (A) and effective fluence rate (B) as a function of depth for the uniform simulation, Sun, CFL, Halogen, Blue LED and Red LED..... 57

Figure 3.3-2: Effective light fluence as a function of time and depth for two different treatment times show how deeper light activation can be achieved by either extending treatment durations or using alternate light sources. The black line shows the expected threshold for PDT response at  $0.7 J_{eff}/cm^2$ . ..... 58

Figure 3.3-3: A model of PpIX concentrations at treatment times of 30 min and 2 hours for light treatments with a fluence rate of  $35mW/cm^2$  for broadband sources, and  $100 mW/cm^2$  for the red and blue sources, where both were incubated for 30 minutes. The black line represents the threshold PpIX concentration (50nM). ..... 60

Figure 3.3-4: The photodynamic dose will differ between 30 minute (left) and 2 hour (right) treatments, for incubation times of 30minutes (top) and 2 hours (bottom)..... 62

Figure 4.2-1: The SolarPathfinder device showing compass alignment and nearby spectroradiometer (A), where the clear plastic dome (inset) reflects the sky. The outline of obstructions is traced (light green shaded region B), which can then be converted to a binary grid of sunny and shaded regions (C). Then as a comparison, the same procedure was conducted in an open untried area outside of the building (C-inset) where morning sunlight was available, but tall trees to the west blocked the afternoon sun. .... 80

Figure 4.3-1: Solar variation from total irradiance measurements is shown, as taken at 5 minute intervals over approximately 5 days, showing high irradiances only in the afternoon hours (pink shaded area) and at least an order of magnitude less in the mornings (blue shade areas). ..... 81

Figure 4.3-2: Spectroradiometer measurements taken at 14:00 on a clear day in June (A), a cloudy day the same week (B), a clear day in October (C), and a partly cloudy day in October (D). The weather report is shown in the upper left of each graph, and the total and PpIX-weighted irradiance are given in the upper right. .... 83

Figure 4.3-3: Scaled daylight spectra measurements of outdoor and indoor daylight (A) and their PpIX-weighted counterparts (B). Snapshots of photodynamic dose after 30 minute incubation for various treatment times (Outdoor: solid, Indoor: dotted) (C) and their corresponding maximal depth of effective PDT dose at depth (D)..... 84

Figure 4.3-4: Comparison of indoor PpIX-weighted spectroradiometer measurements (x-axis) and cloud coverage (A) and UV Index (B), where the blue shaded region provides a 95% confidence interval and the dashed lines provide the 95% prediction limits..... 85

Figure 5.3-1: Geometry of the imaging system used for experimental validation. The LINAC gantry head is placed below the subject, providing a source of high energy photons. The subject is placed on the treatment couch with a mirror above to redirect photons ..... 107

Figure 5.4-1: (A) Monte Carlo estimate of Cherenkov photons produced in 1 mm<sup>2</sup> as the result of: a single radiation pulse (0.03 cGy), 30 pulses (0.83 cGy), 60 pulses (1.67 cGy), and 7200 pulses (2 Gy). (B) Using tissue optical properties reported in S1, the Cherenkov photon attenuation is simulated for 30 pulses (0.83 cGy) observed at the tissue surface for photons emitted at various depths (d<sub>1</sub>). (C) Schematic depicting imaging system and components of interest. (D) Using the inputs reported in S1 and outputs in S2, a simulated photon budget for a Cherenkov source at 3 mm below the tissue surface (d<sub>1</sub>) generated by a 0.83 cGy dose, as detected by a 2 × 2 binned-pixel. The blue dotted line at right represents the usable dynamic range of the sensor..... 110

Figure 5.4-2: (A) Approximate tissue attenuation coefficients overlaid with extinction coefficient for 10 μM PtG4 (left y-axis), and corresponding normalized emission spectrum (right y-axis). (B) Simulated photon count of CEL caused by 0.83 cGy dose for a PtG4 source at various depths (d<sub>1</sub>) within tissue. (C) Schematic depicting imaging system and components of interest. (D) Using the inputs reported in S1 and outputs in S3, a simulated photon budget for PtG4 CEL source at 3 mm below the tissue surface (d<sub>1</sub>) generated by a 0.83 cGy dose, as detected by a 2 × 2 binned-pixel. The blue dotted line at right represents the usable dynamic range of the sensor ..... 112

Figure 5.4-3: Theoretical Signal-to-Background ratio for Cherenkov and CEL detection with a photocathode room temperature, and cooled with dry nitrogen. Cherenkov values are the same..... 114

Figure 5.4-4: Experimental Cherenkov image frames of a mouse phantom captured with varying numbers of accumulations on chip (AOC)..... 117

Figure 5.4-5: (A) Experimental Cherenkov image frame of a mouse phantom captured using 2 AOC; (B) normalized histogram of intensity count for region of image receiving radiation dose (inside white area in (A)); (C) normalized histogram of intensity count for background area around mouse phantom (outside green area in (A)); (D) median pixel intensity for experimentally acquired Cherenkov image of previously defined regions using different AOCs. Error bars show standard deviation of pixel intensities in region; (E) experimentally determined signal-to-background ratio and signal to noise ratio for varying AOCs. .... 118

Figure 5.4-6: Images from in vivo experiment: (A) room-light image of mouse with two flank tumors injected with PtG4. (B) Single Cherenkov frame of interest during scanned imaging. (C) Single phosphorescence frame. (D) Regions of interests identified on phosphorescence frame, which were used to generate values shown in table. ....	121
Figure 6.2-1: Photon energy distributions used in Monte Carlo models.....	132
Figure 6.2-2: A multi-layer tissue model containing a tumor-simulating inclusion is defined (A) where the average $\mu_{\text{eff}}$ is shown for each layer-type (B). The luminescent absorption and emission assigned to the tumor is provided as a contrast agent (C). ....	134
Figure 6.3-1: Cherenkov emissions recorded from simulations of 2.5mm wide photon source (top) or electron source (bottom) in multi-layer tissue volume.....	137
Figure 6.3-2: Experimental Cherenkov measurements of photon and electron beams in water. ....	138
Figure 6.3-3: Analysis of beam width (full-width 80% of max) and penumbra region (gray-shaded) for 3mm wide photon and electron sources, based on the average of measurements between depths of 1mm and 8mm. ....	139
Figure 6.3-4: The spectral distribution of Cherenkov emissions in a model with a tumor inclusion at depth of 2mm, as detected in the tumor (light blue), exiting the tumor (orange), at the surface (surface), or contributing to luminescent excitation (dotted-indigo) (A). The deposited dose for 6MV and 18MV at depths into the tissue model (B) and the corresponding The optical Cherenkov fluence which are clearly affected by the tissue optical properties of each layer. (C) .....	140
Figure 6.3-5: The photon fluence due to external optical illumination or X-ray induce Cherenkov emissions at depth in tissue (A) is compared to the corresponding normalized fluorescence detected at the surface, where the blood-nets (red vertical lines) introduce considerable attenuation(B). 2D-histograms of the surface luminescence are shown (C).....	142
Figure 6.3-6:The Cherenkov-excitation ranking of the top 50 candidate compounds available in the PhotoChemCAD database. The chemical structure of the top three candidates are shown.....	143
Figure 6.3-7: The absorption spectra of compounds with the highest Cherenkov excitation ranking .....	144
Figure 7.3-1: Absorbance and emission spectra for oxygen sensors. The absorbance and fluorescence emission spectra for Ir(btbt) <sub>2</sub> (acac) (blue), MitoID (red), PtG4 (green) and MM2 (gray).....	163
Figure 7.3-2: Comparison of commercially available oxygen sensors in PANC-1 cells. A. MM2 (gray), MitoID (red), and Ir(btbt) <sub>2</sub> (acac) (blue) were incubated with PANC-1	

cells overnight. Fluorescence was measured in the presence of ambient oxygen (light gray, MM2, medium gray, MitoID, and dark gray, Ir(btbt)2(acac)) and with glucose oxidase catalase enzymatic oxygen scavenging (black). B. The brightest commercial oxygen sensors were explored at decreasing concentrations (20  $\mu\text{g}/\text{mL}$ , 2  $\mu\text{g}/\text{mL}$ , 0.2  $\mu\text{g}/\text{mL}$ , and 0.02  $\mu\text{g}/\text{mL}$  to determine the lowest concentration that can be detected. Inset shows fluorescence microscopy of each sensor (20  $\mu\text{g}/\text{mL}$ ) loaded into PANC-1 cells. Excitation and emission were measured at 380 nm and 660 nm, respectively. The fluorescence intensity represents the average of 6 experiments +/- SEM..... 164

Figure 7.3-3: Comparison of CEL with phosphorescent oxygen sensors. Increasing concentrations of each sensor indicated by darker shades of each color (0.02  $\mu\text{g}/\text{mL}$ , 0.2  $\mu\text{g}/\text{mL}$ , 2  $\mu\text{g}/\text{mL}$ , and 20  $\mu\text{g}/\text{mL}$ , MitoID (red), MM2 (gray), PtG4 (green), and Ir(btbt)2(acac) (blue)) were analyzed in ambient oxygen or with enzymatic oxygen scavenger glucose oxidase/catalase (black). A 96-well plate with these reagents in solution (A.) or loaded into PANC-1 cells (B.) was exposed to 6 MV radiation from a LINAC, and the phosphorescence intensity was measured via ICCD..... 165

Figure 7.3-4: CELSI setup and in vivo imaging with PtG4 and Ir(btbt)2(acac). The LINAC gantry head that delivers radiation is placed below the mouse that is positioned on the treatment couch. A mirror above redirects the photons to the ICCD. A. lateral view of the mouse depicting passage of radiation sheet in red B. aerial view as imaged from the ICCD camera. C. Under anesthesia of isoflurane, 2.5 nmol of each reagent was injected into subcutaneous MDA-MB-231luc-D3H2LN tumors. Maximum intensity projection of PtG4 and of Ir(btbt)2(acac) at 4.26  $\mu\text{s}$  delay time, respectively. Tumors are indicated with arrows..... 167

Figure 7.3-5: In vivo lifetime imaging with PtG4 and Ir(btbt)2(acac). Under anesthesia of isoflurane, the animal was imaged at various delay times based on reported lifetimes of each reagent to gain emission lifetime information alive and 30 min after sacrifice, when the drop in blood circulation and respiration causes a marked decrease in pO<sub>2</sub> values. A. comparison of PtG4 phosphorescence intensity at various delay times based on known PtG4 emission lifetime in subcutaneous tumors alive (top) and 30 min after sacrifice (bottom) B. PtG4 emission lifetime maps and box and whiskers plot of emission lifetimes of alive and sacrificed mouse C. pO<sub>2</sub> maps and box and whiskers plot of oxygen levels in alive and sacrificed mouse for PtG4. D. phosphorescence intensity of tumors injected with Ir(btbt)2(acac) at different delay times informed from the reported Ir(btbt)2(acac) emission lifetime, map of emission lifetime, and pO<sub>2</sub> map in sacrificed mouse. All lifetime maps and subsequent pO<sub>2</sub> maps for both reagents were constructed utilizing data from the 4.26  $\mu\text{s}$  delay time. .... 169

Figure 7.3-6: Normalized fluorescence emission of 9 UV-sensitive inks (A) and their corresponding normalized lifetime (B) based on 380nm excitation ..... 170

Figure 7.3-7: Mean intensity of select UV-sensitive tattoo inks in ethanol solution, measured with 380nm UV excitation (A), during the MV X-ray pulse (B) and after the pulse (C). ..... 171

Figure 7.3-8: Select UV-sensitive ink was painted on the surface of a PDMS-based skin-simulation phantom (E inset) and imaged during the X-ray pulse (A), after the pulse (B), and without time gating (C). The same phantom was imaged using a cobalt-60 source and 635 bandpass filter (D). The signal-to-noise (SNR) was measured for each ink using each imaging method (E), and was compared to the same configuration with a 600 longpass filter. The ratio of the SNR with (SNRF) and without (SNRNF) the filter provide insight on the noise (F). characteristics of each method. The SNR for each ink was measured using both a 550nm bandpass filter (left) and 635 bandpass filter (right, where the inset show the filter pass band (gray shaded) in relation to the ink emission (G)). ..... 173

Figure 7.3-9: Red UV ink was tattooed into a skin-simulating phantom (top inset) to test system resolution under room-lights (top), time-gate to X-ray delivery (middle), and continuous acquisition during dose delivery (bottom). ..... 175

Figure 7.4-1: Considerations for CELSI. A. Cherenkov imaging timing. Experimentally the gate width is generally set between 5 - 10 times the deoxygenated lifetime ( $\tau_0$ ) of the reagent of interest. Luminescence is detected at a series of delay times (red blocks) after the Cherenkov emission (blue column) to assess the emission lifetime of phosphorescent agents. The LINAC generates radiation pulses at a repetition rate between 2.7 and 17ms (600MU/min - 100MU/min). B. plot of emission decay curves as a function of quantum yield..... 178

Figure 8.1-1: Representative timing diagram of a clinical linac showing when Cherenkov emissions and Cherenkov-excited luminescence are formed in relation to the pulses (a), and examples of the timing windows used in imaging (b). In previous work image stacks were collected with each setting for 1+Gy (c), whereas the new method automatically cycles the acquisition settings, acquiring frames using less than 10cGy (d). ..... 195

Figure 8.3-1:Using mean ROI intensities summed over multiple frames, the lifetime and resulting pO<sub>2</sub> were determined for PtG4 and Oxyphor 2P solutions. Here, low O<sub>2</sub> solutions have glucose catalase oxidase added to the solution whereas Atm. O<sub>2</sub> are at atmospheric oxygen levels. .... 204

Figure 8.3-2:Intensity images of phosphorescence emitted by Oxyphor 2P in solution using 2x2 pixel binning (a). Histograms of pixel-based lifetime estimates determined through direct calculation of (2) (b)or using a curve-fit of (1) (c)..... 206

Figure 8.3-3:A map of standard deviations for estimated pO<sub>2</sub> values of deoxygenated Oxyphor 2P (a). An example histogram of the pO<sub>2</sub> measurements for 2x2 pixel binning and summation of 8 frames (b), and the corresponding pO<sub>2</sub> map (c). ..... 207

Figure 8.3-4: A demonstration of in vivo pO<sub>2</sub> detection. The Mouse ROI and tumor inclusion are automatically identified and highlighted in (a). The phosphorescence intensity of the direct tumoral injection of Oxyphor 2P at different delays is shown in (b). After 2x2 median pixel binning the lifetime (c) and pO<sub>2</sub> are calculated (d). .... 209

Figure 8.3-5: A box and violin plot showing all the estimated pO<sub>2</sub> values for direct tumoral injections of Oxyphor 2P (N=3 Mice) (a) and for Matrigel injections of Oxyphor 2P (N=3 Mice) (b)..... 210

Figure 8.3-6: Multiple 2Gy dose fractions were delivered to each mouse before and after sacrifice. The median pO<sub>2</sub> is shown relative to either injection time or sacrifice for Oxyphor 2P in either tumor (a) or Matrigel (b), PtG4 in either tumor (c) or Matrigel (d). All estimates were determined from a 4x4 median pixel binning and 8 summed frames. .... 211

## *List of Acronyms*

<b>Acronym</b>	<b>Definition</b>
ADC	Analogue-to-digital converter
AK	Actinic keratosis
ALA	Aminolevulinic acid
AOC	Accumulations on chip
API	Application programable interface
AWS	Amazon Web Services
BCC	Basal cell carcinoma
BOLD-MRI	Blood oxygen level dependent magnetic resonance imaging
CCD	Charged coupled device
CEL	Cherenkov-excited luminescence
CELSI	Cherenkov-excited luminescence Sheet Imaging
CMOS	Complementary metal-oxide semiconductor
CPU	Central processing unit
EBI	Effective background illumination
EBRT	External beam radiotherapy
EC2	Elastic cloud compute
ECR	Elastic container repository
ECS	Elastic container service
FWHM	Full width at half maximum
GAMOS	Geant4 architecture for medically oriented simulations
GATE	Geant4 Application for Emissions Tomography
Geant4	Geometry and Tracking 4
GODCAT	Glucose oxidase and catalase
H&E	Hematoxylin and eosin
ICCD	Intensified charged coupled device
ICMOS	Intensified complimentary metal-oxide semiconductor
LED	Light emitting diode
MCML	Monte Carlo for multi-layer media
MCP	Microchannel plate
MCX	Monte Carlo eXtreme
MCXYZ	Monte Carlo XYZ
MLC	Multi-leaf collimator
MMC	Mesh-based Monte Carlo
NIST	National Institute of Standards and Technology

PBS	Phosphate-buffered saline
PDT	Photodynamic therapy
PET	Positron emission tomography
PpIX	Protoporphyrin IX
QE	Quantum efficiency
RT	Radiotherapy
ROI	Region of Interest
S3	Simple Storage Solution
SCC	Squamous cell carcinoma
vCPU	Virtual central processing unit
X-PDT	X-ray photodynamic therapy

# CHAPTER 1

## 1 Photon interactions with matter

### 1.1 Introduction

This chapter defines key concepts used throughout the thesis. Due to the broad nature of topics addressed, spanning both optics and ionizing radiation, it seems necessary to introduce a common terminology used throughout the text. This is intended to provide a reader with sufficient scientific background, but outside the field, the ability to understand key concepts presented in later chapters. Since the fields of biomedical optics and radiation therapy are often separated into distinct clinical and research silos, the current work aims to present tools utilizing unified models of both light-tissue interactions and radiation physics. A key theme throughout this work is the development of tools to simplify the extraction of information contained in photon interactions. These tools are built upon the laws governing the physical interactions of photons and electrons, and then applied to clinical problems, focusing on monitoring and treating cancer. The goal of this chapter is not to overwhelm the reader with mathematical equations, but instead provide enough information to describe how optical diagnostic tools can be developed utilizing these foundational concepts.

Electromagnetic energy can be conceptualized as continuous waves or discrete quantized packets of energy called photons. Electromagnetic wave theory is built on the foundation of Maxwell's equations proposed during the latter half of the 19<sup>th</sup> century.<sup>1</sup> This set of four partial differential equations relate electric and magnetic fields, and were used by Maxwell to show light is a form of electromagnetism.<sup>2</sup> These concepts can be used to describe light behavior as a wave and provide the mathematical basis for describing reflection and refraction at boundary interfaces. Lorentz then expanded on Maxwell's models by proposing light was related to atomic oscillations, where in a simplified sense, the interactions between an electron and nucleus can be conceptualized as two bodies connected by a spring-like force, related by Hooke's Law.<sup>3</sup> The electron with a certain mass and charge will oscillate around an equilibrium position, and forces due to intrinsic properties of the nucleus and applied fields will either dampen or further drive these oscillations. While the Lorentz model provides the basis for explaining light absorption, it does not account for probabilities of these events occurring, and both Lorentz and Maxwell consider energy as a continuum. Scientific contributions in the early 20<sup>th</sup> century led to the concept of quantum theory which posits energy can only occur and be exchanged in discrete quanta.<sup>4</sup> Using these theories, the concepts of light scattering, absorption and luminescence can be explained more fully.

In the realm of ionizing radiation though, there are many interactions which can occur where the probability of interaction is based on how the incoming photon imparts energy into an atom or molecule. These interactions are primarily influenced by the atomic number of the material and incident photon energy. The photon interacts with the electron cloud,

imparting enough energy to free the electron. Excess photon energy will then either be absorbed by the atom or scattered. At energy levels commonly seen in radiotherapy incident photons will often free an electron and scatter a photon. The photon scattering and ionization process can cascade until the energy of the photon is fully absorbed. A description of common ionizing photon-matter interactions is provided in subsequent sections.

## **1.2 Light Interactions with Matter**

### **1.2.1 Jablonski Diagram**

A visual representation of these interactions is provided in the Jablonski diagram shown in Figure 1.2-1. Biological tissue is a heterogeneous mixture of particles that absorb and scatter light with a range of probabilities defined by the wavelength and the material properties of the particles, with both wave-like scattering and quantum-like absorption and re-emission. Figure 1.2-1 provides an example of the potential interactions which this particle may undergo when acted upon by an external photon.

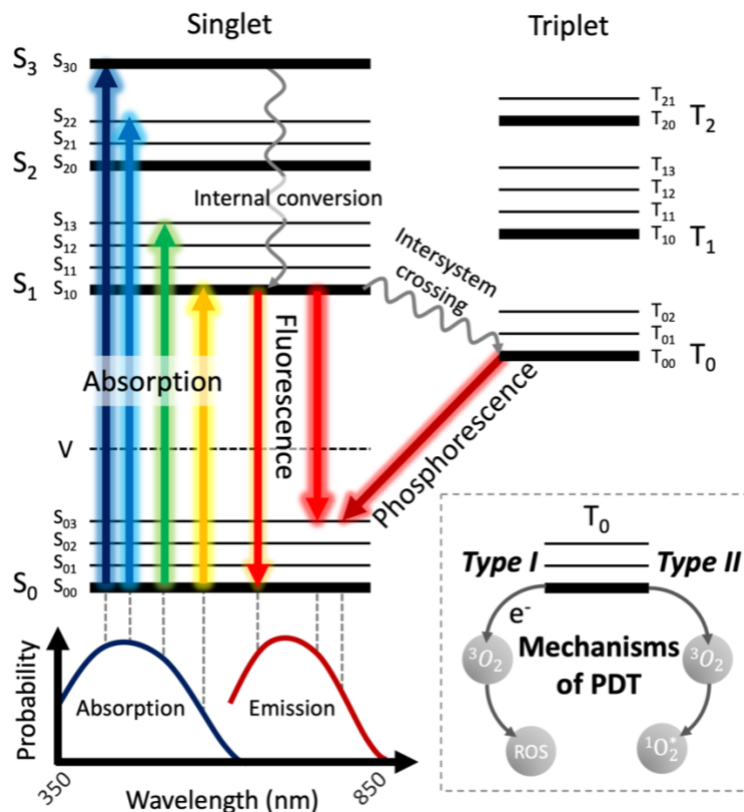


Figure 1.2-1: An example of a Jablonski diagram showing how absorbed optical photons lead to state transitions, where the probability of absorption and emission is shown at the bottom. The inset at the bottom right is a representation of interactions which occur when the excited compound is a photosensitizer.

The Jablonski diagram presented above is used as a visual guide to represent the various states an atom or molecule can assume, where the thick horizontal lines are vibrational ground states of each electronic state ( $S_{00}$ ,  $S_{10}$ ,  $S_{20}$ ,  $T_{00}$ , etc.) and the solid thin horizontal lines are higher-level vibrational states ( $S_{01}$ ,  $S_{11}$ ,  $S_{21}$ ,  $T_{01}$ , etc.). Since the frequency of light can be related to the photon energy through Planck's constant,  $h$ , as shown in equation 1, one can conceptualize an electronic state transition, for example  $S_{00} + \text{photon} \rightarrow S_{10}$ , as driving the Lorentz oscillator at resonance, resulting in the electronic transition. This

transition, termed absorption, is shown as upward arrows in Figure 1.2-1, and results in the annihilation of the incoming photon.

$$E_{\text{photon}} = h\nu \quad (1)$$

$$h = 6.626 \times 10^{-34} \text{J} \cdot \text{s} = 4.136 \times 10^{-15} \text{eV} \cdot \text{s}$$

When the incoming photon energy does not match allowed state transitions, or in the Lorentz model is an off-resonance frequency, the atom or molecule does not transition. In this case, the interaction of the incoming photon with electronic cloud of the target results in a reemission or scattering of the original photon in a modulated direction. This can be conceptualized as a virtual state in a Jablonski diagram (dashed horizontal line Figure 1.2-1) which is a short-lived unobservable state.

When an atom or molecule is in an excited state it can transition to a lower state through radiative or non-radiative transitions. Radiative emissions such as fluorescence or phosphorescence are shown in Figure 1.2-1 as straight arrows pointing down. Non-radiative transitions are represented as curving lines in Figure 1.2-1 which depict internal conversion which is the relaxation of vibrational states through emission of heat, or for intersystem crossing a change in spin states.

### **1.2.2 Interaction Cross sections**

The Jablonski diagram provides a visual description of the energy states of an atom or molecule; however, it does not address the probability of interaction. The concept of cross-sectional area is used in this case, where the cross section is used as a metric of likelihood of interaction. The cross section does not just rely on the physical cross-sectional area of

the particle, but also the permittivity of the particle and the wavelength of the incoming photon. The product of the cross section and density of particles in a given volume is used to define the attenuation coefficient, which will be discussed in subsequent sections.

### **1.2.3 Index of refraction**

The index refraction is based on the ratio of the speed of light in a vacuum and the phase velocity for the given medium. In wave theory the index of refraction is used to describe refraction angles observed at boundaries by applying Snell's law, where the refractive index of a vacuum is defined as 1, air is slightly higher, and water is 1.33. The phase velocity and resulting index of refraction are based on the relative permittivity and permeability of a material, however the permeability is often not considered in naturally occurring materials since it remains relatively constant at 1. The phase velocity is a measure of the rate a wave will propagate in a given medium, which changes based on the degree to which the material can be polarized by an external electric field. In the complex model of the index of refraction, the imaginary portion is considered the extinction coefficient and relates to the absorption of the material for the given light frequency. As incoming light approaches resonant frequencies absorption becomes the dominant process for the given material.

### **1.2.4 Absorption**

As discussed earlier, absorption events result in the annihilation of the incoming photon. Absorption results in a higher electronic state of the absorbing atom or molecule which will be dissipated by vibrational relaxation as heat, or through luminescence emission

which will be discussed in more detail in a subsequent section. If the intensity of the incident light into a system is known ( $I_0$ ), then the output light passing through the system ( $I(h)$ ) can be measured to determine the absorbance of the system. This relation is the Beer-Lambert Law and is shown in equation 2:

$$I(x) = I_0 e^{-\mu_a x} \quad \text{or} \quad (2)$$

$$T = \frac{I(h)}{I_0} = e^{-\mu_a x} = 10^{-A} = 10^{\epsilon c x}$$

Where  $x$  is the distance the incident light travels through the medium under test, and  $\mu_a$  is related to the cross section and density of the material ( $\mu_a = \sigma_a \rho$ ), and  $T$  is the transmittance of light through the system. In chemistry, the absorbance ( $A$ ) of a material is the product of the molar extinction coefficient ( $\epsilon$ ), molar concentration ( $c$ ), and distance traveled ( $x$ ). The units used for the absorption coefficient ( $\mu_a$ ) are commonly inverse millimeters or inverse centimeters, which is a measure of how many absorption events will take place per unit length. Conversely, the inverse of this is mean free path, or how far a photon can be expected to travel without being absorbed.

### 1.2.5 Scattering

Much like absorption, the scattering coefficient is the product of the scattering cross section and density of scattering particles, and the reciprocal of the scattering coefficient is the mean free path. As stated previously, scattering occurs when a photon interacts with the electron cloud of an atom or molecule but is not absorbed into an allowable electronic state. Scattering can be broadly categorized into elastic and inelastic interactions, where the work

presented in this thesis mainly considers elastic scattering, which is defined by a lack of energy transfer. Elastic scattering can again be split into two sub-categories: Rayleigh scattering and Mie scattering. If we first make the assumption a scattering particle has refractive index  $n$  and radius  $a$ , the Rayleigh approximation can be applied when  $na \ll \frac{\lambda}{2\pi}$ . In this regime the scattering cross section ( $\sigma_s$ ) is proportional to  $\frac{1}{\lambda^4}$ , which is to say shorter wavelengths or higher energy light has a much higher probability of being scattered.<sup>5</sup> Mie theory is a set of solutions to Maxwell's equations where Mie scattering is generally considered when the wavelength and particle size are comparable. Mie scattering is highly anisotropic and generally forward directed. The scattering phase function can be described by the anisotropy parameter  $g$ , where  $g = \langle \cos\theta \rangle$ . When  $g = 0$  the system scatters isotropically, whereas when  $g = -1$  this represents backscattering back towards the original photon direction, and  $g = 1$  represents forward scattering, in the direction of travel.

### **1.2.6 Emissions**

Luminescence occurs as a result of a radiative relaxation from a higher to lower electronic states (Figure 1.2-1). The work in this thesis focuses on the photoluminescent phenomena of fluorescence and phosphorescence. Fluorescent emission generally occurs on the order of  $10^{-9}$  seconds when transitioning between singlet states, whereas phosphorescence requires an intersystem crossing to a triplet state before radiative relaxation, which occurs on the order of  $10^{-6}$  seconds or slower. Emissions are generally at a longer wavelength or lower energy as shown in Figure 1.2-1. The Stoke's shift is the wavelength difference between peaks of the absorption spectra and fluorescent emission spectra. Not all absorbed

photons result in luminescent emissions, and the quantum yield is a parameter used to describe the probability of emission, where external quenching can reduce this value. Photodynamic therapy utilizes excited triple state photosensitizers which react either directly (Type II) or indirectly through electron donation (Type I) with molecular oxygen to create locally cytotoxic singlet oxygen or reactive oxygen species as shown in the Figure 1.2-1 inset.

### **1.3 Ionizing Radiation Interaction with Matter**

While the previous sections discussed the interaction of optical photons with matter resulting in an excited electronic state, ionizing radiation occurs when the incoming photon has sufficient energy to *free* an electron. The predominant mechanism of action is based on the photon energy and atomic number ( $Z$ ) of the absorber and is summarized in Figure 1.3-1. Three photon interaction mechanisms are considered and described in subsequent sections: photoelectric effect, Compton effect, and pair production, where all generate a free electron. Rayleigh scattering can also occur at low energy levels, but only redirects the photon and does not produce a free electron. It is also important to note that rarely do these mechanisms occur alone, as the outgoing photons and electrons from the events can undergo a long cascade of events from these secondary particles, and so macroscopically these events are usually somewhat interwoven through multiple interactions.

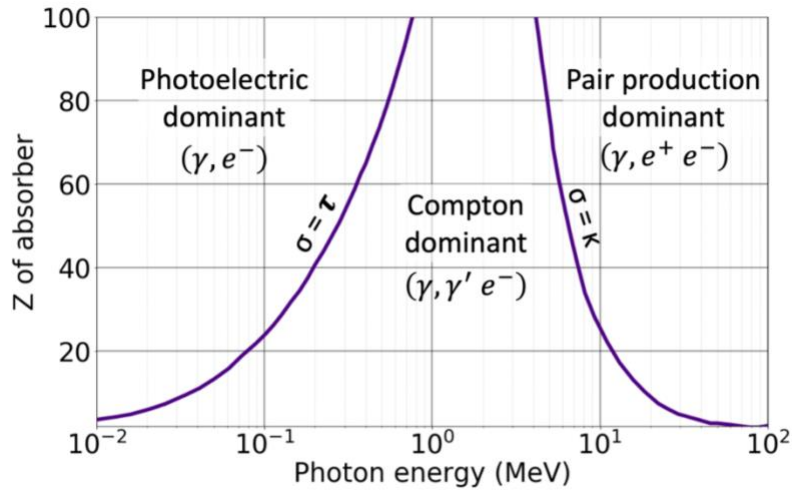


Figure 1.3-1: The relative areas of dominant contribution from the three types of interactions that occur, based upon the energy of the photon ( $\gamma$ ) and the atomic number ( $Z$ ) of the matter. Lines indicate where neighboring types of interaction have equal probability. Based on Figure 7.1 of Attix.<sup>6</sup>

### 1.3.1 Photoelectric effect

The photoelectric effect occurs when an incoming photon of sufficient energy frees an inner-shell electron, which can be conceptualized as a collision of the photon with the electron where the photon is annihilated in this interaction. If the photon energy is greater than that of the binding energy acting on the electron, the electron will be scattered at a non-zero angle relative to the incidence. This angle tends to be sideways for lower energies, due to the interaction of electric fields, and more forward directed for higher energies. The free electron will have kinetic energy equal to the difference of the incoming photon and binding energies.

The probability of these interactions is calculated as the cross section ( $\tau$ ) which is proportional to  $\frac{Z^4}{(h\nu)^3}$  and the resulting mass attenuation coefficient ( $\frac{\tau}{\rho}$ ) is proportional to

$\left(\frac{Z}{h\nu}\right)^3$ .<sup>6</sup> This relation indicates higher Z materials will have a greatly increased photoelectric cross section. In these high Z materials, the binding energy on the electrons nearest the nucleus, such as the K-shell will introduce a step function where photon energies below the binding threshold will not be able to free electrons in this shell, and only higher-order shells will undergo interactions. Once the photon energy passes the threshold to break the binding energy of the inner shell, the photoelectric cross section will increase. The high Z dependence and these step functions at specific energies are used in a practical manner to provide contrast in X-ray imaging.

### **1.3.2 Compton effect**

At higher energy levels, as shown in Figure 1.3-1, the photoelectric effect is replaced by the Compton effect as the dominant mechanism of interaction. In this case the incoming photon is not absorbed but scattered. Both a free electron with certain kinetic energy and angle, and lower-energy photon are emitted at angles measured relative to the incidence and on opposing sides of this axis. If the photon scatter is minimal there will be little energy loss, however, with higher energy incident photons, backscatter photons will have an energy approaching 0.255 MeV, and side-scatter photons will approach 0.511MeV.<sup>6</sup> The probability of interaction is again calculated as the cross section ( $\sigma$ ), which is proportional to Z and the Compton mass attenuation  $\left(\frac{\sigma}{\rho}\right)$  is approximately Z-independent.<sup>6</sup> The Compton effect is predominant mechanism of action in the energy levels commonly seen in clinical radiation therapy.

### **1.3.3 Pair production**

At energies above threshold of 1.022 MeV, but practically above 10MeV, an incident photon can be absorbed giving rise to both an electron and positron. As the incident energy increases the electron and positron emissions will be more forward directed. The pair production cross section per atom ( $\kappa$ ) is approximately proportional to  $Z^2$  and has a logarithmic relation to the incident energy.<sup>6</sup> The mass attenuation coefficient for pair production ( $\frac{\kappa}{\rho}$ ) is proportional to  $Z$ .

## **1.4 Broad spectrum light sources**

Since optical properties of a material are reliant on the incident photon energy, or equivalently wavelength, analytic and even stochastic approaches to determining photon-matter mechanisms of action often assume a narrowband source to simplify the problem. These approaches hold true for applications utilizing laser sources or even some LED sources, however they become more difficult to apply when using a polychromatic light source, which combines multiple energies, often resulting in white light. The specific combinations of wavelengths observed in white or broad-spectrum light depends on how the source is generated, as will be discussed in the next section.

### **1.4.1 Sunlight**

The sun generates electromagnetic radiation over a wide spectrum, from gamma emissions down to radio waves, where optical interactions can be defined for emissions between UV and NIR (See Figure 3-1.2A). The atmosphere provides protection from some of the more

harmful energetic radiation. Since the atmosphere is mainly composed of nitrogen and oxygen molecules, Rayleigh scattering is the dominant interaction and gives the sky its blue color, whereas when the sun is at the horizon the light must travel through additional dense atmosphere and water vapor, allowing longer red wavelengths to pass. Biological systems have developed based on the broad spectral characteristics of solar radiation reaching the surface and while energy transfer can be necessary, like in the case of photosynthesis or vitamin D production, prolonged exposure can be harmful due to excessive UV exposure.

Mutagenic UV-C light (100-280nm) generally does not reach the surface due to absorption by the ozone, however both UV-B (280-320nm) and UV-A (320-400nm) are present. At ground level it is estimated only 5% of UV radiation is UV-B, which is the primary cause of erythema or “sun burns” resulting in chronic skin damage.<sup>7,8</sup> The total UV exposure increases approximately 4% with every 300m increase in elevation, and 65% of UV radiation reaching the surface occurs between the hours of 10AM and 2PM. UV-B and UV-A light can easily be attenuated by glass barriers or the application of chemical sunscreens.<sup>9,10</sup>

### **1.4.2 Lamps and LEDs**

While sunlight is needed to sustain life, its variability and UV components can introduce complications when planning experiments utilizing it as a source. If white light is required, one alternative is to use lamps or light emitting diodes. Lamps can utilize a variety of bulbs (see Figure 3.1-2A for spectral characteristics), the most common being incandescent or

compact fluorescent lights. Incandescent bulbs work by heating a metal filament which generates light in a broad spectrum similar to sunlight without much of the UV components. However, these bulbs can become very hot and emit far into NIR. Compact fluorescent lights are a more energy efficient options, which produce light by exciting a gaseous compound, usually mercury and argon. This generates sustained UV light which interacts with a phosphor coating on the glass walls, emitting visible light. Unlike sunlight or incandescent light, the spectrum of fluorescent lights often contains large spikes across the visible spectrum. Light emitting diodes produce light through solid-state interactions which generally confine the emissions to a single band with a spectral band on the order of 20-50nm. White light LEDs generally produce strong blue light around 450nm which interacts with a phosphor coating designed to emit broadly yellow light. This produces a bi-modal spectrum with a strong blue peak mixing with a broad yellow peak, resulting in the perception of white light.

### **1.4.3 Cherenkov emissions**

Cherenkov emissions occur when a charged particle, like an electron, passes through a dielectric material, such as tissue, with a speed greater than which light can propagate in the medium. It is commonly conceptualized as a “sonic boom” of light, but physically occurs from the electromagnetic torque of the dielectric dipoles relaxing as the charge passes through the medium, resulting in energy release as photons. These Cherenkov photons are generated over a wide spectral range, but within the UV-NIR range the distribution is proportional to  $1/\lambda^2$ , as described by the Frank-Tamm formula, which can

be used to calculate the number of emitted Cherenkov photons for a given input phase velocity ( $\beta$ ) and target refractive index ( $n$ ).<sup>11,12</sup> In the case of the Compton effect where a free electron is scattered, if the electron has sufficient energy (219 keV,  $n=1.4$ ) multiple Cherenkov photons can be generated along the electron path.<sup>13,14</sup> One key characteristic of Cherenkov emissions in tissue which is leveraged in this work is its dose dependence. The maximum dose observed during radiation therapy occurs between approximately 1-3.5cm into tissue, depending on the energy level, thus Cherenkov light is generated deeper in tissue than conventional external illumination can reach. Additionally, MeV radiation can penetrate several cm into tissue, thereby producing light deep into tissue.

## **1.5 Tissue optical properties**

Tissue is a heterogenous mixture of biological material, commonly found in layers of structured composition. As such, the nature of the optical properties of each component will be a contributing factor to photon interactions (See Figure 3.2-1 for optical properties of skin). In both high energy gamma photons as well as optical photons, water, one of the main components of tissue, exhibits a low-absorption therapeutic window.<sup>15</sup>

### **1.5.1 Major chromophores**

To help simplify models of tissue, the optical properties of commonly occurring components can be characterized. These components are generally thought to be dominated by the molecules that absorb the most, namely water, hemoglobin, lipids and melanin. The concentration of water is generally thought to be approximately 80%, and has its lowest

optical absorption around 500nm.<sup>16</sup> Hemoglobin is a major component of red blood cells used to carry oxygen, and its absorption will change based on whether or not it is bound to oxygen. This can be used to help estimate the oxygen saturation of blood present in the capillaries within tissue. Lipids, of fat are stored in the form of adipocytes with diameters of approximately 100 $\mu$ m and a refractive index near 1.5.<sup>5</sup> Melanin is of interest in skin and retinal applications, where it is broadly absorbing with a flat spectrum sloping down towards the red/NIR wavelengths. In the context of scattering, cell and organelle size play a large role on the type and direction of scattering events.

### **1.5.2 Autofluorescence**

Biological systems contain a number of substances which are considered endogenous fluorophores. When excited at the proper wavelength, maximally in the UV, these compounds emit longer wavelength light. This must be considered as a potential source of added background signal when attempting to detect exogenous fluorescence. Common sources of tissue autofluorescence are due to proteins containing aromatic amino acids, NADH, pyridine-based nucleotides, flavins, and collagen, among others.<sup>17,18</sup> When imaging in the red or NIR contributions from porphyrins and other molecules can be more dominant. However, there are many contributors to the autofluorescence response of tissue, at different wavelength bands.

## 1.6 Overview and Aims

The chapters presented in this thesis encompass a range of areas which are slightly disconnected in application area but are brought together by the common theoretical foundations of using photon-matter interaction models to understand limits of broadband radiation propagation. Then the results of both experiments and modeling are applied to specific needs in biomedicine that utilize broad-band spectra and follow light-tissue interactions. These *in vivo* clinical applications attempt to show how similar models can be applied to both Photodynamic Therapy (PDT) and Radiation Therapy (RT).

There are four primary aims which are addressed in this work:

1. Develop a clinically-applicable model-based method to estimate photodynamic dose at depth in tissue for both narrowband and broad-spectrum light sources.
2. Expand the model-based dose planning to incorporate the use of sunlight as an activating spectrum, with real time weather forecast data and clinical feedback to have broader planning and dosimetric utility.
3. Develop models of both Cherenkov emissions and Cherenkov-excited luminescence which can be used to optimize detection using a time-gated intensified camera.
4. Experimentally validate this model by measuring *in vivo* pO<sub>2</sub> at high temporal resolution during fractionated radiotherapy treatments while also investigating how different system parameters effect the overall signal-to-noise ratio.

This work is organized to address these aims. Aim 1 is supported by work in Chapters 2-3. Aim 2 is supported by Chapter 3-4. Aim 3 is supported by Chapters 2 and 5-6. Aim 4 is supported by Chapters 7-8. The final chapter proposes future work and conclusions.

### **1.6.1 Summary of chapters**

The Monte Carlo techniques described in Chapter 2 are the foundation for the majority of the modeling work presented in this thesis. The infrastructure created to efficiently run these simulations has provided the ability to easily scale simulations to consider both broad spectral inputs as well as multiple geometries.

This modeling strategy has been applied in Chapter 3 to better understand light-tissue interactions occurring during photodynamic therapy treatments of skin. While there have been previous reports of simplified models of light fluence at specific blue or red treatment wavelengths, this work describes how 55 wavebands from 350nm to 900nm were simulated to provide estimates of light fluence at depth in tissue. The work further describes how these simulations can be used to estimate light fluence from an arbitrary broad-spectrum source and combines this with estimates of photosensitizer diffusion to determine a depth-dependent photodynamic dose. Expanding on the applications of PDT treatments using sunlight, Chapter 4 describes how weather reports could be used as a surrogate for spectroradiometer measurements, potentially enabling real-time light dose monitoring for daylight PDT treatments.

The concept of radiation-induced Cherenkov emission is explored in Chapter 5, where a photon budget for the generation and detection of Cherenkov and Cherenkov-excited

luminescence was developed. This concept is explored in more depth using the Monte Carlo modeling package in Chapter 6, where Cherenkov-excited luminescence is compared to optical excitation in a multilayer tissue model. While Chapters 5 and 6 focus on models of Cherenkov-related light emissions, the next two chapters take an experimental approach. Potential contrast agents for use during radiation therapy are presented in Chapter 7, which is followed by the presentation of an experimental procedure for estimating *in vivo* pO<sub>2</sub> in near real-time in Chapter 8. Finally, future directions and conclusions are presented in Chapter 9.

## 1.7 References

1. Maxwell, J.C. On Physical Lines of Force. *Philosophical Magazine* **XXI**, (1861).
2. Maxwell, J.C. A Dynamical Theory of the Electromagnetic Field. *Proceedings of the Royal Society of London* **155**, 459–512 (1865).
3. Almog, I.F., Bradley, M.S. & Bulovic, V. The Lorentz Oscillator and its Applications. (2011).
4. Ter Haar, D. On a Heuristic Point of View about the Creation and Conversion of Light. in *The Old Quantum Theory* 91–107 (Pergamon Press, 1967).
5. Boudoux, C. *Fundamentals of Biomedical Optics*. (Blurb, 2019).
6. Attix, F. Gamma- and X-Ray Interactions in Matter. in *Introduction to Radiological Physics and Radiation Dosimetry* 124–159 (John Wiley & Sons, Ltd, 2007). doi:10.1002/9783527617135.ch7.
7. Urbach, F. Phototoxic skin reaction to UVR — is “sunburn” a “burn”? *Photodermatology, Photoimmunology & Photomedicine* **12**, 219–221 (1996).
8. Baron, E. D., Stern, R. S. & Taylor, C. R. Correlating Skin Type and Minimum Erythema Dose. *Arch Dermatol* **135**, 1278–1279 (1999).
9. Urbach, F. Ultraviolet radiation and skin cancer of humans. *Journal of Photochemistry and Photobiology B: Biology* **40**, 3–7 (1997).
10. Trautinger, F. Basic Photodermatology. (2018).

11. Čerenkov, P. A. Visible Radiation Produced by Electrons Moving in a Medium with Velocities Exceeding that of Light. *Physical Review* **52**, 378–379 (1937).
12. Frank, I. & Tamm, Ig. Coherent Visible Radiation of Fast Electrons Passing Through Matter. in *Selected Papers* (eds. Tamm, I. E., Bolotovskii, B. M., Frenkel, V. Ya. & Peierls, R.) 29–35 (Springer, 1991). doi:10.1007/978-3-642-74626-0\_2.
13. Glaser, A. K., Zhang, R., Andreozzi, J. M., Gladstone, D. J. & Pogue, B. W. Cherenkov radiation fluence estimates in tissue for molecular imaging and therapy applications. *Physics in Medicine and Biology* **60**, 6701–6718 (2015).
14. Ciarrocchi, E. & Belcari, N. Cerenkov luminescence imaging: physics principles and potential applications in biomedical sciences. *EJNMMI Phys* **4**, (2017).
15. Palik, E. D. *Handbook of Optical Constants of Solids*. (Academic Press, 1998).
16. Van Gemert, M. J. C., Jacques, S. L., Sterenborg, H. J. C. M. & Star, W. M. Skin optics. *IEEE Transactions on Biomedical Engineering* **36**, 1146–1154 (1989).
17. Monici, M. Cell and tissue autofluorescence research and diagnostic applications. in *Biotechnology Annual Review* vol. 11 227–256 (Elsevier, 2005).
18. Menter, J. M. Temperature dependence of collagen fluorescence. *Photochem. Photobiol. Sci.* **5**, 403–410 (2006).

# CHAPTER 2

## **2 Monte Carlo modeling photon-tissue interaction using on-demand cloud infrastructure**

### **2.1 Introduction**

Stochastic modelling by Monte Carlo (MC) methods are used as the fundamental standard to simulate effects in human tissues. This chapter details the extension of previous efforts by our group, by updating MC radiation-optical software and demonstrating the ability to programmatically deploy multiple copies of a MC software package onto a cloud-based infrastructure for efficiently running complex simulations. The method can be used with positron or beta emitting radiotracers,<sup>1,2</sup> or external beam therapy,<sup>3-5</sup> as a tool to generate optical excitation and emission signals within tissue. While cloud-based MC packages have been proposed previously,<sup>6-8</sup> to date, no distributable MC packages have been deployed on a cloud platform utilizing a container architecture, allowing for scalable parallelization, as was the goal here.

Estimating optical light propagation through heterogeneous turbid media is often addressed through MC methods, where many of the current software solutions stem from the original

work by Wang and Jacques who developed the publicly available Monte Carlo for Multi-Layer media (MCML),<sup>9</sup> which is used to approximate photon fluence in layered tissues. Since the development of MCML, many other optical MC packages have been developed, each solving a specific problem: Monte Carlo XYZ (MCXYZ) uses voxelized optical properties,<sup>10</sup> Monte Carlo eXtreme (MCX) also uses voxelized geometry but is optimized for GPU acceleration,<sup>11</sup> Mesh-based Monte Carlo (MMC) uses a mesh-based geometry to reduce computational complexity,<sup>12</sup> while MCflour is another example which focuses on modelling fluorescence but is limited to homogeneous media.<sup>13</sup> A number of other optical MC packages exist, with many recent publications focusing on optimization of computation time through GPU,<sup>14–16</sup> or parallel execution.<sup>17–19</sup>

The use of MC methods is widely adopted in the field of high energy physics, where Geometry and Tracking (Geant4) software, maintained by an international consortium, is a core resource used by most in the field.<sup>20–22</sup> While Geant4 is widely used, it also has a steep learning curve, requiring the user to write C++ code to define world geometries, input events, and detector processes. In the field of medical physics, the need to write and compile C++ code has been addressed through Geant4 architecture for medically oriented simulations (GAMOS), which is a software package designed to interface with many of the Geant4 features using simple script files which do not need to be compiled by the user.<sup>23</sup> A plug-in for GAMOS to account for optical photon transport, including tissue optical properties and Cherenkov emissions was previously developed and validated by Glaser et al and our current work used the same validation methods before demonstrating the cloud-based deployment functionality.<sup>24</sup>

A diagram showing the relation of Geant4 to GAMOS is provided in Figure 2.1-1A, where the Geant4 kernel has three main components: 1) the underlying physics model, 2) the processes to define the inputs and track the events over multiple steps, and 3) a geometry definition which considers the placement and composition of every aspect of the simulation. GAMOS wraps this implementation so the functionality of Geant4 can be called using a number of plug-ins. A command interpreter is used to convert two text-based

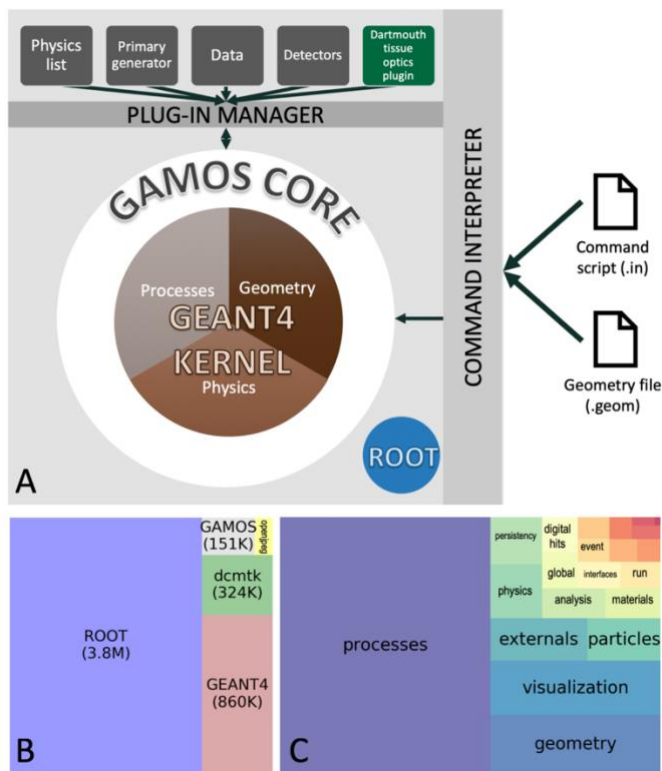


Figure 2.1-1: GAMOS architecture relies on Geant4 and allows for user-defined plug-ins (A). GAMOS is installed with external dependencies, some of which are larger than the base program (B). The complexity of the Geant4 code-base is represented by the number

input files: the command script, and geometry file, which are used to describe all parameters necessary to run a simulation. GAMOS is also configured to utilize ROOT, a software package developed at CERN for visualizing large datasets.<sup>25</sup> While ROOT is not a core component of GAMOS, it is part of the installation package and, as shown in Figure 2.1-1B, accounts for 3.8 million lines of code which is 4X more code than the core dependency Geant4. An analysis of the code structure of Geant4 shows the relative distribution of the code

(Figure 2.1-1C), where processes such as managing transport for different physics lists, accounts for the majority of the logic.

The optical-photon transport functionality was designed as a plug-in to GAMOS which allows users to attach material properties to define wavelength-specific absorption, scattering, anisotropy, refractive index and fluorescence properties.<sup>24</sup> Additionally, routines for generating Cherenkov and scintillation emissions were implemented. These changes allowed the ability run MC simulations involving high-energy physics and tissue optical properties. However, since the tissue optics plugin for GAMOS was first published, GAMOS has transitioned from version 4.0.0 to 6.1.0. As a result, much of the functionality of the original plugin suffered from broken dependencies. While other X-ray-optical interaction MC packages exist,<sup>26-28</sup> many lack the full functionality provided by the Geant4-GAMOS kernel. As part of the current work, the original functionality of the plugin has been restored by addressing the broken dependencies, where all changes are publicly available for review using code versioning, and validation scripts provided with the original publication were used to verify functionality. These modifications have been packaged into both a virtual machine and a low-overhead container architecture. There is a growing trend in MC packages to utilize a combination of multi-threading, GPU optimization and parallel execution to optimize execution time.<sup>17-19,6,8</sup> While GAMOS is not designed for multi-threaded or GPU optimization, we present a method to achieve parallel execution. A demonstration of programmatically deploying multiple cloud-based instances of GAMOS 6.1.0 with the tissue optics plugin is provided in Chapter 6, where

multiple simulations were conducted in parallel to track optical emissions of a tumor model for both optical and X-ray input sources.

## **2.2 Materials and Methods**

The latest version of GAMOS (6.1.0) was downloaded to a virtual machine running Ubuntu 18.04.03 LTS. A version control system (git) was used to track all changes made to the GamosCore source directory. The files added for the tissue optics plugin in GAMOS version 4.0.0 were re-added to their respective sub-directories. Modifications to the appropriate headers and plugin settings were made in the source files. Generally, the overall operation of GAMOS at a function-level remained unchanged. The modified GAMOS was then re-compiled using the provided installation scripts. All validation scripts used for the original tissue optics plugin and available in the supplementary material were then run to verify appropriate functionality.

A full GAMOS installation requires approximately 7.4GB of storage, as shown in Figure 2.2-1A. Since the development was performed on a virtual machine, a snapshot of the system can be exported to a single portable file using the Open Virtualization Format. This was performed using VirtualBox, resulting in an 8.55GB .ova file, which includes the application and the guest OS.

As an additional delivery mechanism, the code was also packaged in a container using an application called Docker.<sup>29,30</sup> Docker uses a single-file script (Dockerfile) to programmatically define a system image which it places in a container, which acts much

like a virtual machine with lower resource requirements. The download scripts commonly used to install GAMOS were retrieved using the `wget` command. The `getGamosFiles.sh` script was modified to add commands to replace the `GamosCore` source directory with the one containing the tissue optics plugin and the corresponding validations. A file used to install additional package dependencies (`installMissingPackages.Docker.Ubuntu.18.04.sh`), mainly required by `ROOT`, was also placed in this directory. An additional script provided to interface with Amazon Web Services (AWS) Batch<sup>31</sup> (`fetch_and_run.sh`) was also placed in this directory.

```
1. FROM ubuntu:18.04
2. # Define working directory to install GAMOS
3. WORKDIR /docker_gamos
4. # Move scripts in current directory into container image
5. ADD . /docker_gamos
6. ADD fetch_and_run.sh /usr/local/bin/fetch_and_run.sh
7. # Setup basic system paramters
8. ARG DEBIAN_FRONTEND=noninteractive
9. RUN apt-get update && \
10. apt-get install -y --no-install-recommends apt-utils
11. # Add sudo permissions for docker admin user
12. RUN apt-get install -y sudo
13. RUN adduser --disabled-password --gecos '' docker
14. RUN adduser docker sudo
15. RUN echo '%sudo ALL=(ALL) NOPASSWD:ALL' >> /etc/sudoers
16. # Use new docker user to install GAMOS
17. USER docker
18. RUN ./installMissingPackages.Docker.Ubuntu.18.04.sh
19. RUN sudo ./installGamos.sh /docker_gamos/gamos
20. RUN source gamos/GAMOS.6.1.0/config/configamos.sh
21. # Define what to do when container starts
22. ENTRYPOINT ["/docker_gamos/fetch_and_run.sh"]
```

The Dockerfile shown above starts with a base Ubuntu 18.04 image (Line 1), much like our initial virtual machine. The GAMOS installation scripts and AWS Batch interface are copied to the container image using the `ADD` command (Lines 5-6). Basic system

configurations used to define how applications are installed from the command line are performed in Lines 7-12, and a docker user is created and given administrator privileges in Lines 13-15. The new user is then used to call the script to install the necessary package dependencies (Lines 17-18) and then run the GAMOS installation (Line 19). GAMOS is then configured and added to the PATH using Line 20. When the container starts it queries the ENTRYPOINT command specified in Line 22, which in this case is a shell script provide by AWS Batch, which expects information about the location of a zip file containing a script it will execute. Alternatively, the ENTRY point can be switched to “/bin/bash” so the when the container is started the user can interface with a basic command prompt.

Once Dockerfile sufficiently describes the desired system parameters the docker build command is used to create the container. This runs the Dockerfile script to create the application image which can be referenced by multiple containers on the same system without interfering with each other or installing multiple guest operating systems like in a virtual machine (Figure 2.2-1 B-C). The container can then be stored in a repository so any system running Docker can retrieve the application image and run one or many containers. In the present example the container repository is AWS Elastic Container Repository (ECR) but the same file is publicly available on DockerHub, linked in Supplementary Material. The newly built container is tagged with a name and pushed to this repository for later retrieval.

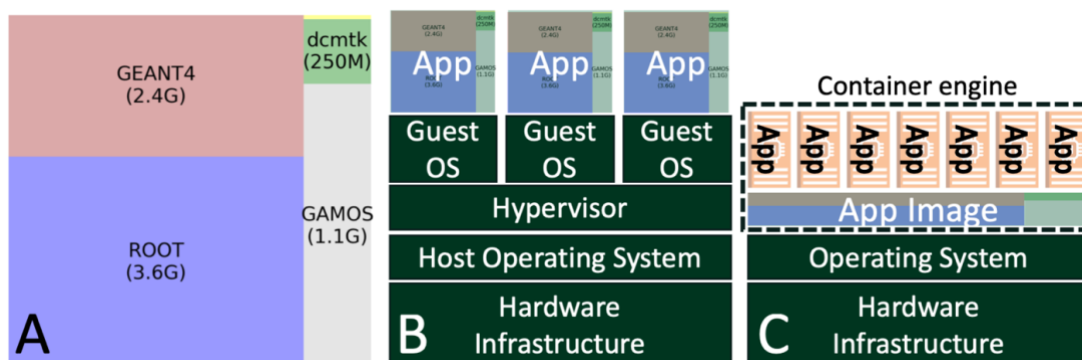


Figure 2.2-1: The relative size of GAMOS and the external packages are shown (A). The concept of how the GAMOS installation is deployed using a Virtual Machine (B) or Container (C) architecture.

Using a Python API interface for AWS (Boto3),<sup>32</sup> the infrastructure needed to access and configure these containers as well as define parameters for parallel execution can be defined. An interactive notebook with all code needed to configure the environment is available in the Supplementary Material.

Using the AWS web interface, a new user with *AdimPowerUser* group security settings can be created and assigned an API token. The Boto3 API will use these configuration settings which can be stored on the local computer with read-only user permissions. Storing the access keys in a file improves security by reducing the chance the secret token is displayed and logged when executing API commands, and also reduces the need to manually specify the security credentials with every API call. Once the local Boto3 package is configured, it can be used to create and modify the infrastructure described in Figure 2.2-2.

To implement large parallel executions of GAMOS, AWS Batch was leveraged to define the computational infrastructure and job queue.<sup>31</sup> Batch provides an interface between the

Elastic Container Service (ECS), compute resources (EC2), and storage services (S3) to efficiently replicate multiple container images and assign tasks in an on-demand basis.

Since GAMOS is a relatively large application for a container, a launch template was used to expand the basic container storage specification. The launch template also specified the default server image and networking parameters used when initializing a new compute resource. With this launch template in place, Batch is used to configure a computing environment, which specifies the total number of virtual CPUs (vCPU) and instance types. The instance types are used to specify the size and specialty of the requested server, where they can be optimized for compute, memory, GPU, etc. In the present example the instance types were limited to EC2 instance types c5.2xlarge, c5.4xlarge, c5.9xlarge, which are the names given by AWS, where the first letter indicates compute-optimized instances, the 5 indicates the hardware is an AWS 5th-generation system, and the size is correlated with the number of vCPUs and system memory available to the system. In this case a c5.2xlarge has 8 vCPUs and 16GB of memory, whereas the c5.9xlarge has 36 vCPUs and 72GB of memory. A maximum of 128 vCPUs was set for this environment which are automatically allocated by AWS Batch when submitting jobs. Additionally, this service is used to automatically stop instances when the queue is empty, after jobs are finished.

A Batch job queue was then defined and given a priority, where the priority is used when multiple queues are active. The previously defined compute environment was added as an available resource associated with this job queue. Once the compute environment and job queue are defined, individual jobs can be created and submitted to the queue. All jobs are given a unique name and provided with specific container and environment properties and

then sent to a queue for processing. The container properties define the location of the container repository and desired container image, as well as what resources to assign to the container. In this case 2 vCPUs and 2 GB of memory were allocated to each container, where 2 vCPUs were chosen because this is the smallest number used by an EC2 instance. The container environment settings then specify the location of a compressed zip file on the network-accessible storage service (S3), and also provide input arguments. The input arguments specify the shell script, contained in the zip file, to execute and additional input arguments specifying a random seed, number of events, and other simulation-specific parameters. Since the job definition is created using a Python script, it can be wrapped in a loop to specify a range of input parameters and submit the job to the queue for processing. The zip file also provides templates of GAMOS input files and any necessary extra inputs needed to run the simulation.

After the job queue becomes populated with jobs, Batch verifies the validity of the environmental parameters. The compute autoscaling service then automatically requests resources, which are loaded with the specified container image (Figure 2.2-1C, Figure 2.2-2), and the container is replicated based on the vCPU and memory allocations defined by the job. For example, since c5.9xlarge instance have 36 vCPUs and 72 GB of memory, and our jobs were allocated to containers with 2 vCPUs and 2 GB of memory, the number of containers on an instance is limited by the number of vCPUs, or 18 containers on this instance.

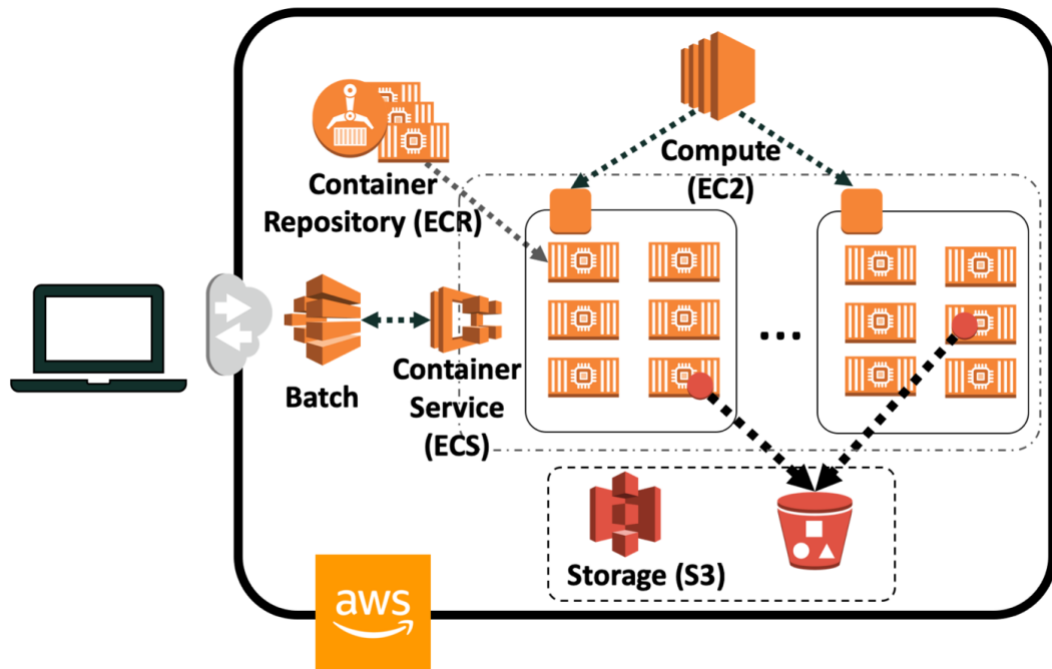


Figure 2.2-2: A programmatically configured cloud-infrastructure can be used to send jobs to individual containers located on multiple servers, which send results to specific storage buckets.

Each container executes the code defined by the provided shell script, using unique input arguments provided in the job definition. The shell script is used to modify the GAMOS input file templates provided to the container and run the GAMOS simulation. While this script runs, the status can be monitored from the AWS CloudWatch web interface, where all standard terminal outputs for each container are logged in real-time. The bash script also contains commands to copy the simulation directory to a container-specific sub-folder of the S3 storage bucket containing the original simulation definition zip file. So, after a set of jobs is complete, all results are stored in sub-folders of a single S3 bucket which can be programmatically retrieved for analysis.

## 2.3 Results

Briefly, the container-based cloud deployment of GAMOS was used to compare the fluorescence emissions of a tumor inclusion and light fluence in a multi-layer tissue model, using a total of 154 simulations and is documented in detail in Chapter 6. The number of interactions that are tracked for each event governs the speed at which these simulations can be run, where the run-time of each of the 154 simulations was recorded and averaged for each of the four source types, as depicted by the average system time in Table 2.3-1. Since 430nm light is highly attenuated by skin, the average execution time of these simulations is on the order of minutes, whereas deeper penetrating 630nm light will propagate further through tissue and more event interactions are tracked, resulting in a longer execution time. When high-energy X-rays are used, multiple optical photons are generated through Cherenkov emissions along the path of scattered high-energy electrons, where each of these secondary emissions are then tracked, further increasing the simulation complexity and execution time.

The compute cluster defined for these simulations specified a maximum number of virtual CPUs as 128, which was the limiting factor for container distribution. With 128 vCPUs, 64 containers could run simultaneously. Each simulation has an approximately 5-minute overhead needed to initiate the container infrastructure, but scaling allows for parallel execution which provides the ability to execute all simulations in the same time required to execute a single simulation. With the Cherenkov simulations, 7 tumor inclusion depths were specified, and each depth had 10 simulations of  $10^6$  events, each with a different

random seed provided as an input argument. Since our compute-environment only specified 64 containers, and the 6MV and 18MV simulations were split into 70 simulations, approximately 90% of these simulations were completed within the average system time required to complete one simulation, but the final 10% required additional time to be executed. However, due to the auto-scaling natures of this system, the final 10% could be finished on a smaller compute resource.

*Table 2.3-1: Execution times for GAMOS simulations with given source events*

	<b>430nm</b>	<b>630nm</b>	<b>6MV</b>	<b>18MV</b>
<b>Depths tested</b>	7	7	7	7
<b>Total simulations</b>	7	7	70	70
<b>Average system time</b>	10 min	55 min	90 min	200 min
<b>Sequential time</b>	70 min	6.5 hr.	105 hr.	233 hr.
<b>Parallel execution time</b>	~15 min	~1 hr.	~3 hr.	~7 hr.

## 2.4 Discussion

GAMOS is a powerful Monte Carlo software package well suited for medical physics simulations. It has a large footprint though, which relies on many dependencies, and can make compilation during installation a time-consuming endeavor. While the plugin architecture provided the opportunity for Glaser et al to expand the capability of GAMOS into the field of biomedical optics, this plugin was not kept current with subsequent

GAMOS releases. As such, since only the source code of the plugin was released, when GAMOS was updated, the functionality to use these features was lost. The current work has provided updates to this optical light transport plugin, so it is again compatible with the latest version of GAMOS. Additionally, both a VM and container of these changes have been made available as a way of removing the need to compile code, the main bottleneck in installation. While efforts will be made to maintain this functionality in future GAMOS releases, in the event this does not occur, the VM and container-based packages will continue to provide needed functionality to users requiring these features.

While other Monte Carlo software packages exist for modeling light transport<sup>6-16</sup> or high-energy physics,<sup>20,33-35</sup> fewer have intersecting capabilities.<sup>23-25</sup> While users may be able to accomplish this through Geant4, it also requires the ability to write sometimes complex C++ code. Other examples of similar software package are the Geant4 wrapper PTSim and TOPAS.<sup>35,36</sup> Much like GAMOS, PTSim and TOPAS provide a similar text-based input structure, targeting particle therapy applications, and currently lack the optical transport plugin provided by Glaser et al.<sup>24</sup> A separate collaboration, Geant4 Application for Emissions Tomography (GATE), has developed similar macro script-based interface for modeling medical imaging applications, specifically targeting movement and temporal-based models.<sup>37</sup> There are also optical transport plugins for GATE, which are capable of modeling bioluminescence and fluorescence.<sup>38</sup> Recent advances to GATE have also demonstrated the ability to simulate and track Cherenkov and scintillation emissions,<sup>39</sup> so much of the same functionality could be achieved with GATE. While each of these

packages target specific user communities, their architecture is such that they could be deployed in a similar container-based infrastructure as described here.

There is a growing trend to use rapidly advancing computational infrastructure to further optimize the execution time needed to run MC simulations. Much of this effort has focused on GPU-optimization,<sup>14–16,28,40</sup> however this generally requires the underlying MC packages to be written such that it can leverage these resources. Another approach has been to develop methods for parallel execution on multiple CPUs or cores.<sup>17–19</sup> These methods often focus on developing a task distribution system for available compute nodes, which can be a time-consuming design endeavor. Others have proposed cloud-based execution previously,<sup>6,8</sup> which the current work employs by describing a method to achieve parallel execution using Python scripts and an on demand infrastructure. This greatly reduces the capital investment needed to purchase and maintain a dedicated server infrastructure and reduces the need to re-write thread-safe or GPU-optimized code.

Through the development of a container, the overall resources needed to run multiple GAMOS instances is greatly reduced. GAMOS is not inherently thread-safe, so containers provide the ability to compartmentalize the execution of simulations with independent compute resource, all on the same server. While the present example is provided for deployment on a cloud-based infrastructure, it could also be run on a locally managed server or a single institution's computing cluster.

The companion code provided with this publication provides an example of how a cloud-based infrastructure can be deployed programmatically. This could be useful for

researchers with limited resources, where a local compute cluster is not available, or a high-end server is impractical. In the provided examples, billing was based mainly on the compute-time required to accomplish, so for example, a simulation utilizing 1 vCPU for 100 hours is billed at a similar rate as 100 vCPUs utilizing 1 hour. While there are limits on the maximum resource which can be utilized at any one time, it may have benefits for users who wish to quickly obtain results, without purchasing a powerful server.

The framework presented by the current work focus on deploying a GAMOS container in a cloud-based infrastructure, but with slight modifications the same framework could be used to deploy any opensource software which can be run from the command line. This provides a simple pathway for other Monte Carlo packages mentioned previously to be run in a similar manner. While the size of the current container was relatively large, many other packages are much smaller and could be easily implemented in a container. It may also be possible to install GAMOS without ROOT, which would reduce the container size by approximately 3.6GB, although this was outside the scope of the current work.

A demonstration of the capability of this platform was conducted by executing over 150 simulations with varying input conditions. If these simulations were run sequentially it would have taken over 14 days of compute time, however using 64 simultaneous containers this was reduced to just over 11 hours.

## **2.5 Conclusions**

The current work presents an update to the optical-propagation plugin for the latest GAMOS release. The features of this Monte Carlo package, namely radiation-induced light signal tracking, have a range of applications from radiation dosimetry to metabolic sensing and therapy, as will be demonstrated in the following chapters. The updates described here are provided in a stand-alone package based on both virtual machine and container architectures to allow for future portability. A method is described for deploying the container-based system using an on-demand cloud infrastructure which can be used to compare models with a range of input parameters, where the resulting time to obtaining can be drastically lower than a sequential model would require. Additionally, this methodology deployment strategy could easily be adapted to fit many other script-base MC packages.

## **2.6 Acknowledgements**

This work was funded by NIH grant R01 EB024498 and R01 EB023909, as well as by a National Science Foundation Graduate Research Fellowship.

## **2.7 Supplementary Material**

1. GAMOS 6.1 GamosCore source code including tissue optics plugin:

[https://github.com/ethanlarochelle/GamosCore/tree/6\\_1](https://github.com/ethanlarochelle/GamosCore/tree/6_1)

2. GAMOS 6.1 Optical plugin validation and example scripts:  
[https://github.com/ethanlarochelle/GAMOS\\_examples](https://github.com/ethanlarochelle/GAMOS_examples)
3. GAMOS 6.1 Cloud infrastructure notebooks (Interactive environment available upon request): <https://github.com/ethanlarochelle/gamos-cloud>
4. Additional GAMOS 6.1 optical plugin information and VM files:  
<https://sites.dartmouth.edu/optmed/research-projects/monte-carlo-software/>
5. GAMOS 6.1 optical plugin container image:  
[https://hub.docker.com/r/ethanlarochelle/gamos\\_6\\_1\\_tissue\\_optics](https://hub.docker.com/r/ethanlarochelle/gamos_6_1_tissue_optics)

## 2.8 References

1. Robertson, R. *et al.* Optical imaging of Cherenkov light generation from positron-emitting radiotracers. *Physics in Medicine and Biology* **54**, N355–N365 (2009).
2. Ran, C., Zhang, Z., Hooker, J. & Moore, A. In Vivo Photoactivation Without “Light”: Use of Cherenkov Radiation to Overcome the Penetration Limit of Light. *Mol Imaging Biol* **14**, 156–162 (2012).
3. Zhang, R. *et al.* Cherenkov-excited luminescence scanned imaging. *Opt. Lett., OL* **40**, 827–830 (2015).
4. Pogue, B. W. *et al.* Maps of in vivo oxygen pressure with submillimetre resolution and nanomolar sensitivity enabled by Cherenkov-excited luminescence scanned imaging. *Nature Biomedical Engineering* **2**, 254–264 (2018).
5. Cao, X. *et al.* Cherenkov excited short-wavelength infrared fluorescence imaging in vivo with external beam radiation. *JBO* **24**, 051405 (2018).
6. Prax, G. & Xing, L. Monte Carlo simulation of photon migration in a cloud computing environment with MapReduce. *JBO* **16**, 125003 (2011).
7. Miras, H., Jiménez, R., Miras, C. & Gomà, C. CloudMC: a cloud computing application for Monte Carlo simulation. *Phys. Med. Biol.* **58**, N125–N133 (2013).
8. Ziegenhein, P., Kozin, I. N., Kamerling, C. P. & Oelfke, U. Towards real-time photon Monte Carlo dose calculation in the cloud. *Phys. Med. Biol.* **62**, 4375–4389 (2017).

9. Wang, L., Jacques, S. L. & Zheng, L. MCML—Monte Carlo modeling of light transport in multi-layered tissues. *Computer Methods and Programs in Biomedicine* **47**, 131–146 (1995).
10. Jacques, S. L. Coupling 3D Monte Carlo light transport in optically heterogeneous tissues to photoacoustic signal generation. *Photoacoustics* **2**, 137–142 (2014).
11. Fang, Q. & Boas, D. A. Monte Carlo Simulation of Photon Migration in 3D Turbid Media Accelerated by Graphics Processing Units. *Opt. Express, OE* **17**, 20178–20190 (2009).
12. Fang, Q. Mesh-based Monte Carlo method using fast ray-tracing in Plücker coordinates. *Biomedical optics express* **1**, 165–75 (2010).
13. Mycek, M.-A. & Pogue, B. W. *Handbook of Biomedical Fluorescence*. (CRC Press, 2019).
14. Cai, F. & Lu, W. A Dynamic Accuracy Estimation for GPU-based Monte Carlo Simulation in Tissue Optics. *Curr. Opt. Photon., COPP* **1**, 551–555 (2017).
15. Correia, A., Hanselaer, P., Cornelissen, H. & Meuret, Y. Radiance based method for accurate determination of volume scattering parameters using GPU-accelerated Monte Carlo. *Opt. Express, OE* **25**, 22575–22586 (2017).
16. Young-Schultz, T., Brown, S., Lilge, L., Lilge, L. & Betz, V. FullMonteCUDA: a fast, flexible, and accurate GPU-accelerated Monte Carlo simulator for light propagation in turbid media. *Biomed. Opt. Express, BOE* **10**, 4711–4726 (2019).
17. Doulgerakis-Kontoudis, M., Eggebrecht, A. T., Wojtkiewicz, S., Culver, J. P. & Dehghani, H. Toward real-time diffuse optical tomography: accelerating light propagation modeling employing parallel computing on GPU and CPU. *JBO* **22**, 125001 (2017)
18. Wang, T. & Kemaq, Q. Parallel computing in experimental mechanics and optical measurement: A review (II). *Optics and Lasers in Engineering* **104**, 181–191 (2018).
19. Yu, L., Nina-Paravecino, F., Kaeli, D. R. & Fang, Q. Scalable and massively parallel Monte Carlo photon transport simulations for heterogeneous computing platforms. *JBO* **23**, 010504 (2018).
20. Agostinelli, S. *et al.* Geant4—a simulation toolkit. *Nuclear Instruments and Methods in Physics Research Section A: Accelerators, Spectrometers, Detectors and Associated Equipment* **506**, 250–303 (2003).
21. Allison, J. *et al.* Geant4 developments and applications. *IEEE Transactions on Nuclear Science* **53**, 270–278 (2006).
22. Allison, J. *et al.* Recent developments in Geant4. *Nuclear Instruments and Methods in Physics Research Section A: Accelerators, Spectrometers, Detectors and Associated Equipment* **835**, 186–225 (2016).

23. Arce, P., Rato, P., Canadas, M. & Lagares, J. I. GAMOS: A Geant4-based easy and flexible framework for nuclear medicine applications. in *2008 IEEE Nuclear Science Symposium Conference Record* 3162–3168 (2008).  
doi:10.1109/NSSMIC.2008.4775023.
24. Glaser, A. K., Kanick, S. C., Zhang, R., Arce, P. & Pogue, B. W. A GAMOS plug-in for GEANT4 based Monte Carlo simulation of radiation-induced light transport in biological media. *Biomedical optics express* **4**, 741–59 (2013).
25. Brun, R. & Rademakers, F. ROOT — An object oriented data analysis framework. *Nuclear Instruments and Methods in Physics Research Section A: Accelerators, Spectrometers, Detectors and Associated Equipment* **389**, 81–86 (1997).
26. Gallas, B. D., Boswell, J. S., Badano, A., Gagne, R. M. & Myers, K. J. An energy- and depth-dependent model for x-ray imaging. *Medical Physics* **31**, 3132–3149 (2004).
27. Badano, A. & Sempau, J. MANTIS: combined x-ray, electron and optical Monte Carlo simulations of indirect radiation imaging systems. *Phys. Med. Biol.* **51**, 1545–1561 (2006).
28. Sharma, D. & Badano, A. Validation of columnar CsI x-ray detector responses obtained with hybridMANTIS, a CPU-GPU Monte Carlo code for coupled x-ray, electron, and optical transport. *Medical Physics* **40**, 031907 (2013).
29. Boettiger, C. An introduction to Docker for reproducible research. *SIGOPS Oper. Syst. Rev.* **49**, 71–79 (2015).
30. Docker Documentation. *Docker Documentation* <https://docs.docker.com/> (2020).
31. AWS Batch Getting Started. *Amazon Web Services, Inc.* <https://aws.amazon.com/batch/getting-started/>.
32. Boto 3 Documentation — Boto 3 Docs 1.11.10 documentation. <https://boto3.amazonaws.com/v1/documentation/api/latest/index.html>.
33. Cloth, P. *et al.* HERMES, a Monte Carlo program system for beam-materials interaction studies. *Unknown* (1988).
34. Golonka, P., Pierzchała, T. & Wąs, Z. MC-TESTER: a universal tool for comparisons of Monte Carlo predictions for particle decays in high energy physics. *Computer Physics Communications* **157**, 39–62 (2004).
35. Perl, J., Shin, J., Schümann, J., Faddegon, B. & Paganetti, H. TOPAS: An innovative proton Monte Carlo platform for research and clinical applications. *Medical Physics* **39**, 6818–6837 (2012).
36. Akagi, T. *et al.* The PTSim and TOPAS Projects, Bringing Geant4 to the Particle Therapy Clinic. *Progress in Nuclear Science and Technology* **2**, 912–917 (2011).

37. Santin, G. *et al.* GATE: a Geant4-based simulation platform for PET and SPECT integrating movement and time management. *IEEE Transactions on Nuclear Science* **50**, 1516–1521 (2003).
38. Cuplov, V., Buvat, I., Pain, F. & Jan, S. Extension of the GATE Monte-Carlo simulation package to model bioluminescence and fluorescence imaging. *JBO* **19**, 026004 (2014).
39. Stockhoff, M., Jan, S., Dubois, A., Cherry, S. R. & Roncali, E. Advanced optical simulation of scintillation detectors in GATE V8.0: first implementation of a reflectance model based on measured data. *Phys. Med. Biol.* **62**, L1–L8 (2017).
40. Townson, R. W. *et al.* GPU-based Monte Carlo radiotherapy dose calculation using phase-space sources. *Phys. Med. Biol.* **58**, 4341–4356 (2013).

# CHAPTER 3

## **3 A model of photodynamic dose at depth in tissue**

*This chapter is derived from:*

E.P.M. LaRochelle, *et al.*, “Modeling PpIX effective light fluence at depths into the skin for PDT dose comparison.” *Photodiagnosis and Photodynamic Therapy*. **25**. (2019) 425-435.

### **3.1 Introduction**

Photodynamic therapy (PDT) for treatment of actinic keratosis (AK) and other non-melanoma skin cancers has been an approved clinical practice for decades,<sup>1-3</sup> and just in the past few years daylight-activated PDT for AK has gained support as an approved treatment method.<sup>4-6</sup> With the shift from conventional PDT use of blue (415nm) or red (633nm) lamp sources, to daylight-PDT, where broadband sources like the sun or other artificial white lights have been explored, the complexity of light dose estimation is increased.

Prescribing a sufficient photodynamic dose requires knowledge of both how light interacts with tissue as well as how the clinical presentation can influence the tissue morphology.

As clinical context for the current study, Figure 3.1-1 shows histopathology examples of actinic keratosis (AK) and other non-melanoma skin cancers, where Table 3.1-1 provides the corresponding depth profile of each lesion. From these case examples it can be observed there is a range over which the photodynamic dose must be effective, and this dose will vary based on both PpIX production and light fluence reaching the entirety of the lesion. Yet, most treatments only consider the light dose at the skin surface.

While there have been proposed methods to estimate the spectrally-weighted light dose relative to the PpIX spectrum,<sup>4,7-10</sup> these approaches do not account for the spectral attenuation in the skin. Using Monte Carlo modeling, the present study aims to provide clinically relevant methods to understand how surface irradiance measurements can be used to estimate the light fluence rate at depth in tissue, which should allow informed decisions about treatment time and appropriate light sources, thus improving the ability to tailor PDT treatments based on the clinical presentation of the disease.

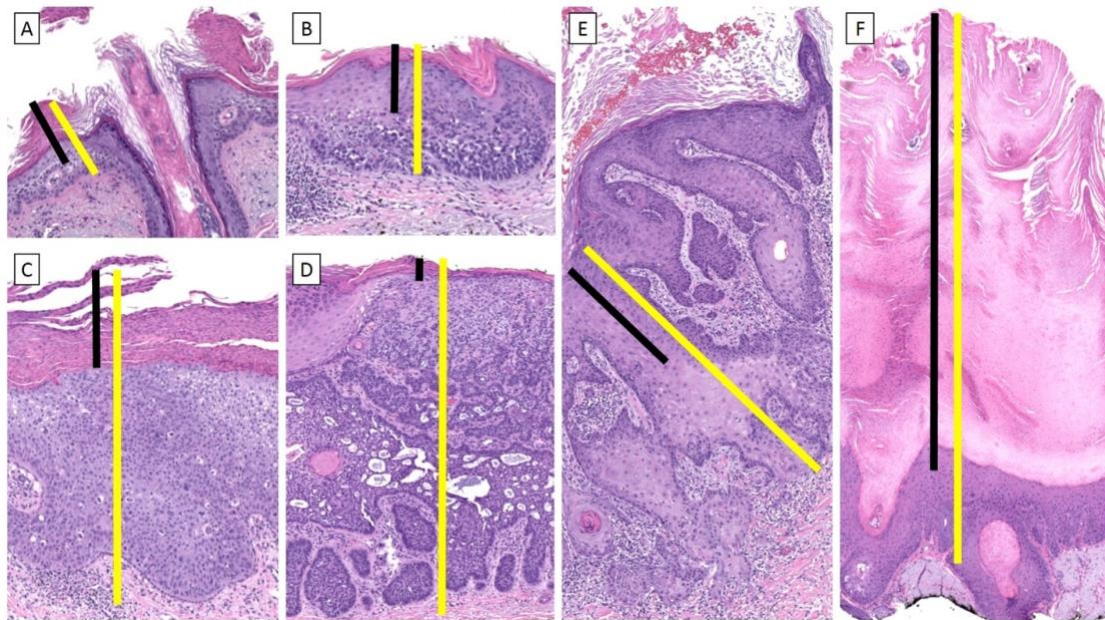


Figure 3.1-1: Representative skin lesions (H&E 40x). The black line represents the distance from the surface of the corneal layer to the surface of the lesion. The yellow line represents the distance from the surface of the corneal layer to the base of the lesion. An example of an actinic keratosis (A), basal cell carcinoma, superficial type (B), squamous cell carcinoma in situ (C), basal cell carcinoma, nodular type (D), invasive well-differentiated squamous cell carcinoma (E), and a hypertrophic actinic keratosis (F).

Table 3.1-1: Depths of Representative Skin Lesions from Figure 3.1-1

		Measurement from surface of corneal layer to surface of lesion ( $\mu\text{m}$ )	Measurement from surface of corneal layer to base of lesion ( $\mu\text{m}$ )
(A)	Actinic keratosis	189	222
(B)	Hypertrophic actinic keratosis	1419	1708

<b>(C)</b>	<b>Squamous cell carcinoma in situ</b>	305	1038
<b>(D)</b>	<b>Invasive squamous cell carcinoma</b>	287	692
<b>(E)</b>	<b>Basal cell carcinoma, superficial type</b>	214	403
<b>(F)</b>	<b>Basal cell carcinoma, nodular type</b>	70	1108

In Europe, Metvix® or MAL is the common form of ALA used for topical PDT, whereas Levulan® is used in the United States.<sup>2</sup> More recently, Ameluz® has been approved in both markets for treatment of AK and tissue debridement. MAL-equivalent Luxerm® and Ameluz® are also approved in Europe for daylight-PDT. For conventional lamp activated PDT, all formulations are applied and let to incubate for a period on the order of minutes to hours and then activated with a blue (415nm 10-25 J/cm<sup>2</sup>)<sup>11,12</sup> or red (633nm, 37 -125 J/cm<sup>2</sup>)<sup>13,14</sup> light. But, in the daylight PDT protocol, this can differ slightly depending on the drug formulation, but generally the incubation is minimized to be near 30 minutes and the activation solar irradiance is much lower.<sup>4,8,10,15-18</sup> In conventional PDT, the PpIX production has been reported to penetrate up to depths of 2mm with 3 hour incubation,<sup>19</sup> whereas during daylight-PDT PpIX is thought to be produced continuously during the treatment<sup>4,5,7,15,20</sup> and few reports on depth are known. The shorter ALA incubation time combined with the lower irradiance and longer PpIX activation time is thought to be the driving factor in reports of lower pain with daylight PDT.<sup>4,16,21,22</sup>

The spectral characteristics of light dictate the depth of potential PpIX activation. Due to tissue optical properties blue light will have a much more superficial activation profile than red light. However, PpIX has peak absorption in the blue (~410nm), but also in Q-bands at 505nm, 540nm, 580nm and 635nm.<sup>23,24</sup> Optimizing these factors, depth of activation and peak absorption, can be easily accomplished with narrowband light sources such as LEDs by altering the irradiance. This optimization becomes slightly more challenging when broad-spectrum light sources are used, especially when using a natural light source such as the sun. The consensus method for comparing broad-spectrum light sources is to weight the measured spectrum by the normalized PpIX spectrum resulting in a measure of effective irradiance.<sup>4,7-10</sup> Briefly, this is accomplished by first measuring the spectrally resolved irradiance at the skin surface (Figure 3.1-2A). This spectrum is then multiplied by a normalized PpIX absorption spectrum,<sup>24</sup> resulting in a measure of effective irradiance (Figure 3.1-2B). The effective irradiance provides a weighting factor for the probability of PpIX activation so that different light sources can be more easily compared. However, in the presence of tissue attenuation, the light fluence rate will vary drastically as a function of both wavelength and depth.

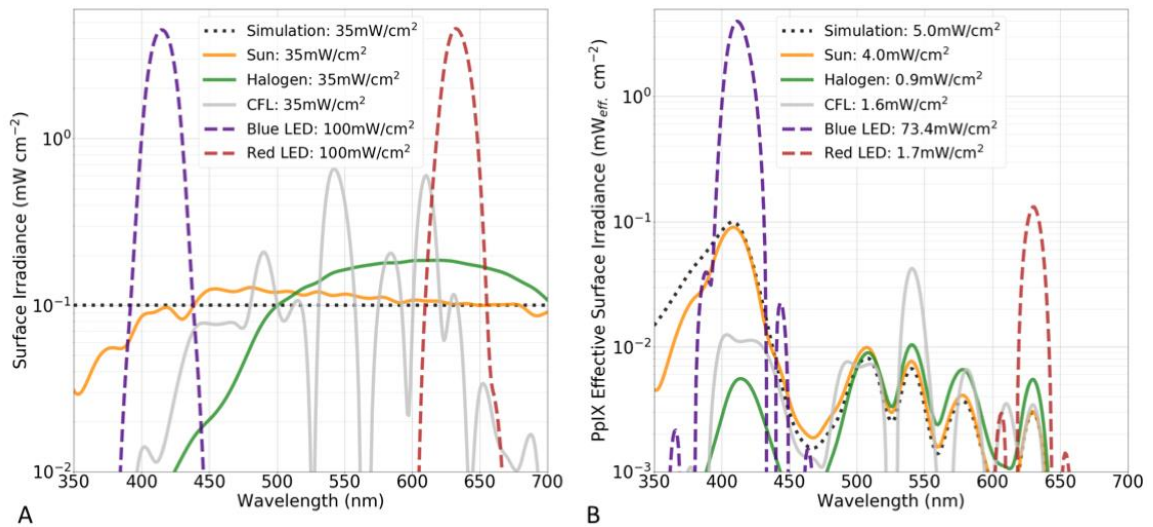


Figure 3.1-2: (A) Spectrum of 6 light sources. The simulation (dotted) is based on a theoretical uniform spectrum, whereas the other white light sources (solid) are of equal irradiance but based on measured spectral distributions. The narrow-band sources (dashed) are based on clinically-relevant irradiance used in conventional PDT and the spectrum is nearly equivalent to the FDA-approved Blue-U (Sun/DUSA) and the RhodaLED (Biofrontera) light sources. (B) PpIX-weighted spectrum showing wide variation in effective irradiance.

Previous Monte Carlo studies have investigated the interactions of light, tissue and PpIX from a variety of perspectives. Comparisons of clinical fluorescence measurements with tissue models have been used to estimate the depth distribution of PpIX.<sup>25</sup> Expanding on this idea, a model using three excitation sources was developed to study the oxygen concentration and resulting reactive oxygen caused by PpIX activation.<sup>26</sup> The most similar work to the present study was conducted by Campbell et al., who modeled both daylight and red-light activation of PpIX for a skin tumor model, and in subsequent work modeled the continuous production of PpIX during both conventional and daylight-PDT treatment.<sup>20,27</sup> The work presented here expands on the previous studies by using a 7-layer

skin model with the ability to Monte Carlo model any light source in the 350-900nm spectral range at 10nm spectral resolution. The resulting light fluence information is then combined with estimates of PpIX production and photobleaching as well as light fluence thresholds to tabulate clinically-relevant treatment times based upon the applied light source and the desired depth of activation in tissue.

A simplified model to determine the potential for PpIX activation may consider only light fluence in tissue, which assumes a sufficient and uniform distribution of PpIX. However, recent models have shown the importance of accounting for PpIX distribution when determining the photodynamic dose.<sup>20,25-27</sup> As such, estimates of PpIX distribution have been considered using both incubation times of 30 minutes or less, commonly used in daylight-PDT protocols, and incubation times of over an hour which better represent conventional-PDT. Since the irradiance used in these protocols cover a wide range, photobleaching will occur over differing time-scales. The present model assumes oxygen concentration remains sufficient throughout the treatment period.

## **3.2 Materials and Methods**

### **3.2.1 Monte Carlo model**

Using the Monte Carlo software GAMOS,<sup>28,29</sup> a 7-layer skin model (Figures 3,4) was defined based on the work of Meglinski.<sup>30</sup> Tissue optical properties ( $\mu_a$ ,  $\mu_s$ ,  $g$ ,  $n$ ) were defined between 350nm-900nm at a 10nm spectral spacing (Figure 3.2-1 and Supplementary Data: S1) using the tissue-optics plugin for GAMOS.<sup>31</sup> The tissue optical

properties assume lightly pigmented skin, which correspond to approximately 1% melanin in the epidermis (Skin layer 2 in Figure 3.2-1). A custom Python script (S2) converted the input file (S1) into a baseline template for a GAMOS geometry file. The total tissue volume was placed in a 20cm x 20cm x 2cm box where the top 7.9mm contained the explicitly defined skin model. A voxelized parallel geometry was defined with 1cm x 1cm x 10 $\mu$ m voxels within the skin to measure the fluence. A 5cm diameter disc-shaped light with 1 $^\circ$  divergence was modeled as the source 60mm above the skin surface. The voxelized geometry is only defined as a single XY volume per 10 $\mu$ m Z-step to reduce the analysis complexity. The overall XY dimensions of the tissue volume are much larger than the voxelized geometry to better simulate a semi-infinite slab geometry. PpIX absorption is not considered in the current model, since it is assumed the concentration would not be large enough to have a substantial impact on the overall tissue optical properties.<sup>25</sup> Simulations were run using 10<sup>7</sup> photons for each of the defined wavelengths.

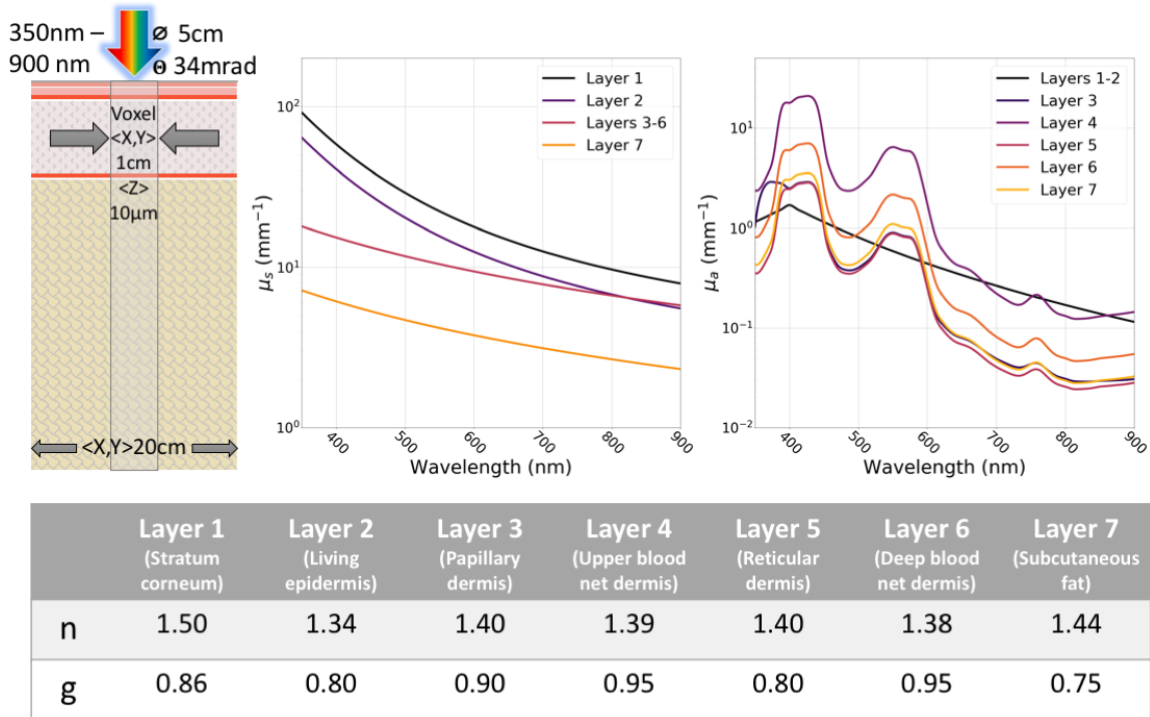


Figure 3.2-1: A representation of the GAMOS geometry is shown in the upper left. Tissue optical properties  $\mu_s$  (middle) and  $\mu_a$  (right) were defined between 350nm and 900nm for each of the 7 tissue layers. A constant refractive index ( $n$ ) and anisotropy ( $g$ ) were assumed for each layer and are provided in the table.

The simulations were run using Amazon Web Services (AWS) Batch service similar to the method described in Chapter 2. Briefly, a simulation template was created and uploaded to and AWS S3 bucket. This template contained a zip file (S3) with the necessary input files and a bash script that processed simulation input arguments (source wavelength, number of photons, and random seed). An AWS Batch job definition was generated programmatically, which specified compute parameters for each simulation job (1-3 virtual CPUS, and 2000-4000MB memory). The jobs were then added to the queue and run in parallel using AWS EC2 instances (c4.large – c4.8xlarge). Simulation outputs were stored

in sub-directories of the S3 Bucket and retrieved using the AWS command line interface for analysis on a local computer. All analysis was done using custom Python scripts (S2).

### **3.2.2 Light Fluence**

The following sections compare narrowband blue and red light at clinically relevant surface irradiance with broadband sources that have been reported in previous daylight and low-fluence-rate PDT models.<sup>10,18</sup> The narrow-band sources are modeled based on clinically available sources, such as the Blue-U (Sun/DUSA) and the RhodaLED (Biofrontera). The broadband sources are based on measurements taken by a spectroradiometer (Apogee SS-110), as reported previously.<sup>18</sup>

Like the PpIX effective surface irradiance, the effective fluence rate was calculated by weighting the fluence rate by the PpIX absorption spectrum. Using the PpIX-weighted effective fluence rate at various depths in tissue, the effective light dose could then be determined for each source.

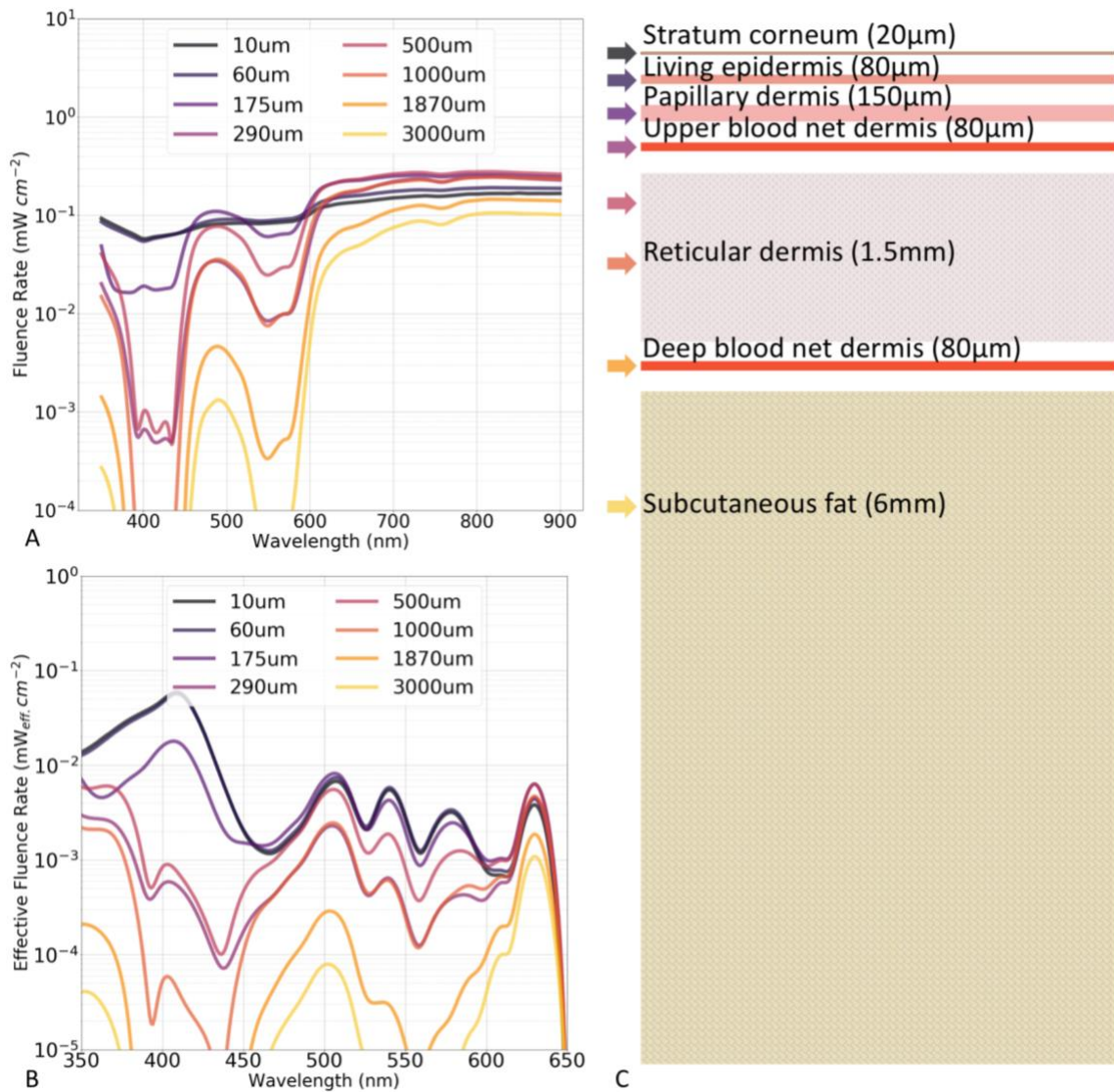


Figure 3.2-2: (A) Fluence rate at various depths in 7-layer tissue model, based on a simulated spectrally uniform light source. (B) The PpIX-weighted effective fluence rate in the same model. (C) Geometry of 7-layer skin model, where arrows indicate depths used in A and B.

In broad-spectrum PDT applications, the effective light dose is often reported as a product of the normalized PpIX absorption spectrum and the source spectrum.<sup>4,7-10</sup> This idea was applied to the fluence rate estimates by first taking the idealized case where each modeled

wavelength had the same number of photons (10<sup>7</sup>), and then extended to match measured light sources by first weighting the model by the measured spectrum (1) and then applying the PpIX absorption weighting (2). The estimated spectral fluence rate at depth z, was:

$$\phi(\lambda, z) \left( mW/cm^2 \right) = E_{meas}(\lambda, 0) * \phi_{model}(\lambda, z) \quad (1)$$

Where  $E_{meas}$  is the spectrally measured irradiance at the surface and  $\phi_{model}$  is the spectral attenuation due to tissue as modeled for the defined wavelength ( $\lambda$ ) at depth z.

Then the effective spectral fluence rate was calculated as:

$$\phi_{eff}(\lambda, z) \left( mW_{eff}/cm^2 \right) = E_{meas}(\lambda, 0) * \phi_{model}(\lambda, z) * A_{PpIX}(\lambda) \quad (2)$$

Where  $A_{PpIX}$  is the normalized spectral attenuation of PpIX.

The effective fluence is the product of the effective fluence rate and the treatment time. The effective threshold fluence is based on previously reported fluence values for studies using at least 0.6mM ALA and a laser or LED light source,<sup>32-34</sup> as summarized by Gonçalves de Faria (Table 3.2-1).<sup>35</sup> Since the wavelength for each study was reported for each cytotoxic probability distribution with mean fluence ( $D_P$ ) and FWHM of the distribution ( $\Delta D$ ),<sup>35</sup> the equivalent effective fluence could then be calculated using the PpIX absorption spectrum weighting (3-5).

$$\zeta_{\lambda} = \int_{\mu-3\sigma}^{\mu+3\sigma} A_{PpIX}(\lambda) d\lambda \quad (3)$$

$$D_{P,eff} = \zeta_{\lambda} D_P, \quad \sigma_{D,eff} = \zeta_{\lambda} \sigma_D \quad (4)$$

$$\sigma_{D,eff,pooled} = \sqrt{\frac{\sum \sigma_{D,n}}{N}} \quad (5)$$

Where  $A_{PpIX}$  is again the normalized spectral attenuation of PpIX over the wavelength range of interest and  $\sigma_D$  is the standard deviation calculated from the probability distribution  $\Delta D$ .

Table 3.2-1: Light dose distribution parameters used to calculate effective cytotoxic threshold

Wavelength (nm)	405	405	514	514	630	634
$D_P (J/cm^2)$	0.14	0.14	0.16	1.11	0.79	1.54
$\sigma_D (J/cm^2)$	0.13	0.13	0.09	0.24	0.27	1.49
$D_{P,eff} (J_{eff}/cm^2)$	0.12	0.12	0.01	0.07	0.01	0.03
$\sigma_{D,eff} (J_{eff}/cm^2)$	0.11	0.11	0.01	0.01	0.01	0.02

### 3.2.3 PpIX production and photobleaching

Since the Monte Carlo model only considers light fluence, and not PpIX production or photobleaching, Python scripts (S2) were developed to perform this portion of the analysis. PpIX production was estimated based on the model that is well summarized by Campbell et al. 20 and the parameters used in this study match those presented by Campbell. Briefly, the PpIX concentration is based on the diffusion rate of the pro-drug (6), and the rate and efficiency the drug is converted to PpIX (7).

The pro-drug concentration  $M$  is first calculated at depth  $z$  and time  $t$  using:

$$M(z, t) = M_0 \left( 1 - erf \left( \frac{z}{\sqrt{4Dt}} \right) \right) \quad (6)$$

Where  $M_0$  is the initial concentration of the pro-drug applied to the surface ( $z=0$ ) at time  $t=0$  and is assumed to be  $6 \times 10^{16} \text{ cm}^{-3}$ .  $D$  is the diffusion coefficient and assumed to be  $6.9 \times 10^{-7} \text{ cm}^2 \text{ s}^{-1}$ . The resulting PpIX production at depth  $z$  and time  $t$  can be calculated using:

$$P(z, t) = \frac{\varepsilon_p}{\tau_{ap}} \int_0^t e^{-\frac{t-t'}{\tau_p}} M(z, t') dt' \quad (7)$$

Where  $\varepsilon_p$  is the yield or proportion of pro-drug converted to PpIX, which is assumed to be 0.5, and  $\tau_{ap}$  is the relaxation time or rate of conversion of the pro-drug and is assumed to be 8640s. The rate of PpIX clearance is reflected in  $\tau_p$  and is assumed to be 4680s. The result of this calculation is the number of PpIX molecules per cubic centimeter. In the current study, this was converted to molar concentration to allow for better comparison with clinical findings.

Photobleaching was estimated as a simple exponential decay based on the initial PpIX concentration and fluence rate,<sup>20,25,27</sup> but with two modifications:

$$C(z, t) = C_0(z) e^{-\phi_{eff}(z)t/\beta} \quad (8)$$

first,  $\phi_{eff}(z)$  is the PpIX-weighted effective fluence, and second, the photobleaching dose constant ( $\beta$ ) is calculated for the peak PpIX absorption at 410nm ( $0.65 \text{ J cm}^{-2}$ ) using the method presented by Campbell to determine the wavelength-dependent photobleaching dose constant, assuming  $\beta(630\text{nm})$  to be  $14 \text{ J cm}^{-2}$ , as reported by Valentine<sup>25</sup>.  $C_0(z)$  is the initial PpIX concentration at the specified depth,  $z$ .

PpIX concentrations resulting from different incubation periods, when light is assumed to be negligible, are first calculated using equations 6 and 7. Then, both PpIX production and

photobleaching must be considered during the light treatment phase. The PpIX concentration at depth is updated iteratively to account for both processes during treatment.

### **3.2.4 Photodynamic Dose**

Initial incubation times of 5, 30, 60, and 120 minutes were assumed. For each light source the fluence rate at depths in tissue was linearly scaled to represent a range of surface irradiance values. Through iteratively calculating the PpIX distribution based on these input parameters, the photodynamic dose can be determined over a range of times and resulting effective fluence values. An effective photodynamic dose is defined as the product of the threshold effective fluence and a PpIX concentration of 50nM.

## **3.3 Results**

Using the normalized PpIX absorption spectrum as a weighting factor is common method to compare the effective irradiance of different broadband light sources. For the light sources considered in the present work, even though the broadband sources have an equal irradiance, the PpIX-effective irradiance demonstrates up to a 5x difference (Figure 3.1-2). Similarly, the blue and red LED sources have respective effective fluence rates of just 73% and 2% of the unweighted values

While PpIX-weighting improves the ability to compare surface irradiance, it does not consider tissue optical properties. Figure 3.2-2A shows how the fluence rate of a spectrally uniform light source is attenuated by tissue, as simulated with the 7-layer skin model. Furthermore, when the normalized PpIX absorption is used as a weighting factor, the

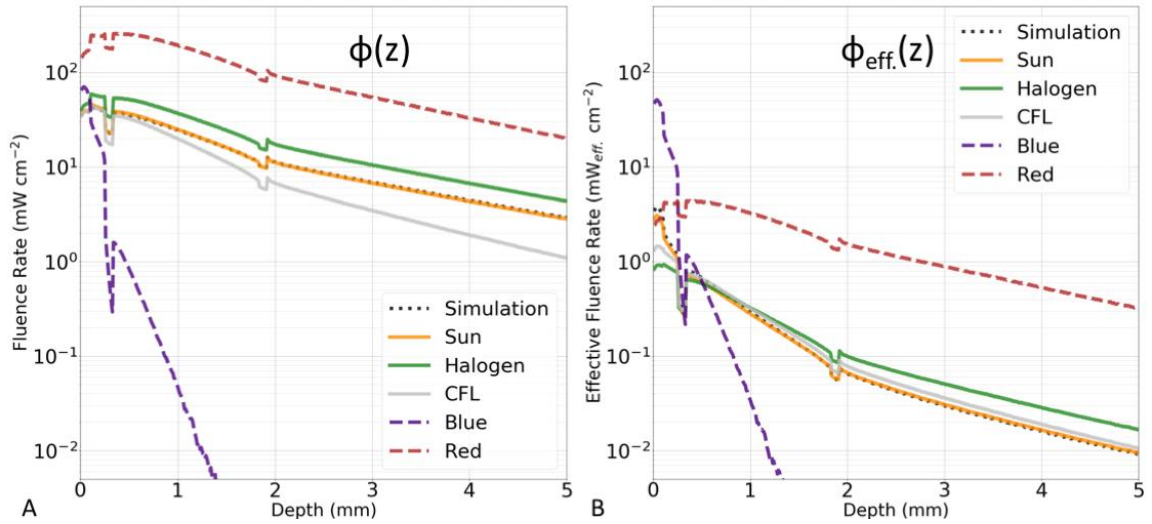


Figure 3.3-1: A comparison of the fluence rate (A) and effective fluence rate (B) as a function of depth for the uniform simulation, Sun, CFL, Halogen, Blue LED and Red LED

spectral characteristics of effective fluence rates are again modified (Figure 3.2-2B). This fluence rate can be estimated for each light source at a spacing of the  $10\mu\text{m}$  voxels throughout the depth of the model by summing over the spectral range of interest (350nm-700nm). Similarly, the effective fluence rate can be calculated by considering the normalized PpIX absorption weighting factor. The results are the fluence rate and effective fluence rate as a function of depth,  $\phi(z)$  and  $\phi_{\text{eff.}}(z)$ , respectively (Figure 3.3-1).

To determine an appropriate effective threshold fluence, a scalar value ( $\zeta_\lambda$ ) was determined based on the reported central wavelength and assumed an 10nm or 20nm full-width half maximum (FWHM) distribution for laser and LED sources, respectively. The scaling can be thought of as the integral of the normalized PpIX spectrum in this spectral range. The PpIX-weighted equivalents of the dose distributions were calculated using (4), where  $\Delta D$  was first converted to standard deviation ( $\sigma_D$ ). Then the effective pooled standard deviation

( $\sigma_{D,eff,pooled}$ ,  $0.21 J_{eff}/cm^2$ ) was determined using (5). The mean effective threshold fluence ( $0.06 J_{eff}/cm^2$ ) was summed with  $3x$  the effective pooled standard deviation to give the effective fluence threshold ( $0.70 J_{eff}/cm^2$ ) used as shown in Figure 3.3-2.

However, the effective fluence threshold only accounts for the availability of light to activate a sufficient amount of PpIX. Since the photodynamic dose is the product of the light fluence and photosensitizer availability, the PpIX concentration is needed to calculate the threshold photodynamic dose.

The PpIX concentration at depth in the tissue model was found using equations 6-8. The incubation time dictates the initial concentration before photobleaching (8) is considered. Diffusion of the pro-drug during both incubation and treatment allows for deeper PpIX production. Assuming an incubation period of 30 minutes, which is common in many

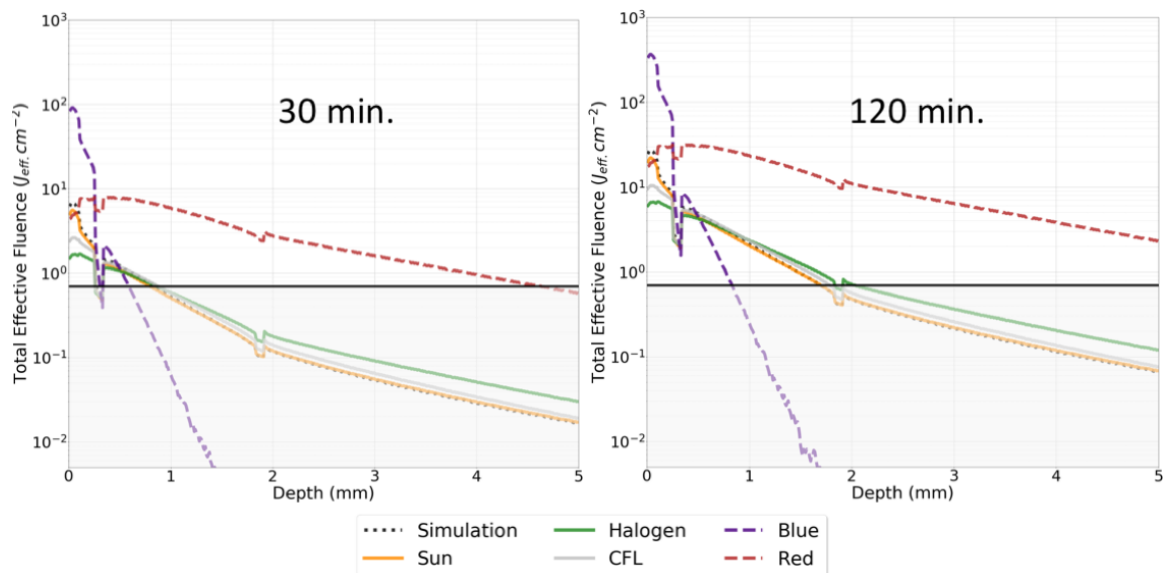


Figure 3.3-2: Effective light fluence as a function of time and depth for two different treatment times show how deeper light activation can be achieved by either extending treatment durations or using alternate light sources. The black line shows the expected threshold for PDT response at  $0.7 J_{eff}/cm^2$ .

daylight-PDT protocols, Figure 3.3-3 shows how the PpIX distribution changes over the treatment period, from 30 minutes to 2 hours. The concentration spikes shown in this figure, which are mainly observed in the blue light source, are due to the low-fluence in this tissue layer due to the higher concentration of blood. Using blue-light treatment, with PpIX concentration is higher around 1mm because of the minimal light penetration, whereas the red-light treatment has lower PpIX concentrations at depth because the red light is able to propagate further into the tissue and cause additional photobleaching.

A threshold PpIX concentration was considered based on literature reports of *in vitro* and *ex vivo* studies, which indicate effective cell killing can occur when nano-molar concentrations of PpIX are present.<sup>36,37</sup> As a conservative measure, a threshold concentration of 50nM PpIX was chosen for the current study and is shown as the black line in Figure 3.3-3.

The product of effective fluence threshold ( $0.70 J_{eff}/cm^2$ ) shown in Figure 3.3-2 and the threshold PpIX concentration (50nM) was then then calculated. The resulting photodynamic dose of  $0.035 \mu M J_{eff}/cm^2$  is used as the threshold of cytotoxicity for the current study.

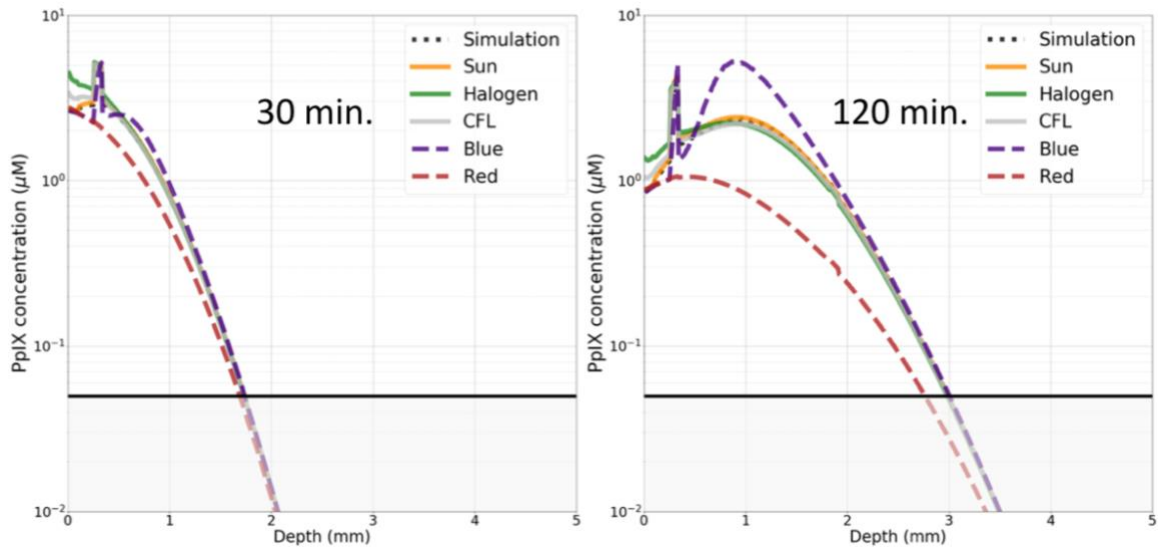


Figure 3.3-3: A model of PpIX concentrations at treatment times of 30 min and 2 hours for light treatments with a fluence rate of 35mW/cm<sup>2</sup> for broadband sources, and 100 mW/cm<sup>2</sup> for the red and blue sources, where both were incubated for 30 minutes. The black line represents the threshold PpIX concentration (50nM).

Using the effective fluence estimates, PpIX depth distribution and threshold photodynamic dose, the maximal depth of effective PpIX-activated cell death can be tabulated for each source and at various treatment times (Table 3). Even though the light sources investigated have very different effective surface irradiances, over a 20-minute treatment window all light sources are able to activate PpIX at a depth of approximately 1 mm, while the blue LED is just shallow of this and the red LED has a much deeper effect. If only the light fluence is considered for all light sources except the red LED, the depth to reach the fluence threshold within 30 minutes of treatment is approximately 50-60% less than if the photodynamic dose is considered, whereas for the red LED, the opposite is true and the light fluence over-reports the depth of activation by a similar amount.

Table 3.3-1: Depth( $\mu\text{m}$ ) of threshold photodynamic dose for different treatment times after 30 min incubation.

Light Source	Surface Irradiance (mW/cm <sup>2</sup> )	Effective Surface Irradiance (mW <sub>eff</sub> /cm <sup>2</sup> )	10 min	20 min	30 min	60 min	90 min	120 min
Uniform	35.0	5.0	930	1170	1270	1530	1720	1830
Sun	35.0	4.0	920	1160	1270	1530	1720	1830
CFL	35.0	1.6	940	1190	1290	1560	1760	1900
Halogen	35.0	0.9	940	1190	1310	1590	1790	2000
Blue	100	73.4	760	880	930	1030	1090	1150
Red	100	1.7	1260	1600	1730	2100	2400	2650

The duration of the incubation time will impact the initial depth distribution of PpIX. Depending on the spectrum and fluence rate of the treatment light, as well as the duration of light treatment, the PpIX distribution will dynamically change during treatment. Figure 8 shows a representation of how incubation time and treatment time can impact the depth of activation. Longer incubation and treatment times allow for more PpIX diffusion and result in deeper photodynamic effect. The depth of the threshold photodynamic dose is similar for the 30-minute incubation with 2-hour treatment, compared to the 2-hour incubation with 30-minute treatment, however the surface photodynamic dose is slightly higher with the longer incubation.

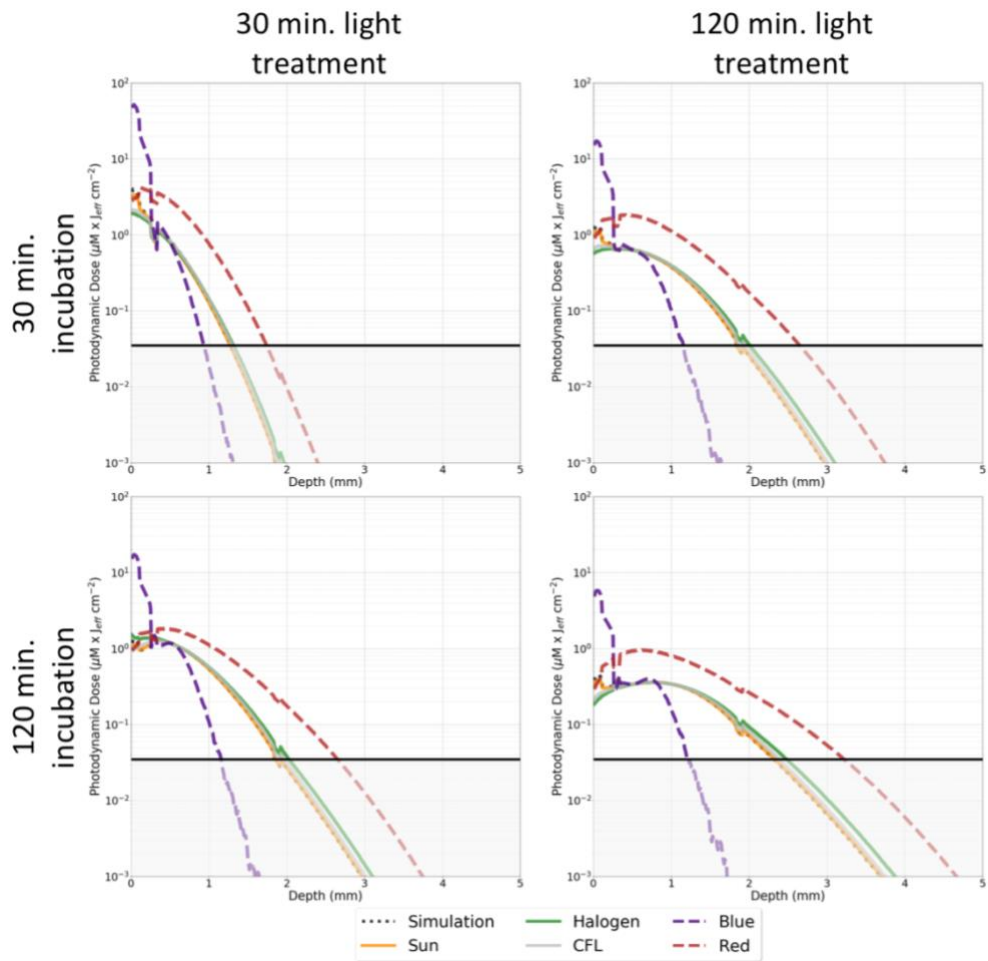


Figure 3.3-4: The photodynamic dose will differ between 30 minute (left) and 2 hour (right) treatments, for incubation times of 30 minutes (top) and 2 hours (bottom).

If the desired depth of activation can be estimated, lookup tables for treatment time needed for cytotoxic effect at various depths can also be tabulated (S4 and summarized in Table 4). The inputs required to generate this table are the light spectrum, fluence rate, incubation time and desired depth of activation. Table 3.3-2 shows a representative example of such a lookup table for the Sun spectrum irradiance values typically seen in different seasons, and for incubation times of 5 or 30 minutes.

Table 3.3-2: Minimum treatment times needed for PpIX-induce cytotoxicity for various Sun irradiance (350nm-800nm) values based on uniformly scaled irradiance measurements taken with Apogee SS-110 and reported previously by Marra et. al.<sup>18</sup> Yellow-highlighted cells indicate treatment times between 2-2.5 hours, whereas red is treatments over 2.5 hours. Additional data is provided in S4

Source	Irradiance (mW/cm <sup>2</sup> )	Latitude 45° - 60° Daily Avg. <sup>38</sup>	Effective Irradiance (mW <sub>eff</sub> /cm <sup>2</sup> )	Incubation time (min.)	Treatment time (minutes) needed for PDD threshold						
					100 μm	250 μm	500 μm	750 μm	1000 μm	1500 μm	2000 μm
Sun	10	Winter	1.1	5	1	4	13	26	50	126	>210
Sun	10		1.1	30	<1	1	2	11	25	101	>210
Sun	30	Spring, Autumn	3.4	5	<1	2	9	17	33	84	172
Sun	30		3.4	30	<1	<1	1	4	13	59	147
Sun	50	Summer	5.7	5	<1	1	7	14	27	72	145
Sun	50		5.7	30	<1	<1	1	2	11	47	120

### 3.4 Discussion

As daylight PDT continues to gain clinical adoption, it will be increasingly important to develop a standard for reporting the administered light dose, especially in the settings where the solar spectrum is known to vary. While the actual absorption spectrum used is not yet fully agreed on, resulting in slight variations in effective irradiance estimates reported by different groups,<sup>16,18,39</sup> the method of using the normalized PpIX-weighting factor is the first step to improve repeatability, both clinically as well as between studies.

With narrowband excitation performed during conventional PDT, a simple photodiode-based power meter (Thorlabs PM100D) can be used to measure surface irradiance which should remain relatively constant in the clinical setting. However, the increased variability of broad-spectrum irradiance combined with outdoor treatments have led to the

introduction of numerous methods to estimate the spectral irradiance. These data collection techniques have utilized wearable photodiodes,<sup>21,40–42</sup> regional weather patterns,<sup>5,8,22,43,44</sup> lux meters,<sup>4,9,15</sup> and spectroradiometers,<sup>15,18,39</sup> or simply set a treatment time irrespective of the irradiance.<sup>45–47</sup>

While a wearable photodiode seems like an ideal solution for the accurate measure of continuous irradiance, placement of the device proximal to the treatment field can be difficult, and wrist-based systems can introduce additional error. Additionally, the ability to acquire a commercially available device suitable for the clinic is currently limited. Many groups have turned to weather reports and almanac data to provide a generalized estimate of sunlight available at a given location throughout the year, however transient localized weather confounds the ability to predict treatment times. Illuminance measurements with a lux meter have been used by many groups, but illuminance is a measure of light intensity perceived by the human eye, with a peak sensitivity at 555nm and a weighting of nearly 0 in the UV/blue region. While there has been work to relate solar irradiance with illuminance measurements,<sup>9</sup> the current complexity is prohibitive for most clinical uses. Additionally, illuminance measurements are not ideal for comparing different broadband sources, especially those with a significant UV/blue contribution. We have previously reported collecting continuous measurements using a field-portable spectroradiometer (Apogee SS-110) commonly used in agricultural studies.<sup>18</sup> Measurements of spectrally-resolved irradiance provide the ability to perform PpIX weighting without the introduction of an additional arbitrary weighting inherent in illuminance measurements, however patient positioning relative to the light can still confound results. A study by Manley et al.

reported spectroradiometer measurements introduce the least error (13%) when calculating the effective light dose, whereas other methods can introduce 22-83% error.<sup>23</sup>

Moving further, the tissue optical properties should be considered in addition to PpIX-weighting when estimating the effective light fluence. Even though the PpIX absorption has already been considered at the surface, other tissue chromophores will absorb and scatter light. This fact is further complicated by broad-spectrum light sources.

In the current study, while equivalent surface irradiance was considered for each broadband light source, the resulting effective irradiance showed up to a 5x difference as shown in Figure 3.1-2. Even so, with these substantial differences in effective irradiance at the surface, below the more superficial skin layers (~250 $\mu$ m), the effective fluence of these lights are similar. PpIX absorption is not explicitly addressed in the Monte Carlo simulations because of its negligible effect, so instead a normalized PpIX weighting factor is applied. While inter-patient and intra-patient PpIX production can vary greatly, PpIX production was considered based on the work summarized by Campbell.<sup>20</sup> The effective fluence rate within the tissue model can then be used to estimate the photobleaching effect that occurs during treatment. This was combined with the fluence data generated by Monte Carlo simulations to estimate the photodynamic dose.

The multi-layer tissue model provides the ability to define different optical properties due to the stratified anatomy observed in the skin as shown in Figures 3 & 4. One result of this stratified model is observed in Figures 5 & 6, where there are two sharp drops in the fluence rate at depths of 250 $\mu$ m and 1.83mm. This is due to the higher concentration of blood

assumed in these layers. While modeling the blood content as a thin sheet is an oversimplification of the actual anatomy, it shows how various chromophores concentrations can impact the tissue fluence rates. Additionally, the build-up region after each of these regions can be attributed to the increase in refractive index, as observed between the air and skin surface.

It is worth noting the model for the red LED excitation has a more pronounced buildup region in the most superficial layers of skin than the other light sources, which is expected and was summarized in detail by Moes et al.<sup>48</sup> Due to the dose buildup observed with longer wavelengths, fluence rates at a depth of 150-500 $\mu\text{m}$  are 57% higher than within the first 10 $\mu\text{m}$ . While this higher fluence rate may be able to activate more PpIX, it also results in increased photobleaching, so for long treatments the total photodynamic dose in this range is not greatly increased.

The incident beam size will also impact the tissue fluence rate. This effect is depth-dependent and more pronounced with longer wavelengths, where our model indicates a 21 $\text{cm}^2$  beam at the surface, corresponding to 25mm radius source, will have 1.1 - 1.7 $x$  greater fluence within the same voxel space than a beam with surface area of 1 $\text{cm}^2$ . This study used the larger spot size (25mm radius source) to better simulate field illumination as used in daylight-PDT protocols. While clinically, actual field illumination area may be larger, for this simulation the 21 $\text{cm}^2$  illumination area is sufficiently larger than the 1 $\text{cm}^2$  voxel area used to track photon interactions.

Considering both the available light and the dynamically changing PpIX concentration at depth in tissue, is a complex procedure in clinical practice. The complexity of considering these factors needs to be reduced to a clinically digestible format. To that end, we propose the use of a lookup table that can be used in the clinic to modify light treatments. While Table 3.3-1 provides an estimate of the depth of potential PpIX activation as a function of treatment time for each light source considered in the current study, the example in Table 3.3-2 is likely more clinically applicable. Since it is likely the light irradiance will fluctuate, Table 3.3-2 and S4 provide clinically-relevant dose planning information to define treatment times required to achieve activation at specific depths for each of the light sources over a range of irradiance values and PpIX incubation times. Table 3.3-2 also has a column to indicate the seasons most commonly associated with the given irradiance for latitudes between 45° and 60° based on measurements reported by Morton et al,<sup>38</sup> where lower latitudes would have a higher average irradiance. These seasonal variations are based on historical data for specific locations, so daily weather patterns should still be considered when planning daylight-PDT treatments.

The proposed clinical workflow involves the clinician determining the type of skin lesions that needs treatment and using their judgment to estimate the depth. Using the depth estimate, a specific light source, and a simple measurement of the total irradiance, the information in S4 can be used to estimate a desired incubation and minimum treatment time. If conventional-PDT is desired, longer incubation times with narrowband light sources may be considered, whereas for daylight-PDT shorter incubation times would be used. From these lookup tables it can be observed that blue light is unable to have a

photodynamic effect much beyond 1mm, irrespective of incubation time. However, for deeper lesions (>1mm) longer incubation may be required to allow activation within a 2-hour window. Ultimately, it is up to the clinician to understand the clinical presentation and determine which light or light combination would be appropriate for treatment. For example, a more superficial AK may benefit from light with additional light dose deposited superficially, whereas a nodular BCC could benefit from a boost of red light to activate PpIX at deeper layers.

While pathology examples presented in Figure 3.1-1 and Table 3.1-1 show AK and BCC with depths of less than 500 $\mu$ m, which according to the lookup table, would take minimal time to treat, it is important to remember the times reported in S4 are to reach the minimum threshold photodynamic dose. So longer treatment times would still be appropriate. While not all the lesions shown in Figure 3.1-1 are commonly treated with PDT, it provides evidence that the effective photodynamic range in tissue could be sufficient to cause some cell death. So further investigations may be appropriate.

Further dermpathologic characterization of AKs and BCCs could help improve the Monte Carlo geometry used in the current study. Chromophore concentrations observed in neoplastic tissues, along with more refined stratification of layers, may prove useful in improving fluence estimates. Additionally, detailed investigation of pro-drug diffusion rates and PpIX production rates in these tissue samples could help better estimate the photodynamic dose.

The lookup tables presented in the present study could be further modified to include factors such as lesion type, estimated depth, melanin content and PpIX production rate. The choice would then be to measure the surface irradiance of a light source with known spectrum and estimate the desired depth of activation. Using these two values the treatment time of a single light source or light combination could then be prescribed. This type of lookup table is something that could easily be included in a web or phone-based application or further automated in a tool used to measure spectral irradiance.

### **3.5 Conclusions**

The current study presented the application of a 7-layer Monte Carlo model to estimate the light fluence in tissue for multiple light sources that have been previously reported for use in PpIX-PDT. The commonly used weighting factor based on the PpIX absorption spectrum was used to find both the effective irradiance at the skin surface as well as the effective fluence rate in tissue. The effective fluence rate was then used to find the total effective fluence for various treatment times. An effective fluence threshold ( $0.70 J_{eff}/cm^2$ ) was introduced based on a meta-analysis of previously published ALA-PpIX induced cell death. The PpIX concentration was estimated for various incubation and treatment durations for a range of fluence rates. Using the product of this fluence threshold and an estimate for the threshold concentration of PpIX (50nM), a photodynamic dose of  $0.035 \mu M J_{eff}/cm^2$  is used as the threshold of cytotoxicity. The depth of PpIX-induced cytotoxicity was estimated for various treatment times for each light source at the investigated irradiance values. Even though there was up to a 5x reduction between the

effective surface irradiance of the broadband light sources, the effective fluence below 250 $\mu$ m was relatively equivalent. Clinically-relevant lookup tables were introduced to provide a simplified method to estimate treatment times for various light sources over a range of irradiances. From these lookup tables it can be observed that blue light is unable to have a photodynamic effect much beyond 1mm, irrespective of incubation time. However, for deeper lesions (>1mm) longer incubation may be required to allow activation within a 2-hour window. The data provided in the lookup tables is compared to clinically relevant histopathology samples to provide context on clinical applications. Moving forward, this model could be extended to include common disease morphologies, melanin contents and PpIX production rates.

### **3.6 Acknowledgments**

This work was funded by the National Institutes of Health and the National Cancer Institute grant P01 CA084203 and by a National Science Foundation Graduate Research Fellowship.

### **3.7 Supplementary Material**

S1: [Monte Carlo input tissue optical properties](#)

S2: [Interactive code on Code Ocean](#)

S3: [Monte Carlo execution files](#)

S4: [Photodynamic dose lookup tables](#)

### 3.8 References

1. Peng, Q. *et al.* 5-Aminolevulinic acid-based photodynamic therapy. *Cancer* **79**, 2282–2308 (1997).
2. Braathen, L. R. *et al.* Guidelines on the use of photodynamic therapy for nonmelanoma skin cancer: An international consensus. *J. Am. Acad. Dermatol.* **56**, 125–143 (2007).
3. Morton, C. A., Szeimies, R.-M., Sidoroff, A. & Braathen, L. R. European guidelines for topical photodynamic therapy part 1: treatment delivery and current indications - actinic keratoses, Bowen's disease, basal cell carcinoma. *J. Eur. Acad. Dermatology Venereol.* **27**, 536–544 (2013).
4. Wiegell, S. R. *et al.* Daylight photodynamic therapy for actinic keratosis: an international consensus. *J. Eur. Acad. Dermatology Venereol.* **26**, 673–679 (2012).
5. Morton, C. A. *et al.* Practical approach to the use of daylight photodynamic therapy with topical methyl aminolevulinate for actinic keratosis: a European consensus. *J. Eur. Acad. Dermatology Venereol.* **29**, 1718–1723 (2015).
6. Vignion-Dewalle, A.-S. *et al.* Photodynamic therapy for actinic keratosis: Is the European consensus protocol for daylight PDT superior to conventional protocol for Aktilite CL 128 PDT? *J. Photochem. Photobiol. B Biol.* **174**, 70–77 (2017).
7. Wiegell, S. R., Heydenreich, J., Fabricius, S. & Wulf, H. C. Continuous ultra-low-intensity artificial daylight is not as effective as red LED light in photodynamic therapy of multiple actinic keratoses. *Photodermatol. Photoimmunol. Photomed.* **27**, 280–285 (2011).
8. Spelman, L. *et al.* Treatment of face and scalp solar (actinic) keratosis with daylight-mediated photodynamic therapy is possible throughout the year in Australia: Evidence from a clinical and meteorological study. *Australas. J. Dermatol.* **57**, 24–28 (2016).
9. O'Mahoney, P. *et al.* The use of illuminance as a guide to effective light delivery during daylight PDT in the UK. *Br. J. Dermatol.* (2016). doi:10.1111/bjd.15146
10. de Souza, A. L. R. *et al.* Assessing daylight & low-dose rate photodynamic therapy efficacy, using biomarkers of photophysical, biochemical and biological damage metrics in situ. *Photodiagnosis Photodyn. Ther.* **20**, 227–233 (2017).
11. *OPERATING MANUAL BLU-U® Blue Light Photodynamic Therapy Illuminator Model 4170 Operating Manual BLU-U® Blue Light Photodynamic Therapy Illuminator Model 4170 Operating Manual.* at <<http://www.dusapharma.com/assets/files/blu-u-manuals/MAN-1211AW-EN Rev G.pdf>>
12. THE PEAK 415 BLUE LIGHT. at <<https://www.smarterlights.com/The-Peak->

415-Blue-Light-HP-LED-Powerhead-p/e-lt-415.htm>

13. Omnilux. at <<http://omniluxled.com/products/omnilux-revive2/>>
14. *Tailored for PDT. The reference in LED\* lamp technology for PhotoDynamic Therapy (PDT) in Dermatology.* at <[https://www.galderma.se/Portals/3/images/2014/files/Brochure\\_4p\\_AKTILITE\\_201303.pdf](https://www.galderma.se/Portals/3/images/2014/files/Brochure_4p_AKTILITE_201303.pdf)>
15. Lerche, C., Heerfordt, I., Heydenreich, J. & Wulf, H. Alternatives to Outdoor Daylight Illumination for Photodynamic Therapy—Use of Greenhouses and Artificial Light Sources. *Int. J. Mol. Sci.* **17**, 309 (2016).
16. Wiegell, S. R. *et al.* Continuous activation of PpIX by daylight is as effective as and less painful than conventional photodynamic therapy for actinic keratoses; a randomized, controlled, single-blinded study. *Br. J. Dermatol.* **158**, 740–746 (2008).
17. Sotiriou, E. *et al.* Daylight Photodynamic Therapy vs. Conventional Photodynamic Therapy as skin cancer preventive treatment in patients with face and scalp cancerization: an intra-individual comparison study. *J. Eur. Acad. Dermatology Venereol.* (2017). doi:10.1111/jdv.14177
18. Marra, K. *et al.* Comparison of Blue and White Lamp Light with Sunlight for Daylight-Mediated, 5-ALA Photodynamic Therapy, *in vivo*. *Photochem. Photobiol.* (2018). doi:10.1111/php.12923
19. Peng, Q., Soler, A. M., Warloe, T., Nesland, J. M. & Giercksky, K.-E. Selective distribution of porphyrins in skin thick basal cell carcinoma after topical application of methyl 5-aminolevulinate. *J. Photochem. Photobiol. B Biol.* **62**, 140–145 (2001).
20. Campbell, C. L., Brown, C. T. A., Wood, K. & Moseley, H. Modelling topical photodynamic therapy treatment including the continuous production of Protoporphyrin IX. *Phys. Med. Biol.* **61**, 7507–7521 (2016).
21. Wiegell, S. R., Haedersdal, M., Eriksen, P. & Wulf, H. C. Photodynamic therapy of actinic keratoses with 8% and 16% methyl aminolaevulinate and home-based daylight exposure: a double-blinded randomized clinical trial. *Br. J. Dermatol.* **160**, 1308–1314 (2009).
22. Fagnoli, M. C. *et al.* Conventional vs. daylight methyl aminolevulinate photodynamic therapy for actinic keratosis of the face and scalp: an intra-patient, prospective, comparison study in Italy. *J. Eur. Acad. Dermatology Venereol.* **29**, 1926–1932 (2015).
23. Manley, M., Collins, P., Gray, L., O’Gorman, S. & McCavana, J. Quantifying the radiant exposure and effective dose in patients treated for actinic keratoses with topical photodynamic therapy using daylight and LED white light. *Phys. Med. Biol.* (2017). doi:10.1088/1361-6560/aa9ea7

24. Taniguchi, M. & Lindsey, J. S. Database of Absorption and Fluorescence Spectra of >300 Common Compounds for use in PhotochemCAD. *Photochem. Photobiol.* **94**, 290–327 (2018).
25. Valentine, R. M., Brown, C. T. A., Moseley, H., Ibbotson, S. & Wood, K. Monte Carlo modeling of in vivo protoporphyrin IX fluorescence and singlet oxygen production during photodynamic therapy for patients presenting with superficial basal cell carcinomas. *J. Biomed. Opt.* **16**, 048002 (2011).
26. Liu, B., Farrell, T. J. & Patterson, M. S. Comparison of photodynamic therapy with different excitation wavelengths using a dynamic model of aminolevulinic acid-photodynamic therapy of human skin. *J. Biomed. Opt.* **17**, 0880011 (2012).
27. Campbell, C. L., Wood, K., Valentine, R. M., Brown, C. T. A. & Moseley, H. Monte Carlo modelling of daylight activated photodynamic therapy. *Phys. Med. Biol.* **60**, 4059–4073 (2015).
28. Arce, P., Rato, P., Canadas, M. & Lagares, J. I. GAMOS: A Geant4-based easy and flexible framework for nuclear medicine applications. in *2008 IEEE Nuclear Science Symposium Conference Record* 3162–3168 (IEEE, 2008). doi:10.1109/NSSMIC.2008.4775023
29. Arce, P. *et al.* Gamos: A framework to do Geant4 simulations in different physics fields with an user-friendly interface. *Nucl. Instruments Methods Phys. Res. Sect. A Accel. Spectrometers, Detect. Assoc. Equip.* **735**, 304–313 (2014).
30. Meglinski, I. V & Matcher, S. J. Quantitative assessment of skin layers absorption and skin reflectance spectra simulation in the visible and near-infrared spectral regions. *Physiol. Meas.* **23**, 741–753 (2002).
31. Glaser, A. K., Kanick, S. C., Zhang, R., Arce, P. & Pogue, B. W. A GAMOS plug-in for GEANT4 based Monte Carlo simulation of radiation-induced light transport in biological media. *Biomed. Opt. Express* **4**, 741–59 (2013).
32. Berlanda, J., Kiesslich, T., Engelhardt, V., Krammer, B. & Plaetzer, K. Comparative in vitro study on the characteristics of different photosensitizers employed in PDT. *J. Photochem. Photobiol. B Biol.* **100**, 173–180 (2010).
33. Casas, A. *et al.* Tumor cell lines resistant to ALA-mediated photodynamic therapy and possible tools to target surviving cells. *Int. J. Oncol.* **29**, 397–405 (2006).
34. Hartl, B. A., Hirschberg, H., Marcu, L. & Cherry, S. R. Characterizing low fluence thresholds for in vitro photodynamic therapy. *Biomed. Opt. Express* **6**, 770 (2015).
35. de Faria, C. M. G., Inada, N. M., Kurachi, C. & Bagnato, V. S. Determination of the threshold dose distribution in photodynamic action from in vitro experiments. *J. Photochem. Photobiol. B Biol.* **162**, 168–175 (2016).
36. Schmitz, L., Novak, B., Hoeh, A.-K., Luebbert, H. & Dirschka, T. Epidermal penetration and protoporphyrin IX formation of two different 5-aminolevulinic

- acid formulations in ex vivo human skin. *Photodiagnosis Photodyn. Ther.* **14**, 40–46 (2016).
37. Novak, B., Heesen, L., Scharly, N. & Lübbert, H. The influence of different illumination parameters on protoporphyrin IX induced cell death in squamous cell carcinoma cells. *Photodiagnosis Photodyn. Ther.* **21**, 385–392 (2018).
  38. Morton, C. A. *et al.* Practical approach to the use of daylight photodynamic therapy with topical methyl aminolevulinate for actinic keratosis: a European consensus. *J. Eur. Acad. Dermatology Venereol.* **29**, 1718–1723 (2015).
  39. Rubel, D. M. *et al.* Daylight photodynamic therapy with methyl aminolevulinate cream as a convenient, similarly effective, nearly painless alternative to conventional photodynamic therapy in actinic keratosis treatment: a randomized controlled trial. *Br. J. Dermatol.* **171**, 1164–1171 (2014).
  40. Thieden, E., Agren, M. S. & Wulf, H. C. The wrist is a reliable body site for personal dosimetry of ultraviolet radiation. *Photodermatol. Photoimmunol. Photomed.* **16**, 57–61 (2000).
  41. Heydenreich, J. & Wulf, H. C. Miniature Personal Electronic UVR Dosimeter with Erythema Response and Time-stamped Readings in a Wristwatch. *Photochem. Photobiol.* **81**, 1138 (2005).
  42. Wiegell, S. R. *et al.* A randomized, multicentre study of directed daylight exposure times of 1½ vs. 2½ h in daylight-mediated photodynamic therapy with methyl aminolaevulinate in patients with multiple thin actinic keratoses of the face and scalp. *Br. J. Dermatol.* **164**, 1083–1090 (2011).
  43. Grinblat, B. *et al.* Feasibility of daylight-mediated photodynamic therapy for actinic keratosis throughout the year in Central and South America: a meteorological study. *Int. J. Dermatol.* **55**, e488–e493 (2016).
  44. See, J.-A. *et al.* Consensus recommendations on the use of daylight photodynamic therapy with methyl aminolevulinate cream for actinic keratoses in Australia. *Australas. J. Dermatol.* **57**, 167–174 (2016).
  45. Braathen, L. Daylight Photodynamic Therapy in Private Practice in Switzerland: Gain Without Pain. *Acta Derm. Venereol.* **92**, 652–653 (2012).
  46. Neittaanmäki-Perttu, N., Karppinen, T. T., Grönroos, M., Tani, T. T. & Snellman, E. Daylight photodynamic therapy for actinic keratoses: a randomized double-blinded nonsponsored prospective study comparing 5-aminolaevulinic acid nanoemulsion (BF-200) with methyl-5-aminolaevulinate. *Br. J. Dermatol.* **171**, 1172–1180 (2014).
  47. Lacour, J.-P. *et al.* Daylight photodynamic therapy with methyl aminolevulinate cream is effective and nearly painless in treating actinic keratoses: a randomised, investigator-blinded, controlled, phase III study throughout Europe. *J. Eur. Acad. Dermatology Venereol.* **29**, 2342–2348 (2015).

48. Moes, C. J., van Gemert, M. J., Star, W. M., Marijnissen, J. P. & Prahl, S. a. Measurements and calculations of the energy fluence rate in a scattering and absorbing phantom at 633 nm. *Appl. Opt.* **28**, 2292–6 (1989).

# CHAPTER 4

## **4 Weather-based dose planning for Daylight-PDT of skin**

*This chapter is derived from:*

E.P.M. LaRochelle, *et al.*, “Weather-informed Light-tissue Model-Based Dose Planning for Indoor Daylight Photodynamic Therapy.” *Photochemistry and Photobiology*. (2019).

### **4.1 Introduction**

Using daylight as an activation mechanism for photodynamic therapy (PDT) of skin has been investigated over the past decade, and is now widely accepted in several countries, as a less painful and equally effective treatment mechanism when compared to conventional red or blue light activation.<sup>1-3</sup> However, seasonal daylight availability and transient weather conditions complicate light dose estimations, especially in northern latitudes.<sup>4-6</sup> Clinically, appropriate treatment months are identified based on latitude and season, and patients are treated for approximately 2 hours where appropriate sunlight is expected.<sup>7,8</sup> Yet, the changes in solar irradiance due to the time of day and transient weather conditions confound reproducibility. In this current work, a method involving a one-time site

assessment is proposed combined with programmatically acquired weather data to provide real time estimates of light fluence rates and photodynamic dose at depth in tissue.

Daylight-PDT and similar low-fluence rate activation methods have been reported to be less painful than conventional PDT. Additionally, the ability to treat multiple patients simultaneously has economic benefits in certain healthcare systems.<sup>9</sup> While lights used in conventional treatments are regulated medical devices that have well characterized narrowband spectra and fluence rates, daylight is broad spectrum and the fluence rate changes on a continuous basis. Despite these well-known fluctuations, daylight-PDT is an approved treatment in many countries without explicit guidance on dealing with daily weather prediction. While reasonable approaches to delivering daylight PDT are always implemented, a more formalized approach to estimating light potential seems warranted.

With the variable nature of sunlight versus cloud, it is natural to question how much light is required to deliver an appropriate photodynamic dose. An international consensus by Wiegell et al. provides guidance on the minimum effective fluence needed to activate PpIX and provides a table of appropriate treatment months based on latitude.<sup>10</sup> A model developed by O'Mahoney et al. provides a method for estimating the PpIX-weighted light fluence based on a simple low-cost lux meter measurement.<sup>6</sup> While weather conditions have been reported in past studies, the recorded parameters are not standardized. Many clinical teams have patients sit outside for a fixed 2-2.5 hour period, but it is still unclear if clearance could be achieved with less time, or conversely if more time would be beneficial.<sup>11</sup> Additionally, inter-site comparisons and reproducibility become an issue when the continuous irradiance rate are not considered. The following sections describe

methods to improve dose planning without placing a large burden on clinical staff, by limiting spectral measurements to a one-time site assessment, and then using automatically acquired weather reports to track transient conditions during daylight treatments. These methods can be applied to both indoor and outdoor daylight treatments, where indoor treatments provide the added benefit of reliable climate control and reduce the need to apply sunscreen due to the UV-blocking nature of many windows, however the spectral changes introduced by this barrier need to be characterized for proper light-dose estimation.

## **4.2 Materials and Methods**

A solar site analysis was performed using a Solar Pathfinder (The SolarPathfinder Company, Linden, TN, USA), which is a basic tool commonly used in the photovoltaic industry to site solar panels for maximal annual exposure. The tool consists of a grid showing solar time (vertical lines) which are intersected by months (horizontal lines) as shown in Figure 4.2-1A. The grid is specific to a range of latitudes and printed as white lines on black paper. The base is oriented such that the paper grid fits in the plastic base at a specific orientation, and the whole system is aligned using a built-in compass. A clear plastic dome with open sides is placed on top of the base (Figure 4.2-1A insert, and B). A white wax pencil is used to mark the paper grid to denote the boundaries of objects blocking the reflected sky (Figure 4.2-1B, green outline). The grid is then removed from the base and the times and months indicated by markings are entered into a spreadsheet, which is visualized in Figure 4.2-1C.

A field spectroradiometer (SS-110, Apogee Instruments, Logan, UT) was used to collect spectral data at 5-minute time intervals over the course of multiple weeks. Calibration of the device was performed by the manufacturer using National Institute of Standards and Technology (NIST) traceable light sources. The device was leveled and placed on a window sill in close proximity to where the site assessment was performed and where patients are to be treated (Figure 4.2-1A upper left). The total irradiance was calculated by integrating spectral measurements between 350nm and 800nm.

A weighting based on the absorption spectrum of PpIX<sub>12</sub> was used to find the effective irradiance. The PpIX absorption spectra was first normalized and then multiplied by the spectroradiometer measurements. This provides a metric of the PpIX-weighted effective irradiance, which when combined with treatment time, provides the effective light dose.

Using a Python script to interface with an application programming interface (API), hourly weather data was programmatically accessed from weatherbit.io for an airport approximately 5km from the treatment site. These data provide formatted key-value pairs of various weather parameters. The main values considered are a model-based solar irradiance estimate assuming clear skies, percentage of cloud coverage based on satellite imagery and UV-index. Temperature and humidity values are also provided, however only need to be considered for outdoor treatments.

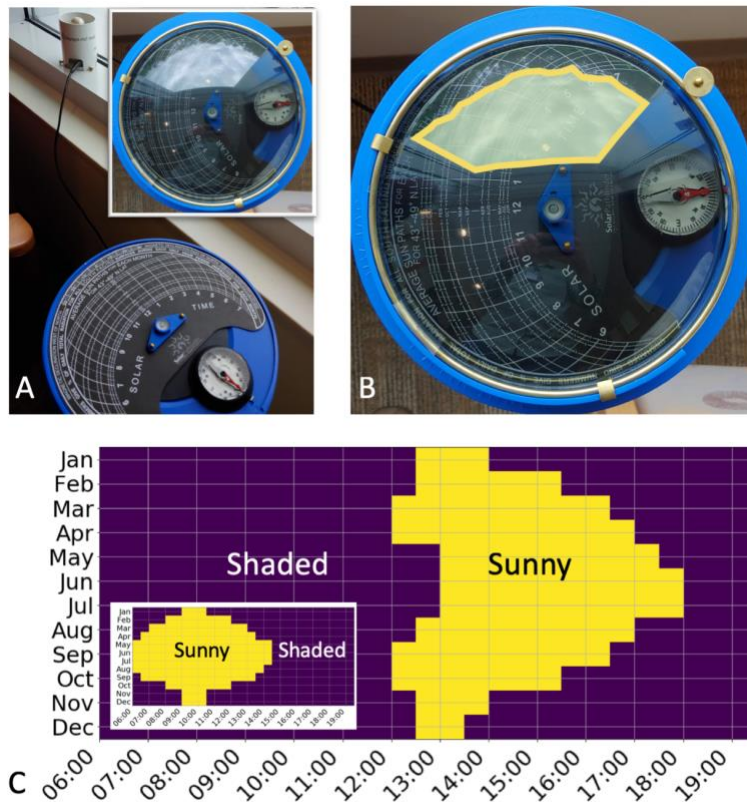
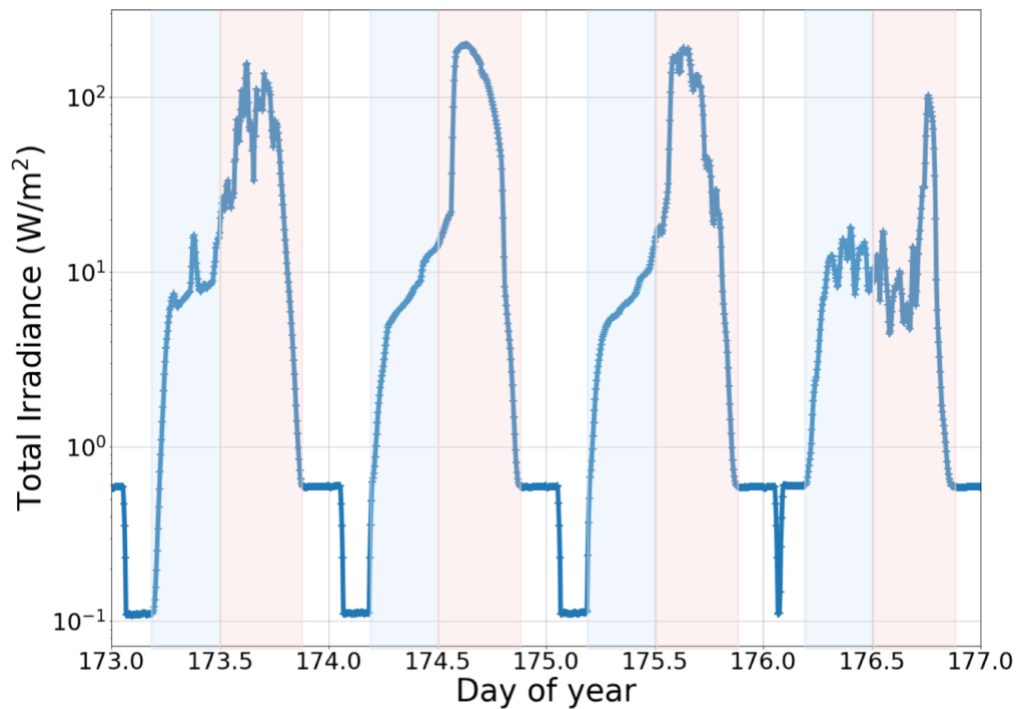


Figure 4.2-1: The SolarPathfinder device showing compass alignment and nearby spectroradiometer (A), where the clear plastic dome (inset) reflects the sky. The outline of obstructions is traced (light green shaded region B), which can then be converted to a binary grid of sunny and shaded regions (C). Then as a comparison, the same procedure was conducted in an open untried area outside of the building (C-inset) where morning sunlight was available, but tall trees to the west blocked the afternoon sun.

### 4.3 Results

The solar site analysis was performed in the waiting area of the Dermatology clinic at Dartmouth Hitchcock Medical Center in Lebanon, NH (Latitude 43.6°N). This area is on the 2<sup>nd</sup> floor and has large Southwest facing windows. The analysis shows there are between 1-5 hours of direct sunlight each afternoon for this location (Figure 4.2-1C). During the months of mid-April through mid-August there is a decrease in noon-time sunlight due to the building awning. Mid-October through mid-January have less than 2 hours of direct sunlight due to the building orientation. A site assessment was also



*Figure 4.3-1: Solar variation from total irradiance measurements is shown, as taken at 5 minute intervals over approximately 5 days, showing high irradiances only in the afternoon hours (pink shaded area) and at least an order of magnitude less in the mornings (blue shade areas).*

conducted in a nearby picnic area where the sky was unobstructed in the morning, but tall trees just to the west blocked afternoon sunlight (Figure 4.2-1C-inset).

As an example of the variability observed in the total irradiance, measurements collected over a 5-day period are provided in Figure 4.3-1, where the blue shaded regions are in the morning when the building blocks direct sunlight, and the red-shaded regions are the direct afternoon sunlight. The first two days show how cloudy conditions can impact the irradiance. A clear and mostly clear day are shown on the 174<sup>th</sup> and 175<sup>th</sup> days of the year, respectively, while day 176 is mostly overcast. Even on the clear day, the total irradiance can fluctuate over a 2-hour window and the peak irradiance is only observed over a short period of time. The horizontal lines during the night represent the baseline indoor lighting, which is turned off just after midnight most nights.

While Figure 4.3-1 shows the total irradiance at 5-minute time resolution, Figure 4.3-1 provides representative examples of the spectral distribution at 14:00 on days in different seasons and with different weather conditions. Figure 4.3-1A provides the spectral characteristics measured indoors on a clear day in mid-June, whereas 4.3-1B is on an overcast day the same week. The overcast day reports just 2% of the total irradiance for the same time two days previous. To compare seasons, Figure 4.3-1C provides spectral measurements for a clear day in mid-October, where the overall total irradiance is slightly less than June, but still sufficient for treatment. However, a partly cloudy day in October has approximately 10% as much light. The indoor CFL lights can be observed in Figure 4.3-1B (Spectral peaks at approximately 440nm, 560nm, and 610nm) and provide a significant portion of the irradiance due to the overcast conditions at that time. Using the

spectroradiometer measurements with our previously published light-tissue model, and also described in Chapter 3,<sup>13</sup> an estimate of the photodynamic dose at depths can be determined. This was performed for daylight spectra collected both outdoors and indoors. The spectral measurements are shown in Figure 4.3-2A, where for comparison purposes the intensities were uniformly scaled such that the indoor irradiance is 75% of the corresponding total outdoor irradiance, which is similar to reports by others.<sup>14</sup> The actual

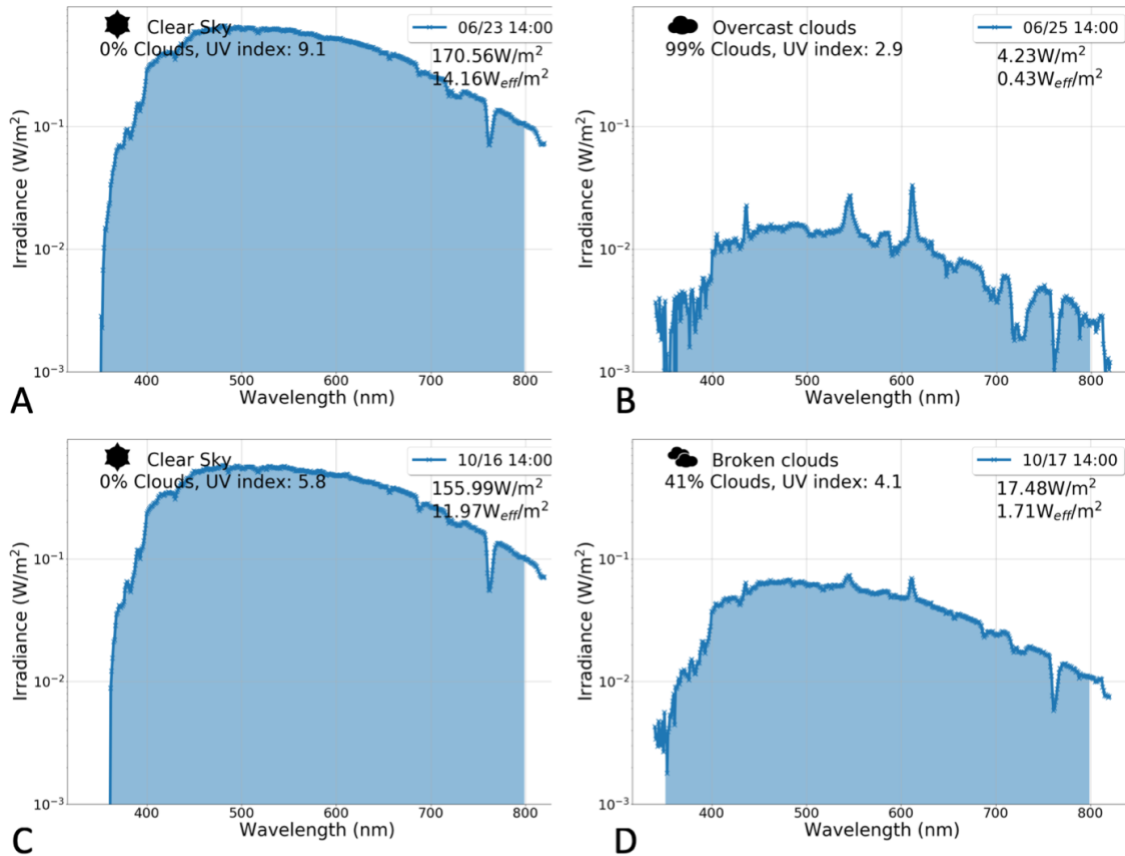


Figure 4.3-2: Spectroradiometer measurements taken at 14:00 on a clear day in June (A), a cloudy day the same week (B), a clear day in October (C), and a partly cloudy day in October (D). The weather report is shown in the upper left of each graph, and the total and PpIX-weighted irradiance are given in the upper right.

reduction is dependent on the transmission of the glass or acrylic barrier which is concisely summarized by O’Mahoney et al. for many common materials.<sup>15</sup>

Most investigations of daylight PDT report light dose as the effective fluence, which is the fluence weighted by the PpIX absorption spectrum.<sup>16,4,14,6,17,18</sup> So even though the total

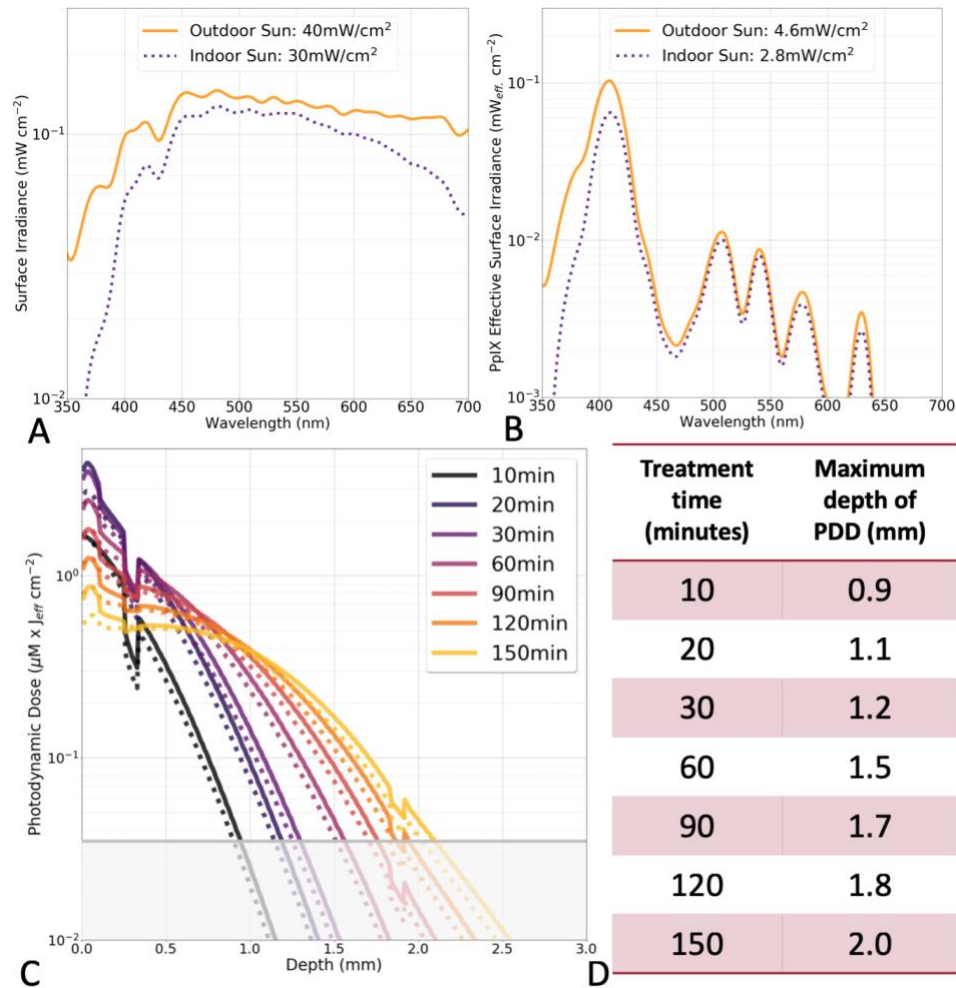


Figure 4.3-3: Scaled daylight spectra measurements of outdoor and indoor daylight (A) and their PpIX-weighted counterparts (B). Snapshots of photodynamic dose after 30 minute incubation for various treatment times (Outdoor: solid, Indoor: dotted) (C) and their corresponding maximal depth of effective PDT dose at depth (D).

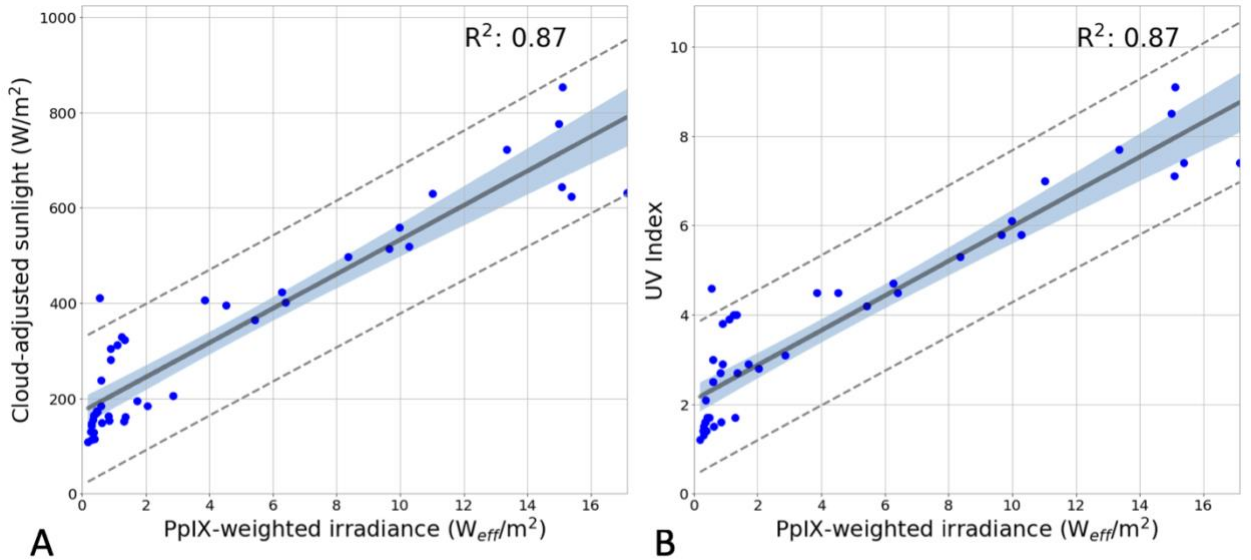


Figure 4.3-4: Comparison of indoor PpIX-weighted spectroradiometer measurements (x-axis) and cloud coverage (A) and UV Index (B), where the blue shaded region provides a 95% confidence interval and the dashed lines provide the 95% prediction limits.

irradiance of indoor daylight is 75% of its outdoor counterpart, the PpIX-weighted effective irradiance indoors is 60% of the outdoor complement because more UV light is blocked by the window (Figure 4.3-3B). While the PpIX-effective irradiance aims to account for the spectral characteristics of broad-spectrum activation, when these irradiance values are used to estimate photodynamic dose at depth in tissue after a 30 minute incubation period, where a combination of fluence rate, PpIX production rates, photobleaching and time are all considered, the overall depth of activation is largely similar (Figure 4.3-3C-D).

To determine if specific weather-based metrics could be used as surrogate for spectroradiometer measurements, time-correlated measurements were compared with corresponding weather data. Spectroradiometer measurements were averaged for over a 10-minute window around each new hour for times that were previously determined to be in the “Sunny” region of Figure 4.2-1C. These irradiance values were then compared to the product of the cloud percentage and the modeled ideal sunlight (Figure 4.3-4A), or the UV-

index (Figure 4.3-4B), reported by the weather station at the local airport. When only the modeled sunlight is assumed the correlation is poor ( $R^2$ : 0.49, not shown), but both the cloud-corrected sunlight and UV-index show a strong correlation ( $R^2$ : 0.87).

#### **4.4 Discussion**

While weather data has been incorporated in previous studies of daylight-PDT,<sup>4,11,14</sup> the reporting mechanism is not standardized. Wiegell et al. asked patients to record weather conditions based on a 1-5 scale and retrieved maximal UV index during the treatment from an external source. This study further found UV index could not be used as a predictor of daylight-PDT light dose. However, these results may be limited by the reporting mechanism, whereas our more specific time-correlated method indicates a correlation. A recent review by Philipp-Dormston et al. found there have been no clinical studies showing an impact of average daylight light dose on daylight-PDT efficacy, once a minimal threshold is met.<sup>19</sup> While our model indicates there is a link between total light fluence and photodynamic dose, it also indicates treatment could be sufficient in well under 2 hours on many sunny days, and even some cloudy days in the summer.

Before implementing a daylight-PDT protocol, a site assessment should be performed ideally, to verify potential light exposure. Seasonal variations in the solar path at the treatment location are important to understand and various sites may have better seasonal or daily value. While the current study proposes an indoor daylight PDT protocol so the building orientation is the driving factor, outdoor treatments could have similar obstructions and can be vetted in the same manner. The seasonal solar availability at

specific sites can be used for long term clinical scheduling. For example, in our case the sun was generally available only in the afternoon so patients should only be scheduled during this period, however, an outdoor site near the building was identified that provides daylight from the early morning through mid-afternoon. Just as clinical procedures are scheduled in specific rooms, daylight-PDT locations could be scheduled based on solar availability of the site.

While seasonal solar availability is one important aspect of a site assessment, another is the spectral characteristics of the location. The spectral characteristics of daylight behind a glass window or outside are different, especially in the UV region. Spectroradiometer measurements taken during a site assessment can be used as an input to our model-based dose planning tool. Using this tool with the input spectra, an estimate of photodynamic dose at depth in tissue can be obtained for different incubation and treatment periods.

Since the primary spectral changes introduced by a clear barrier are a reduction in UV-Blue light, the PpIX-weighted effective irradiance will be reduced to a greater degree than the total irradiance changes. However, since these spectral changes are UV-weighted their impact at depth in tissue will be minimal and changes in the photodynamic dose will primarily be localized to the first few hundred microns of tissue. It is also interesting to note as the treatment time increases, there is more photobleaching at superficial tissue layers, so the overall photodynamic dose at specific treatment times is reduced near the surface. Even though the indoor effective irradiance is reported to be 60% of the outdoor counterpart, the PDT dose at depth remains equivalent beyond the first 200 $\mu$ m of tissue. Additionally, within the 15 minutes of treatment after a 30-minute incubation there is

sufficient photodynamic dose to depths of approximately 1mm for the given irradiance, however, to treat the next mm, the treatment time needs to be lengthened by 10x.

While indoor daylight PDT requires less vigilance in applying sunscreen, careful consideration should be taken when choosing a sunscreen for outdoor treatments.<sup>6</sup> The chosen sunscreen should not block wavelengths that are predominantly absorbed by PpIX. If sunscreens are applied, this model would need to be adjusted to account for higher light scattering in the superficial layers of the multi-layer skin model. In some cases, a glass gazebo has been used to block UV, and reduce the need for applying sunscreen effectively providing indoor daylight.<sup>14</sup> With treatment locations that are identified to have full-day sunlight, the spectral composition of UV light will change throughout the day,<sup>20</sup> which should be considered when performing the one-time site assessment.

The light dose given during daylight PDT is often reported to be 2-2.5 hours in a range of weather conditions, seasons and latitudes. While others have placed a wrist-based dosimeters on patients,<sup>21-23</sup> the ideal dosimeter would be placed on the treatment site, yet current technology and large treatment fields have made this impractical. It may be feasible to place a spectroradiometer near the patient(s) being treated to provide better estimates of light dose, which can then be correlated with clearance, however, this is still slightly cumbersome and impractical.

As a middle-ground solution for improved dose planning we propose a one-time site assessment. After this site assessment, weather data can be used as a surrogate for continuous spectroradiometer measurements. While seasonal and in some cases weekly or

daily variations have been presented previously by others as a way to determine if sufficient sunlight is available, we have shown transient weather conditions will impact the light availability (Figures 4.3-1, 4.3-2). However, by collecting weather data at a higher time resolution that more closely aligns with the treatment period, a more accurate light dose estimate can be obtained. Using either satellite data for cloud coverage, or UV-index provide a strong correlation to spectroradiometer measurements (Figure 4.3-4). This method can be used for both indoor and outdoor daylight-PDT protocols.

Weather data can be acquired programmatically and is generally available from many locations such as airports. This automated process could easily be incorporated into an application on a mobile device, so real time dose estimates could be obtained with minimal effort. Furthermore, the weather data can be used to estimate the light fluence rate based on the spectral data from the one-time site assessment. This can be used with the lookup tables generated by the dose-planning model, so real time estimates of photodynamic dose at depth can be monitored. As weather forecasts become more accurate, the same method could transition from dose-estimation to a dose-planning mechanism.

## **4.5 Conclusions**

Measuring light dose during daylight-PDT is difficult due to a number of reasons, including the length of treatment, broad spectral characteristics, seasonal changes, site latitude and continuously variable weather conditions. It is unrealistic to expect the clinical team to monitor these factors continuously during treatments, and as a result many treatment periods are set to 2 hours. Yet, for the sake of reproducibility, quantifying the light dose is

important to better understand the depth of treatment and potential clearance. We propose methods to improve dose planning without placing a large burden on clinical staff, by limiting spectral measurements to a one-time site assessment. Furthermore, automatically acquired weather data can be used to routinely account for transient conditions during daylight treatments. Using this data in a previously described model, a lookup table can be generated to propose minimal treatment times based on the desired depth of treatment. A simple standardized method for estimating light dose during daylight-PDT could help improve inter-site reproducibility while minimizing treatment times and optimizing clearance rate.

## 4.6 Acknowledgments

This work was funded by the National Institutes of Health and the National Cancer Institute grant P01 CA084203 and by a National Science Foundation Graduate Research Fellowship.

## 4.7 References

1. Wiegell, S. R. *et al.* Continuous activation of PpIX by daylight is as effective as and less painful than conventional photodynamic therapy for actinic keratoses; a randomized, controlled, single-blinded study. *British Journal of Dermatology* **158**, 740–746 (2008).
2. Rubel, D. M. *et al.* Daylight photodynamic therapy with methyl aminolevulinate cream as a convenient, similarly effective, nearly painless alternative to conventional photodynamic therapy in actinic keratosis treatment: a randomized controlled trial. *British Journal of Dermatology* **171**, 1164–1171 (2014).
3. Lacour, J.-P. *et al.* Daylight photodynamic therapy with methyl aminolevulinate cream is effective and nearly painless in treating actinic keratoses: a randomised,

- investigator-blinded, controlled, phase III study throughout Europe. *Journal of the European Academy of Dermatology and Venereology* **29**, 2342–2348 (2015).
4. Wiegell, S. R. *et al.* Weather conditions and daylight-mediated photodynamic therapy: protoporphyrin IX-weighted daylight doses measured in six geographical locations. *British Journal of Dermatology* **168**, 186–191 (2013).
  5. Spelman, L. *et al.* Treatment of face and scalp solar (actinic) keratosis with daylight-mediated photodynamic therapy is possible throughout the year in Australia: Evidence from a clinical and meteorological study. *Australasian Journal of Dermatology* **57**, 24–28 (2016).
  6. O’Mahoney, P. *et al.* Use of illuminance as a guide to effective light delivery during daylight photodynamic therapy in the U.K. *British Journal of Dermatology* **176**, 1607–1616 (2017).
  7. Morton, C. A. *et al.* Practical approach to the use of daylight photodynamic therapy with topical methyl aminolevulinate for actinic keratosis: a European consensus. *Journal of the European Academy of Dermatology and Venereology* **29**, 1718–1723 (2015).
  8. Grinblat, B. *et al.* Feasibility of daylight-mediated photodynamic therapy for actinic keratosis throughout the year in Central and South America: a meteorological study. *International Journal of Dermatology* **55**, e488–e493 (2016).
  9. Neittaanmäki-Perttu, N., Grönroos, M., Karppinen, T. T., Snellman, E. & Rissanen, P. Photodynamic Therapy for Actinic Keratoses: A Randomized Prospective Non-sponsored Cost-effectiveness Study of Daylight-mediated Treatment Compared with Light-emitting Diode Treatment. (2016). doi:info:doi/10.2340/00015555-2205
  10. Wiegell, S. R. *et al.* Daylight photodynamic therapy for actinic keratosis: an international consensus. *Journal of the European Academy of Dermatology and Venereology* **26**, 673–679 (2012).
  11. Wiegell, S. R. *et al.* A randomized, multicentre study of directed daylight exposure times of 1½ vs. 2½ h in daylight-mediated photodynamic therapy with methyl aminolaevulinate in patients with multiple thin actinic keratoses of the face and scalp. *British Journal of Dermatology* **164**, 1083–1090 (2011).
  12. Taniguchi, M. & Lindsey, J. S. Database of Absorption and Fluorescence Spectra of >300 Common Compounds for use in PhotochemCAD. *Photochemistry and Photobiology* **94**, 290–327 (2018).
  13. LaRochelle, E. P. M. *et al.* Modeling PpIX effective light fluence at depths into the skin for PDT dose comparison. *Photodiagnosis and Photodynamic Therapy* **25**, 425–435 (2019).
  14. Lerche, C., Heerfordt, I., Heydenreich, J. & Wulf, H. Alternatives to Outdoor Daylight Illumination for Photodynamic Therapy—Use of Greenhouses and

- Artificial Light Sources. *International Journal of Molecular Sciences* **17**, 309–309 (2016).
15. O'Mahoney, P., Khazova, M., Ibbotson, S. & Eadie, E. The effects of sunscreen use and window glass on daylight photodynamic therapy dosimetry. *British Journal of Dermatology* **181**, 220–221 (2019).
  16. Wiegell, S. R., Heydenreich, J., Fabricius, S. & Wulf, H. C. Continuous ultra-low-intensity artificial daylight is not as effective as red LED light in photodynamic therapy of multiple actinic keratoses. *Photodermatology, Photoimmunology & Photomedicine* **27**, 280–285 (2011).
  17. de Souza, A. L. R. *et al.* Assessing daylight & low-dose rate photodynamic therapy efficacy, using biomarkers of photophysical, biochemical and biological damage metrics in situ. *Photodiagnosis and photodynamic therapy* **20**, 227–233 (2017).
  18. Marra, K. *et al.* Comparison of Blue and White Lamp Light with Sunlight for Daylight-Mediated, 5-ALA Photodynamic Therapy, in vivo. *Photochemistry and Photobiology* (2018). doi:10.1111/php.12923
  19. Philipp-Dormston, W. G. *et al.* Daylight PDT with MAL – current data and practical recommendations of an expert panel. *JDDG: Journal der Deutschen Dermatologischen Gesellschaft* **13**, 1240–1249 (2015).
  20. McLellan, L. J. *et al.* Ultraviolet radiation exposure during daylight Photodynamic Therapy. *Photodiagnosis and Photodynamic Therapy* **27**, 19–23 (2019).
  21. Thieden, E., Agren, M. S. & Wulf, H. C. The wrist is a reliable body site for personal dosimetry of ultraviolet radiation. *Photodermatology, Photoimmunology and Photomedicine* **16**, 57–61 (2000).
  22. Heydenreich, J. & Wulf, H. C. Miniature Personal Electronic UVR Dosimeter with Erythema Response and Time-stamped Readings in a Wristwatch. *Photochemistry and Photobiology* **81**, 1138–1138 (2005).
  23. Wiegell, S. R., Haedersdal, M., Eriksen, P. & Wulf, H. C. Photodynamic therapy of actinic keratoses with 8% and 16% methyl aminolaevulinate and home-based daylight exposure: a double-blinded randomized clinical trial. *British Journal of Dermatology* **160**, 1308–1314 (2009).

# CHAPTER 5

## 5 Estimating signal intensity for *in vivo* imaging of Cherenkov and excited luminescence

*This chapter is derived from:*

E.P.M. LaRochelle, *et al.*, “Signal intensity analysis and optimization for *in vivo* imaging of Cherenkov and excited luminescence.” *Physics in Medicine & Biology*. **63**(8). (2019).

### 5.1 Introduction

Cherenkov based dosimetry or luminescence imaging have recently been developed for sensing within a range of applications including radiation therapy dosimetry.<sup>1-6</sup> The generated light is an example of a signal that is linearly related to the applied radiation to the tissue.<sup>2,7</sup> In general, the light signals available to be detected are quite low, being near the single photon per pixel level for most detection systems. The detection approaches to dealing with these signals are advanced, but the choice of ideal detection device strongly depends upon knowledge of the signal intensity, especially at this range where it could be below or above the single photon per pixel level.<sup>8</sup> In this study, a rigorous theoretical analysis of the signal level available was completed and validated through both *ex vivo* and *in vivo* experiments, in order to assess where optimizations might best be made. The studies

described in the current chapter are designed to provide guideposts on potential areas of detection optimization while supporting Monte Carlo simulations are provided in Chapter 6.

There are a number of single photon detection strategies using specialized signal processing to ensure that the signal read out from the camera is real, and not attributed to noise. One of the dominant factors in deciding the detection scheme is the speed of readout desired, because the number of photons per pixel per unit time will affect the acceptable noise and readout noise. Long integration times of seconds to minutes can be achieved with low noise cameras such as a cooled CCD. However, when the readout time is the range of milliseconds, then the ideal choice might be a cooled sCMOS sensor. Yet again when the timing of acquisition needs to be in the microsecond range, then few options exist for this fast gating, other than a time-gated image intensifier. In the application of Cherenkov mediated imaging from a linear accelerator, this latter approach is required, with fast temporal gating, with on and off times in the nanosecond range. As a result, much of this study focuses on an image intensified camera, where the initial detection event occurs at the entry photocathode, and after amplification, follows through to a phosphor plate.

The photon budget considers several parameters, including: the number of Cherenkov source photons, attenuation due to tissue optical properties, lens type and placement, photocathode quantum efficiency, micro-channel plate gain, phosphor plate quantum efficiency, and CCD efficiency. Noise introduced by the photocathode, CCD, and analog-to-digital converter (ADC) are also considered. Where possible, the budget tracks photon

wavelength within the range of 350-900nm with 10nm resolution. A series of Python scripts were developed to track the photon counts at each stage, from Cherenkov emission through digitization at the ADC.

The scheme of how to maximize the signal to noise in these cameras depends upon a better understanding of the signal and noise levels. This current investigation provides the basis for a photon budget for both Cherenkov emission imaging, as well as Cherenkov excited luminescence (CEL) imaging from two phosphorescent compounds used experimentally. The work begins with an in-depth theoretical treatment of all aspects of the imaging situation which affect the signal strength, and then progresses to experimental studies that are used to validate the predictions. Ultimately the results of this study can then guide optimization with this type of camera, or alternatively other detection systems which are optimized for single photon imaging.

## **5.2 Theory**

### **5.2.1 Signal Source**

Cherenkov photons are generated over a wide spectral range, but within the UV/optical/NIR range the distribution is proportional to  $1/\lambda^2$ , as described by the Frank-Tamm formula, which can be used to calculate the number of emitted Cherenkov photons for a given input phase velocity ( $\beta$ ) and target refractive index ( $n$ ).<sup>9,10</sup> Extensive Monte Carlo simulations have been performed previously to relate the Cherenkov photon fluence

to EBRT dose rates (Gy/sec).<sup>7</sup> These spectrally-resolved photon fluence values can then be used to estimate the number of Cherenkov photons produced during CEL imaging.

CEL imaging relies upon the emission of Cherenkov photons to excite a localized phosphorescent compound within the medium. Unlike fluorescence imaging, which generally use an external light source for excitation, CEL is accomplished through the local production of photons within a target, such as tissue. Localized Cherenkov photons are produced when high-energy charged particles, such as electrons, move through a dielectric medium at a speed faster than the phase velocity of light for the given target.<sup>9</sup> For medical-imaging applications the high-energy electron source is generally caused by either a radioisotope implanted in the target tissue,<sup>11–13</sup> or from an external beam radiotherapy (EBRT).<sup>1,2,14</sup> This paper will focus on the latter, although Monte Carlo simulations have been used to relate the photons generated by the two sources.<sup>7,15,16</sup>

### **5.2.2 Tissue Optical Properties**

While the Cherenkov emission spectrum is heavily UV/blue-weighted, with *in vivo* imaging, much of this spectrum is attenuated due to tissue optical properties. Tissue is composed of several smaller structures, each with unique absorption and scattering properties. The bulk summation of these optical properties can be assessed based on estimates of the proportions of contributing factors such as hemoglobin, water, and lipids. These estimates can then be applied to Monte Carlo simulations for boundary interactions or applied to diffusion theory estimates of light propagation deeper in tissue.

When Cherenkov photons are emitted deep within tissue, surface detection will be red-shifted due to the light attenuation introduced by tissue.<sup>2</sup> Additionally, the light scattering in tissue further increases pathlength of travel, compounding the absorption due to blood, and as a result the dominant light signal available is within the 650-950nm range. Since there are reduced numbers of Cherenkov photons in this part of the spectrum, the overall signal is reduced, and the detection is more difficult. It has been a bit unclear if the optimal excitation of a CEL should be in the blue or red wavelengths, but recent data suggests that red excitation is superior to blue for maximal CEL signal.<sup>17</sup> The red Cherenkov photons produced within tissue can be absorbed and re-emit photons at a longer NIR wavelength, which travel further in tissue. Several factors come into play when selecting an appropriate compound. As with fluorescence imaging, the quantum yield ( $\Phi$ ) of the compound is one important factor which dictates the efficiency of the compound. In CEL imaging time gating is used to separate Cherenkov emissions from luminescence, so phosphorescence lifetime ( $\tau$ ) is also an important factor. Medical Linear accelerators have a 3-4 microsecond radiation pulse, and so this moderate pulse time limits most time gating to the microsecond regime. The luminescent agents which are available with microsecond lifetimes are phosphorescent. It has not been feasible to detect fluorescent agents which by definition have nanosecond lifetimes, other than through wavelength filtering and continuous wave detection.<sup>17</sup> In medical applications biocompatibility and the ability to target areas of interest are also important factors, however these are outside the scope of the current investigation.

### 5.2.3 Detection Hardware

In EBRT, a linear accelerator delivers 3-4 microsecond bursts of radiation at a specific duty cycle, often in the range of 100-400 Hz, which can be synchronized to the gating of the shutter of a sensitive camera. The speed of this gating is not conducive to mechanical shuttering, requiring the use of electronic gating approaches such as an image intensifier can. In previous work, an ICCD was chosen as the optimal camera for both sensitivity and time-gating reasons.<sup>8</sup> This current investigation focuses on time-gated discrimination of Cherenkov emission and luminescence, and what level of signal is available within this constraint, however the estimation of photon levels can also be applied to assess the applicability of other camera systems.

Camera position and lens selection are two factors that influence resolution, field of view, and photon sensitivity. Several other inherent camera properties can also influence detection. In an ICCD, the intensifier has three components: the photocathode, microchannel plate (MCP), and phosphor screen, which each play a role in the sensitivity. The photocathode converts photons to electrons by the photoelectric effect. Then a high voltage applied across the MCP attracts the electrons to the nearest channel, where they are multiplied through multiple wall collisions, often to 10,000x more than the entering electron numbers. This amplified electron flow then exits the MCP onto a phosphor screen, which converts these fast electrons into photons. The phosphor screens have a certain quantum efficiency (QE) for producing light from these electrons, and then this optical signal must be imaged by a camera, like a CCD or CMOS sensor, for pixelated electronic imaging. In the case studied here, the CCD converts these photons back to an electric

charge, based on the QE of the sensor. Other CCD properties like dark current and full well capacity will also influence detection. The analog to digital converter (ADC) will also introduce a certain amount of uncertainty when quantizing the analog signal into bins with 16-bit resolution. The readout noise is also usually a dominant factor in what is detectable with a sensor, and so determining how fast to read the signal or how long to integrate for is often determined by the intensity of the signals on the chip.

Environmental conditions may also impact the ability to discriminate signal from background. While time-gating reduces the impact of ambient lighting during Cherenkov detection, ambient light is unnecessary background and often needs to be minimized. Within the ICCD a certain level of effective background illumination (EBI) will be introduced by the intensifier. Additionally, thermal dark noise ( $\sigma_D$ ) and shot noise ( $\sigma_S$ ) will be introduced by the CCD. For detection, usually the target signal must be greater the sum of the noise components, or else more elaborate methods for signal averaging or signal processing must be employed.

### **5.3 Methods**

A photon budget for EBRT CEL imaging was developed based on previously reported camera configurations and imaging geometries. Estimates of photon counts were made between 350nm and 900nm with a 10nm resolution for each step in the Cherenkov and CEL imaging process. The estimates in the following section are for quanta (photons or

electrons) as they travel from their source through the final step of being detected and digitized at a single (2x2-binned) pixel with the resolution of 315 $\mu$ m (0.1mm<sup>2</sup>).

The input parameters for each component in the imaging system are provided in the supplementary material (S1). Python code was developed to read this input file and determine the quanta at each stage based on the input radiation dose and total exposure time. The quanta for wavelengths of interest are recorded in an output file which is organized by tissue depth of the source photons. Output files were created for Cherenkov detection (S2), and phosphorescence detection (S3).

### **5.3.1 Cherenkov**

Previous Monte Carlo simulations documented by Glaser et al. <sup>7</sup> provide the fluence rate over a wide spectral range for Cherenkov photons produced in tissue as the result of an external 6MV X-ray photon beam. These simulations assume a constant refractive index ( $n=1.37$ ), but account for tissue scattering and absorption from 250nm-850nm at 1nm spectral resolution. From this, the average fluence rate (nW/cm<sup>2</sup>) is provided as a function of radiation dose rate (Gy/sec) and can be converted to photon flux (photons/cm<sup>2</sup>) by accounting for the energy at each wavelength. The photon flux is then dependent on the radiation dose rate, which can be simplified to be assumed at a standard 0.1Gy/sec (600MU/min, the standard Monitor Unit rate of the Varian Clinac2100CD at 6MV). The Varian higher energy clinical linear accelerator (Clinac 2100C) referenced in previous CEL publications provides a 3-4 $\mu$ s radiation pulse at a variable repetition rate of 60Hz-360Hz, but commonly at 360 Hz for the higher MU/min.<sup>6,8,18</sup>

The number of Cherenkov photons can then be estimated for the area detected by a single pixel (0.1mm<sup>2</sup>) based on the total dose delivered. For simplicity, this is calculated for the following: a single pulse (0.028 cGy), 30 pulses (0.83 cGy), 60 pulses (1.67 cGy), and 7200 pulses (2 Gy), where 2Gy is a typical daily dose given during fractionated radiotherapy.

### **5.3.2 Luminescence**

The number of photons absorbed by a phosphorescent compound is governed by the molar extinction coefficient and concentration of the compound. The quantum yield provides a metric of how efficiently the compound emits photons when one is absorbed. Two phosphorescent compounds are considered in this photon budget: PtG4 ( $\lambda_{\text{Ex}}$ : 435nm, 623nm,  $\lambda_{\text{Em}}$ : 772nm)<sup>19</sup> and Ir(btp)<sub>2</sub>(acac) ( $\lambda_{\text{Ex}}$ : 337nm, 480nm,  $\lambda_{\text{Em}}$ : 620nm)<sup>20</sup>. It is assumed 50 $\mu$ L of a 50 $\mu$ M solution is injected into a tumor with a total volume of 250mm<sup>3</sup>. So, assuming the compound is distributed homogeneously throughout the tumor and does not leak, the final concentration in the tumor would be 10 $\mu$ M or a total number of 2.5 nanomoles. Since both compounds have primary excitation peaks below 500nm, it can be assumed the Cherenkov-excitation must originate within 1mm (defined as  $d_0$  in Table 5.4-1) due to the attenuation of shorter wavelengths in tissue.

### **5.3.3 Tissue Optics**

Tissue optical properties from previously published Monte Carlo simulations of photon interactions with a multi-layer skin model were adapted for the present investigation.<sup>2</sup> The

spectral distribution of the absorption coefficient ( $\mu_a$ ) and the reduced scattering coefficient ( $\mu_s'$ ) were used to calculate the effective attenuation coefficient ( $\mu_{eff}$ ) using (1):

$$\mu_{eff}(mm^{-1}) = \sqrt{3\mu_a(\mu_a + \mu_s')} \quad (1)$$

For a diffuse approximation of the number of photons present at a given distance the Beer-Lambert Law can be applied with the effective attenuation coefficient as shown in (2):

$$I_{d_1} = I_0 \exp^{-d_1 \mu_{eff}} \quad (2)$$

Where  $d_1$  is the distance (mm) from the photon source to tissue surface and  $I_0$  is the number of photons at the source. This approximation can be applied to estimate either the number of Cherenkov photons, or the number of Cherenkov-excited luminescent photons which reach the surface.

### 5.3.4 System Configuration

Two specific combinations of camera position and lens specification were considered as a way to demonstrate practical set ups. First, a 135mm f/1.8 lens positioned 1.3m from the target, and secondly a 50mm f/1.2 lens positioned 0.63m from the target. The numerical aperture can be approximated from the f-number using (3) and (4) to determine the acceptance angle:

$$NA \sim \frac{1}{2 * f\_number} \quad (3)$$

$$\theta = \sin^{-1}(NA) \quad (4)$$

Since it was assumed that the light at the surface of the target tissue would emit light isotropically, only half the emitted light would leave the tissue and the total light captured by the lens ( $N_{lens}$ ) must be adjusted using (5):

$$N_{lens} = \frac{2\theta}{\pi} \quad (5)$$

The photons would then diffuse from the source proportional to  $1/d^2$ , where  $d$  is the distance from the target to the lens, assuming each point on the tissue acts like an isotropic emitter. Since the 50mm f/1.2 lens positioned 0.63m collects more photons, only values using this lens configuration are reported in the simulation output files (S2-S3). Additionally, experimental validation reported in subsequent sections uses a 50mm f/1.2 at this approximate distance.

#### 5.3.4.1 Image Intensifier

The photocathode QE is applied to the number of photons collected by the lens to determine the number of electrons entering the next stage of the intensifier. The current photon budget assumed that the photocathode is a filmless Gen III device with high red quantum efficiency<sup>21</sup>, so that the photocathode introduces noise in the form of EBI, which is near 0.02 photoelectrons/pixel/second at room temperature and an order of magnitude lower with active cooling.<sup>21</sup> So, the total input EBI ( $N_{EBI}$ ) is calculated using (6):

$$N_{EBI} = EBI(e/p/s) * N_{pixels} * t(sec) \quad (6)$$

Where  $N_{pixels}$  is 4 because of the 2x2 pixel binning, and  $t$  is the total exposure time while the intensifier is on, which is the product of the gate width and number of accumulations on chip (AOC).

Multiple stages of MCPs can be chained together where typical amplification values are approximately  $10^4$  (single stage),  $10^6$  (double stage),  $10^7$  (triple stage). These amplification values are used to determine the number of detected electrons which interact with the phosphor screen. The amplification is also applied to  $N_{EBI}$  to determine the background noise levels.

Two phosphor screens were considered: P43 and P46. P43 has a higher quantum efficiency (200 photons/electron) but a longer decay time (1.5-3.2 ms), whereas P46 has a lower quantum efficiency (95 photons/electron), but quicker decay time (0.2 - 20  $\mu$ s).<sup>22</sup> The P43 and P46 phosphor screens emit photons at different wavelengths, which must be considered when factoring the CCD detection QE.

#### 5.3.4.2 CCD Sensor

The CCD can be coupled to the intensifier by fibers, or with an air gap. The former is slightly more efficient, but with added cost, whereas the latter is more economical, but less efficient. A coupling efficiency of 50% is used in this budget. The noise characteristics of the CCD must also be combined with the EBI noise introduced at the photocathode. The CCD noise is characterized as shot noise ( $\sigma_s$ ), which is defined by the square root of the number of incident photons, and dark current noise ( $\sigma_D$ ) which is provided as a device specification.<sup>21</sup> The total CCD noise is given by (7):

$$Noise_{CCD} = \sqrt{\sigma_S^2 + \sigma_D^2} \quad (7)$$

While the CCD noise, combined with the EBI provides a lower limit of detection, the full-well capacity of the CCD pixel provides an upper limit, and the current budget assumes a full well capacity of 130 ke- per pixel.<sup>21</sup> Since 2x2 pixel binning is assumed, this value is quadrupled. After the CCD converts the photons to electrons, the analog-to-digital converter (ADC) will introduce a certain amount of uncertainty, between 10 e- and 70 e-, based on the rate of conversion, between 2 MHz and 32 MHz, respectively.<sup>21</sup>

#### 5.3.4.3 Phantom Imaging

A mouse phantom (XFM-2X Fluorescence Phantom, PerkinElmer) with  $\mu_{\text{eff}} \in [0.1, 3]$  mm<sup>-1</sup>, and spectral response similar to tissue, was used for experimental validation of the Cherenkov photon sensitivity. As shown in Figure 5.3-1, a linear accelerator (Varian, Clinac 2100C, California, USA) produced a 6MV X-ray photon beam which was shaped by the multi-leaf-collimator (MLC) into a 5mm thick sheet across the midline of the phantom. A PiMAX4 ICCD (Princeton Instruments, New Jersey, USA) was triggered by the LINAC to acquire images 0.03 $\mu$ s after the beginning of the radiation pulse and for a gate width of 3.25 $\mu$ s, which is within the duration of each radiation pulse. The number of AOC was varied, while keeping the total dose fixed at 100MU (1Gy). The photocathode was not actively cooled during imaging, but the CCD was kept at -20°C.

#### 5.3.4.4 *In vivo Imaging*

Human breast adenocarcinoma (MDA-MB-231, Caliper LifeSciences) cells were implanted subcutaneously in two locations on the left and right lower flank of two nude mice. The tumors were allowed to grow until they were visible, but not ulcerated, approximately 100-250 mm<sup>3</sup>, as measured with calipers. Each mouse was anesthetized using isoflurane during imaging and placed prone on a black surface. Each tumor was injected with 50 $\mu$ L of a 50 $\mu$ M solution of each phosphorescent compound (2.5 nmol). Imaging was performed during anesthesia and 30 minutes after sacrifice, and a warming pad was used to regulate the mouse temperature for the duration of imaging.

Similar to the ex vivo phantom imaging, a linear accelerator produced a 6MV X-ray photon beam which was shaped by the multi-leaf-collimator (MLC) into a 5mm thick sheet. However, in this experiment the radiation sheet traveled orthogonally from the ventral to dorsal region of the mouse, scanning from a position cranial to the tumor and moving in the caudal direction. A PiMAX4 ICCD was triggered by the LINAC to acquire images 4.26 $\mu$ s after the beginning of the pulse, so each frame is collected after the radiation pulse. Data from approximately 65 pulses were accumulated on chip before being read off the CCD. The gate width was between 5 and 10 times the deoxygenated effective lifetime of the given phosphorescent compound. The photocathode was not actively cooled during imaging, but the CCD was kept at -20°C.

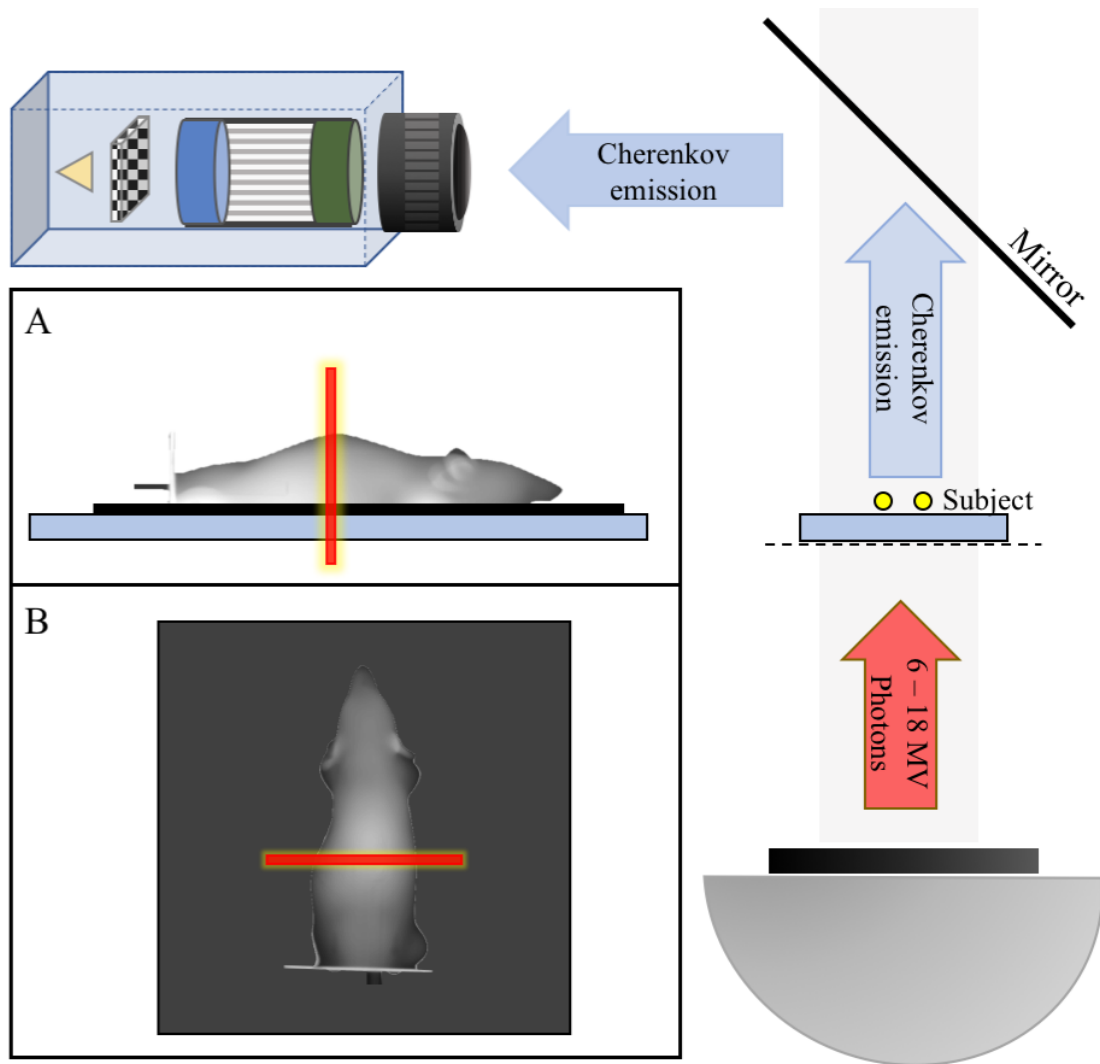


Figure 5.3-1: Geometry of the imaging system used for experimental validation. The LINAC gantry head is placed below the subject, providing a source of high energy photons. The subject is placed on the treatment couch with a mirror above to redirect photons

## 5.4 Results and Discussion

The parameters considered for each component of the imaging system are presented in Table 5.4-1, with corresponding typical ranges expected in EBRT. The associated quanta

estimates using these ranges are also provided to demonstrate the magnitude of changes between elements. A more detailed breakdown of these interactions using a specific set of input parameters are provided in the following sections and the supplementary material.

Python code was developed to parse the spectrally-resolved input data provided in S1. The code is compartmentalized based on the 9 components listed in Table 5.4-1, where each component generally had an input and output spectrum. The simulations were run for varying input radiation doses. Additionally, the structure of the code allowed for multiple parameters to be tested, such as the absorption and emission spectra of the phosphorescent compounds, lens NA and placement ( $d_2$ ), and photocathode type (P43, P46). At each component the outputs are recorded, and a summary is provided in S2 and S3 for Cherenkov and CEL imaging, respectively.

Table 5.4-1: Parameters considered in photon budget and typical range of quanta available at each stage.

<b>Component</b>	<b>Parameters</b>	<b>Parameter range</b>	<b>Quanta range (N/mm<sup>2</sup>)</b>
<b>Radiation</b>	$\gamma$ - (MV) or e- (MeV), Dose (Gy), Rate (Gy/s)	6-18(MV), 6-18(MeV), 0-2(Gy), 0.017 - 0.1 (Gy/s)	
<b>Cherenkov</b>	$\beta$ , n	0.81 – 0.98, 1.3-1.5	1.0E+07 – 2.0E+11
<b>Tissue <math>\mu</math>-environment</b>	$exp^{-d_0\mu_a}$ (mm-1)	$d_0$ : <1mm $\mu_a$ : 0.02-20.0 (mm-1)	8.0E+06 – 2.0E+11
<b>Luminescence</b>	$\Phi$ (%), $\tau$ ( $\mu$ s)	0.01-0.3, 1-300 ( $\mu$ s)	8.0E+04 – 6.0E+10
<b>Tissue diffusion</b>	$exp^{-d_1\mu_{eff}}$ (mm-1)	$d_1$ : 1-20 (mm)	5.0E+02 – 5.0E+07

			$\mu_{\text{eff}}: 0.1 - 10.0 \text{ (mm}^{-1}\text{)}$			
<b>Camera placement</b>	$1/d_2^2$		d <sub>2</sub> : 300 – 2000 (mm)		1.0E-04 – 6.0E+02	
<b>Lens</b>	$\frac{2\sin^{-1}(NA)}{\pi}$		NA: 0.09 - 0.42		7.0E-06 – 2.0E+02	
	<b>Signal</b>	<b>Background</b>	<b>Signal</b>	<b>Background</b>	<b>Signal</b>	<b>Background</b>
<b>Photocathode</b>	QE( $\lambda$ ) (%)	EBI (ph/pix/s)	0.01-0.35	0.002 – 0.02	7.0E-08 - 6.0E+01	8.0E-08 – 1.0E-04
<b>MCP</b>	Gain		10 <sup>4</sup> -10 <sup>7</sup>		7.0E-04 - 6.0E+08	8.0E-04 - 1.0E+03
<b>Phosphor plate</b>	$\eta$ (ph/e)	$\tau$ (ms)	95-200	0.2 $\mu$ s – 3ms	7.0E-02 - 1.0E+11	
<b>Coupling</b>	50%		30 – 80 %		3.0E-02 - 6.0E+10	
<b>CCD</b>	QE( $\lambda$ ) (%)	$\sigma_S, \sigma_D$	0.3-0.5	$\sqrt{N}$ , <2	1.0E-02 - 2.0E+10	
<b>ADC</b>	Rate (MHz)	Read noise (e-)	2-32	10-70 (e-)		

### 5.4.1 Cherenkov Emission

The Cherenkov photon density in tissue due to a 6MV photon beam as calculated based on the output of the Monte Carlo simulations reported previously<sup>7</sup>, is given in Figure 5.4-1A for doses ranging from 0.03cGy to 2Gy. When considering tissue optical properties ( $\mu_a, \mu'_s$ ), tissue acts as a long pass filter as can be seen in Figure 5.4-1 B and D. Shorter wavelength light is attenuated, so even though more Cherenkov photons are generated at shorter wavelengths, much of the detected signal originating from depths greater than 1mm in the tissue will be due to longer wavelengths. Figure 5.4-1D shows the Cherenkov photon budget for a source 3mm deep in tissue, where wavelengths shorter than 600nm are just

above the noise floor, whereas wavelengths longer than 600nm are about two orders of magnitude above the noise floor. If we assume 30 pulses, corresponding to a dose of 0.83cGy, are accumulated on chip, then there are enough Cherenkov photons to be distinguished from the background, as shown in Figure 5.4-1D where all the lines are above the silver shaded region at the CCD.

Camera properties, such as lens placement also have a large impact on the detectable signal.

Without accounting for distance, the f/1.2 lens can capture a maximum of 27.4% of the

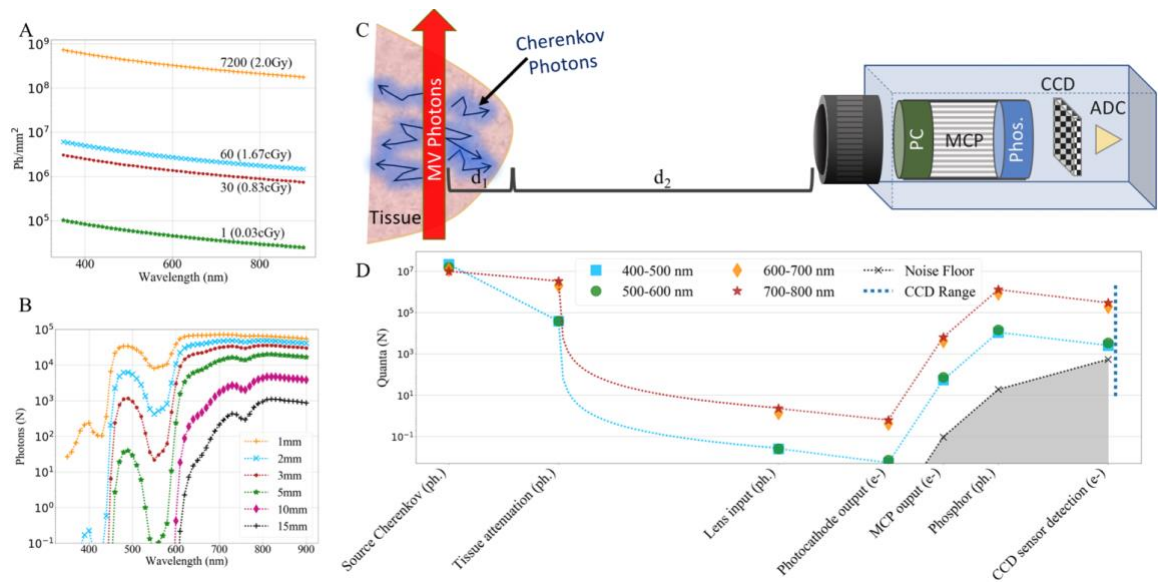


Figure 5.4-1: (A) Monte Carlo estimate of Cherenkov photons produced in 1 mm<sup>2</sup> as the result of: a single radiation pulse (0.03 cGy), 30 pulses (0.83 cGy), 60 pulses (1.67 cGy), and 7200 pulses (2 Gy). (B) Using tissue optical properties reported in S1, the Cherenkov photon attenuation is simulated for 30 pulses (0.83 cGy) observed at the tissue surface for photons emitted at various depths (d<sub>1</sub>). (C) Schematic depicting imaging system and components of interest. (D) Using the inputs reported in S1 and outputs in S2, a simulated photon budget for a Cherenkov source at 3 mm below the tissue surface (d<sub>1</sub>) generated by a 0.83 cGy dose, as detected by a 2 × 2 binned-pixel. The blue dotted line at right represents the usable dynamic range of the sensor.

emitted light, while the f/1.8 captures up to 17.9%, however, when distance to the object is considered, the intensity obeys an inverse square relation, dramatically reducing the detected signal. The photon budget indicates the lens may only receive approximately a single photon for each binned-pixel. While this value is small, the intensifier can amplify the signal sufficiently for detection by the CCD.

The first stage of the intensifier, the photocathode, introduces a small amount of background intensity. The EBI is also amplified through the next two stages of the intensifier, depicted by the silver shaded region in Figures 2D and 3D. Cooling can help reduce the EBI by reducing the background by 10-20x, however this has little impact on the detectable Cherenkov signal as shown in Figure 5.4-3 where the ratio remains the same after cooling.

### **5.4.2 Cherenkov-excited Luminescence**

While it is possible to detect Cherenkov-photons with sufficient signal at depths of centimeters, it is not an ideal modality for targeted imaging often used to determine properties of subcutaneous lesions. Phosphorescent compounds can be used to absorb Cherenkov photons in tissue at depths of greater than a centimeter. The two compounds investigated in this study, PtG4 and Ir(btp)<sub>2</sub>(acac) absorb photons at shorter wavelengths and emit longer wavelengths after the 4 $\mu$ s radiation pulse has stopped. Figure 5.4-2A shows the excitation and emission spectrum of PtG4, where the excitation overlaps with much of the Cherenkov emission. Even though both these compounds have quantum yields much lower than 1, the longer wavelengths are less affected by tissue attenuation and there is still sufficient signal for detection. The number of phosphorescence photons originating

from a 10 $\mu$ M PtG4 inclusion at various tissue depths ( $d_1$ ) is shown in Figure 5.4-2B. Since the phosphorescence shifts the output to a longer wavelength, there are no photons within the 400-500 or 500-600nm range shown beyond the Cherenkov source for the photon budget depicted in Figure 5.4-2D. Additionally, for this compound the photons between 600-700nm are not detectable without further processing because they are below the noise floor, shown as the silver shaded region.

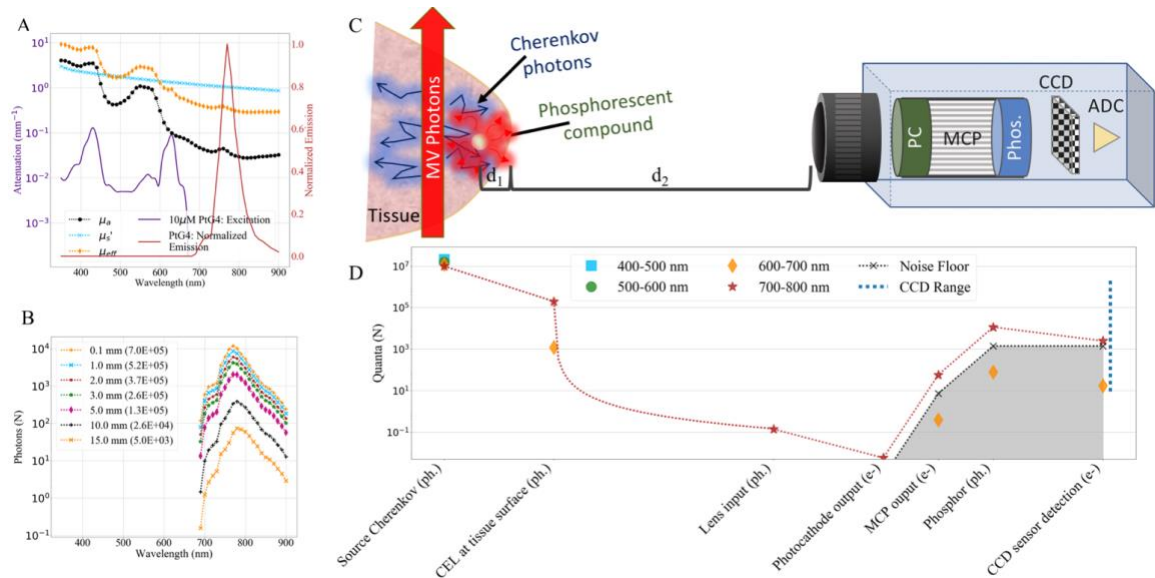


Figure 5.4-2: (A) Approximate tissue attenuation coefficients overlaid with extinction coefficient for 10  $\mu$ M PtG4 (left y-axis), and corresponding normalized emission spectrum (right y-axis). (B) Simulated photon count of CEL caused by 0.83 cGy dose for a PtG4 source at various depths ( $d_1$ ) within tissue. (C) Schematic depicting imaging system and components of interest. (D) Using the inputs reported in S1 and outputs in S3, a simulated photon budget for PtG4 CEL source at 3 mm below the tissue surface ( $d_1$ ) generated by a 0.83 cGy dose, as detected by a  $2 \times 2$  binned-pixel. The blue dotted line at right represents the usable dynamic range of the sensor.

As with the Cherenkov detection, the distance from the camera to the object of interest ( $d_2$ ) has a very strong influence on the final signal due to the  $1/d_2^2$  relation. Since phosphorescence imaging has a lower overall signal than Cherenkov imaging, camera placement is one method that could greatly improve system sensitivity.

Since phosphorescence images are acquired after the  $4\mu\text{s}$  radiation pulse and generally have a longer gate width ( $55\mu\text{s}$  -  $300\mu\text{s}$ ), the EBI will have a larger influence because this background signal is directly related to the gate width and the number of accumulations on chip. The estimated signal and background intensities based on the simulated photon budget are summarized in Table 5.8-1 and used to calculate the signal-to-background ratios in Figure 5.4-3. Since EBI impacts phosphorescence detection more so than Cherenkov detection, background reduction through photocathode cooling will more positively influence CEL imaging, as can be seen in Figure 5.4-3. Without cooling, the photon budget indicates  $\text{Ir}(\text{btp})_2(\text{acac})$  is detectable at depths of approximately 3.5mm in tissue, and PtG4 is detectable at depths of approximately 3mm, however, with cooling these values increase to 8mm and 10mm, respectively. The difference in slope is due to the comparison of different wavelength ranges, where both Cherenkov and PtG4 have their highest SBR in the 700-800nm range, whereas  $\text{Ir}(\text{btp})_2(\text{acac})$  has a peak emission at 620nm, so the 500-600nm range was used to compute SBR for this compound.

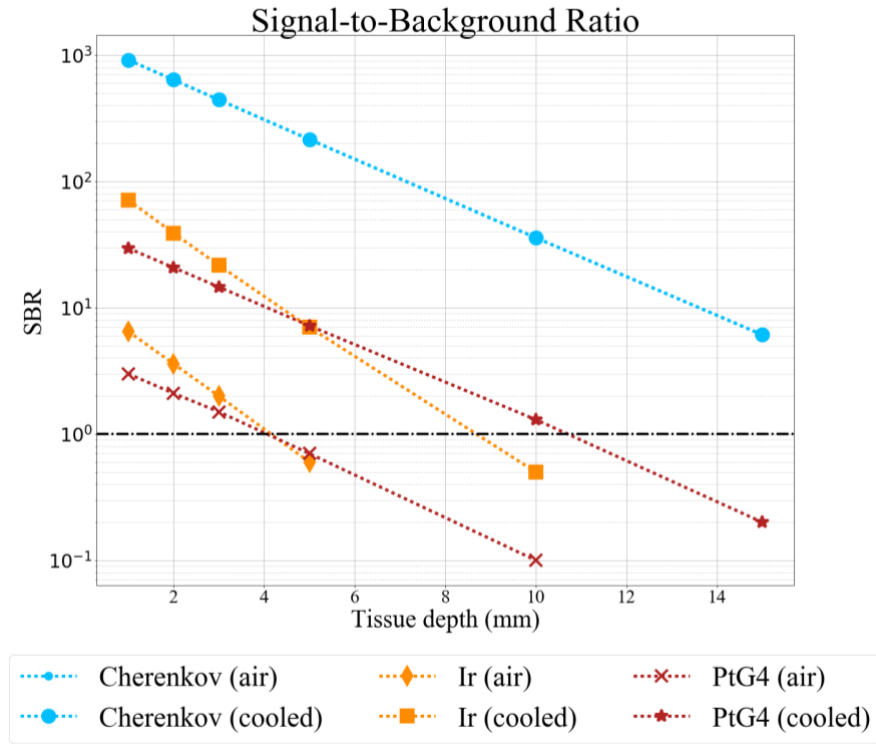


Figure 5.4-3: Theoretical Signal-to-Background ratio for Cherenkov and CEL detection with a photocathode room temperature, and cooled with dry nitrogen. Cherenkov values are the same.

### 5.4.3 Experimental validation

#### 5.4.3.1 Phantom Imaging

Images of the mouse phantom acquired during the radiation pulse show detectable Cherenkov signal. As the number of AOC are increased, the image signal increases as seen in Figures 5. Higher AOC increase the signal intensity, but also increase radiation dose and background intensity levels.

To further quantify the relation of the signal and background, two regions of interest were defined for each image stack. The Cherenkov signal is defined as the region within the

white boundary in Figure 5.4-5A, which is where the radiation beam is delivered to the mouse phantom. The background is defined as the region outside of the green boundary around the mouse phantom. The normalized distribution of pixel intensities for each region are shown for a Cherenkov image collected using 2 AOC as shown in Figure 5.4-5A-C. The distribution of the background appears Gaussian and pixel intensity is centered at 600 counts, which is the offset used by the PiMAX, whereas the distribution of the detected Cherenkov photons centered at 705 and follows a Poisson distribution. As the number of accumulations increases, the variability of the pixel intensities for both regions grow, however it increases more rapidly for the background region. The ratios of the median pixel intensity for each region provides the signal-to-background ratio, as shown in Figure 5.4-5E for a single frame. Since there is an offset used in the camera, the signal-to-noise ratio is calculated as:

$$SNR = \frac{Med(Beam)-600}{\sigma_{Bg}} \quad (8)$$

where  $\sigma_{Bg}$  is the standard deviation of pixel intensities in the background region. While both SBR and SNR increase with the number of AOC, the radiation dose required to capture each image also increases as shown in the upper x-axis of Figures 6D and 6E. The SNR was also determined for a fixed radiation dose of just under 7cGy by taking the temporal median of the acquired image frames, where 2 frames were used from the set of images acquired with 128 AOC, and 128 frames were used from the set acquired with 2 AOC. These parameters more closely match previously reported acquisition settings where

temporal median filtering is often used to reduce noise from high-energy particles.<sup>8,14,17</sup> In this setting it can be seen in Figure 5.4-5E that the SNR plateaus between 64 and 128 AOC. In this phantom study, the image stacks captured with lower AOC values have lower photon flux due to the shorter CCD exposure times. In this region (<64 AOC) the primary factors contributing to noise are dark current and read noise from the ADC. In the read-noise-limited detection the signal is expected to increase linearly with the number of exposures, while the noise remains relatively constant. So, in this region, combining multiple exposures will increase the SNR by the square root of the number of exposures. However, as the photon flux increases with longer CCD exposure times (>64AOC), the primary factors contributing to noise are EBI from the photocathode and shot-noise in the CCD. In this photon-noise-limited region combining additional frames does not improve the overall SNR, as seen in Figure 5.4-5E. While the SNR should remain relatively unchanged, a single frame may still contain artifacts from high-energy particles, so in practice multiple frames are still acquired using a temporal median filter to reduce their influence on the final image.

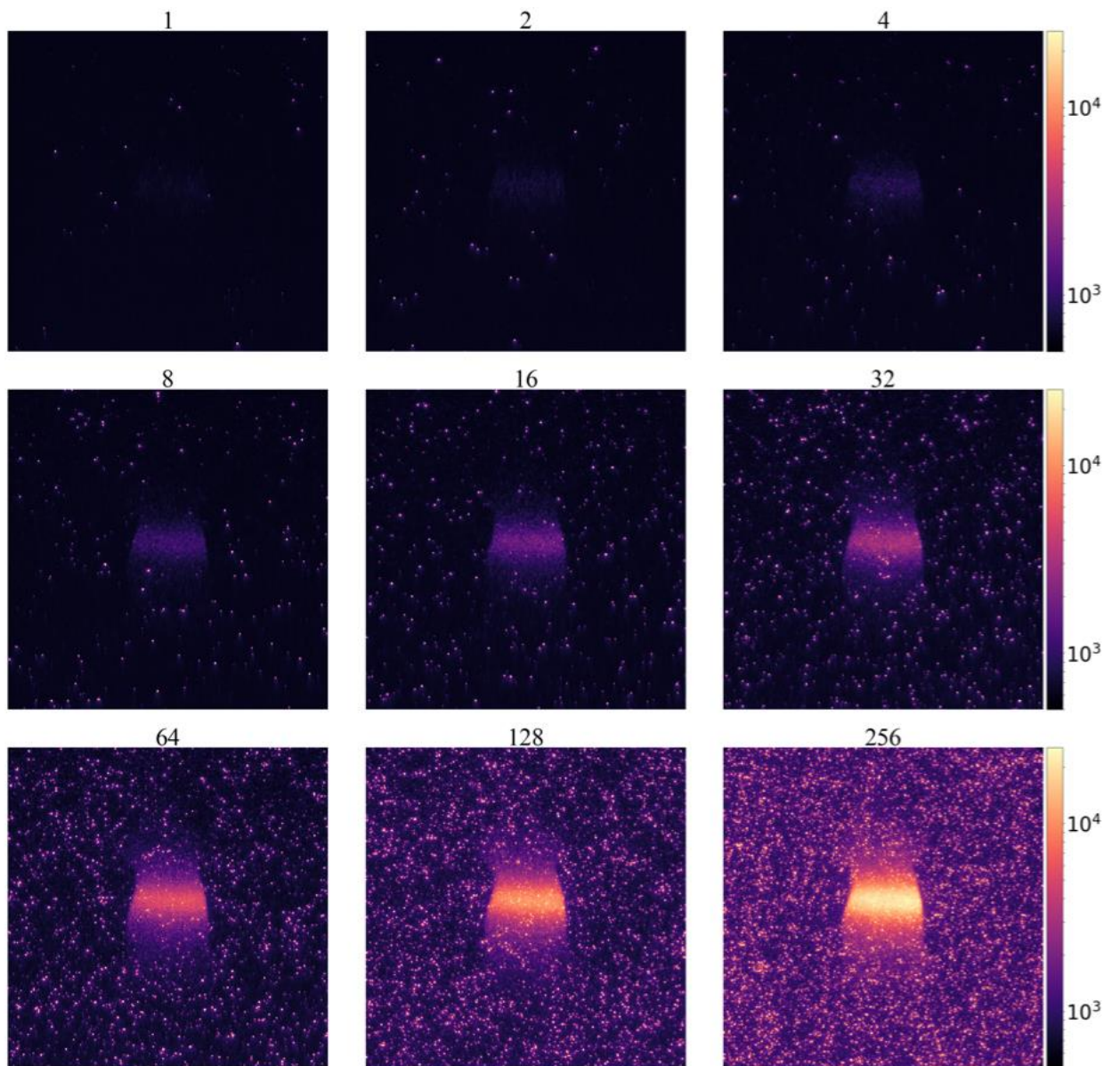


*Figure 5.4-4: Experimental Cherenkov image frames of a mouse phantom captured with varying numbers of accumulations on chip (AOC).*

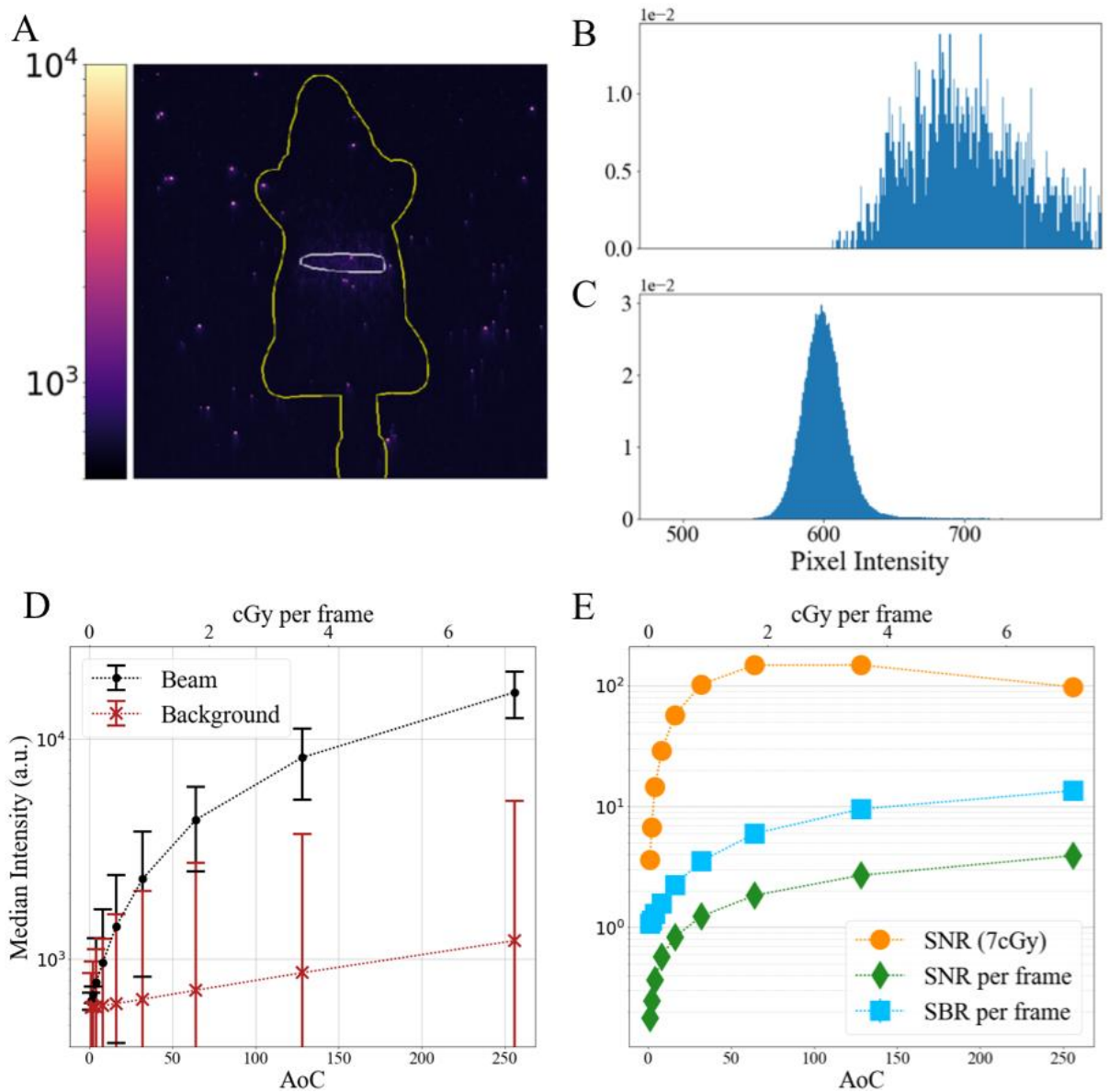


Figure 5.4-5: (A) Experimental Cherenkov image frame of a mouse phantom captured using 2 AOC; (B) normalized histogram of intensity count for region of image receiving radiation dose (inside white area in (A)); (C) normalized histogram of intensity count for background area around mouse phantom (outside green area in (A)); (D) median pixel intensity for experimentally acquired Cherenkov image of previously defined regions using different AOCs. Error bars show standard deviation of pixel intensities in region; (E) experimentally determined signal-to-background ratio and signal to noise ratio for varying AOCs.

#### 5.4.3.2 *In vivo* imaging

Data collected from *in vivo* imaging of mice with subcutaneous tumors injected with PtG4 and Ir(btp)<sub>2</sub>(acac) produce a detectable signal in a single frame. Tumors were estimated to be between 100 and 250 mm<sup>3</sup> which corresponds to an approximate average dimension between 4.6 and 6.3 mm. Approximating the thickness of mouse skin to be between 0.5 and 1.5 mm, and assuming there is additional tissue between the surface and tumor, we can estimate the phosphorescent signal will diffuse between 1 and 4mm in tissue before reaching the surface. From Figure 5.4-3 we see the simulated signal-to-background ratio in this range is estimated to be between 3.0 – 1.1 and 6.5 – 1.3 for PtG4 and Ir(btp)<sub>2</sub>(acac), respectively.

A single frame for both Cherenkov and PtG4 phosphorescence detection are shown in Figure 5.4-6B and C, respectively. The Cherenkov image was collected using 32 accumulations on chip with a gate width of 3.5us, for a total dose of 0.89cGy. The phosphorescence frame was collected with 64 accumulations on chip and a gate width of 300us, for a total dose of 1.78cGy. From these images, we observe the Cherenkov pixel intensity values are on the order of 10<sup>4</sup> counts, whereas the phosphorescence is an order of magnitude weaker, even though the Cherenkov image received half the dose. While the photon budget indicates the Cherenkov pixel intensity should be approximately 100x higher than the PtG4 intensity for equal radiation dose, as shown in Table 5.8-1, or 50x for half the dose, the *in vivo* PtG4 is localized below the skin whereas the Cherenkov originates at multiple locations within the mouse, which can account for the slight discrepancy.

While the photon budget indicates Cherenkov imaging exhibits a relatively strong signal with low background, the impact of high-energy particles observed as high-intensity speckle (Figure 5.4-6B) cannot be fully ignored, however, it can be overcome with temporal-median filtering. The short gate width and low number of accumulations needed to acquire an adequate Cherenkov frame help keep the background levels low, although higher photon counts will increase the CCD shot noise which can explain why in Table 5.8-1 Ir(btp)<sub>2</sub>(acac) has lower noise than the Cherenkov image, even though the CEL image uses a longer gate width.

Regions of interest for each tumor were created from a processed image set. Briefly, a processed image set is created by temporally and spatially median filtering multiple frames. Temporal median filtering can be achieved because the MLC scans the radiation beam across the midline of the mouse and multiple frames are acquired at each MLC position, which provides the opportunity to take the median of sequential frames. A maximum intensity projection is performed on the resulting image stack, and a threshold is used to identify the area of maximum phosphorescence (white boundary in Figure 5.4-6D).

The background is defined as the area outside of the tumor regions and is also overlaid as the darker area around the tumors in the phosphorescence frame shown in Figure 5.4-6D. There is a small amount of padding between the tumor and background regions to avoid diffusion of the phosphorescent signal and to account for a certain amount of uncertainty in tumor and injection locations. The median value of each region is determined for each frame and these values were used to calculate the SBR. The PiMAX4 adds an arbitrary offset to the pixel values of approximately 600 counts, so this is accounted for in this

experiment by subtracting the background minimum from both regions in the same frame as shown in (9).

$$SBR = \frac{Med(Tumor) - Min(Bg.)}{Med(Bg.) - Min(Bg.)} \quad (9)$$

The maximum experimentally determined SBR for PtG4 was found to be between 2.1 and 2.2, and between 1.8 and 1.9 for Ir(btp)<sub>2</sub>(acac), which are both within the estimated ranges of the photon budget. Additionally, if we subtract the arbitrary offset, the median pixel values for the tumors are similar to those estimated by the photon budget, with the photon budget only slightly underestimating the actual values.

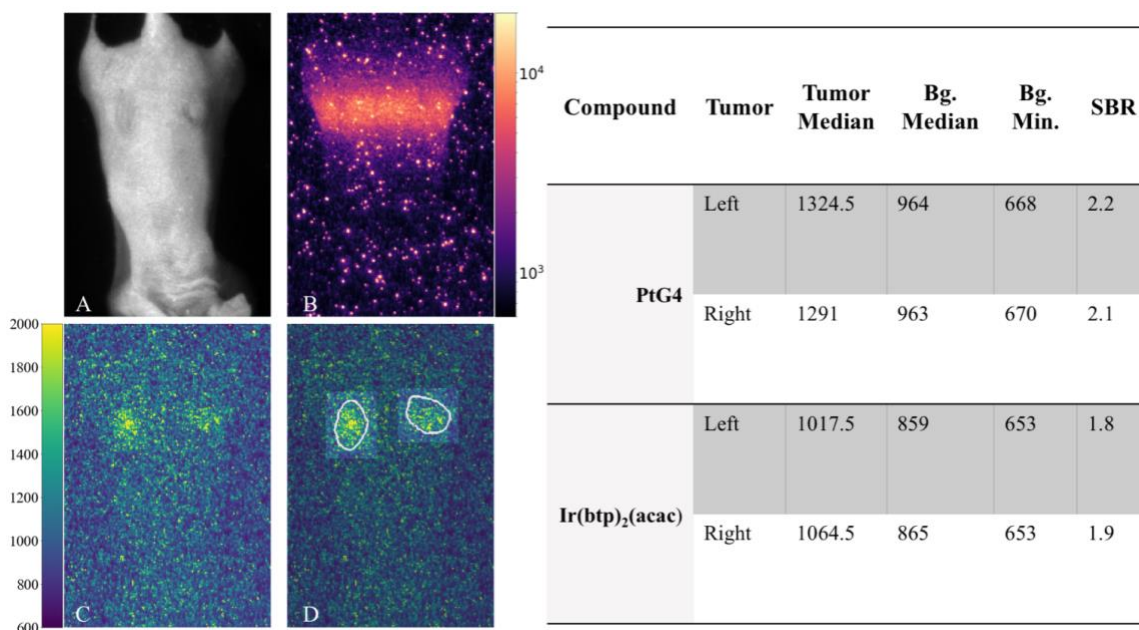


Figure 5.4-6: Images from in vivo experiment: (A) room-light image of mouse with two flank tumors injected with PtG4. (B) Single Cherenkov frame of interest during scanned imaging. (C) Single phosphorescence frame. (D) Regions of interests identified on phosphorescence frame, which were used to generate values shown in table.

While phosphorescence lifetime is not directly considered in the photon budget, experimentally the gate width is generally set between 5 - 10 times the deoxygenated lifetime ( $\tau_0$ ). By accounting for gate width in the photon budget, we are indirectly compensating for the needed shift in detection time. While this works to reduce the noise floor, as can be observed when comparing the estimated noise intensity of PtG4 and Ir(btp)<sub>2</sub>(acac) (Table 5.8-1), there are practical limitations in applicable lifetimes.

The time between radiation pulses is one factor that will limit the maximum lifetime when choosing a phosphorescent compound. The LINAC generates radiation pulses at a repetition rate between 2.7 and 17ms (600MU/min - 100MU/min), where the slower rates require longer treatment times, which can be impractical for *in vivo* imaging applications. Additionally, the phosphor plate in the image intensifier also has a decay which is generally provided in technical specifications. For example, P43 the decay to 10% or 1% the original signal is 1.5 and 3.2 ms, respectively, whereas P46 is ranges from 0.2 and 20  $\mu$ s at the sacrifice of quantum efficiency and spatial resolution.<sup>22</sup> In the current experiments a dose rate of 500MU/min, corresponding to a repetition rate of 3.3ms, was used to reduce the impact of ghosting between frames, which could be introduced at higher dose rates due to the limitations of the P43 decay time.

Shorter lifetimes can be difficult to discriminate from the radiation-induced Cherenkov light. The LINAC radiation pulse does not immediately turn off, and both stray charge and Cherenkov emissions may be detected during the transition phase. Phosphorescent compounds with lifetimes in this range (<4.5 $\mu$ s) will be difficult to detect. While

Ir(btp)<sub>2</sub>(acac) has a deoxygenated effective lifetime beyond this range, when it is in a well-oxygenated environment it may be more difficult to detect, whereas PtG4 can be detected both in the presence and absence of oxygen.

## 5.5 Conclusions

### 5.5.1 Imaging system

There are many factors that influence the detection of Cherenkov emission and Cherenkov-excited luminescence *in vivo*. While there are detectable signals in both imaging modalities, photon flux during imaging can be very close to the noise floor but discriminating the signal from the noise can be improved by optimizing several camera parameters. Phantom experiments demonstrated how SNR saturates when increasing the camera AOC value. This is thought to be the transition between the read-noise-limited and photon-noise-limited regimes. This transition point is where the SNR can be maximized without unnecessary increases to radiation dose. However, the transition point will change based on camera parameters such as position, ADC rate, and cooling temperature, as well as the inherent photon flux of the system being imaged.

As can be observed in Table 5.4-1, and Figures 2C and 3C, detection signal is most sensitive to camera-to-target distance. The inverse square relation of distance from the source can be accommodated by designing the optical path such that the camera is placed proximal to the target, without placing the camera hardware in the path of the radiation beam.

While the intensifier can overcome the low photon count, the CEL signals are still very low and the system is noise-limited. While additional MCP stages could theoretically help improve the overall signal, this comes at great cost. Additionally, if the EBI is greater than the photon count at the photocathode, additional MCP stages will not improve the problem. Maintaining low noise levels is particularly important with CEL imaging, where photocathode cooling may produce an up to 3x increase in depth sensitivity.

### **5.5.2 In vivo properties**

While we have observed *in vivo* Cherenkov emission to be on the order of 100x stronger than Cherenkov-excited phosphorescence for the compounds discussed in this investigation, much of Cherenkov light is being absorbed by nearby tissue, and thus never reaches the surface for detection. This absorption-dominated process can still be leveraged by localizing compounds which shift this energy to longer wavelengths which are impacted less by absorption. At these longer wavelengths, light attenuation in tissue is dominated by scatter and can travel further distances.

Tissue optical properties have a large impact on the overall signal, which is observed at greater depths. This is less of a concern for the implementation of Cherenkov for surface dosimetry. However, using CEL the detection of signals at depths is generally very important. One method to reduce the impact of this issue is to identify a phosphorescent compound with an emission less influenced by absorption. As can be seen in Figure 5.4-3 Ir(btp)<sub>2</sub>(acac) has a more negative slope than PtG4, so while Ir(btp)<sub>2</sub>(acac) has a slightly

higher SBR at shallow depths, PtG4 is more robust at depth due to its emission peak at 772 nm, as opposed to the Ir(btp)<sub>2</sub>(acac) emission peak at 620nm.

To optimize CEL, compounds which are excited by wavelengths shorter than approximately 500nm should be located as close to the targeted tissue as possible to maximize the energy transfer. The multiple dendritic chains of PtG4 allow it to circulate in blood with little degradation, whereas Ir(btp)<sub>2</sub>(acac) can be endocytosed by cells.<sup>20,23</sup> While both methods can deliver the compound to the tumor microenvironment, they are not molecularly targeted, which could further enhance the *in vivo* applications of CEL imaging.

### **5.5.3 Model**

The current investigation was limited to Cherenkov detection, and detection of CEL for two specific phosphorescent compounds. The input parameters for this model are organized in a single spreadsheet (S1), which allows for easily incorporating changes to the imaging environment. Additionally, simulating other compounds with known extinction coefficient, quantum yield, and lifetime would be trivial, as no code would need to be modified. While more detailed Monte Carlo simulations could be developed, the current model provides an estimate of which compounds warrant further investigation.

## **5.6 Acknowledgments**

This work was funded by the National Institutes of Health grants R01 EB024498 and R01 EB023909, as well as by a National Science Foundation Graduate Research Fellowship.

## 5.7 Supplementary Material

S1: [Photon budget input parameters \(S1\\_Photon\\_Budget\\_inputs.xlsx\)](#)

S2: [Cherenkov photon budget output for select parameters organized by Cherenkov source depth in tissue \(S2\\_Photon\\_Budget\\_outputs\\_30pulses\\_Cherenkov.xlsx\)](#)

S3: [CEL photon budget for PtG4 and Ir\(btp\)<sub>2</sub>\(acac\) for select parameters organized by depth of the phosphorescent compound in tissue \(S3\\_Photon\\_Budget\\_outputs\\_30pulses\\_Phosphorescence.xlsx\)](#)

## 5.8 References

1. R. Zhang et al., “Čerenkov radiation emission and excited luminescence (CREL) sensitivity during external beam radiation therapy: Monte Carlo and tissue oxygenation phantom studies,” *Biomed. Opt. Express* **3**(10), 2381, Optical Society of America (2012) [doi:10.1364/BOE.3.002381].
2. R. Zhang et al., “Superficial dosimetry imaging based on Čerenkov emission for external beam radiotherapy with megavoltage x-ray beam,” *Med. Phys.* **40**(10), 101914 (2013) [doi:10.1118/1.4821543].
3. A. K. Glaser et al., “Optical dosimetry of radiotherapy beams using Cherenkov radiation: the relationship between light emission and dose,” *Phys. Med. Biol.* **59**(14), 3789–3811, IOP Publishing (2014) [doi:10.1088/0031-9155/59/14/3789].
4. A. K. Glaser et al., “Optical cone beam tomography of Cherenkov-mediated signals for fast 3D dosimetry of x-ray photon beams in water,” *Med. Phys.* **42**(7), 4127–4136, American Association of Physicists in Medicine (2015) [doi:10.1118/1.4922135].
5. R. Zhang et al., “Cherenkov-excited luminescence scanned imaging,” *Opt. Lett.* **40**(5), 827, Optical Society of America (2015) [doi:10.1364/OL.40.000827].
6. R. W. Holt et al., “Cherenkov excited phosphorescence-based pO<sub>2</sub> estimation during multi-beam radiation therapy: phantom and simulation studies.,” *Phys. Med. Biol.* **59**(18), 5317–5328, NIH Public Access (2014) [doi:10.1088/0031-9155/59/18/5317].
7. A. K. Glaser et al., “Cherenkov radiation fluence estimates in tissue for molecular

- imaging and therapy applications,” *Phys. Med. Biol.* **60**(17), 6701–6718, IOP Publishing (2015) [doi:10.1088/0031-9155/60/17/6701].
8. J. M. Andreozzi et al., “Camera selection for real-time *in vivo* radiation treatment verification systems using Cherenkov imaging,” *Med. Phys.* **42**(2), 994–1004, American Association of Physicists in Medicine (2015) [doi:10.1118/1.4906249].
  9. P. A. Čerenkov, “Visible Radiation Produced by Electrons Moving in a Medium with Velocities Exceeding that of Light,” *Phys. Rev.* **52**(4), 378–379, American Physical Society (1937) [doi:10.1103/PhysRev.52.378].
  10. I. Frank and I. Tamm, “Coherent Visible Radiation of Fast Electrons Passing Through Matter,” in *Selected Papers*, pp. 29–35, Springer Berlin Heidelberg, Berlin, Heidelberg (1991) [doi:10.1007/978-3-642-74626-0\_2].
  11. A. E. Spinelli et al., “Cerenkov radiation allows *in vivo* optical imaging of positron emitting radiotracers,” *Phys. Med. Biol.* **55**(2), 483–495, IOP Publishing (2010) [doi:10.1088/0031-9155/55/2/010].
  12. A. Ruggiero et al., “Cerenkov luminescence imaging of medical isotopes,” *J. Nucl. Med.* **51**(7), 1123–1130, Society of Nuclear Medicine (2010) [doi:10.2967/jnumed.110.076521].
  13. R. Robertson et al., “Optical imaging of Cerenkov light generation from positron-emitting radiotracers,” *Phys. Med. Biol.* **54**(16), N355–N365, IOP Publishing (2009) [doi:10.1088/0031-9155/54/16/N01].
  14. A. K. Glaser et al., “Projection imaging of photon beams by the Čerenkov effect,” *Med. Phys.* **40**(1), 12101, American Association of Physicists in Medicine (2012) [doi:10.1118/1.4770286].
  15. A. K. Glaser et al., “A GAMOS plug-in for GEANT4 based Monte Carlo simulation of radiation-induced light transport in biological media,” *Biomed. Opt. Express* **4**(5), 741–759 (2013) [doi:10.1364/BOE.4.000741].
  16. E. Ciarrocchi and N. Belcari, “Cerenkov luminescence imaging: physics principles and potential applications in biomedical sciences,” *EJNMMI Phys.* **4**(1), 14 (2017) [doi:10.1186/s40658-017-0181-8].
  17. H. Lin et al., “Comparison of Cherenkov excited fluorescence and phosphorescence molecular sensing from tissue with external beam irradiation,” *Phys. Med. Biol.* **61**(10), 3955–3968, IOP Publishing (2016) [doi:10.1088/0031-9155/61/10/3955].
  18. J. Axelsson et al., “Quantitative Cherenkov emission spectroscopy for tissue oxygenation assessment,” *Opt. Express* **20**(5), 5133–5142, Optical Society of America (2012) [doi:10.1364/oe.20.005133].
  19. T. V. Esipova et al., “Two New ‘Protected’ Oxyphors for Biological Oximetry: Properties and Application in Tumor Imaging,” *Anal. Chem.* **83**(22), 8756–8765,

- American Chemical Society (2011) [doi:10.1021/ac2022234].
20. S. Zhang et al., “Phosphorescent Light–Emitting Iridium Complexes Serve as a Hypoxia-Sensing Probe for Tumor Imaging in Living Animals,” *Cancer Res.* **70**(11) (2010).
  21. “PI-MAX 4: 1024i Datasheet,” Princet. Instruments.
  22. Stanford Computer Optics, “The Phosphor Screen of the Image Intensifier,” <<http://www.stanfordcomputeroptics.com/technology/image-intensifier/phosphor-screen.html>> (accessed 10 August 2017).
  23. T. Yoshihara et al., “Intracellular and in Vivo Oxygen Sensing Using Phosphorescent Ir(III) Complexes with a Modified Acetylacetonato Ligand,” *Anal. Chem.* **87**(5), 2710–2717, American Chemical Society (2015) [doi:10.1021/ac5040067].

Table 5.8-1: Summary of photon budget parameters for different source depths in tissue, using optimal wavelength range.

Imaging Type	Cherenkov										CEL: PIG4										CEL: Ir															
Pulses	30																																			
Dose (cGy)	0.83																																			
Gate Width (us)	300																																			
Wavelength (nm)	700-800																																			
Depth	1		2		3		5		10		15		1		2		3		5		10		15		1		2		3		5		10		15	
	9.76E+06																																			
Source	9.76E+06																																			
Tissue output	6.78E+06	4.71E+06	3.28E+06	1.59E+06	2.67E+05	4.58E+04	3.98E+05	2.80E+05	1.97E+05	9.75E+04	1.71E+04	3.07E+03	1.40E+05	7.68E+04	4.28E+04	1.39E+04	9.89E+02	8.25E+01	4.67E+00	3.25E+00	2.26E+00	1.10E+00	1.84E-01	3.16E-02	2.74E-01	1.93E-01	1.36E-01	6.72E-02	2.12E-03	9.68E-02	5.29E-02	2.95E-02	9.57E-03	6.82E-04	5.69E-05	
Lens output (f/1.2 0.63m)	1.31E+00	9.07E-01	6.31E-01	3.06E-01	5.09E-02	8.69E-03	1.15E-02	8.09E-03	5.69E-03	2.82E-03	4.93E-04	8.82E-05	4.54E-03	2.48E-03	1.38E-03	4.48E-04	3.19E-05	2.66E-06	1.31E+04	9.07E+03	6.31E+03	3.06E+03	5.09E+02	8.69E+01	1.15E+02	8.09E+01	5.69E+01	2.82E+01	4.93E+00	8.82E-01	4.54E+01	2.48E+01	1.38E+01	4.48E+00	3.19E-01	2.66E-02
Photocathode output	2.61E+06	1.81E+06	1.26E+06	6.12E+05	1.02E+05	1.74E+04	2.30E+04	1.62E+04	1.14E+04	5.63E+03	9.86E+02	1.76E+02	9.08E+03	4.96E+03	2.77E+03	8.97E+02	6.38E+01	5.32E+00	4.96E+05	3.45E+05	2.40E+05	1.16E+05	1.93E+04	3.30E+03	4.38E+03	3.07E+03	2.16E+03	1.07E+03	1.87E+02	3.35E+01	1.72E+03	9.43E+02	5.25E+02	1.70E+02	1.21E+01	1.01E+00
MCP detection	7.20E-04																																			
Photocathode EBI	9.60E-06																																			
MCP EBI	9.60E-02																																			
Phosphor screen EBI	1.92E+01																																			
CCD noise	5.41E+02																																			
Total noise	5.41E+02																																			
Approximate Pixel Intensity	62518	43438	30207	14648	2439	416	552	387	272	135	24	4	217	119	66	21	2	0	917.1	637.2	443.1	214.9	35.8	6.1	3.0	2.1	1.5	0.7	0.1	0.0	6.5	3.6	2.0	0.6	0.0	0.0
Approximate Noise Intensity	182																																			
Signal to Background Ratio	33																																			

# CHAPTER 6

## **6 Models of Cherenkov spread and limits of detection in tissue**

### **6.1 Introduction**

The previous chapter presented system components involved in detecting Cherenkov emissions and Cherenkov-excited luminescence. In the current chapter, Monte Carlo simulations pertinent to this imaging system will be explored. While conventional fluorescence imaging, utilizing an excitation laser or LED can generally assume exponential decay of the source as it propagates into tissue, Cherenkov emissions are the result of secondary interactions which are more difficult to model. One method to improve spatial resolution of Cherenkov-excited luminescence images is to utilize known information about the beam geometry, which has previously been accomplished experimentally by delivering thin sheets of X-rays.<sup>1,2</sup> This method applies a deconvolution kernel to account for the beam shape, assuming an XY gaussian distribution of the Cherenkov emissions corresponding to the MLC leaf opening,<sup>1</sup> and also accounting for the depth dependence of the Cherenkov emissions.<sup>2</sup> Both the XY-spread and depth-dependence of Cherenkov emissions rely on a number of factors, such as the shape and

energy of the beam, and the optical properties of the object being imaged. Additionally, since Cherenkov emissions are correlated with dose, but not a direct measurement of dose, deconvolution can also be applied to improve the spatial resolution of the estimated delivered dose based on images of surface Cherenkov emissions.

The following sections present Monte Carlo models of Cherenkov emissions and Cherenkov-excited luminescence. First, the seven-layer skin model introduced in Chapter 3 is used to estimate Cherenkov emission spread resulting from the delivery of a narrow X-ray or electron beams. Expanding on this approach, additional adipose tissue and muscle are added to the model geometry to compare the limits of detection for wide-field optical illumination and Cherenkov-excited luminescence. Finally, the spectrum of Cherenkov light in the modeled tumor inclusion is used in conjunction with a chemical database to demonstrate how new Cherenkov-excited luminescent compounds could be computationally identified for future work. The aim of this work is to demonstrate how Monte Carlo simulations can be used as a tool to better understand the complex interactions occurring during this form of imaging, which could then inform improved deconvolutions kernels and detection mechanisms.

## **6.2 Materials and Methods**

Two sets of simulations were performed using the GAMOS tissue optics plugin described in Chapter 2. All validation scripts previously described by Glaser et al were run to verify functionality of the updated GAMOS 6.1 tissue optics plugin.<sup>3</sup>

## 6.2.1 Cherenkov spread

A skin equivalent geometry based on a 7-layer skin model, <sup>4,5</sup> and describe previously in Chapter 3 was used to estimate the spread of Cherenkov emissions. This model simulated a 2.5mm x10mm thin sheet of high energy photons or electrons incident on the skin geometry and originated 0.2m above the tissue volume. A total of  $10^6$  events were generated for each photon energy of 6MV and 18MV, as well as electron energies of 6MeV and 18MeV. The energy distribution of the photon beams is provided in Figure 6.2-1. The photon simulations were split into 10 separate simulations, and the electron simulations were split into 100. Each simulation was given a unique random seed and executed using the cloud infrastructure described in Chapter 2. Each photon simulation required approximately 30-50 minutes to execute depending on the energy level, whereas each electron simulation required 15-30 minutes. The initial and final position of each optical Cherenkov emission was recorded.

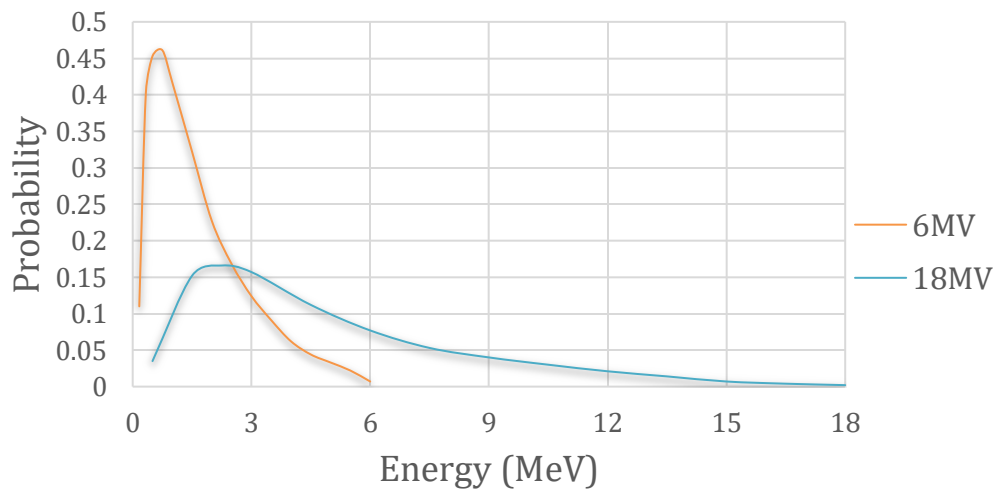


Figure 6.2-1: Photon energy distributions used in Monte Carlo models

Experimental measurements were collected with an intensified CMOS camera (CDose, Dose Optics) where a 3mm x 40mm sheet of 6MV and 18MV photons was delivered into water in a clear plastic container with the water surface at isocenter. Using the 6x6 electron beam collimator with a custom 3mm x 40mm Cerrobend insert, electron energies of 6MeV, 9MeV, 12MeV and 18MeV were also imaged. The camera was positioned such that it was level with the surface of the water. A 500nm short-pass filter (500FL07-50, Andover Corporation) was attached to the front of a 50mm f/1.2 lens. The camera was placed on the couch approximately 0.7m from the water container. Images were processed using Python 3.7 and scikit-image 0.16.2.

### **6.2.2 Limits of detection**

A tissue equivalent geometry containing an inclusion with fluorescence contrast was defined, where the inclusion depth and primary excitation source were varied using input arguments. The multi-layer tissue-equivalent geometry based on a 7-layer skin model,<sup>4,5</sup> combined with additional layers of adipose and muscle.<sup>6-8</sup> The surface dimensions for each layer were 10cm x 10cm, and the entire tissue geometry was 5cm in depth (Figure 6.2-2). The properties of the 7-layer skin model have been documented in previous publications,<sup>4,5</sup> and are summarized Chapter 3 and Figure 6.2-2B. Each layer has a specific density and mixture of pre-defined materials as well as optical properties ( $\mu_a$ ,  $\mu_s$ ,  $g$ ,  $n$ ) for wavelengths between 350nm and 900nm. A 1cm diameter spherical inclusion was also defined with a set of optical properties and additional properties for fluorescence absorption and emission, which most closely resemble the luminescent optical agent PtG4,<sup>9</sup> which has been used in

many previous experimental studies.<sup>1,10</sup> This molecule has absorption peaks near 430nm and 630nm with luminescence emission near 770nm, with a lifetime that is effected by the local oxygen concentration in tissue.

Simulations of a 1cm square source with  $0.97^\circ$  divergence placed 0.9m above the tissue geometry were run with  $10^7$  optical photons (430nm, 630nm) and the same number of X-ray photons (6MV, 18MV). With the beam divergence, the total area of the incident events on the tissue surface is approximately 4cm x 4cm. Tumor inclusion depths, measured from

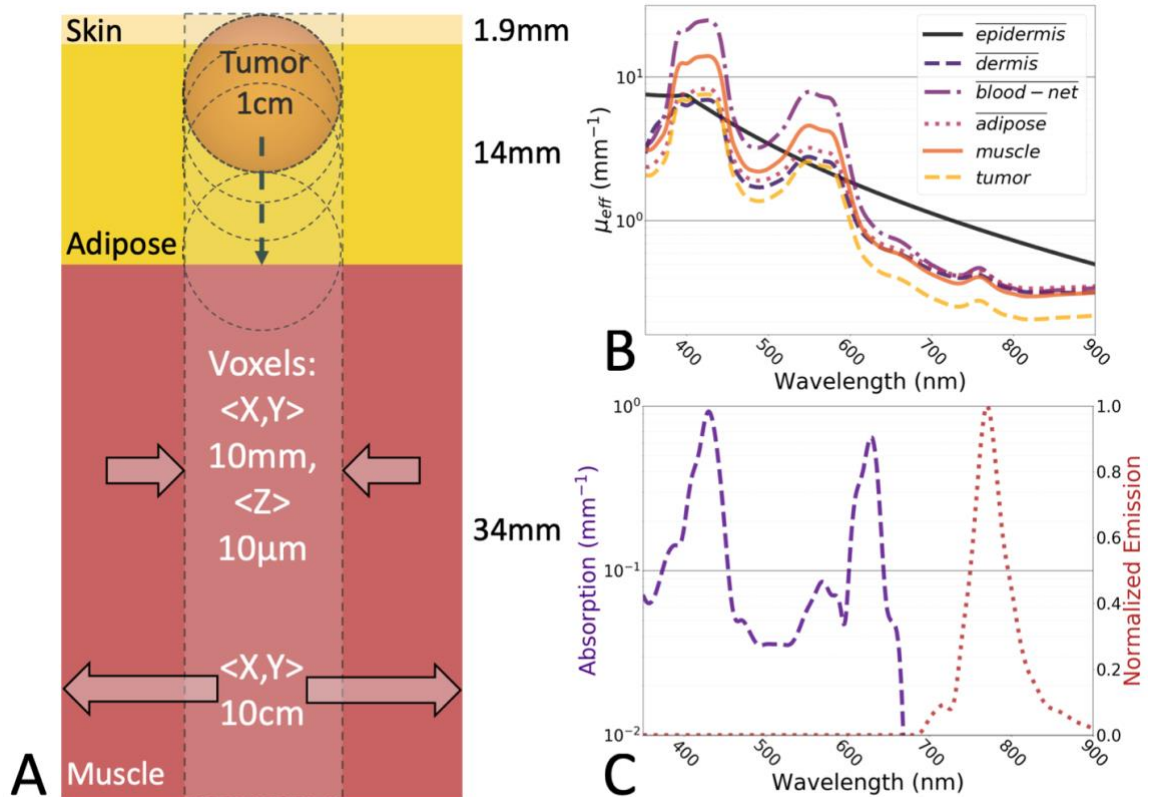


Figure 6.2-2: A multi-layer tissue model containing a tumor-simulating inclusion is defined (A) where the average  $\mu_{eff}$  is shown for each layer-type (B). The luminescent absorption and emission assigned to the tumor is provided as a contrast agent (C).

the top of the tumor to the tissue surface were defined between 0 and 10mm. A parallel world voxel geometry was defined with 1cm x 1cm x 10um voxels used to measure light fluence and for high-energy sources, dose deposited. Additional filters and detectors were defined to determine the position and wavelength of Cherenkov and fluorescence emissions starting in the tumor inclusion, exiting the tumor inclusion, and reaching the surface. Simulations for the 6MV and 18MV source were split into 10 simulations of  $10^6$  events for each tumor inclusion depth, whereas the lower complexity of the 430nm and 630nm optical excitation simulations allowed for single  $10^7$  event simulations to be executed in a short amount of time. Experimental comparison of the luminescent tumor geometry was not performed, but *in vivo* applications were briefly discussed in the previous chapter, and a more in-depth investigation of applications are presented in Chapter 8.

The spectral characteristics of the Cherenkov emissions in the tumor inclusion (Figure 6.3-4) were compared to the absorption spectrum of compounds in the PhotoChemCAD database.<sup>11,12</sup> This database is publicly available and contains the absorption and emission spectra and quantum yield of many compounds. The entire database can be downloaded in the form of a text file. This file contains a list of chemicals and their properties and links to files containing the absorption, and emission spectra, as well as links to images of the compound's chemical structure. A Python script was written to parse this text file and the corresponding absorptions files. All compounds with reported absorbance between 350nm and 850nm were considered for analysis. The Cherenkov spectra was interpolated and resampled to match the reported absorption spectra of each compound. The product of these two spectra were integrated between the previously stated bounds and the result was

multiplied by the quantum yield. The result was a scalar ranking, where all values were normalized to the highest ranked compound.

## **6.3 Results**

### **6.3.1 Cherenkov spread**

Text files recording the initial and final position of Cherenkov emissions were generated using filter detectors in the GAMOS simulations. While the simulation was a 3D geometry, the XZ positions were tabulated, effectively reducing the dimensionality of the data. The resulting photon counts generated from  $10^6$  initial events are shown in Figure 6.3-1. From these simulations it can be observed there are approximately 100x more Cherenkov emissions generated due to the electron source. This is expected due to the higher energy of the electrons compared to the photon energy distribution and because each electron at this high energy level will result in numerous Cherenkov emissions, whereas high energy photons must first undergo a scattering event before electrons are freed. These simulations also indicate the electron source will have a wider penumbra. In the simulations this effect is more pronounced in lower energy electron sources, mainly due to the shorter mean free path and higher likelihood of electron scattering. The lower optical emissions in the first 1.5mm of tissue are likely due to the higher absorption coefficients, whereas below this depth the volume is defined as adipose tissue.

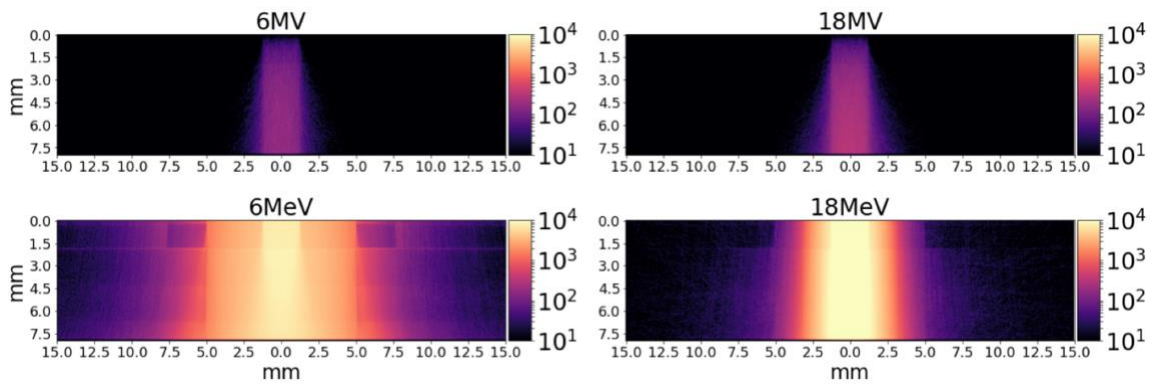


Figure 6.3-1: Cherenkov emissions recorded from simulations of 2.5mm wide photon source (top) or electron source (bottom) in multi-layer tissue volume.

Cherenkov imaging of water was performed as a comparison to the simulated results. Images were collected with both photons and electrons and are shown in Figure 6.3-2. From these images it can be observed the photon source have largely similar distributions within the first 10mm of water. However, the Cherenkov emission distributions of the electron sources are highly energy dependent.

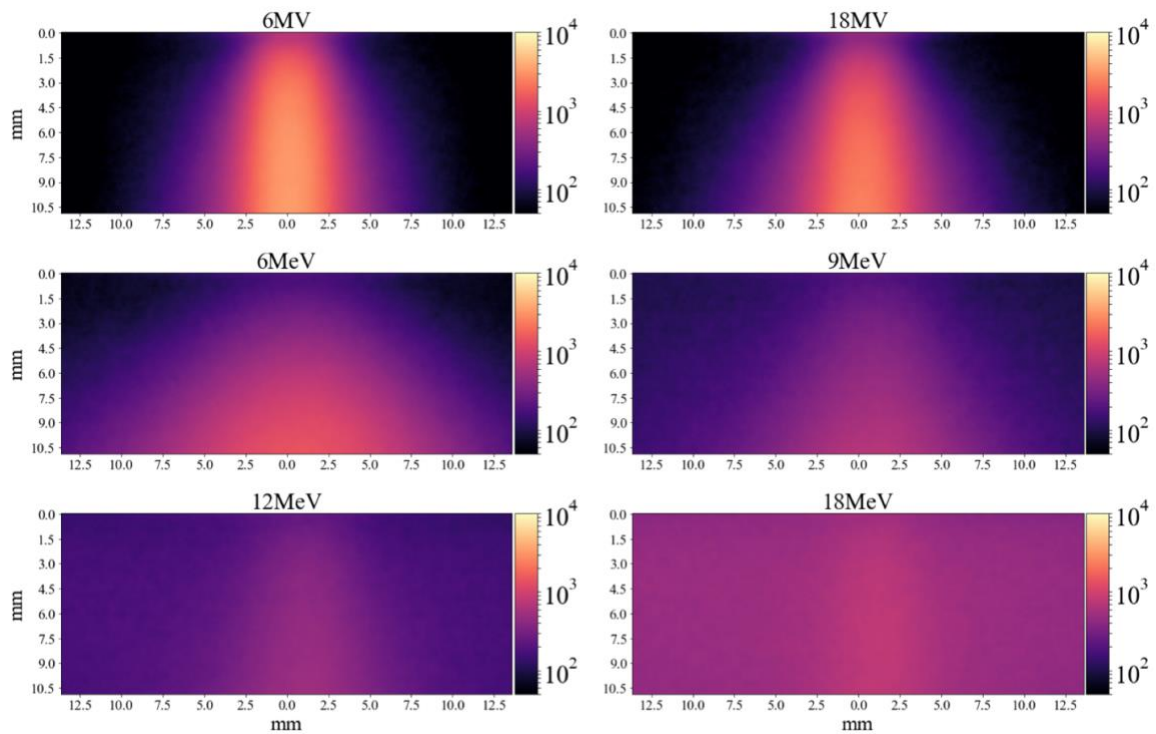


Figure 6.3-2: Experimental Cherenkov measurements of photon and electron beams in water.

The center of the beam was determined for both the simulations and experiments based on the average location of the maximum intensity along the Z-axis. From this value, a threshold of 80% of this maximum was defined as FW80M (Full-width at 80% maximum). The distance between the 80% thresholds is used to define the optically observed beam width, and the penumbra region was defined as the region between 80% and 20% of the maximum, where both values are shown in Figure 6.3-3. While both the simulation and experimental data show an expansion of the penumbra (gray shaded region) in Figure 6.3-3, there is a much larger region in the experimental data.

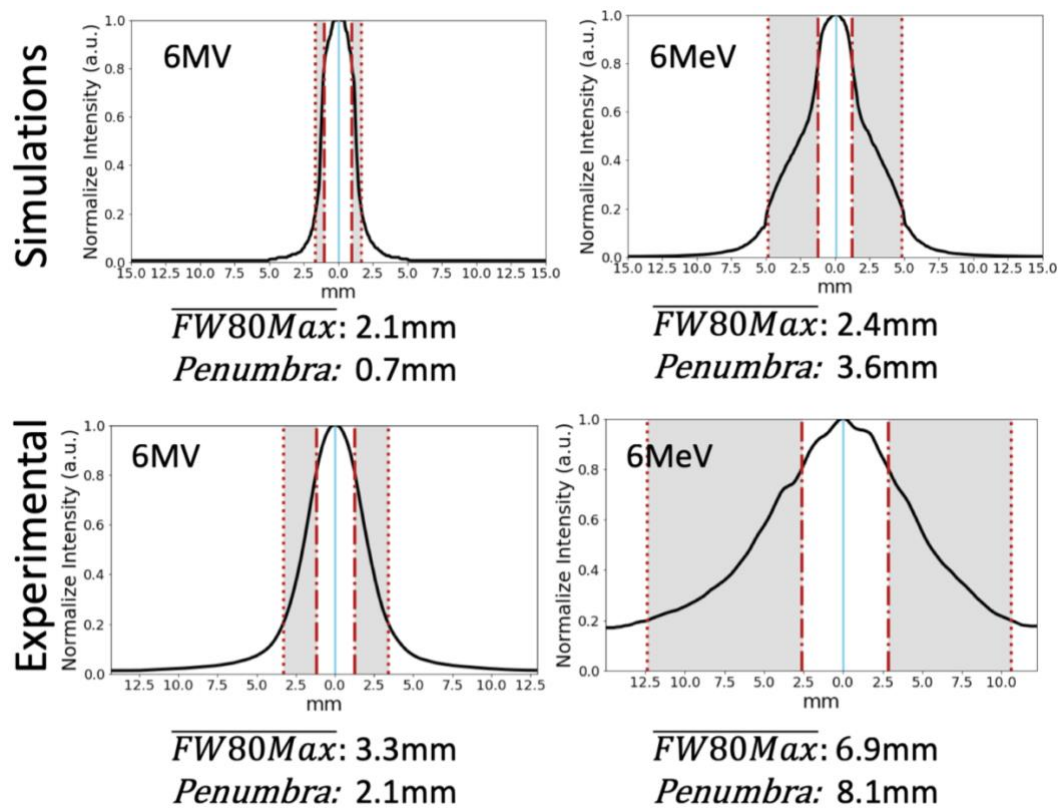


Figure 6.3-3: Analysis of beam width (full-width 80% of max) and penumbra region (gray-shaded) for 3mm wide photon and electron sources, based on the average of measurements between depths of 1mm and 8mm.

### 6.3.2 Limits of detection

Using detector filters to monitor the track of Cherenkov emissions, the spectral distribution can be monitored at various locations in the model. The spectral emissions are expected to follow a  $1/\lambda^2$  distribution,<sup>13</sup> which is generally observed in the tumor, with small increases at areas of lower attenuation, likely due to emissions originating outside the tumor and then being counted when entering the tumor (Figure 6.3-4A). As these emissions exit the tumor, another detector can tabulate the spectral characteristics, showing a small

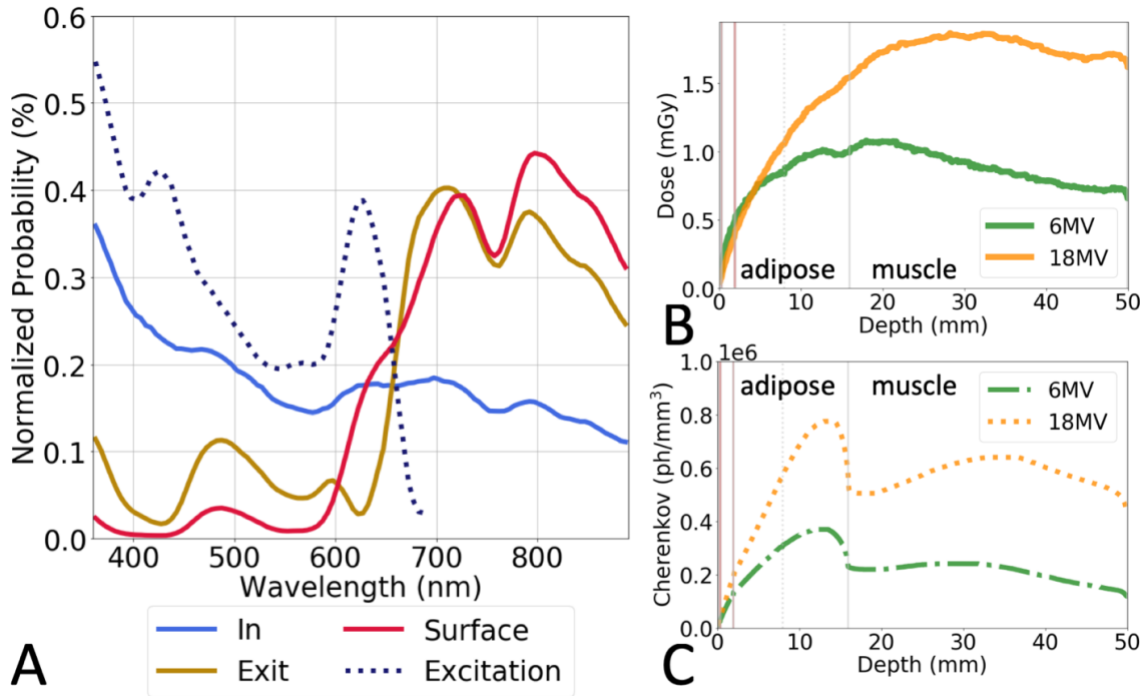


Figure 6.3-4: The spectral distribution of Cherenkov emissions in a model with a tumor inclusion at depth of 2mm, as detected in the tumor (light blue), exiting the tumor (orange), at the surface (surface), or contributing to luminescent excitation (dotted-indigo) (A). The deposited dose for 6MV and 18MV at depths into the tissue model (B) and the corresponding The optical Cherenkov fluence which are clearly affected by the tissue optical properties of each layer. (C)

peak around 480nm while the majority is distributed beyond 600nm, due to the longer mean free path in this spectral region. A similar long-pass filtering effect is seen at the surface, where the emissions are mainly in the red-NIR range. While the tumor fluorescence absorption is modelled after PtG4 (Figure 6.2-2C), the  $1/\lambda^2$  spectral distribution of the Cherenkov emissions must also be considered. This model provides the ability to determine the actual excitation wavelength distribution of the Cherenkov-excited luminescence, as shown in Figure 6.3-4A.

The Cherenkov emissions are related to the deposited dose which increases with depth into the tissue, where the maximum dose ( $D_{max}$ ) is expected to be 1.5cm for 6MV and 3.5cm

for 18MV photon beams which is similar to our simulation results (Figure 6.3-4B). While in a homogeneous medium Cherenkov emissions are thought to be directly correlated with deposited dose, Figure 6.3-4C shows how the higher attenuation of muscle and blood can greatly decrease the overall light fluence, which corresponds with previous studies of Cherenkov emissions in the presence of tissue optical properties.<sup>14-16</sup>

As expected, these simulations of multi-layer a tissue volume show the fluence rate for the 430nm source drops significantly in under 1 mm, and the 630nm source follows suit after a few millimeters (Figure 6.3-5A). The light gray vertical lines in Figure 6.3-5A show the skin layer boundaries, with light red shaded regions indicating blood-nets in the skin, which correspond with sharp drops in fluence due to the high absorption of these layers. By placing a detector at the surface, all fluorescence emissions exiting the tissue volume can be counted. GAMOS has the ability to count the origination of all fluorescent photons and those exiting the tumor, which shows approximately 90% of the fluorescent emissions leave the tumor, but those reaching the tissue surface is much lower (0-23%) and dependent on tumor depth. In our model, at a tumor depth of 7mm, just over 2% of fluorescent photons reach the surface for both 6MV and 18MV. A comparison of surface fluorescence emission intensity for excitation by either 430nm, 630nm optical or a 6MV X-ray source is provided in Figures 6.3-2B-C. A plot of the mean photon count at the surface, relative to the peak value observed by 630nm excitation, are plotted by tumor depth (Figure 6.3-5B), where the depth indicates the distance between the surface and the top of the 1cm diameter inclusion. Here it can be observed the 430nm source has the poorest depth sensitivity of approximately 250 $\mu$ m, while the 630nm excitation source has improved depth sensitivity

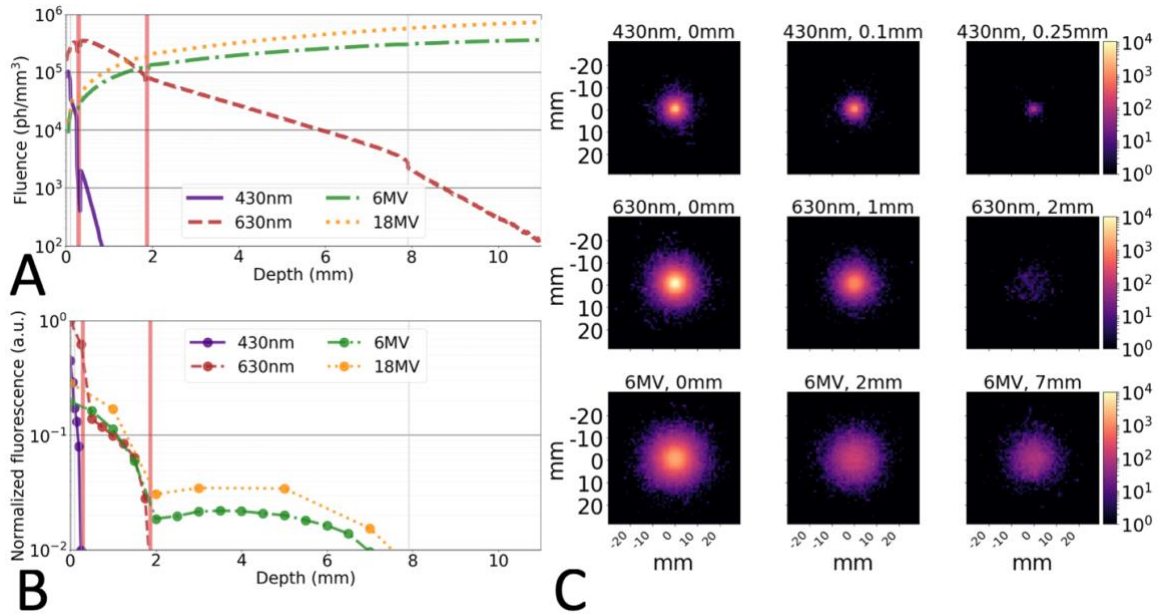


Figure 6.3-5: The photon fluence due to external optical illumination or X-ray induce Cherenkov emissions at depth in tissue (A) is compared to the corresponding normalized fluorescence detected at the surface, where the blood-nets (red vertical lines) introduce considerable attenuation(B). 2D-histograms of the surface luminescence are shown (C)

of approximately 2mm, and the in these simulations the Cherenkov depth sensitivity is approximately 7.5mm. The sharp drop in depth sensitivity appears to be limited by the absorption of the blood-nets, which is approximately 2X higher in absorption at the fluorescence peak (770nm) compared to the surrounding tissue. While the Cherenkov excitation shows the greatest depth sensitivity, the 430nm excitation source provides the highest potential resolution due to its short path length and resulting smaller tumor cross section (Figure 6.3-5C).

To identify other potential fluorophores which would be ideal candidates for Cherenkov excitation, a computational ranking of fluorescent compounds was performed. These rankings, the product of the *in vivo* Cherenkov spectra, fluorescence absorption spectra and quantum yield of each candidate compound are presented in Figure 6.3-6.

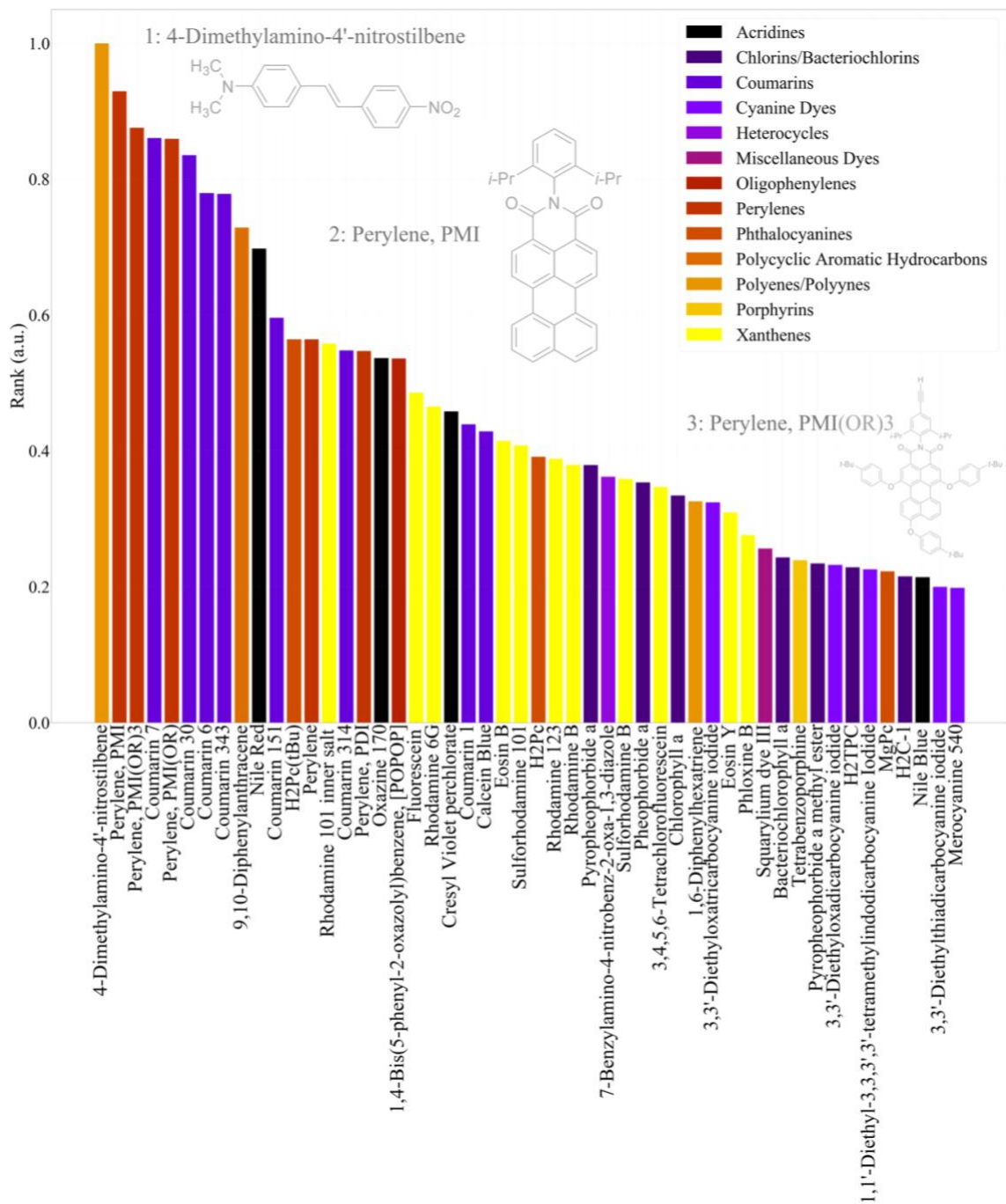


Figure 6.3-6: The Cherenkov-excitation ranking of the top 50 candidate compounds available in the PhotoChemCAD database. The chemical structure of the top three candidates are shown.

The PhotoChemCAD database organizes each compound into a chemical class, which are color-coded in the above figure, which presents the top 50 candidates. An alternative method of using a  $1/\lambda^2$  spectral distribution for the Cherenkov emissions produces similar results where the ranking for a few of the compounds is rearranged by 1-2 places. These rankings do not take into account biocompatibility or lifetime which is generally on the order of nanoseconds for these compounds. The system does not consider the emissions spectra or how it would interact with tissue optical properties, although this could be implemented using the given data. The absorption spectrum of the top-ranked compounds is presented in Figure 6.3-7.

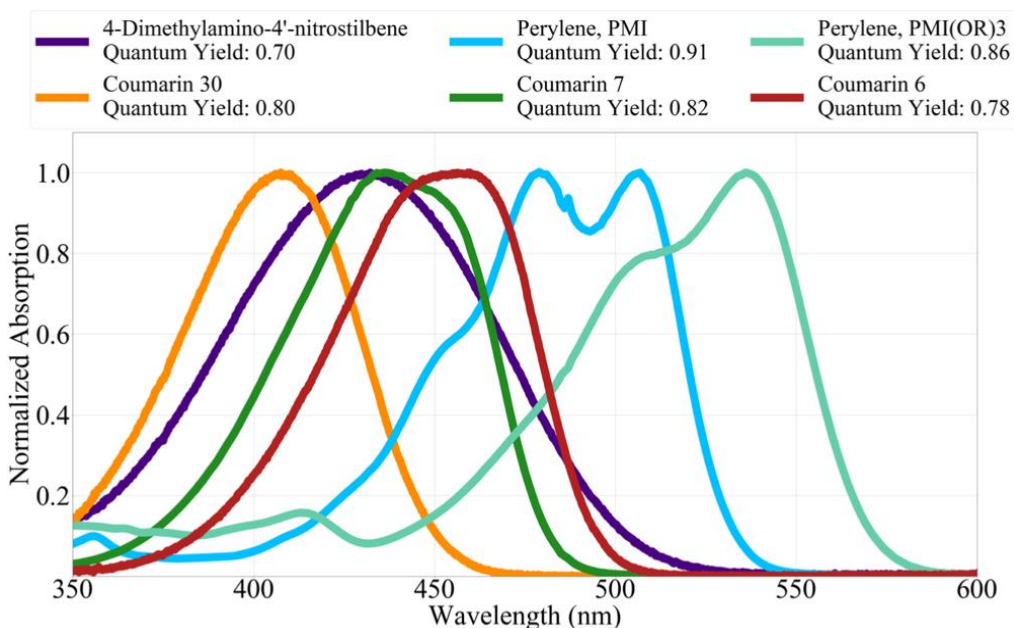


Figure 6.3-7: The absorption spectra of compounds with the highest Cherenkov excitation ranking

## **6.4 Discussion**

### **6.4.1 Cherenkov spread**

While the narrow-beam simulations and experimental data follow similar trends when comparing photon and electron sources, there is disagreement around the absolute divergence of the optical emissions. This observed disagreement may be due to a number of differences in the geometry and optical properties of the system in question. The simulated tissue model has much higher absorption than water, so Cherenkov emissions will not travel as far, leading to a smaller penumbra. Additionally, the likely primary driver of this disagreement is due to the simulation geometry, which places the source 0.2m from the tissue volume and assumes no explicit beam divergence which will lower the overall spread.

Electron sources are generally used to provide surface dose due the increased probability of electron scatter resulting in short penetration depths. Since electrons are charged particles, as they travel through tissue they can exhibit three types of interactive forces: soft collisions, hard collisions, or Coulomb-Force interactions. Soft collisions are the most common and occur when the incident electron passes at a considerable distance to an atom, and can result in Cherenkov emissions.<sup>17</sup> In this case, the electron loses very little energy and continues in an undisturbed trajectory. With a hard collision the incident electron interacts directly with an atom's electron which is often ejected, often generating a characteristic X-ray.<sup>17</sup> In Coulomb-Force interactions the incident electron interacts primarily with an atom's nucleus and is elastically scattered, however in a small percentage

of cases an inelastic interaction occurs and the electron transfers most energy to the atom, resulting in an X-ray photon emission, also known as a bremsstrahlung emission.<sup>17</sup>

The variety of photon and electron interactions with matter, which often cascade, results in a spreading of the Cherenkov emissions. Developing a model of the spread function is important to improve spatial localization for the delivered dose or for Cherenkov-excited scanned images. While the currently presented work demonstrates how simulations can be developed for developing these models, there are improvements which need to be made to the simulation before a deconvolution kernel with clinical utility can be defined. A very similar investigation has been previously conducted by Brost *et al* which determined the Cherenkov scatter function in a multi-layer tissue model for a number of LINAC energies.<sup>18,19</sup>

#### **6.4.2 Limits of detection**

A series of simulations were developed to better understand the limits of detection for a luminescent inclusion at varying depths in tissue. These simulations compared the light fluence from an external optical source as well as Cherenkov-emissions generated within the multi-layer tissue model. While the purely optical simulation for measuring fluence could be performed in a package like MCML, the physics-engine required for Cherenkov emissions as well as the ability to simulate fluorescence is missing.

While Cherenkov emissions are correlated with deposited dose, these simulations show how tissue optical properties will influence the observed emissions. It is difficult to measure the spectral properties of Cherenkov emission inside tissue, and so these

simulations provide insight on how tissue acts as a long-pass wavelength filter, allowing mainly red and NIR to pass to the surface for detection, even though the signal generated inside the tissue is broadband. While an 18MV beam generates approximately 2.5X more Cherenkov emissions, since the maximum dose occurs at 3.5cm, much of these optical photons are absorbed before reaching the tissue surface, which is in agreement with previous studies.<sup>15,20</sup>

Cherenkov-excited luminescence was also compared to purely optical luminescence in these example simulations. It has been reported previously red or NIR light from Cherenkov emissions are actually the predominant wavelength available for luminescence excitation.<sup>15</sup> While our simulation was able to demonstrate this, it also shows that the UV-Blue contribution is as important for the given compound's excitation (Figure 6.2-3A). While it is well known 630nm light will have a much higher penetration depth than 430nm excitation, the complexity of Cherenkov emissions within tissue complicates depth estimates. In the present example the 6MV and 630nm sources had largely similar luminescence reaching the surface when the tumor inclusion was 1mm below the surface, but when the inclusion depth was moved to 5mm, the Cherenkov excitation resulted in a surface luminescence over 10X that of the 630nm excitation. Models such as the one provided in the current work could be help provide insight on how multimodal luminescence imaging could be used for improved depth discrimination.

A system for computational ranking potential compounds to be used in Cherenkov-excited luminescence imaging was demonstrated. While similar datasets are available for scintillators,<sup>21</sup> neither data sources consider long-lived phosphoresce (>10 $\mu$ s). If the

current available data were expanded and standardized to report lifetime and scintillation yield, the currently demonstrated method could easily be expanded to identify additional means of contrast. Additionally, if this functionality could be expanded to include triplet quantum yields in addition to fluorescence quantum yields, this computational search could be expanded to identify potential Cherenkov-excited or X-ray excited photosensitizers. While many of the compounds identified by the current work would not be appropriate for the time-delayed phosphorescent imaging discussed in Chapter 5 and later chapters, the basis demonstrates a method to quickly identify potential compounds based on empirical data.

## **6.5 Conclusions**

The simulation environment utilized in this work allows for a number of system variables to be tested simultaneously, or for simulations to be easily split into smaller chunks, allowing for faster execution. Using this system, models of Cherenkov spread in tissue and limits of detection for Cherenkov-excited luminescence were demonstrated. Models of thin X-ray and electron sources were compared with experimental measurements, showing similar trends in energy and source type. The limits of detection of a luminescent inclusion were also demonstrated through modelling. From these models it was demonstrated 630nm excitation and Cherenkov excitation have similar surface remittance from an inclusion at 1mm depth, but when the depth is increased to 5mm the Cherenkov-excited luminescence at the surface is 10x higher than that generated by 630nm excitation. Additionally, at an inclusion depth of 7mm, approximately 2% of the luminescence generated in the tumor

reaches the surface. These models provided further evidence of the filtering effects introduced by tissue and could be used as a basis for improving spatial accuracy and depth sensitivity of Cherenkov imaging systems. A method for computationally ranking potential Cherenkov-excited compounds was demonstrated as a means for quickly identifying potential contrast agents in future experimental work.

## 6.6 References

1. Zhang, R. *et al.* Cherenkov-excited luminescence scanned imaging. *Opt. Lett., OL* **40**, 827–830 (2015).
2. Brůža, P. *et al.* Light sheet luminescence imaging with Cherenkov excitation in thick scattering media. *Optics Letters* **41**, 2986–2986 (2016).
3. Glaser, A. K., Kanick, S. C., Zhang, R., Arce, P. & Pogue, B. W. A GAMOS plugin for GEANT4 based Monte Carlo simulation of radiation-induced light transport in biological media. *Biomedical optics express* **4**, 741–59 (2013).
4. Meglinski, I. V. & Matcher, S. J. Quantitative assessment of skin layers absorption and skin reflectance spectra simulation in the visible and near-infrared spectral regions. *Physiological Measurement* **23**, 741–753 (2002).
5. LaRochelle, E. P. M. *et al.* Modeling PpIX effective light fluence at depths into the skin for PDT dose comparison. *Photodiagnosis and Photodynamic Therapy* **25**, 425–435 (2019).
6. Bashkatov, A. N., Genina, E. A., Kochubey, V. I. & Tuchin, V. V. Optical properties of human skin, subcutaneous and mucous tissues in the wavelength range from 400 to 2000 nm. *J. Phys. D: Appl. Phys.* **38**, 2543–2555 (2005).
7. Bashkatov, A. N., Genina, E. A. & Tuchin, V. V. OPTICAL PROPERTIES OF SKIN, SUBCUTANEOUS, AND MUSCLE TISSUES: A REVIEW. in (2011). doi:10.1142/S1793545811001319.
8. Jacques, S. L. Optical properties of biological tissues: a review. *Phys. Med. Biol.* **58**, R37–R61 (2013).
9. Esipova, T. V. *et al.* Two New “Protected” Oxyphors for Biological Oximetry: Properties and Application in Tumor Imaging. *Analytical Chemistry* **83**, 8756–8765 (2011).

10. Pogue, B. W. *et al.* Maps of in vivo oxygen pressure with submillimetre resolution and nanomolar sensitivity enabled by Cherenkov-excited luminescence scanned imaging. *Nature Biomedical Engineering* **2**, 254–264 (2018).
11. Taniguchi, M. & Lindsey, J. S. Database of Absorption and Fluorescence Spectra of >300 Common Compounds for use in PhotochemCAD. *Photochemistry and Photobiology* **94**, 290–327 (2018).
12. Taniguchi, M., Du, H. & Lindsey, J. S. PhotochemCAD 3: Diverse Modules for Photophysical Calculations with Multiple Spectral Databases. *Photochemistry and Photobiology* **94**, 277–289 (2018).
13. Frank, I. & Tamm, Ig. Coherent Visible Radiation of Fast Electrons Passing Through Matter. in *Selected Papers* 29–35 (Springer Berlin Heidelberg, 1991). doi:10.1007/978-3-642-74626-0\_2.
14. Glaser, A. K., Zhang, R., Davis, S. C., Gladstone, D. J. & Pogue, B. W. Time-gated Cherenkov emission spectroscopy from linear accelerator irradiation of tissue phantoms. *Opt. Lett., OL* **37**, 1193–1195 (2012).
15. Glaser, A. K., Zhang, R., Andreozzi, J. M., Gladstone, D. J. & Pogue, B. W. Cherenkov radiation fluence estimates in tissue for molecular imaging and therapy applications. *Physics in Medicine and Biology* **60**, 6701–6718 (2015).
16. Hachadorian, R. *et al.* Correcting Cherenkov light attenuation in tissue using spatial frequency domain imaging for quantitative surface dosimetry during whole breast radiation therapy. *JBO* **24**, 071609 (2018).
17. Attix, F. Charged-Particle Interactions with Matter. in *Introduction to Radiological Physics and Radiation Dosimetry* 160–199 (John Wiley & Sons, Ltd, 2007).
18. Brost, E. & Watanabe, Y. Characterization of the Cerenkov scatter function: a convolution kernel for Cerenkov light dosimetry. *JBO* **23**, 105007 (2018).
19. Brost, E. E. & Watanabe, Y. A mathematical deconvolution formulation for superficial dose distribution measurement by Cerenkov light dosimetry. *Medical Physics* **45**, 3880–3892 (2018).
20. Lin, H. *et al.* Comparison of Cherenkov excited fluorescence and phosphorescence molecular sensing from tissue with external beam irradiation. *Physics in Medicine and Biology* **61**, 3955–3968 (2016).
21. Derenzo, S. E. *et al.* Design and Implementation of a Facility for Discovering New Scintillator Materials. *IEEE Transactions on Nuclear Science* **55**, 1458–1463 (2008).

# CHAPTER 7

## 7 Cherenkov-excited luminescence and luminescent compounds for use in radiotherapy

*This chapter is derived from the following two publications:*

J.R Shell\*, E.P. LaRochelle\*, *et al.* “Comparison of phosphorescent agents for noninvasive sensing of tumor oxygenation via Cherenkov-excited luminescence imaging.” *Journal of Biomedical Optics*. **24**(3). (2019) \*Denotes equal contributions

E.P.M. LaRochelle, *et al.* “Imaging luminescent tattoo inks for direct visualization of linac and cobalt irradiation.” *Medical Physics*. (2020)

### 7.1 Introduction

Contrast agents are commonly used in medical imaging to boost a signal of interest within a field. Compounds often target specific molecular processes like the presence or absence of oxygen, or they can be used to provide insight on anatomical structures by localizing in vasculature or being placed as surface fiducial markings. The current chapter describes both methodologies for applications in radiation therapy, first focusing on a number of compounds which are designed to provide a metric of local oxygenation, and then how topically applied markings could be used to improve contrast in field verification.

Radiation treatment with MV photons or MeV electrons causes the production of Cherenkov light in tissue. This optical emission occurs when high-energy primary or secondary electrons pass through the dielectric medium, like tissue, at a velocity greater than the speed of light. This optical signal has been imaged to visualize surface dose in radiation therapy.<sup>1-3</sup> In addition, early pilot studies in tissue phantoms and individual animals have shown utilization of Cherenkov emission as the excitation source in imaging applications, including the detection of fluorophores and phosphors in conjunction with radiation therapy.<sup>4</sup> Scintillation is another excitation mechanism where a luminescent emission can be generated by direct X-ray excitation. In some instances, it can be difficult to distinguish which mechanism triggers luminescence, however, for the purpose of imaging contrast agents, it is not always necessary to know the mechanism of action.

### **7.1.1 Oxygenation**

Extent of oxygenation in tumors is a known indicator of the success of radiation therapy, partly due to the oxygen enhancement ratio,<sup>5</sup> as well as due to oxygen being a surrogate marker for other features of the tumor aggressiveness.<sup>6</sup> Therefore, monitoring of tumor oxygenation during fractionated radiation therapy would be advantageous to gauge the likelihood of response, or even to estimate if treatment plan alternations such as a boost to hypoxic areas might be beneficial. Previous studies have used oxygen electrodes have to measure hypoxia.<sup>7-9</sup> While this method allows direct measurement of oxygen levels in tumors, it is invasive and only provides a localized estimate. Tumor biopsies with indirect measurements for hypoxia including pimonidazole staining and immunostaining for HIF-1 $\alpha$ , provide valuable information of individual tumor microenvironments,<sup>10-14</sup> but these

methods are also invasive and do not provide real time measurement of tumor oxygenation levels. Blood oxygen level dependent magnetic resonance imaging (BOLD-MRI),<sup>15,16</sup> electron paramagnetic resonance oximetry<sup>17,18</sup> and near infrared spectroscopic tomography<sup>19</sup> provide real time information based on hemoglobin saturation. Positron emission tomography (PET), also measures real time levels of hypoxia utilizing <sup>18</sup>F-labeled nitroimidazole derivatives, whose emission are dependent on oxygen levels, yet the resolution can be limited.<sup>20,21</sup> Despite the potential value, there has not been any clinical convergence on a method for imaging tumor oxygenation that is non-invasive, precise, and quantitative. In this study, oxygen-related mapping in tumors is demonstrated with Cherenkov excited luminescence scanned imaging (CELSI), which uses the inherent delivery of radiation to get maps of oxygen-dependent luminescence signal from injected chemical sensors. Current reagents utilized for phosphorescent sensing of oxygen that can be utilized for noninvasive determination of oxygen content (PtG4, MM2, Ir(btbt)<sub>2</sub>(acac), and MitoID) are evaluated. The potential to sense tumor oxygenation through CELSI with the phosphorescent reagent PtG4 has been shown by our group, because the PtG4 phosphorescence is quenched in the presence of oxygen, reducing the observed lifetime of emission. In the presence of ambient oxygen pressure (pO<sub>2</sub>), the PtG4 phosphorescence lifetime is 16.9 μs, and in low pO<sub>2</sub> it is 47 μs.<sup>22,23</sup>

In this current study, this agent was compared to other oxygen-quenched chemical agents, and each was examined for their potential to sense tumor hypoxia by directly measuring pO<sub>2</sub> levels in vivo with mice bearing subcutaneous tumors.<sup>24</sup> In the end of the study, the

spatial confidence in mapping pO<sub>2</sub> was estimated, using doses typical of fractionated radiotherapy.

### **7.1.2 Field Verification**

The use of permanent tattoos with black ink has been a common practice in the field of fractionated radiotherapy patient alignment as a way of providing permanent fiducial markers.<sup>25-27</sup> The use of UV-sensitive fluorescent ink has been studied in human trials to assess the value for preserving positional alignment accuracy while allowing for near invisible appearance to the patient.<sup>28,29</sup> These inks are less noticeable under normal room or day light conditions, while still being visible by eye under UV “black light” (~395nm) illumination. While these markings are used as an initial coarse alignment, and modern systems use kV imaging for final positioning, this is not always the case, especially in low- and middle-income countries. The current work examines the potential to expand the application of these UV-sensitive inks to include field verification through luminescence imaging with direct excitation by MV radiation. A clinical linear accelerator using both time-gated and continuous image acquisition, as well as a cobalt-60 source were used for irradiation of skin-simulating phantoms and topically applied UV-sensitive tattoo inks.

Tattoo ink is composed of a non-specific mixture, with the chromatically active components being pigmented polymorphous granules. These are inserted into the skin, with static preservation of them at the junction of the papillary and reticular dermis.<sup>30</sup> Tattoo pigments have been shown to be approximately 0.2-5µm in diameter.<sup>29,30</sup> The set of UV-sensitive inks investigated in the present study does not have an exact composition that

is well documented, but they are manufactured and sold for human use, however in the United States the inks are not regulated by the FDA. The inks under investigation all exhibit luminescent properties under X-ray excitation. This luminescence phenomenon could be direct scintillation where X-ray energy is converted into luminescent emission, or Cherenkov-excited luminescence, where the predominantly UV Cherenkov emissions in tissue excite luminescence in the ink. In either case, in the presence of high-energy X-rays these inks emit light with a microsecond lifetime. This light can be imaged during treatment to provide real-time feedback on dose delivery. While tattoo inks are traditionally injected into the skin, surface application provides a semi-permanent delivery mechanism. Both methods are demonstrated in the current work as potential fiducial markers or methods of entrance/exit field visualization.

The central questions addressed in this study was an assessment of which combination of spectral properties and light yields provide the most detectable signal from skin-equivalent phantoms, and what image acquisition parameters could be utilized for detection during the pulsed X-rays of a linear accelerator or the continuous dose delivered by a cobalt-60 source. The ultimate goal of this work is not to replace modern patient-alignment and field verification mechanisms, but instead to demonstrate the potential of additional tools for field verification, especially in low-resource settings.

## 7.2 Methods and Materials

### 7.2.1 Oxygenation

#### 7.2.1.1 Chemicals

PtG4 (platinum II G4) was provided by Sergei Vinogradov and colleagues.<sup>23</sup> MM2 was purchased from Luxcel Bioscience, Cork, Ireland,<sup>31</sup> Bis(2-phenylbenzothiazolato)-(acetylacetonate)iridium(III) ( $\text{Ir}(\text{btb})_2(\text{acac})$ )<sup>32</sup> was purchased from Sigma Aldrich, Saint Louis, MO and Mito-ID intracellular oxygen sensor was purchased from Enzo Life Sciences, Farmingdale, NY. MDA-MB-231 luc-D3H2LN cells were obtained from Perkin Elmer (Waltham, MA) and PANC-1 cells were obtained from ATCC (CRL-1469, Manassas, VA). DMEM, FBS, PBS, and 0.05% trypsin were purchased from Thermo Fisher Scientific (Waltham, MA). Molecular Devices Gemini XS (Sunnyvale, CA) was utilized for fluorescence plate reader measurements, Agilent Cary 50 UV-Vis (Santa Clara, CA) was utilized for absorbance spectra, Horiba Fluorolog-3 (Edison, NJ) was utilized for emission spectra. Fluorescence microscopy was performed on a Zeiss LSM 800 (Jena, Germany) confocal microscope.

#### 7.2.1.2 Assessment of Absorbance and Fluorescence Emission Spectra

The absorbance and fluorescence emission spectra of PtG4 (1  $\mu\text{M}$ ,  $\lambda_{\text{ex}}=435$  nm,  $\lambda_{\text{em}}=772$  nm),  $\text{Ir}(\text{btb})_2(\text{acac})$  (1  $\mu\text{M}$ ,  $\lambda_{\text{ex}}=337, 480$  nm,  $\lambda_{\text{em}}=620$  nm), MM2 (1  $\mu\text{M}$ ,  $\lambda_{\text{ex}}=400$  nm,  $\lambda_{\text{em}}=650$  nm), and MitoID (1  $\mu\text{M}$ ,  $\lambda_{\text{ex}}=380$  nm,  $\lambda_{\text{em}}=650$  nm) were measured as validation prior to employing these reagents in cell and in vivo studies.

### *7.2.1.3 Cell culture*

PANC-1 cells and MDA-MB-231 luc-D3H2LN cells were grown in DMEM with 10% FBS in an incubator at 37°C with 5% CO<sub>2</sub>, and 100% humidity and divided utilizing 0.05% trypsin when desired confluency was reached.

### *7.2.1.4 Fluorescence Assay In Vitro*

PANC-1 cells were seeded in black 96-well plates with a clear bottom at 5,000 cells/well. MM2, Ir(bt<sub>b</sub>)<sub>2</sub>(acac), and MitoID (10,20,30 µg/mL in PBS) were added to the cells and allowed to incubate for 24 h at 37°C. Media containing the reagents was removed and cells were rinsed with PBS. 10%FBS in PBS with or without glucose oxidase catalase oxygen scavenger (100 nM glucose oxidase, 1.5 µM catalase, and 56 mM glucose) was added after rinsing and the fluorescence intensity was analyzed with an excitation of 380 nm and emission of 660 nm. For limits of detection studies, 20, 2, 0.2 and 0.02 µg/mL of MM2 and Ir(bt<sub>b</sub>)<sub>2</sub>(acac) were utilized in the same fashion as described above. A student's t-test was utilized to assess differences in fluorescence between oxygenated versus oxygen scavenged conditions.

### *7.2.1.5 Cherenkov Imaging*

Cherenkov emission was induced by a linear accelerator (Varian LINAC 2100CD, Palo Alto, CA). The imaging system consisted of a time-gated intensified CCD camera (ICCD, PI-MAX4 1024i, Princeton Instruments, USA), a commercial lens (Canon EF 135mm f/2L USM). The camera was focused on a mirror that reflected the imaging field approximately one meter away. The time-gated ICCD camera was synchronized to the radiation pulses

(approximately 3.25  $\mu\text{s}$  duration, 360 Hz repetition rate) with the intensifier set as  $\times 100$  and turned on at a 4.26  $\mu\text{s}$  or 1000  $\mu\text{s}$  gate delay following each radiation pulse for phosphorescence or background measurement, and luminescence generated during 85.60  $\mu\text{s}$  gate width (PtG4 and MM2), or 7.77  $\mu\text{s}$  ( $\text{Ir}(\text{btb})_2(\text{acac})$ ) was integrated via this ICCD. Images of the luminescence at different delay times between LINAC pulse and phosphorescence emission were acquired to construct emission lifetime. To maximize signal and minimize background interference, the room lights were shut off throughout these studies, and all lights in the room were masked off with black cloth and black tape.

#### *7.2.1.6 CEL studies in vitro*

Concentrations of 20, 2, 0.2 and 0.02  $\mu\text{g}/\text{mL}$  of MM2,  $\text{Ir}(\text{btb})_2(\text{acac})$ , MitoID, and PtG4 were utilized 96-well plate as above. For solution studies, 300  $\mu\text{L}$  of each solution with and without oxygen scavenger were utilized. For cellular studies, PANC-1 cells were seeded in black 96-well plates with a clear bottom at 5,000 cells/well. The reagents were added to the cells and allowed to incubate for 24 h at 37°C. Media containing the reagents was removed and cells were rinsed with PBS. 10% FBS in PBS was added after rinsing.

#### *7.2.1.7 General Animal Imaging*

All animal procedures were approved by the Institutional Animal Care and Use Committee, and the studies here were carried out in compliance with these approved procedures.

#### *7.2.1.8 In vivo imaging*

Briefly, 10<sup>5</sup> MDA-MB-231 luc-D3H2LN cells were injected under the skin on the flank of a nude mouse (2 tumors per mouse, 8 tumors per reagent studied). After approximately 3

weeks of growth, animals were chosen for use when their tumor was approximately 6x6x3mm<sup>3</sup> in size. The CELSI scan was completed vertically. Images of the luminescence at different delay times between LINAC pulse and phosphorescence emission were acquired to construct emission lifetime. Under general anesthesia of inhaled isoflurane, 50  $\mu$ L of 50  $\mu$ M of each reagent was directly injected into the tumors and the animal was imaged alive and then again at 30 min after sacrifice, which allows determination of emission lifetime at ambient pO<sub>2</sub> (alive) low pO<sub>2</sub> environments (dead), respectively.

#### *7.2.1.9 Statistical analysis*

The tissue pO<sub>2</sub> was determined utilizing the Stern-Volmer relationship. The differences between the live and dead conditions, as displayed in Figure 7.3-5 with  $n = 8$  paired samples each, was assessed using a two-tailed Students  $t$ -test, with  $\alpha = 0.05$  and resulting  $P < 0.001$ . This shows that there are significant differences between the values of both emission lifetime and pO<sub>2</sub> of the animals alive versus dead. Figure 7.3-5 was generated using Python 3.4.3 with the library matplotlib 2.0.0.

### **7.2.2 Field Verification**

#### *7.2.2.1 Assessment of Fluorescence Emission Spectra and Lifetime*

Optical properties were measured for a set of 9 colors of UV-sensitive tattoo inks (Mom's Nuclear Millennium Colors Inc., West Babylon, NY). The inks consist of a proprietary pigment in a solution of distilled water, glycerin, propylene glycol and Hamamelis Virginiana Extract (witch hazel). The inks were further diluted with ethanol and their emission spectra and lifetime were measured on a spectrofluorometer (Fluoromax4,

Horiba, Kyoto, Japan). 500 $\mu$ L of ink was diluted with 1500 $\mu$ l of 70% ethanol, then 30 $\mu$ L was immediately aliquoted into a quartz cuvette and measured on the spectrofluorometer. Excitation was maintained at 380nm with a 5nm slit for all samples and emission was measured from 400nm to 700nm with a 2nm slit. The 70% ethanol was measured as a control and subtracted from the emissions measurements. The phosphorescence lifetime was measured by delay with excitation again at 380nm with 5nm slit, and peak emission wavelengths for each sample were monitored with a 5nm slit. A total of 100 flashes per measurement were collected with 80ms between flashes. A 100 $\mu$ s window was used for all measurements, with an initial delay of 5 $\mu$ s incrementing by 5 $\mu$ s up to a max delay of 500 $\mu$ s. The diluted samples with longer emission wavelengths (Red Dawn, Radiant Pink, Smoldering Orange) as well as the white ink (Invisible Fallout) were chosen to be measured using 6MV X-ray radiation delivered by a clinical linear accelerator (Clinac 2100CD, Varian Medical Systems, Palo Alto, CA) delivering approximately 2Gy dose. 150 $\mu$ L of each diluted sample, were placed in a black-wall 96-well plate. The well plate was placed on top of a 1.4cm water-equivalent phantom and a 15cm x 15cm beam was delivered from beneath the samples, similar to geometries reported previously.<sup>33,34</sup> A time-gated intensified CMOS camera (C-Dose™, DoseOptics, Lebanon, NH) was used to image the delivery of the X-rays and the luminescence with the room lights off. The linac delivers irradiation in short 4 $\mu$ s pulses at a 360Hz repetition rate. Images of Cherenkov and fast scintillation emissions were collected during the 4 $\mu$ s X-ray pulses over a 56ms exposure time, equating to 20 pulses per frame. Delayed phosphorescence was imaged with a 5 $\mu$ s

delay after the start of each pulse for a duration of  $100\mu\text{s}$  over the same 56ms CMOS exposure time. This latter acquisition approach eliminated the Cherenkov light from the tissue, which is only detectable during the x-ray pulse, thereby cutting the background signal down significantly.

#### 7.2.2.2 *Phantom Imaging: LINAC*

Three of the more optimal ink colors (Red Dawn, Smoldering Orange, Afterglow Yellow) were chosen to be painted on the surface of a 2mm thick PDMS-based skin-simulating phantom. The optical properties of the phantom ( $\mu_s$ : 3.7-2.4  $\text{mm}^{-1}$ ,  $\mu_a$ : 0.1-0.03  $\text{mm}^{-1}$  for  $\lambda \in 471\text{-}851\text{nm}$ ) were measured using spatial frequency-domain imaging (Reflect RS, Modulim Imaging, Irvine, CA). A second 3mm thick silicone-based skin-simulating phantom (Practice Skin Silicone Pad, Segbeauty, Alhambra, California) with similar optical properties ( $\mu_s$ : 2.8-1.1  $\text{mm}^{-1}$ ,  $\mu_a$ : 0.2-0.01  $\text{mm}^{-1}$  for  $\lambda \in 471\text{-}851\text{nm}$ ) was given to a tattoo artist to make a resolution chart using the red ink. Both skin phantoms were placed on a 1.4cm water-equivalent phantom and a 15cm x 15cm beam was delivered from beneath the samples. Three imaging techniques were compared: (1) during the x-ray pulses using time-gating, which captures both Cherenkov and fast scintillation signals, (2) after the x-ray pulses, using time-gating to capture just the phosphorescence images, and (3) continuous measurement with the camera always on throughout the irradiation, not time-gated to the pulse. To capture emissions during the X-ray pulse the CMOS exposure was again 56ms with no pulse delay and  $4\mu\text{s}$  intensifier on-time. Phosphorescence mode also has a CMOS exposure of 56ms with  $5\mu\text{s}$  delay and  $100\mu\text{s}$  duration. The continuous mode

was not triggered by the linac X-ray and repeatedly enables the intensifier for 4ms every 40ms. These three modes were used to image the skin phantom without any filtering, and again using a 600nm long pass filter placed before the photocathode.

### *7.2.2.3 Phantom Imaging: Cobalt-60*

The PDMS-based skin phantom was also imaged during irradiation with a cobalt-60 source (Equinox 100, Theratronics, Ottawa, Ontario). The phantom was placed on a 0.5cm silicone base with the bottom surface at 100cm SSD and irradiated from below with the gantry head at 180°. The camera was placed on a tripod next to the couch at an angle of approximately 45° and imaging distance of 0.86m. The room lights were off, however, numerous security cameras equipped with LED rings emitting at 850nm remained on. The camera system used a bandpass filter centered at 550nm (FB550-40, Thorlabs, Newton, NJ) or 635nm (RPB610-660, Omega Optical, Brattleboro, VT). Images were collected in a continuous mode for a 5ms duration at a rate of 30 frames per second. A background image was collected before each irradiation to collect and subtract any stray ambient light in the room. The phantom was irradiated for 1.46 minutes, or approximate dose of 2Gy.

## 7.3 Results

### 7.3.1 Oxygenation

The set of 4 phosphorescent oxygen sensors were directly compared to determine which of these reagents would be ideal for use in CELSI in tumors. These agents were chosen based upon published data and they represented the most promising mix of agents for use in vivo with longer lifetime emission from phosphorescence. The absorbance and emission spectra of PtG4 (green), MM2 (gray), Ir(btbt)<sub>2</sub>(acac) (blue), and MitoID (red) are shown in Figure 7.3-1.<sup>31,32</sup> Relative brightness of the commercially available MM2, Ir(btbt)<sub>2</sub>(acac), and MitoID was assessed at increasing concentrations (10, 20, and 30 µg/mL) in PANC-1 cells in the presence and absence of ambient oxygen, through the addition of the enzymatic oxygen-scavenging system of glucose oxidase and catalase (GODCAT). Measurements of emission were taken via fluorescence plate reader. MM2 and Ir(btbt)<sub>2</sub>(acac) exhibited the

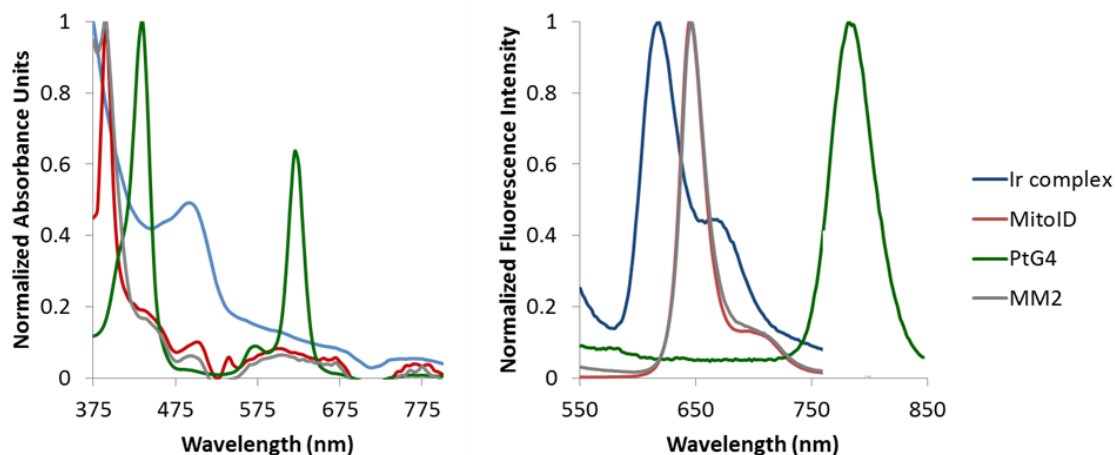


Figure 7.3-1: Absorbance and emission spectra for oxygen sensors. The absorbance and fluorescence emission spectra for Ir(btbt)<sub>2</sub>(acac) (blue), MitoID (red), PtG4 (green) and MM2 (gray).

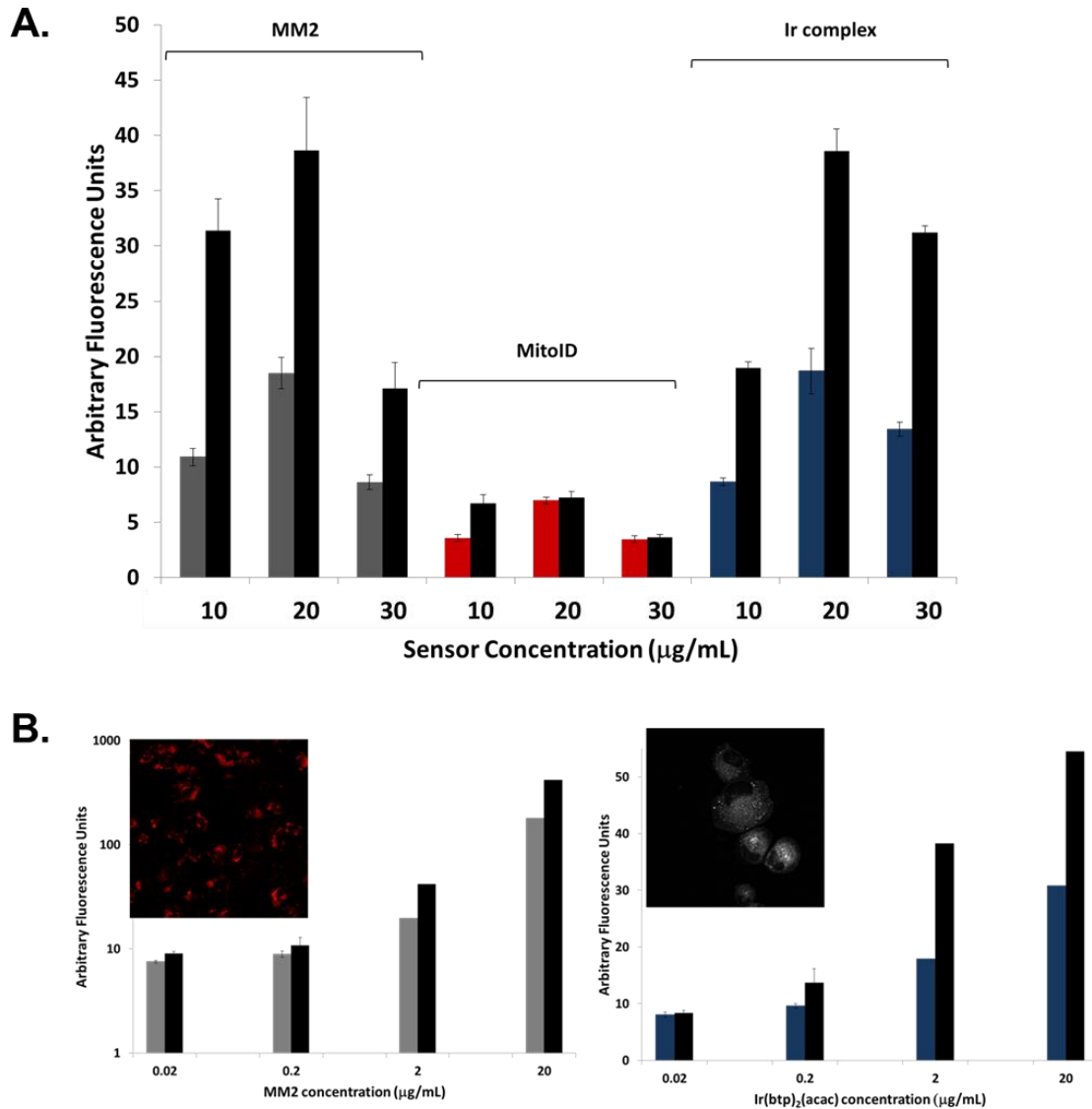


Figure 7.3-2: Comparison of commercially available oxygen sensors in PANC-1 cells. A. MM2 (gray), MitoID (red), and Ir(btpt)<sub>2</sub>(acac) (blue) were incubated with PANC-1 cells overnight. Fluorescence was measured in the presence of ambient oxygen (light gray, MM2, medium gray, MitoID, and dark gray, Ir(btpt)<sub>2</sub>(acac)) and with glucose oxidase catalase enzymatic oxygen scavenging (black). B. The brightest commercial oxygen sensors were explored at decreasing concentrations (20 µg/mL, 2 µg/mL, 0.2 µg/mL, and 0.02 µg/mL) to determine the lowest concentration that can be detected. Inset shows fluorescence microscopy of each sensor (20 µg/mL) loaded into PANC-1 cells. Excitation and emission were measured at 380 nm and 660 nm, respectively. The fluorescence intensity represents the average of 6 experiments +/- SEM.

maximum signal under deoxygenated conditions at 20  $\mu\text{g}/\text{mL}$ , while the MitoID intensity in the presence and absence of oxygen scavengers was lower in comparison (Figure 7.3-2a). Statistically significant changes in oxygenation can be detected at concentrations as low as 0.2  $\mu\text{g}/\text{mL}$  for  $\text{Ir}(\text{btb})_2(\text{acac})$  and 0.02  $\mu\text{g}/\text{mL}$  for MM2 (Figure 7.3-2b), as assessed by a student's t-test.

We sought to evaluate the effectiveness of these reagents to be imaged with Cherenkov excited luminescence (CEL). Solutions of PtG4, MM2,  $\text{Ir}(\text{btb})_2(\text{acac})$ , and MitoID at decreasing concentrations (20, 2, 0.2, and 0.02  $\mu\text{g}/\text{mL}$ ) were placed in a 96-well plate with and without GODCAT and evaluated via epi-luminescence. The background corrected

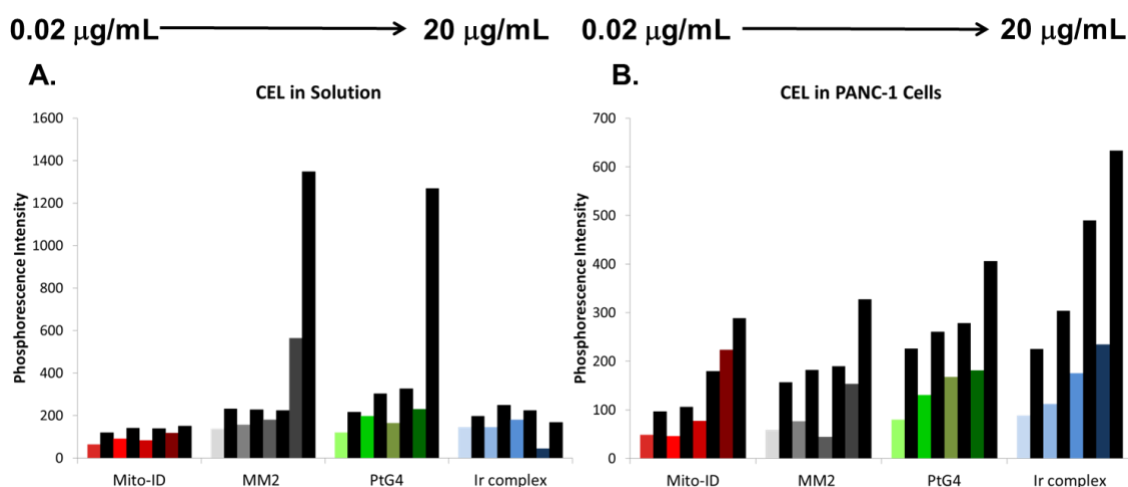


Figure 7.3-3: Comparison of CEL with phosphorescent oxygen sensors. Increasing concentrations of each sensor indicated by darker shades of each color (0.02  $\mu\text{g}/\text{mL}$ , 0.2  $\mu\text{g}/\text{mL}$ , 2  $\mu\text{g}/\text{mL}$ , and 20  $\mu\text{g}/\text{mL}$ , MitoID (red), MM2 (gray), PtG4 (green), and  $\text{Ir}(\text{btb})_2(\text{acac})$  (blue)) were analyzed in ambient oxygen or with enzymatic oxygen scavenger glucose oxidase/catalase (black). A 96-well plate with these reagents in solution (A.) or loaded into PANC-1 cells (B.) was exposed to 6 MV radiation from a LINAC, and the phosphorescence intensity was measured via ICCD

phosphorescence intensities from this experiment at the maximum concentration of 20  $\mu\text{g}/\text{mL}$  are as follows (first number for each compound represents ambient oxygen, second number represents GODCAT): MM2 (565, 1349); PtG4 (230, 1269); Ir(bt<sub>2</sub>)<sub>2</sub>(acac) (45.7, 168); MitoID(119, 150)(Figure 7.3-3a). This experiment was repeated by loading all of these reagents into PANC-1 cells with and without GODCAT and imaging via CEL. The phosphorescence intensities from this experiment at the maximum concentration of 20  $\mu\text{g}/\text{mL}$  are as follows (first number for each compound represents the signal under ambient oxygen, and the second number is the signal deoxygenated with GODCAT): MM2 (153, 376); PtG4(181, 406); Ir(bt<sub>2</sub>)<sub>2</sub>(acac) (235, 633); MitoID (223, 288) (Figure 7.3-3b).

A murine experiment to sense tissue oxygenation was completed in mice with subcutaneous MDA-MB-231luc-D3H2LNtumors. The setup for CELSI is depicted in Figure 7.3-4a-b. Briefly, gantry head of the linear accelerator that delivers the radiation is positioned below the mouse, which is located on the treatment couch. A mirror is placed that redirects the photons to the ICCD camera for imaging. A total of 4 tumors per compound were imaged, with local injection of 50 $\mu\text{L}$  of each reagent (50  $\mu\text{M}$  PtG4, 2.5 nmol, 1.75 mg per tumor and 50  $\mu\text{M}$  Ir(bt<sub>2</sub>)<sub>2</sub>(acac), 2.5 nmol, 35  $\mu\text{g}$  per tumor). Each mouse was imaged while alive and then repeated 30 minutes after sacrifice to capture both normoxic and hypoxic conditions, respectively. In the euthanized animal, the drop in blood circulation and respiration causes a dramatic decrease in pO<sub>2</sub> values. Temperature was controlled using a heating pad under each animal, throughout the study, and the CELSI scan was completed vertically for these cases. Images of the luminescence were captured at different delay times after the LINAC pulse to determine emission lifetimes for each

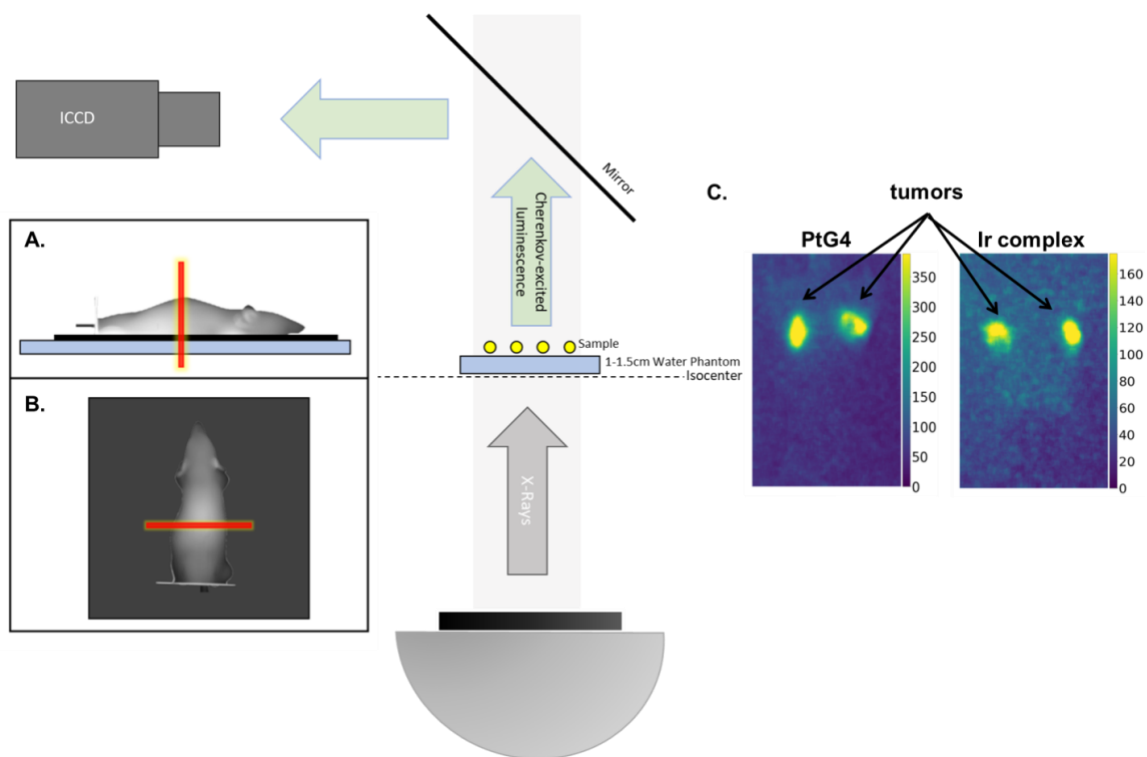


Figure 7.3-4: CELSI setup and in vivo imaging with PtG4 and Ir(btbt)<sub>2</sub>(acac). The LINAC gantry head that delivers radiation is placed below the mouse that is positioned on the treatment couch. A mirror above redirects the photons to the ICCD. A. lateral view of the mouse depicting passage of radiation sheet in red B. aerial view as imaged from the ICCD camera. C. Under anesthesia of isoflurane, 2.5 nmol of each reagent was injected into subcutaneous MDA-MB-231luc-D3H2LN tumors. Maximum intensity projection of PtG4 and of Ir(btbt)<sub>2</sub>(acac) at 4.26  $\mu$ s delay time, respectively. Tumors are indicated with arrows.

reagent. The maximum intensity projection images of CELSI from both PtG4 and Ir(btbt)<sub>2</sub>(acac) at a delay time of 4.26  $\mu$ s are shown in Figure 7.3-4c. A comparison of the intensity differences between PtG4 phosphorescence at various delay times in an alive and dead mouse are shown in Figure 7.3-5a. The emission lifetimes were mapped for the alive and sacrificed mouse for PtG4 and are quantified and displayed via a box and whiskers plot

(Figure 7.3-b). Using the Stern-Volmer equation, we estimated the average tissue  $pO_2$  with the reported quenching constant for PtG4<sub>35</sub> (Figure 7.3-5c). The phosphorescence at different delay times for a sacrificed mouse are shown for Ir(bt<sub>b</sub>)<sub>2</sub>(acac) (Figure 7.3-5d). In addition, we created a map of emission lifetimes and estimated the average  $pO_2$  using the reported quenching constant for Ir(bt<sub>b</sub>)<sub>2</sub>(acac) using the Stern-Volmer relationship.<sup>18</sup>

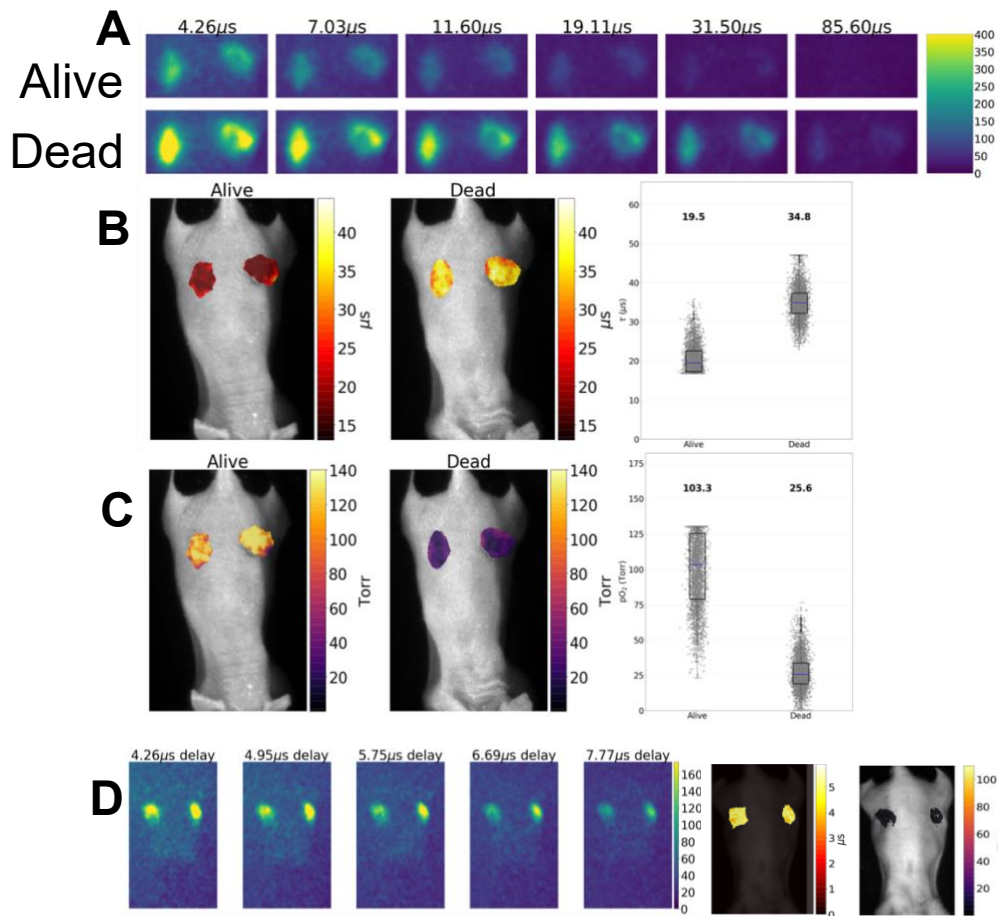


Figure 7.3-5: *In vivo* lifetime imaging with PtG4 and Ir(btbt)2(acac). Under anesthesia of isoflurane, the animal was imaged at various delay times based on reported lifetimes of each reagent to gain emission lifetime information alive and 30 min after sacrifice, when the drop in blood circulation and respiration causes a marked decrease in pO<sub>2</sub> values. A. comparison of PtG4 phosphorescence intensity at various delay times based on known PtG4 emission lifetime in subcutaneous tumors alive (top) and 30 min after sacrifice (bottom) B. PtG4 emission lifetime maps and box and whiskers plot of emission lifetimes of alive and sacrificed mouse C. pO<sub>2</sub> maps and box and whiskers plot of oxygen levels in alive and sacrificed mouse for PtG4. D. phosphorescence intensity of tumors injected with Ir(btbt)2(acac) at different delay times informed from the reported Ir(btbt)2(acac) emission lifetime, map of emission lifetime, and pO<sub>2</sub> map in sacrificed mouse. All lifetime maps and subsequent pO<sub>2</sub> maps for both reagents were constructed utilizing data from the 4.26 μs delay time.

### 7.3.2 Field Verification

The normalized emission spectra of each of the 9 UV-sensitive inks is provided in Figure 7.3-6A. The white ink, “Invisible Fallout” most closely matches the spectral properties of inks used in previous studies, meaning it is barely visible under room lights, whereas the other 8 colors are visible under room light, and fluoresce brighter under UV-excitation. While the white appears to have the highest intensity (Figure 7.3-6A), in our phantom imaging the orange, red and yellow reported the highest intensity. This is likely due to the red-sensitive photo-cathode used in the intensified-CMOS system which has peak sensitivity between approximately 570nm and 800nm.<sup>36</sup> The lifetimes of each color range from approximately 11-16 $\mu$ s (Figure 7.3-6B). The proprietary compounds used in these inks which would correspond to the observed emission spectra and lifetimes are still unknown.

Integrating the emission spectra above 550nm collected during UV-excitation (380nm) provides an estimate of the relative sensitivity of our imaging system (Figure 7.3-7A). A

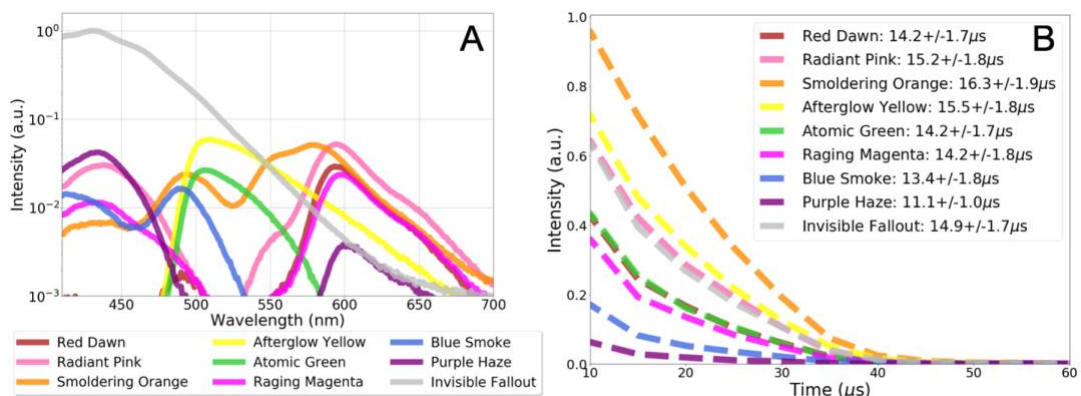


Figure 7.3-6: Normalized fluorescence emission of 9 UV-sensitive inks (A) and their corresponding normalized lifetime (B) based on 380nm excitation

subset of these samples shows intensities higher than the control both during the X-ray pulse (Figure 7.3-7B), and after the pulse (Figure 7.3-7C). The intensity observed during the X-ray pulse was approximately six times greater than that of the phosphorescence observed after the pulse. It was unclear whether the light generated during the X-ray pulse was due to direct X-ray scintillation, or due to the heavily UV-weighted Cherenkov excitation. The low white intensity was likely due to red-sensitive photocathode used in the imaging system.

Skin phantoms with ink painted on the surface (Figure 7.3-8) or tattooed into the phantom (Figure 7.3-9) were imaged in 3 modes: During the X-ray pulse, after the pulse (phosphorescence), and continuous, all with and without a 600nm long pass filter. The optical properties of both skin phantom fall within expected biological values for skin.<sup>37</sup> A room-light color photo of the painted phantom is shown as an inset in Figure 3E, and each unfiltered mode is shown with different intensity scales in Figure 7.3-8A-C. The image collected during the X-ray delivery (Figure 7.3-8A) shows the highest intensity for each ink, however it also has the highest background values. The phosphorescence image

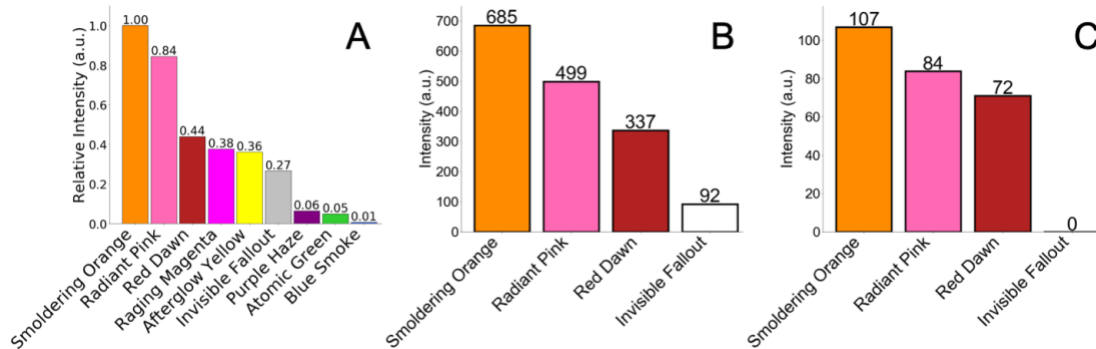


Figure 7.3-7: Mean intensity of select UV-sensitive tattoo inks in ethanol solution, measured with 380nm UV excitation (A), during the MV X-ray pulse (B) and after the pulse (C).

shown in Figure 3B has the lowest overall intensity but also very low background, whereas the continuous-mode image (Figure 7.3-8C) has intensities between both. The signal-to-noise ratio (1) is used as a metric to compare the quality of the respective imaging methods:

$$SNR = \frac{\mu_{ink}}{\sigma_{bg}} \quad (1)$$

where  $\mu_{ink}$  is the mean intensity of each ink region and  $\sigma_{bg}$  is the standard deviation of a similar-size region on the skin phantom without ink. From this metric it can be observed the image collected during the pulse has the highest SNR without a filter (Figure 7.3-8E) and with a 600 long-pass filter. The SNR is increased during the X-ray pulse and continuous mode with the addition of a 600nm longpass filter, whereas it is decreased for phosphorescence (Figure 7.3-8F). This can be attributed to the noise characteristics observed during each imaging mode, where phosphorescence imaging has inherently lower background due to the time gating of the intensifier after the X-ray pulse.<sup>33</sup> The increase in SNR is seen more predominantly by the red ink because the filter better matches the emission spectrum of this ink.

Filtering during continuous mode helped improve the SNR by approximately 10%. This mode most closely resembles a cobalt-60 source, which delivers dose continuously. An image of the same phantom collected during cobalt-60 irradiation and using a 635nm bandpass filter is shown in Figure 7.3-8D, where an affine image transformation has been applied to account for the differing imaging geometry. Figure 7.3-8G compares the SNR observed for each color of ink using the two bandpass filters. When the cobalt-60 gantry

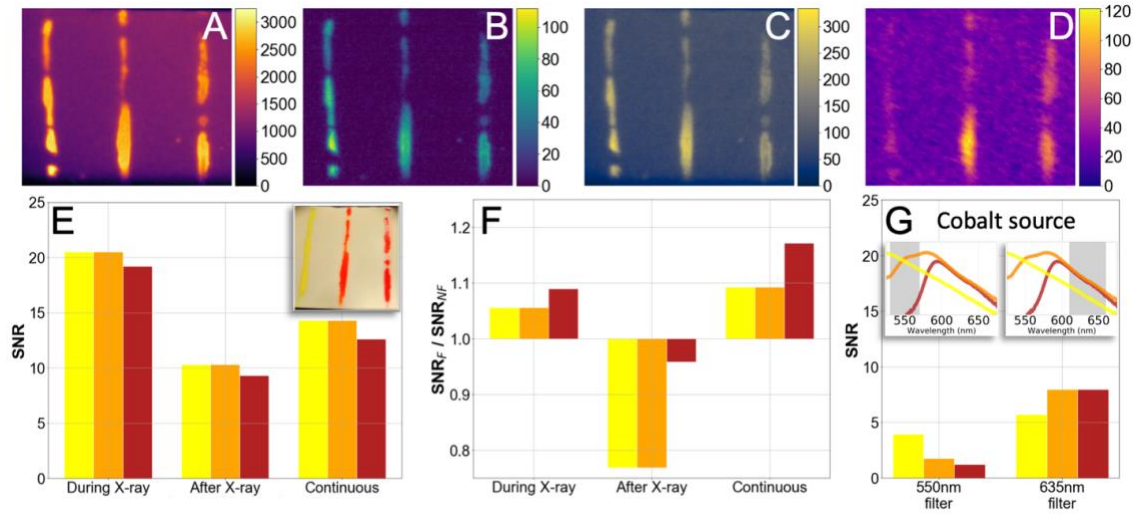


Figure 7.3-8: Select UV-sensitive ink was painted on the surface of a PDMS-based skin-simulation phantom (E inset) and imaged during the X-ray pulse (A), after the pulse (B), and without time gating (C). The same phantom was imaged using a cobalt-60 source and 635 bandpass filter (D). The signal-to-noise (SNR) was measured for each ink using each imaging method (E), and was compared to the same configuration with a 600 longpass filter. The ratio of the SNR with (SNRF) and without (SNRNF) the filter provide insight on the noise (F) characteristics of each method. The SNR for each ink was measured using both a 550nm bandpass filter (left) and 635 bandpass filter (right, where the inset show the filter pass band (gray shaded) in relation to the ink emission (G)).

was moved from 180° to 315°, the observed SNR was reduced by approximately 20%, likely due to the smaller surface dose of the entrance beam, but the background was also observed to be higher which may be caused by the camera's closer proximity to the source.

A resolution test phantom was made by tattooing the red ink into a silicone skin phantom. A monochrome room-light image of the phantom is shown in Figure 7.3-9 (top row) where the 3 lines are distinguishable to the 3<sup>rd</sup> largest size, or 1.4mm. The images shown in Figure 4 are all background subtracted based on the mean background intensity of a region on the

skin phantom, this resulted in the filtered image collected during the X-ray pulse having slightly higher intensity due to the decreased background signal. A line profile was generated by taking the mean along the vertical axis defined by the white box overlaid on each image and the maximum resolution was defined as the smallest region where the 3 peaks are still distinguishable. Figure 4 shows how this resolution target was nearly indistinguishable without a filter, whereas the first and possibly second line pairs are detectable using a 600 long-pass filter for an estimated resolution of 1.6mm.

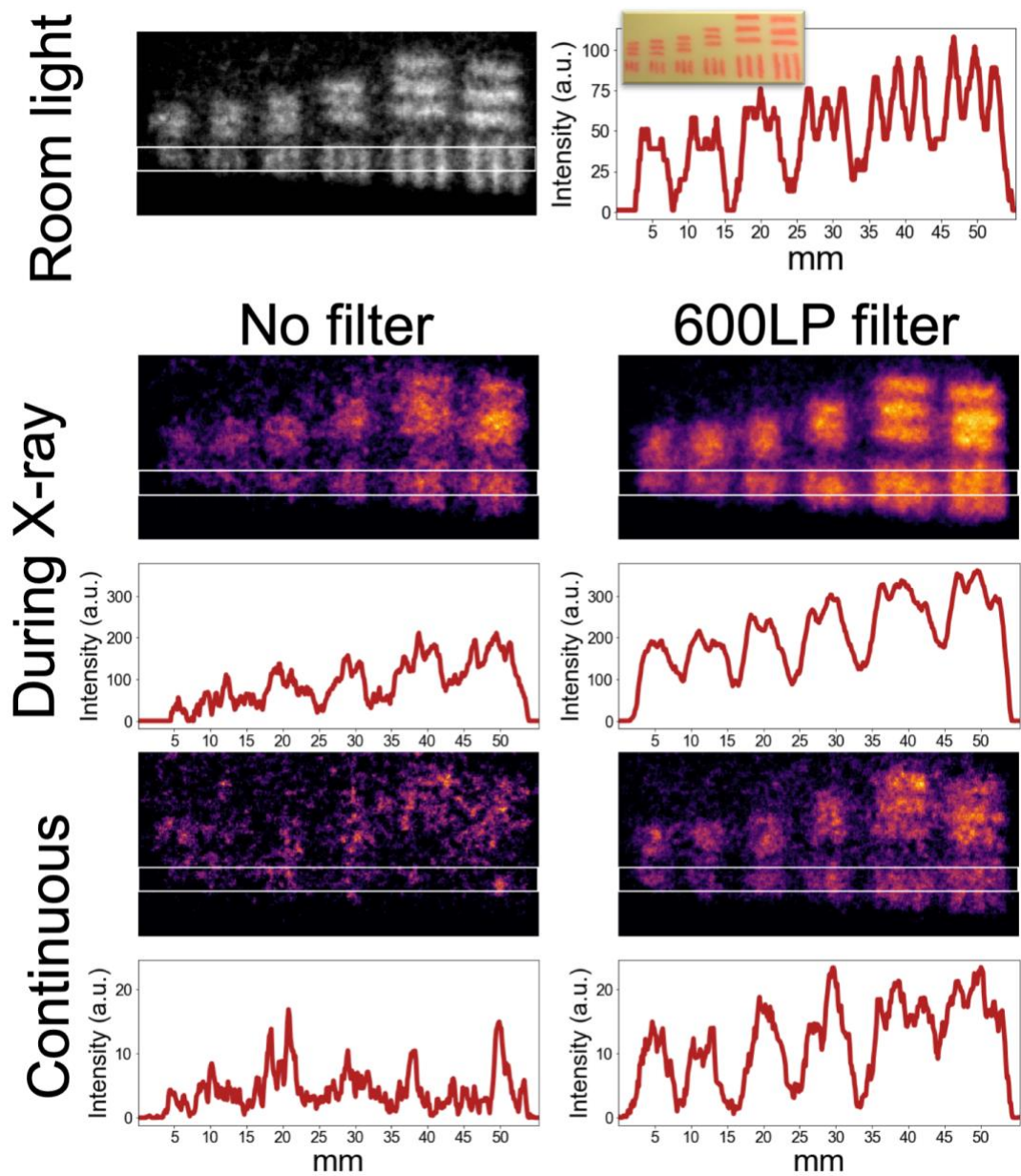


Figure 7.3-9: Red UV ink was tattooed into a skin-simulating phantom (top inset) to test system resolution under room-lights (top), time-gate to X-ray delivery (middle), and continuous acquisition during dose delivery (bottom).

## 7.4 Discussion

### 7.4.1 Oxygenation

Due to the red-shifted emission of PtG4 (772 nm) in comparison to the other reagents, it was originally hypothesized that this reagent would be the most effective for imaging in tumors, since this wavelength would achieve the most effective tissue penetration. However, we wanted to compare PtG4 with other commercially available phosphorescent oxygen sensors to identify the reagents with the best qualities for utilization in CELSI. Several factors are involved in the selection of ideal compounds. As with fluorescence imaging, the quantum yield of the compound is a significant factor which determines the efficiency of imaging. In CEL imaging time gating is used to separate Cherenkov emissions from luminescence, so luminescence lifetime is also important to consider. Medical LINACs have a 4  $\mu$ s radiation pulse, and so this moderate pulse time limits the time gating to the microsecond regime, and without significant change to the LINAC or acquisition, nanosecond lifetimes would not be possible to measure. The luminescent agents that are available with microsecond lifetimes are typically phosphorescent. It has not been feasible to detect fluorescent agents which have nanosecond lifetimes, other than through wavelength filtering and continuous wave detection.<sup>4</sup> The typical timing used for image acquisition that is coupled to the LINAC is depicted in Figure 7.4-1a. Experimentally the gate width is generally set between 5 - 10 times the deoxygenated lifetime of the reagent of interest ( $\tau_0$ ). The CEL is then detected at multiple delay times in order to determine the emission lifetime of each phosphorescent agent. The time between radiation pulses is one

factor that will limit the maximum lifetime when choosing a phosphorescent compound. The LINAC generates radiation pulses at a repetition rate between 2.7 and 17ms (600MU/min - 100MU/min). Shorter lifetimes can be difficult to discriminate from the radiation-induced Cherenkov light. The LINAC radiation pulse does not immediately turn off, and both stray charge and Cherenkov emissions may be detected during the transition phase. Phosphorescent compounds with lifetimes in this range ( $<4.5\mu\text{s}$ ) will be difficult to detect. A plot of the decay curves depicting lifetime measurements as a function of quantum yield for each compound used in the study is shown in Figure 7.4-1b. Ir(bt<sub>2</sub>)<sub>2</sub>(acac) has been utilized in light emitting diode (LED) applications and has a high quantum yield of 0.33,<sup>32</sup> which should also impart ideal imaging properties; however, its shorter emission lifetime of 5.8  $\mu\text{s}$ <sup>32</sup> may limit its application in CELSI. While PtG4, MM2 and MitoID have lower quantum yields, their longer emission lifetimes should be advantageous for signal detection. In addition MM2 and MitoID are nanoparticles with multiple copies of oxygen sensitive porphyrins,<sup>31</sup> which should provide enhanced signal to noise ratio.

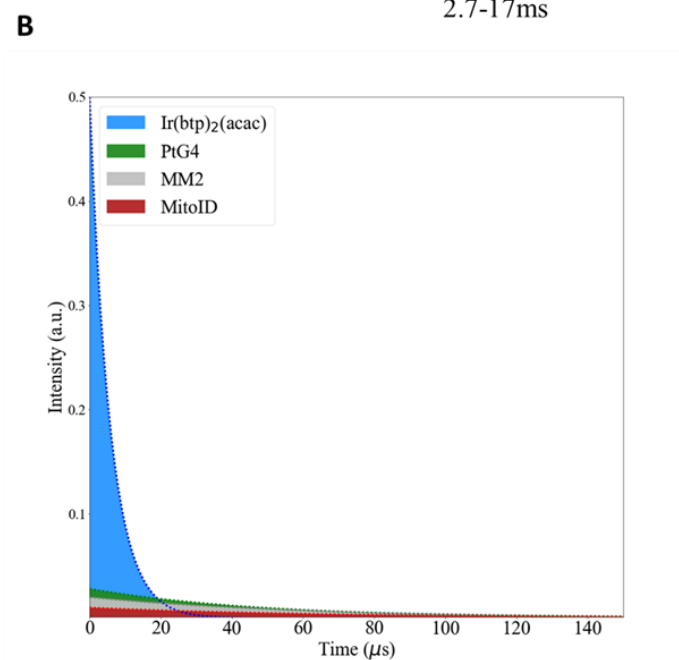
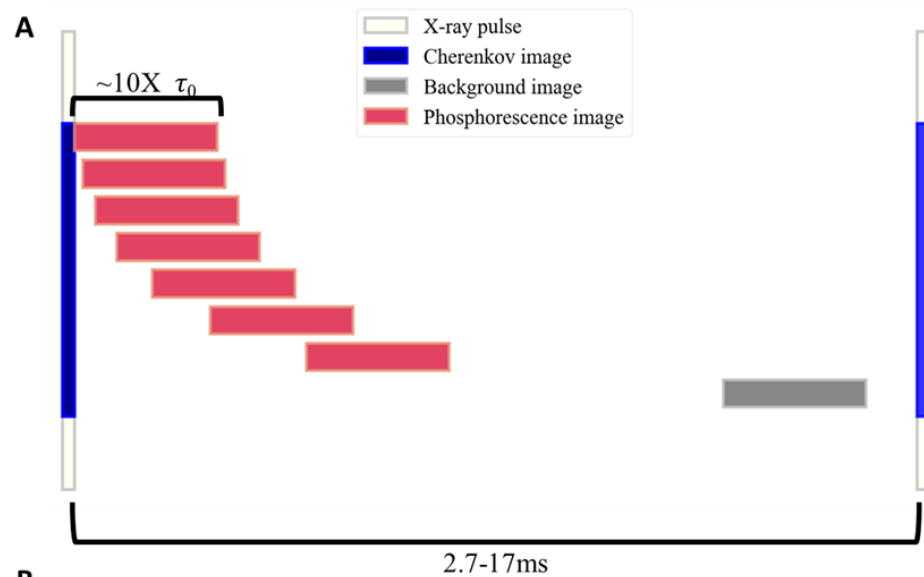


Figure 7.4-1: Considerations for CELSI. A. Cherenkov imaging timing. Experimentally the gate width is generally set between 5 - 10 times the deoxygenated lifetime ( $\tau_0$ ) of the reagent of interest. Luminescence is detected at a series of delay times (red blocks) after the Cherenkov emission (blue column) to assess the emission lifetime of phosphorescent agents. The LINAC generates radiation pulses at a repetition rate between 2.7 and 17ms (600MU/min - 100MU/min). B. plot of emission decay curves as a function of quantum yield

With optimization in mind, a comparison of commercially available oxygen sensors was completed in vitro, comparing signals in ambient oxygen to that in the presence of oxygen-scavenging GODCAT. These conditions were employed since phosphorescent oxygen sensors exhibit maximum luminescence in the absence of oxygen. PtG4 was not employed in this study since the maximum cutoff for the fluorescence emission of the plate reader is shorter than the PtG4 fluorescence emission. As expected, these reagents show a signal enhancement in the presence of GODCAT conditions, indicating a response to change in oxygenation levels. MM2 and Ir(bt<sub>b</sub>)<sub>2</sub>(acac) gave the most robust responses in sensing oxygen changes via steady state fluorescence (Figure 7.3-2a). At the highest concentration utilized (30 µg/mL), the signal was attenuated in comparison to the 20 µg/mL samples, which could be attributed to self-quenching, although further investigation of this was not done. Due to these observations, since MM2 and Ir(bt<sub>b</sub>)<sub>2</sub>(acac) gave the best signal, the next focus was to determine the lowest concentration of each sensor that could be utilized to detect oxygen levels in vitro. We found that Ir(bt<sub>b</sub>)<sub>2</sub>(acac) still elicited a luminescence signal in response to oxygen changes in PANC-1 cells at 0.2 µg/mL. While MM2 exhibited a statistically significant response to oxygen scavenging conditions at a lower concentration (0.02 µg/mL), the responses to oxygenation changes were not robust at concentrations lower than 2 µg/mL (Figure 7.3-2b).

We investigated CEL both in solution and loaded into PANC-1 cells of the previously studied PtG4 as well as MM2, Ir(bt<sub>b</sub>)<sub>2</sub>(acac), and MitoID. Both PtG4 and MM2 exhibited strong phosphorescence at 20 µg/mL in solution, particularly with oxygen scavenging, when excited by Cherenkov emission, with phosphorescence intensities of 1349 and 1269,

respectively, whereas Ir(bt<sub>b</sub>)<sub>2</sub>(acac) and MitoID did not display significant phosphorescence in solution, with intensities of 250 and 150 respectively. (Figure 7.3-3a). We have previously seen excellent results with CELSI with PtG4 (19, 21, 22), and since MM2 contains multiple copies of a porphyrin grafted to a nanoparticle, enhanced signal in response to oxygen was anticipated for both of these reagents. As expected, we found that the intracellular phosphorescence intensity was markedly decreased in comparison to the phosphorescence measured in solution. Interestingly, Ir(bt<sub>b</sub>)<sub>2</sub>(acac) exhibits a much better phosphorescence signal in cells versus solution, giving the largest detectable signal in comparison to the other reagents (Figure 7.3-3b). This is likely due to the fact that this complex binds to albumin or another cellular protein, thereby enhancing permeability. However previous reports indicate that it is no longer sensitive to oxygen when bound to albumin in vitro. Our results and other cell studies with Ir(bt<sub>b</sub>)<sub>2</sub>(acac) that show oxygen sensitivity indicate that binding to albumin is not the mechanism that imparts enhanced signal in cells vs. solution.<sup>32</sup> The performance of MM2 was diminished intracellularly, possibly due to lower cell permeability than Ir(bt<sub>b</sub>)<sub>2</sub>(acac). In fact, Ir(bt<sub>b</sub>)<sub>2</sub>(acac) was found to penetrate cells far more rapidly than MM2 (30 min vs. 24 h). PtG4 gave a robust response to oxygenation changes in cells; however, the intensity was somewhat attenuated in comparison to Ir(bt<sub>b</sub>)<sub>2</sub>(acac). One critical advantage of PtG4 is that the dendrimer shell prevents its interaction with other biomolecules that could potentially perturb its emission lifetime and thus pO<sub>2</sub> estimations. This is considered to be a key factor in making this agent a linear reporter of tissue pO<sub>2</sub>, and in fact PtG4 and similar reagents have been calibrated appropriately in extensive studies.<sup>2-4,22-24,35</sup> While MitoID displays an enhanced

signal in cells vs. solution, it still elicits the weakest phosphorescent response to changes in oxygen concentration.

PtG4, Ir(bt<sub>b</sub>)<sub>2</sub>(acac), and MM2 seemed to have promise for use in CELSI. Therefore, we investigated these reagents for sensing oxygenation levels in subcutaneous tumors. We were unable to detect significant phosphorescence with MM2 in vivo. However, we were able to sense emission lifetime and as such calculate tissue oxygenation utilizing CELSI for both PtG4 and Ir(bt<sub>b</sub>)<sub>2</sub>(acac) at the nmol level (Figure 7.3-5b,c,d). Unfortunately, we were not able to measure fluorescence lifetime or tissue pO<sub>2</sub> in live mice with Ir(bt<sub>b</sub>)<sub>2</sub>(acac). This is likely because the luminescence lifetime in a fully oxygenated sample of Ir(bt<sub>b</sub>)<sub>2</sub>(acac) is shorter than we can detect since the shortest delay time feasible for imaging after the radiation pulse is 4.26μs. We also observed quenching with Ir(bt<sub>b</sub>)<sub>2</sub>(acac) at concentrations higher than 50 μM in subcutaneous tumors, as we did in the fluorescence plate reader experiments.

A summary of the results as well as a comparison of the pros and cons of the oxygen sensors we utilized for this study are illustrated in Table 7.4-1. Briefly, both PtG4 and Ir(bt<sub>b</sub>)<sub>2</sub>(acac) are stable indefinitely, while MM2 and MitoID nanoparticles have a short shelf life of only 1-2 weeks once resuspended. PtG4 has a dendrimer shell that prevents its interaction with biomolecules, allowing accurate determinations of fluorescence lifetime and pO<sub>2</sub> calculations. Ir(bt<sub>b</sub>)<sub>2</sub>(acac) and MitoID appear to interact with biomolecules in some way, given the difference in phosphorescent intensities discovered in solution vs. cells. Finally,

we have observed that MM2, MitoID and Ir(btbt)<sub>2</sub>(acac) exhibit self-quenching at higher concentrations, where we have not seen this effect with increasing concentrations of PtG4.

*Table 7.4-1: Side-by-side comparison of phosphorescent oxygen sensors utilized for CEL*

Compound	CEL solution	CEL cells	CEL in vivo	Biomolecule Interaction	Stability	Self- quenching
<b>PtG4</b>	+	+	+	-	+	-
<b>Ir(btbt)<sub>2</sub>(acac)</b>	+	+	+	+	+	+
<b>MM2</b>	+	+	-	-	-	+
<b>MitoID</b>	-	+	-	+	-	+

## 7.4.2 Field Verification

The use of tattoo and semi-permanent inks is a widely used a method for treatment alignment in radiation therapy.<sup>25,26</sup> Utilizing UV-excited ink provides patients with a cosmetically appealing option of a tattoo that is less visible, resulting in improved self-image.<sup>29</sup> In these instances the patient is aligned under the aid of a UV light source by the therapist, who uses UV-A and visible light in the range of 385-405nm to visualize the ink. At these wavelengths there is minimal carcinogenic potential to the therapist and safety glasses can be worn to minimize any adverse effects of prolonged ocular exposure. While these methods provide a mechanism to align patients before daily dose fractions, many modern radiotherapy systems use kV imaging often delivered via cone-beam CT. Patient alignment systems such as Vision RT and ExacTrac can also be used to monitor patient

alignment but are not directly monitoring beam delivery. However, in low- and middle-income countries these modern resources for alignment are often not available. The visualization of these inks during treatment is one method to provide feedback on both field delivery and alignment, which would otherwise not be available.

The active compounds that exist within these inks are commonly undocumented due to the nature of the tattoo industry. Previous reports of similar UV inks indicate the active compound was coumarin-based,<sup>29</sup> but the spectral properties coumarins generally absorb UV and emit wavelengths under 530nm,<sup>38,39</sup> which does not explain the red emission observed in some of these inks or the microsecond lifetime. Nevertheless, these inks provide a potentially low-cost method for patient alignment, and also direct verification of radiation delivery, either by scintillation or Cherenkov-excited luminescence. The methods demonstrated in the current work are similar to those reported by Jenkins *et al* where thin (0.8mm) scintillating silicone films were used for beam visualization.<sup>40</sup> However, we have demonstrated commercially available inks (Available for \$15/30mL) can be directly painted or transferred onto skin-phantoms covering a large area. This application demonstrates how currently used tattoo-based fiducial markings could utilize the same inks over a larger area, and applied in a semi-permanent topical manner, to visualize entrance and exit beams for field delivery verification. If surface delivery of the ink (Figure 7.3-8) was calibrated, this could provide a low-cost and low-resource mechanism for dosimetry similar to how scintillating disks have been used to correlate with dose measured by TLDs.<sup>41</sup> In this geometry, tissue optical properties are not a concern, so the brightest inks could be matched with peak photocathode quantum efficiency. As such, the white or yellow

inks appear as ideal candidates for surface imaging as long as the corresponding similar photocathode quantum efficiency profile.

While the resolution test sample created by delivering the ink below the phantom surface has a lower overall intensity, it provides evidence that these inks may still be visible at low concentration even in the presence of tissue optical properties. The absolute pixel resolution attained by the imaging system under normal room illumination is 1.4 mm, whereas the resolution observed during the X-ray pulse is approximately 1.6 mm, which is slightly larger than the average deviation reported by Jenkins (mean: 0.5mm, max: 2.0mm) using a similar experimental setup.<sup>40</sup> The observed resolution is likely limited by camera detection optics, as the resolution degrades only slightly between room illumination and X-ray excitation. In situations where portal imaging is used for alignment, which is common in low to middle income countries, average treatment variations of 3mm have been shown.<sup>42</sup> While the modern trend aims for sub-mm accurate patient alignment, luminescent inks show promise as a potential metric for visualizing radiation dose delivery with high spatial accuracy.

The long microsecond lifetime of the measured inks was unexpected but can prove to be a beneficial contrast mechanism when high background environments are imaged. The X-rays delivered by the linear accelerator will scatter high energy electrons, which generate Cherenkov emission in dielectric media such as tissue. The observed intensity of these Cherenkov emissions will fluctuate depending on parameters such as dose build-up and tissue optical properties. By imaging after the X-ray pulse, the variable Cherenkov emission can be suppressed.

Another method to suppress background is to use optical filters. While Cherenkov emissions are largely blue, the spectral properties follow a  $1/\lambda^2$  distribution.<sup>43</sup> Additionally, since much of the blue light is absorbed within the tissue, before reaching the surface, the Cherenkov surface emissions are largely red. In the linac study, a 600nm longpass filter was used to understand the possibility of suppressing excess light generated during the X-ray pulse. As shown in Figure 7.3-8F, this filter boosts the SNR of the red ink by approximately 8-15% during the X-ray and continuous imaging modes. Filtering was used during cobalt-60 irradiation to suppress excess light mainly due to IR LEDs on security cameras in the bunker. Filters centered at 635nm were able to discriminate the red and orange inks with similar SNR, whereas the filter centered at 550 suppressed red and orange and allowed for detection of the yellow ink. On the linear accelerator, filtering after the pulse lowers the SNR because much of the light is generated by the ink and there is very low background, so in this low-photon environment filtering is not beneficial.

The continuous mode imaging demonstrated on the linear accelerator was translated for use with a cobalt-60 source currently used in Honduras. While cobalt-60 systems are becoming less common and currently account for 22-33% of all radiotherapy systems worldwide, their prevalence is estimated to be much higher in low and middle income countries.<sup>44,45</sup> These systems generally lack many modern features such as cone beam CT alignment. In these situations, UV- and MV-excited fiducial markers which have the dual purpose of real-time field verification, provide an additional tool to help reduce potential delivery errors.

## **7.5 Conclusion**

### **7.5.1 Oxygenation**

When used in vitro in PANC-1 cells at the same concentrations, the signal strengths suggest that the optimal agents would be Ir(bt<sub>b</sub>)<sub>2</sub>(acac), followed by PtG4, and then MM2 and MitoID. However, in vivo, only PtG4 and Ir(bt<sub>b</sub>)<sub>2</sub>(acac) were found to be measurable at nmol doses in the tumors, and assessment of tissue oxygenation accomplished. On the timescale of LINAC produced x-ray imaging, PtG4 is the more ideal agent, because of the lifetime on the scale of tens of microseconds, versus Ir(bt<sub>b</sub>)<sub>2</sub>(acac) which has a lifetime of a few microseconds which hinders detection at higher tissue pO<sub>2</sub> values. This work represents: (1) a unique way to harness Cherenkov emission for imaging purposes in conjunction with radiotherapy, (2) a noninvasive determination of tumor pO<sub>2</sub>, and (3) a direct comparison of phosphorescent sensors available to probe tissue oxygenation.

### **7.5.2 Field Verification**

The UV-sensitive fluorescent tattoo inks investigated in the present study exhibit luminescent properties which were imaged during radiation therapy. The practice of tattooing or placing semi-permanent markings during medical procedures has been reported previously and is a common clinical procedure. The current work demonstrates the ability to image UV-sensitive fluorescent inks during radiation therapy using both a linear accelerator or cobalt-60 source. Using a linear accelerator, imaging can be time-gated with the X-ray delivery as well as after the pulse due to the phosphorescent properties of the inks. Phosphorescence imaging provides the ability to greatly reduce the background

intensity due to the reduced Cherenkov emissions during this period. In addition to imaging in solution, the inks are visible as ink painted on the surface or tattooed into skin-simulating phantoms with a spatial resolution near 1.6mm. The spectral variation of these inks could be used to provide multiplexed imaging during dose delivery which was demonstrated using bandpass filters with cobalt-60 irradiation. Further work is needed to study the clinical efficacy of this workflow

## 7.6 Acknowledgments

This work was financially supported by the Department of Defense, Congressionally Directed Medical Research Program (CDMRP) Breast Cancer Innovator Award (BC150584P1), as well as the National Institutes of Health NIBIB R01 EB024498, and the NCI Cancer Center Support Grant P30 CA023108. This material is also based on work supported by the National Science Foundation Graduate Research Fellowship.

## 7.7 References

1. Glaser, A. K. *et al.* Projection imaging of photon beams by the Čerenkov effect. *Medical Physics* **40**, 012101–012101 (2012).
2. Zhang, R. *et al.* Čerenkov radiation emission and excited luminescence (CREL) sensitivity during external beam radiation therapy: Monte Carlo and tissue oxygenation phantom studies. *Biomedical Optics Express* **3**, 2381–2381 (2012).
3. Zhang, R., Glaser, A. K., Gladstone, D. J., Fox, C. J. & Pogue, B. W. Superficial dosimetry imaging based on Čerenkov emission for external beam radiotherapy with megavoltage x-ray beam. *Medical Physics* **40**, 101914 (2013).
4. Lin, H. *et al.* Comparison of Cherenkov excited fluorescence and phosphorescence molecular sensing from tissue with external beam irradiation. *Physics in Medicine and Biology* **61**, 3955–3968 (2016).

5. Vaupel, P., Mayer, A. & Höckel, M. Impact of Hemoglobin Levels on Tumor Oxygenation: the Higher, the Better? *Strahlenther Onkol* **182**, 63–71 (2006).
6. Evans, S. M. & Koch, C. J. Prognostic significance of tumor oxygenation in humans. *Cancer Letters* **195**, 1–16 (2003).
7. Bussink, J., Kaanders, J. H. A. M., Strik, A. M. & van der Kogel, A. J. Effects of nicotinamide and carbogen on oxygenation in human tumor xenografts measured with luminescence based fiber-optic probes. *Radiotherapy and Oncology* **57**, 21–30 (2000).
8. Turaka, A. *et al.* Hypoxic Prostate/Muscle Po<sub>2</sub> Ratio Predicts for Outcome in Patients With Localized Prostate Cancer: Long-Term Results. *International Journal of Radiation Oncology\*Biophysics* **82**, e433–e439 (2012).
9. Vaupel, P. & Kelleher, D. K. Blood Flow and Oxygenation Status of Prostate Cancers. in *Oxygen Transport to Tissue XXXIV* (eds. Welch, W. J., Palm, F., Bruley, D. F. & Harrison, D. K.) 299–305 (Springer, 2013). doi:10.1007/978-1-4614-4989-8\_42.
10. Genbacev, O., Krtolica, A., Kaelin, W. & Fisher, S. J. Human Cytotrophoblast Expression of the von Hippel–Lindau Protein Is Downregulated during Uterine Invasion in Situ and Upregulated by Hypoxia in Vitro. *Developmental Biology* **233**, 526–536 (2001).
11. Koch, C. J. A Two-Component Assay for Hypoxia Incorporating Long-Term Nitroreduction and Short-Term DNA-Damage Allows Differentiation of the Three Hypoxia Sub-types. *Radiation Research* **190**, 72–87 (2018).
12. Loftus, S. K., Baxter, L. L., Cronin, J. C., Fufa, T. D. & Pavan, W. J. Hypoxia-induced HIF1 $\alpha$  targets in melanocytes reveal a molecular profile associated with poor melanoma prognosis. *Pigment Cell & Melanoma Research* **30**, 339–352 (2017).
13. Stone, H. B. & Withers, H. R. Tumor and Normal Tissue Response to Metronidazole and Irradiation in Mice. *Radiology* **113**, 441–444 (1974).
14. Aguilera, K. Y. & Brekken, R. A. Hypoxia Studies with Pimonidazole in vivo. *Bio Protoc* **4**, (2014).
15. Gonçalves, M. R. *et al.* Decomposition of spontaneous fluctuations in tumour oxygenation using BOLD MRI and independent component analysis. *British Journal of Cancer* **113**, 1168–1177 (2015).
16. Li, D., Wang, X., Wang, S. & Cheng, J. Correlation between BOLD-MRI and HIF expression level in renal carcinoma. *Int J Clin Exp Pathol* **8**, 13759–13763 (2015).
17. Gustafsson, H. *et al.* EPR Oximetry of Cetuximab-Treated Head-and-Neck Tumours in a Mouse Model. *Cell Biochem Biophys* **75**, 299–309 (2017).

18. Swartz, H. M. The Measurement of Oxygen in Vivo Using EPR Techniques. in *In Vivo EPR (ESR): Theory and Application* (ed. Berliner, L. J.) 403–440 (Springer US, 2003). doi:10.1007/978-1-4615-0061-2\_15.
19. Srinivasan, S. *et al.* In Vivo Hemoglobin and Water Concentrations, Oxygen Saturation, and Scattering Estimates From Near-Infrared Breast Tomography Using Spectral Reconstruction. *Academic Radiology* **13**, 195–202 (2006).
20. Kelada, O. J. *et al.* Quantification of Tumor Hypoxic Fractions Using Positron Emission Tomography with [18F]Fluoromisonidazole ([18F]FMISO) Kinetic Analysis and Invasive Oxygen Measurements. *Mol Imaging Biol* **19**, 893–902 (2017).
21. Stieb, S., Eleftheriou, A., Warnock, G., Guckenberger, M. & Riesterer, O. Longitudinal PET imaging of tumor hypoxia during the course of radiotherapy. *Eur J Nucl Med Mol Imaging* **45**, 2201–2217 (2018).
22. Zhang, R. *et al.* Oxygen tomography by Čerenkov-excited phosphorescence during external beam irradiation. *JBO* **18**, 050503 (2013).
23. Esipova, T. V. *et al.* Two New “Protected” Oxyphors for Biological Oximetry: Properties and Application in Tumor Imaging. *Analytical Chemistry* **83**, 8756–8765 (2011).
24. Dmitriev, R. I. & Papkovsky, D. B. Intracellular probes for imaging oxygen concentration: how good are they? *Methods Appl. Fluoresc.* **3**, 034001 (2015).
25. Baluyot, S. T. & Shumrick, D. A. Pre-Irradiation Tattooing. *Arch Otolaryngol* **96**, 151–153 (1972).
26. Wurstbauer, K., Sedlmayer, F. & Kogelnik, H. D. Skin markings in external radiotherapy by temporary tattooing with henna: Improvement of accuracy and increased patient comfort. *International Journal of Radiation Oncology\*Biological\*Physics* **50**, 179–181 (2001).
27. Vassileva, S. & Hristakieva, E. Medical applications of tattooing. *Clinics in Dermatology* **25**, 367–374 (2007).
28. David, J. E. & Mossi, K. Localization Tattoos: An Alternative Method Using Fluorescent Inks. in (2006).
29. Landeg, S. J. *et al.* A randomized control trial evaluating fluorescent ink versus dark ink tattoos for breast radiotherapy. *BJR* **89**, 20160288 (2016).
30. Taylor, C. R., Anderson, R. R., Gange, R. W., Michaud, N. A. & Flotte, T. J. Light and Electron Microscopic Analysis of Tattoos Treated by Q-Switched Ruby Laser. *Journal of Investigative Dermatology* **97**, 131–136 (1991).
31. Dmitriev, R. I. & Papkovsky, D. B. Optical probes and techniques for O<sub>2</sub> measurement in live cells and tissue. *Cellular and Molecular Life Sciences* **69**, 2025–2039 (2012).

32. Zhang, S. *et al.* Phosphorescent Light-Emitting Iridium Complexes Serve as a Hypoxia-Sensing Probe for Tumor Imaging in Living Animals. *Cancer Res* **70**, 4490–4498 (2010).
33. LaRochelle, E. P. M., Shell, J. R., Gunn, J. R., Davis, S. C. & Pogue, B. W. Signal intensity analysis and optimization for *in vivo* imaging of Cherenkov and excited luminescence. *Physics in Medicine and Biology* (2018) doi:10.1088/1361-6560/aab83b.
34. Shell, J. R. *et al.* Comparison of phosphorescent agents for noninvasive sensing of tumor oxygenation via Cherenkov-excited luminescence imaging. *Journal of Biomedical Optics* **24**, 1–1 (2019).
35. Sullender, C. T. *et al.* Imaging of cortical oxygen tension and blood flow following targeted photothrombotic stroke. *NPh* **5**, 035003 (2018).
36. Alexander, D. A. *et al.* Assessment of imaging Cherenkov and scintillation signals in head and neck radiotherapy. *Phys. Med. Biol.* **64**, 145021 (2019).
37. Jacques, S. L. Optical properties of biological tissues: a review. *Phys. Med. Biol.* **58**, R37–R61 (2013).
38. Taniguchi, M., Du, H. & Lindsey, J. S. PhotochemCAD 3: Diverse Modules for Photophysical Calculations with Multiple Spectral Databases. *Photochemistry and Photobiology* **94**, 277–289 (2018).
39. Taniguchi, M. & Lindsey, J. S. Database of Absorption and Fluorescence Spectra of >300 Common Compounds for use in PhotochemCAD. *Photochemistry and Photobiology* **94**, 290–327 (2018).
40. Jenkins, C. H., Naczynski, D. J., Yu, S.-J. S. & Xing, L. Monitoring external beam radiotherapy using real-time beam visualization. *Medical Physics* 5–13 (2017) doi:10.1118/1.4901255@10.1002/(ISSN)2473-4209.MedicalPhysicsLetter.
41. Bruza, P. *et al.* Time-gated scintillator imaging for real-time optical surface dosimetry in total skin electron therapy. *Phys. Med. Biol.* **63**, 095009 (2018).
42. Rabinowitz, I., Broomberg, J., Goitein, M., McCarthy, K. & Leong, J. Accuracy of radiation field alignment in clinical practice. *International Journal of Radiation Oncology\*Biography\*Physics* **11**, 1857–1867 (1985).
43. Frank, I. & Tamm, Ig. Coherent Visible Radiation of Fast Electrons Passing Through Matter. in *Selected Papers* 29–35 (Springer Berlin Heidelberg, 1991). doi:10.1007/978-3-642-74626-0\_2.
44. Datta, N. R. & Rajasekar, D. Improvement of radiotherapy facilities in developing countries: a three-tier system with a teleradiotherapy network. *The Lancet Oncology* **5**, 695–698 (2004).

45. Page, B. R. *et al.* Cobalt, Linac, or Other: What Is the Best Solution for Radiation Therapy in Developing Countries? *International Journal of Radiation Oncology\*Biology\*Physics* **89**, 476–480 (2014).

# CHAPTER 8

## **8 Near real-time non-contact *in vivo* pO<sub>2</sub> estimation during fractionated external beam radiotherapy**

### **8.1 Introduction**

The tumor microenvironment often exhibits abnormal morphology which may increase permeability or decrease perfusion.<sup>1,2</sup> This can lead to a locally hypoxic environment, which has been correlated with a poor prognosis.<sup>3</sup> Radiotherapy is a common option used to treat tumors, but in part relies on the formation of reactive oxygen species generated by the ionizing radiation. With hypoxic regions of tumors, the effectiveness of radiotherapy can be reduced and may lead to the survival of more aggressive phenotypes.<sup>4,5</sup> The oxygen enhancement ratio is used to describe the change in radiation sensitivity between normoxic and hypoxic cells, where 2.5-3 times more dose is required to have the same effect on hypoxic cells.<sup>6</sup> Most radiotherapy treatments involve the patient receiving their treatment in daily fractionated doses of approximately 2Gy delivered daily over a period of weeks to months, however there are few clinically available indicators to monitor the tumor microenvironment during this period.

Blood oxygen level-dependent (BOLD) MRI has been used to assess tumor oxygen partial pressure ( $pO_2$ ),<sup>7,8</sup> however this method is mainly sensitive to blood flow and deoxyhemoglobin concentration and has generally been used to sense trends in whole-tumor  $pO_2$  levels.<sup>9</sup> Another clinically used method for imaging tumor hypoxia is  $^{18}F$ -MISO PET. This method uses the radiotracer  $^{18}F$ -MISO to selectively bind to macromolecules in hypoxic environments, but relies on blood flow to deliver the agent, as such it is not sensitive to necrotic regions.<sup>10</sup> The gold standard method continues to be microsensor technique which involves generating a  $pO_2$  histogram from a series of randomly sampled needle electrode measurements.<sup>11</sup>

Recent advancements have reported on using Cherenkov-excited luminescence imaging during external beam radiotherapy to determine *in vivo*  $pO_2$ .<sup>12-14</sup> While this method has required the delivery of a 4-12 Gy dose to determine an estimate for a single time point, it demonstrates the possibility of measuring  $pO_2$  during treatment. In the current work we present a method for determining  $pO_2$  rapidly during the process of delivering a 2Gy dose fraction. The peak X-ray energy levels delivered by a linear accelerator during radiotherapy are often 6-18 MV, and as these photons pass through tissue, Compton scattering events occur resulting in high-energy secondary electrons. Electrons that have energy greater than approximately 220KeV in tissue create a light shockwave known as Cherenkov emission.<sup>15</sup> As discussed in previous chapters, these optical emissions exhibit a  $1/\lambda^2$  spectral distribution which means the light is predominantly observed in the UV-Blue region when tissue optical properties are not present, but the spectrum is actually broadband and emissions can be detected out into the near infrared.<sup>16</sup> This broadband light can be used to

excite molecular probes within the tissue, and therefore provides the opportunity to biochemically sense inside the tumor during treatment. Perhaps most interesting is the idea that sensing of tissue  $pO_2$  could allow preferential steering of the treatment to boost dose to areas of known hypoxia.<sup>17-20</sup>

Biochemical sensing of luminescent species is optimally done in temporal emission, because the clinical linear accelerator (linac) systems deliver trains of  $4\mu s$  bursts of X-ray photons at a rate of 360Hz, with 2.8ms between pulses. A representative example of the timing diagram is provided in Figure 8.1-1a, where the ON time is exaggerated. Cherenkov emissions are generated during each pulse and luminescent molecules can be excited which emit their signal decaying between each X-ray pulse. For this configuration an appropriate lifetime longer than the x-ray pulses, and between 10 - 600 $\mu s$  allows for sufficient luminescence imaging and baseline measurements between pulses.<sup>21</sup> Cherenkov emissions can be imaged by directly gating a camera to the linac pulses, with delays over 5 $\mu s$  used to image the Cherenkov-excited luminescence (CEL) decay, and background images acquired to account for fluctuations in ambient room light (Figure 8.1-1b).<sup>22</sup> Since the phosphorescence lifetime is related to local oxygen concentration, lifetime estimates can be used to estimate  $pO_2$ . Our previously reported work estimated phosphorescence lifetimes by manually changing the intensifier delay setting with each 1-2+Gy dose (Figure 8.1-1c) and utilized 4 or more time delays to estimate phosphorescence lifetimes<sup>14,23</sup> The work presented in this chapter demonstrates the ability to automatically update the acquisition settings during imaging, where up to 5 settings can be configured and cycled after set exposure periods (Figure 8.1-1d).

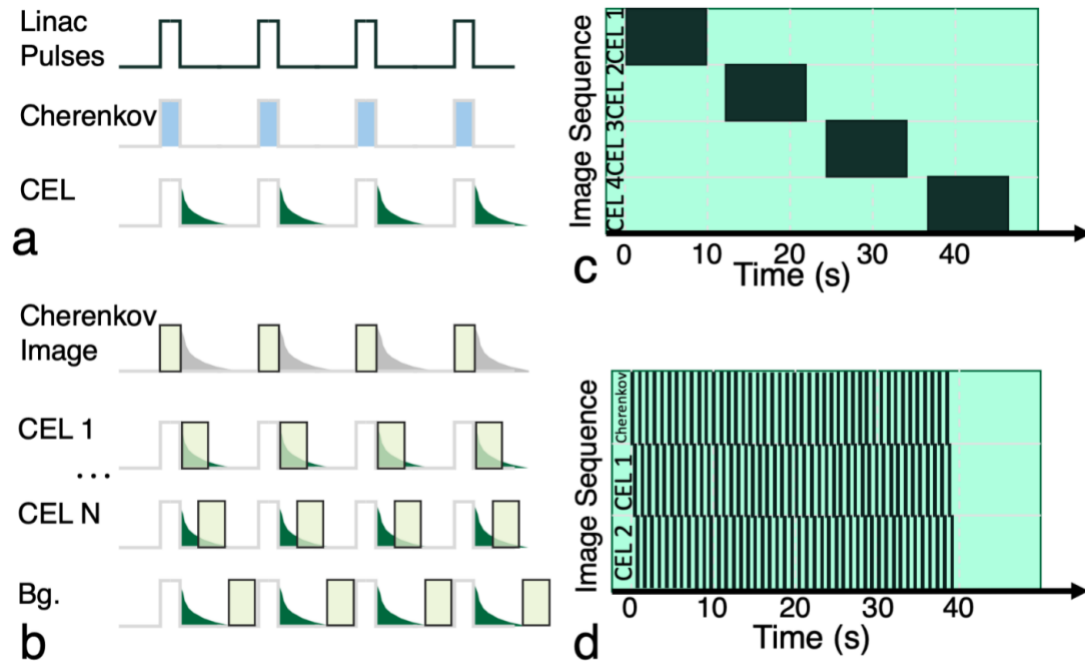


Figure 8.1-1: Representative timing diagram of a clinical linac showing when Cherenkov emissions and Cherenkov-excited luminescence are formed in relation to the pulses (a), and examples of the timing windows used in imaging (b). In previous work image stacks were collected with each setting for 1+Gy (c), whereas the new method automatically cycles the acquisition settings, acquiring frames using less than 10cGy (d).

To demonstrate the potential application of this revised detection method a series of experiments were performed. Limits of spatial and temporal resolution were determined using solutions of two oxygen-sensitive compounds under normoxic and hypoxic conditions. The reliability of different analysis techniques was tested to identify which methods to use during *in vivo* studies. An *in vivo* mouse model was used to demonstrate the ability to sample pO<sub>2</sub> at near real-time with high spatial resolution.

## 8.2 Methods

### 8.2.1 Imaging system

A time-gated intensified CMOS (ICMOS) camera with a red-sensitive photocathode (C-Dose, DoseOptics LLC, Lebanon, NH) was connected to a remote trigger unit and time-gated to the pulses of a clinical linear accelerator (CLINAC C2100, Varian Medical, Palo Alto, CA). The camera was placed a horizontal distance of approximately 0.5m from isocenter. A mirror at  $45^\circ$  was placed above the sample to redirect the optical light towards the camera objective. The camera objective was a Nikon NIKKOR 50mm f/1.2 and the pixel resolution for all experiments is approximately  $150\mu\text{m}$  and  $300\text{cm}^2$  field of view. Cherenkov images were collected during the  $4\mu\text{s}$  X-ray pulse, while phosphorescence images were collected after a 5-50 $\mu\text{s}$  delay from the bringing of the pulse, as shown in Figure 8.1-1a. The linear accelerator delivered pulses at a rate of 360Hz and the image sensor integrated for multiple pulses ( $\sim 10$ -30) before being transmitted from the camera.

A customized branch of the C-Dose Research acquisition software (Version 2.04) was used to acquire frames with varied delays. Briefly, while the standard software automatically collects a Cherenkov or phosphorescence image with a set intensifier delay and duration, this change allowed for the acquisition of frames with up to 5 different intensifier delay and duration settings. The delay setting indicates the time relative to the trigger signal when the intensifier is enabled, the intensifier will then remain on for the time specified by the duration, and the exposure setting controls the total time, which is proportional to the number of linac pulses, integrated on the CMOS sensor before being read off and

transferred to a computer. The camera acquires a frame using the delay-duration pair for the set exposure time before updating the intensifier setting to the next delay-duration pair and continues to cycle through these pairs for the duration of the acquisition.

### **8.2.2 Luminescent pO<sub>2</sub> sensor**

Two oxygen-sensitive platinum porphyrins, PtG4 and Oxyphor 2P, were used in this study.<sup>24–26</sup> These compounds both contain a protective dendritic structure which greatly improves *in vivo* viability due to the protective assembly, which also acts to slow oxygen diffusion to a rate which improves sensitivity. The multiple excitation peaks in both the blue and red are shown in Table 8.2-1 which allow for absorption of the predominantly UV-Blue Cherenkov emissions, but also the longer wavelength Cherenkov emissions which will propagate much further in tissue and thus have a higher probability of interaction. The peak phosphorescence emission between 750nm and 775nm allow for detection at depths up to approximately 3mm in tissue.<sup>21</sup> The lifetime of both compounds is directly related to the presence of oxygen, where high oxygen levels will result in a short lifetime, but under hypoxic conditions the luminescence is quenched and the lifetime extends to approximately 38-45 $\mu$ s. Oxyphor 2P has been synthesized with extra chemical antenna to allow for 2-photon excitation in the NIR, while also boosting the overall quantum yield by approximately 3x over PtG4.

### **8.2.3 In vitro**

A black-wall 96-well plate containing PtG4 and Oxyphor 2P was imaged using this camera system. The 96-well plate was placed at isocenter on 1.2cm water-simulating acrylic

phantom and a 15cm x 15cm 6MV 2Gy dose was delivered from below the samples. The water phantom was used so the maximum dose delivered to the phantoms, which occurs at a depth approximately 1.5cm. To determine the relative oxygen sensitivity of the system, 50 $\mu$ L of 50 $\mu$ M PtG4 and Oxyphor 2P in PBS solutions were placed in the four wells of the 96-well plate. To deprive one samples of oxygen a solution of glucose-oxidase-catalase was added to one well of each solution just before imaging. Samples of PBS and PBS with glucose-oxidase-catalase were also imaged as controls. Images were collected using delays between 0 and 50 $\mu$ s, where the 0 $\mu$ s delay was the Cherenkov image and had a duration of 4 $\mu$ s, and the other frames had a duration of 300 $\mu$ s. An exposure of 56000 $\mu$ s was used to acquire a single frame, which corresponded to 20 linac pulses or 0.56cGy dose.

#### **8.2.4 In vivo**

This study was approved by the Dartmouth Institutional Animal Care and Use Committee, and all procedures followed this approved protocol. A total of 5 healthy nude mouse (Charles River Labs, Wilmington, MA) were implanted with a subcutaneous flank tumor (FaDu) and allowed to grow to an average volume of 129 $\pm$ 58mm<sup>3</sup>. When tumors were of sufficient size, each was injected with either 50 $\mu$ L of 50 $\mu$ M PtG4 (N=2) or the same volume and concentration of Oxyphor 2P (N=3). The opposite flank of each mouse was injected with a 50 $\mu$ L mixture of either Oxyphor 2P or PtG4 (25 $\mu$ L at 100 $\mu$ M) in Matrigel (25 $\mu$ L). Using the same camera geometry as previously described, the mouse was placed at isocenter and given a whole-body 6MV 2Gy dose (200MU) at the following timepoints: 2 points after injection while under isoflurane, while awake, and 2 or more times after

sacrifice. Each mouse was placed inside a chamber for imaging with a 15cm diameter 30cm tall black plastic cylinder, which acts to reduce background light and allowed the mouse to move more freely while awake.

### **8.2.5 Image Analysis**

The raw data and meta data are processed by a Python script and saved as a TIFF stack using the scikit-image library,<sup>27</sup> where each frame corresponds to one of the four acquisition settings. A separate Python function was used to split the single tiff stack into 4 separate files corresponding to each of the settings. The function first identified the Cherenkov frames using the high-prevalence of single pixel saturated X-ray, or ‘salt’, noise. It also checked to verify the mean intensity of the frame sequence was monotonically decreasing before splitting frames into separate files. This process required approximately 15 seconds for a typical 2Gy dose fraction, although could be further automated. This function is also used on darkfield data, acquired with the lens cap on. A temporal median of the darkfield image stack for each setting was then subtracted from all subsequent image frames with corresponding settings. A flatfield image was also acquired by imaging a flat surface with uniform illumination. This was used to account for any non-uniform pixel gains.

For the *in vitro* study, since this scene was static throughout the acquisition and the intent was to analyze areas of luminescence, a temporal median of the Cherenkov image stack was used to automatically identify areas of interest. The temporal median suppresses the observed X-ray noise, so that Otsu thresholding simplified the identification of wells

containing the solution for further temporal processing for extraction of lifetime and subsequent estimation of pO<sub>2</sub>.

Similar to the *in vitro* image set, Cherenkov images were used to determine the mouse location, where a simple threshold could be used. To identify the tumor and Matrigel inclusions, the phosphorescence image with the shortest delay was transformed into frequency space. Since the Matrigel and tumor were approximately the same size, a bandpass filter was applied to detect ‘blobs’ of the expected size. The resulting image was transformed back into spatial domain a threshold was taken. A logical AND operation was then applied between the mouse and tumor masks to identify areas for lifetime analysis.

The lifetime could then be calculated using the intensity of each pixel within the identified regions of interest at the known delays. Two methods were implemented to estimate the lifetime of the given samples: an iterative curve fitting algorithm using 3 frames, and a ratio-based method using three combinations of 2 frames. The curve fitting method utilized the Python `scipy.optimize.curve_fit` for data to fit equation (1), utilizing the trust region reflective algorithm and boundary range of  $(0.1\tau_0, 1.1\tau_0)$ , where  $\tau_0$  is the lifetime of PtG4 or Oxyphor 2P when pO<sub>2</sub> is 0 mmHg. The returned covariance was used to calculate the standard error, and all values with error above 20% of  $\tau_0$  were removed from further analysis. The ratio method used (2) to directly calculate lifetimes. The ratio-based method did not produce an estimate of error, so values outside of the boundaries used by the curve fitting were removed from further analysis.

$$I(t) = I_0 e^{-t/\tau} \quad (1)$$

$$\tau = \frac{\Delta t}{\ln(I_{t_1}/I_{t_2})} \quad (2)$$

Temporal summing of the acquired frames was investigated as a way to suppress statistical variation due to the low photon counts. Sequential frames were grouped in sets of 2, 3, 5 or 8 frames, which for the 56ms exposure time, and assuming a background image is taken for every frame, corresponds to a dose per set of 2.2, 3.3, 5.5 or 8.8 cGy, respectively. Spatial pixel binning was also investigated to gain better statistics and applied to regions of interest in bin sizes of 2, 4, 8, and 16 pixels and the median value of these area was used. This reduces the pixel resolution from approximately 150 $\mu$ m to a range between 0.3mm and 2.4mm, depending on the bin size.

The Stern-Volmer approximation shown in equation 3 is generally used to relate measured the lifetimes with estimates of pO<sub>2</sub>, where  $k_q$  is the quenching constant and  $\tau_0$  is the lifetime at pO<sub>2</sub>=0.

$$pO_2(\tau) = \frac{1}{k_q} \left( \frac{1}{\tau} - \frac{1}{\tau_0} \right) \quad (3)$$

While this method can provide an estimate for the pO<sub>2</sub>, the relation assumes a simple molecular triplet state where the quenching constant and  $\tau_0$  both remain constant. To improve the accuracy of pO<sub>2</sub> estimates for the more complex molecules of PtG4 and Oxyphor 2P has been utilized, which accounts for the temperature (T) dependence of both factors, as shown in equations 4 and 5.

$$k_q(T) = k_q^0 + \beta T \quad (4)$$

$$pO_2(\tau, T) = \frac{1}{(k_q^0 + \beta T)} \left( \frac{1}{a \times \tau^p} - \frac{1}{\tau_0 + \alpha T} \right) \quad (5)$$

The parameters used in equation 5 were provided with the calibration data of compounds, based on empirically determined values for Oxyphor 2P where  $\tau_0$  will only change slightly for temperatures between 25-40°C. The parameters  $a=14.8$  and  $p=1.266$  account for the exponential curvature of the relation between  $pO_2$  and  $\tau$ . All times in (5) are in seconds and temperature (T) is in °C.

Table 8.2-1: Phosphorescence properties of PtG4 and Oxyphor 2P

	<b>PtG4</b>	<b>Oxyphor 2P</b>
<b>Peak <math>\lambda_{Ex}</math></b>	435nm, 623nm	420nm, 630nm, (2P) 960nm
<b>Peak <math>\lambda_{Em}</math></b>	772nm	758nm
<b>Quantum yield</b>	0.07	0.23
<b><math>\tau</math></b>	44.6 $\mu$ s	38 $\mu$ s
<b><math>k_{q0}</math></b>	95 mm Hg <sup>-1</sup> s <sup>-1</sup>	106.134 mm Hg <sup>-1</sup> s <sup>-1</sup>
<b><math>\beta</math></b>	13	18.89
<b><math>a</math></b>	14.8	14.8
<b><math>p</math></b>	1.257	1.266
<b><math>\alpha</math></b>	-5.945E-8	

### 8.3 Results

The current method saved all image sequences into a single stack, as opposed to separate files for each sequence setting. A Python script was developed to parse the settings file and

split the image stack based on the multiple sequence parameters. Since multiple sequences are collected during the dose delivery, there is no longer a need to stop treatment or lose frames while manually updating the camera acquisition settings. This provides a higher temporal resolution where lifetime and subsequent pO<sub>2</sub> can be estimated on the scale of single seconds, whereas previously reported methods were two orders of magnitude slower. Since both Cherenkov and CEL frames can be collected simultaneously, the Cherenkov images, which have a much stronger signal, can be used to identify regions within the region receiving radiation dose. Thresholding can be performed on the Cherenkov images to automatically identify these regions. As the field of view changes, the subsequent Cherenkov images can be used to update the regions of interest.

### **8.3.1 In vitro**

Lifetimes were calculated per pixel using the cropped region of interest (ROI) from each of the CEL image sequences. The normoxic and hypoxic solutions contained in the 96-well plate were used to verify system sensitivity. To confirm the pO<sub>2</sub> conversions used by PtG4 and Oxyphor 2P, the mean value of the respective ROIs was recorded for each frame and all frames were summed. The mean intensities (Figure 8.3-1) were then used to perform a fit of (1). Using the resulting lifetime, the pO<sub>2</sub> was estimated using (5) and the parameters defined in Table 8.2-1. These values, shown in Figure 8.3-1 are considered the truth for subsequent *in vitro* comparisons.

The *in vitro* images were used to compare methods using both equations (1) and (2). Two methods were compared: using an iterative curve fitting of (1) with three delays or using

(2) with combinations of just two delays. Figure 8.3-2a shows the *in vitro* Oxyphor 2P samples imaged at increasing delays, where it can be observed the low-oxygen sample is much brighter than the solution mixed with just PBS. The mean intensity of each of these regions are plotted in Figure 8.3-1, showing the exponential decrease and relative difference between the two solutions. Oxyphor 2P is approximately 2.5-3x brighter, as shown in Figure 8.3-1. It can also be noted that at atmospheric oxygen levels, there is essentially no signal at a pulse delay of 50 $\mu$ s and is the likely cause for the larger error in the lifetime estimate shown in Figure 8.3-1. However, since sensing low oxygen is the primary goal, lower precision at higher oxygen levels is less of a concern. Even so, *in vivo* data was collected over shorter time delays (5 $\mu$ s,15 $\mu$ s,25 $\mu$ s) to help avoid this issue.

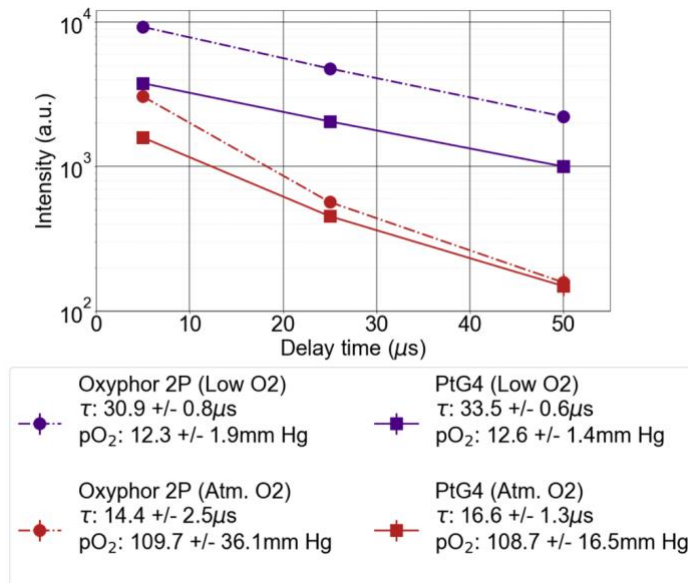


Figure 8.3-1: Using mean ROI intensities summed over multiple frames, the lifetime and resulting  $pO_2$  were determined for PtG4 and Oxyphor 2P solutions. Here, low O<sub>2</sub> solutions have glucose catalase oxidase added to the solution whereas Atm. O<sub>2</sub> are at atmospheric oxygen levels.

An example of the pixel-based lifetime estimation is presented in Figure 8.3-2, where 2x2 binned phosphorescence images of Oxyphor 2P are shown. It can be observed there is strong agreement between the curve fitting method and ratio method, however there are some limitations. Computationally, the resources required to perform an iterative curve fitting of (1) are much higher than directly calculating (2). For a region of interest of 600 pixels the curve fitting method requires approximately 2-3s of computing time on a conventional laptop (2.5GHz i7, 16GB RAM, Radeon R9 M370X), whereas the lifetime for the same region can be calculated using (2) in approximately 0.5ms. While optimizations can still be implemented to improve the speed of both methods, there is currently over three orders of magnitude difference in their computation times. This is further compounded when large regions of interest and multiple sequences are collected during a radiotherapy fraction. However, the ratio method is prone to artifacts which must be filtered, resulting in a lower number of estimates (N) and slightly higher standard deviation ( $\sigma$ ) shown in Figure 8.3-2b.

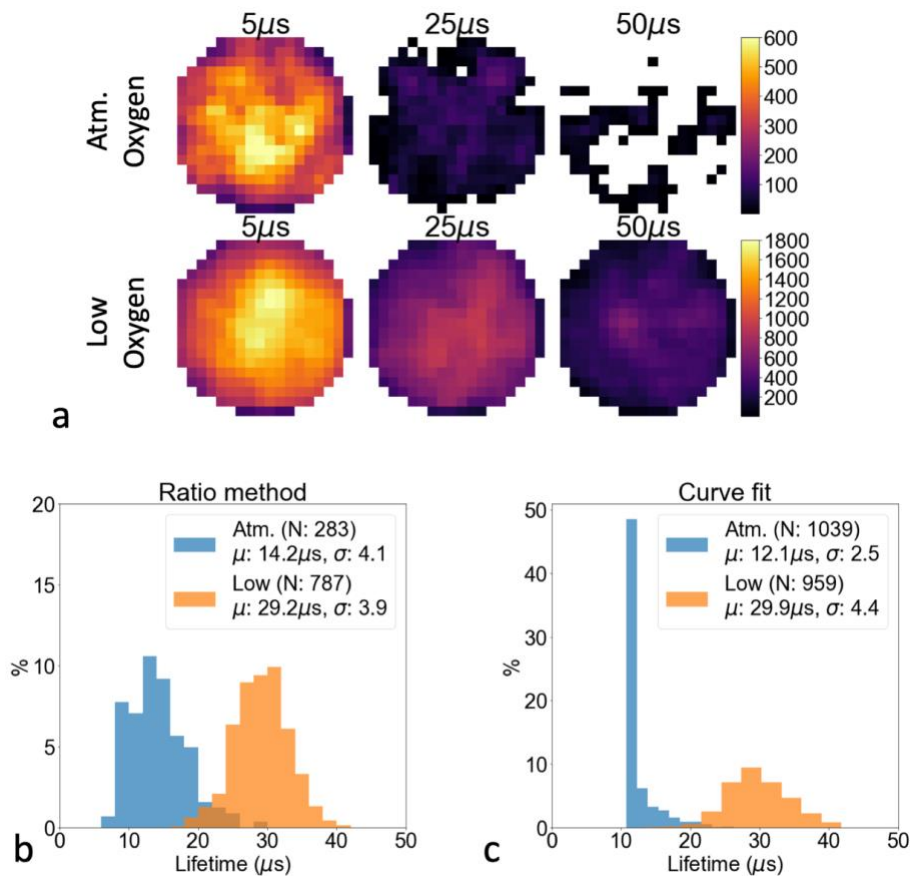


Figure 8.3-2: Intensity images of phosphorescence emitted by Oxyphor 2P in solution using 2x2 pixel binning (a). Histograms of pixel-based lifetime estimates determined through direct calculation of (2) (b) or using a curve-fit of (1) (c)

To further investigate the limits of detection in both the spatial and temporal domain, a series of CEL images were collected during a 2Gy (200MU) dose fraction. Multiple frames were summed in groups of 2,3,5 and 8 frames, effectively reducing the overall frame rate but improving the detected signal. Spatial pixel binning was performed by taking the median of a square kernel of 2, 4, 8 and 16 pixels along each edge, which effectively reduces spatial resolution while suppressing noise. The lifetimes were estimated for each sample and converted to pO<sub>2</sub> using (1) and (5), respectively. Since these solutions should

have uniform pO<sub>2</sub> the goal was to identify where the standard deviation of the pO<sub>2</sub> was minimized, while still having adequate spatial and temporal resolution. An example of this method is shown for deoxygenated Oxyphor 2P in Figure 8.3-3, where Figure 8.3-3a is a map of pO<sub>2</sub> standard deviations measured at decreasing frame rate (x-axis) and reduced spatial resolution (y-axis). There is a trade-off between the two options, which is demonstrated by the generally diagonal contour lines depicting the standard deviation. A pO<sub>2</sub> histogram is provided in 8.3-3b, where the vertical black line is the previously defined truth value, and the corresponding pO<sub>2</sub> map generated from 2x2 pixel binning and summing 8 frames is shown in Figure 8.3-3c.

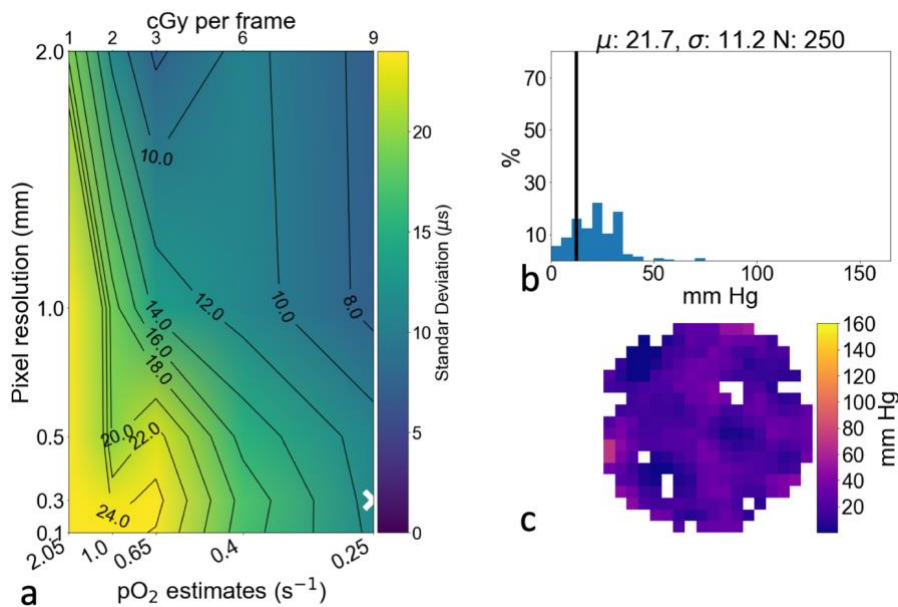


Figure 8.3-3: A map of standard deviations for estimated pO<sub>2</sub> values of deoxygenated Oxyphor 2P (a). An example histogram of the pO<sub>2</sub> measurements for 2x2 pixel binning and summation of 8 frames (b), and the corresponding pO<sub>2</sub> map (c).

### 8.3.2 In vivo

A total of 5 nude mice with a FaDu tumor implanted in the flank were imaged using the CEL technique. Each mouse was injected with equal volumes and concentrations of PtG4 and Oxyphor 2P, either in Matrigel or directly in the tumor. One mouse was injected with both PtG4 and Oxyphor 2P Matrigel inclusions, as well as a direct tumoral inject of Oxyphor 2P, shown in Figure 8.3-4. The mouse outline in thick white in Figure 8.3-4a was determined automatically by a threshold of the Cherenkov image, while the thin white outline of the tumor was found based on a Fourier bandpass filter of the CEL images. The image shown in this Figure 8.3-4a has an initial pixel resolution is approximately  $150\mu\text{m}$ , and a  $2 \times 2$  pixel median binning is applied before performing the lifetime estimate, effectively halving the resolution. The phosphorescence intensity of the Oxyphor 2P in tumor at different pulse delays is shown in Figure 8.3-4b. Using these values, and a third delay, the lifetime is estimated by applying the previously described curve-fitting of (1) (Figure 8.3-4c). Invalid estimates outside the boundary conditions were removed. Then, using (5) the  $p\text{O}_2$  can be calculated and is shown in Figure 8.3-4d.

Since multiple image sequences are collected during dose delivery, the temporal lifetime and  $p\text{O}_2$  changes can be observed throughout treatment. During a 2Gy fraction approximately 50 frames are collected per sequence where each frame is acquired over 20 linac pulses, or 56ms. Additional frames could be collected if no Cherenkov frame is required. The data shown in Figure 8.3-4 has a relatively low temporal resolution since 8

frames are summed, producing a pO<sub>2</sub> map every 4 seconds, which corresponds to a total of 5 maps in a standard 2Gy dose.

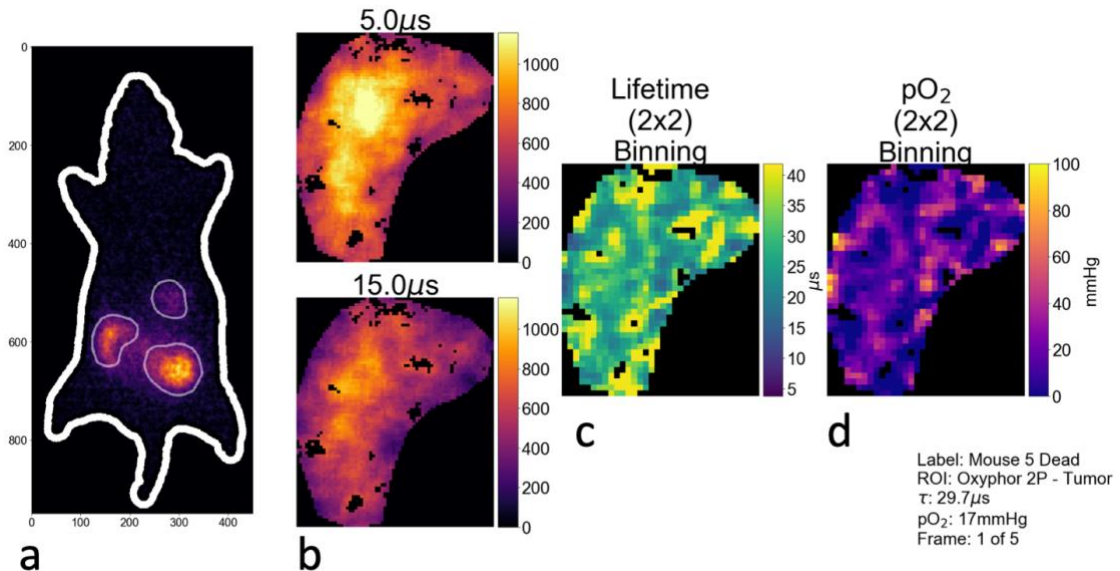


Figure 8.3-4: A demonstration of *in vivo* pO<sub>2</sub> detection. The Mouse ROI and tumor inclusion are automatically identified and highlighted in (a). The phosphorescence intensity of the direct tumoral injection of Oxyphor 2P a different delay is shown in (b). After 2x2 median pixel binning the lifetime (c) and pO<sub>2</sub> are calculated (d).

To demonstrate the *in vivo* response to oxygen levels the mice were imaged while under anesthesia, while awake and mobile, and after sacrifice. The most pronounced oxygen change is expected when comparing alive and dead mice. A box and violin plot of the pO<sub>2</sub> estimate for Oxyphor 2P inclusions are shown in Figure 8.3-5 comparing Matrigel inclusions (N=3 mice) and direct tumoral injections (N=3 mice) at 2-3 timepoints for both anesthetized mice and after sacrifice. From this data it can be observed the tumor has a lower median pO<sub>2</sub> and higher hypoxic fraction than Matrigel. The hypoxic fraction is defined as the percentage of estimates below 10 mmHg (HF<sub>10</sub>) or below 5 mmHg (HF<sub>5</sub>).<sup>11</sup>

While the boxes in this figure indicate the median and quartiles, the blue shaded region of the violin plot provides a more descriptive representation of the overall pO<sub>2</sub> distribution. After sacrifice both inclusions have a median pO<sub>2</sub> below 10 mmHg.

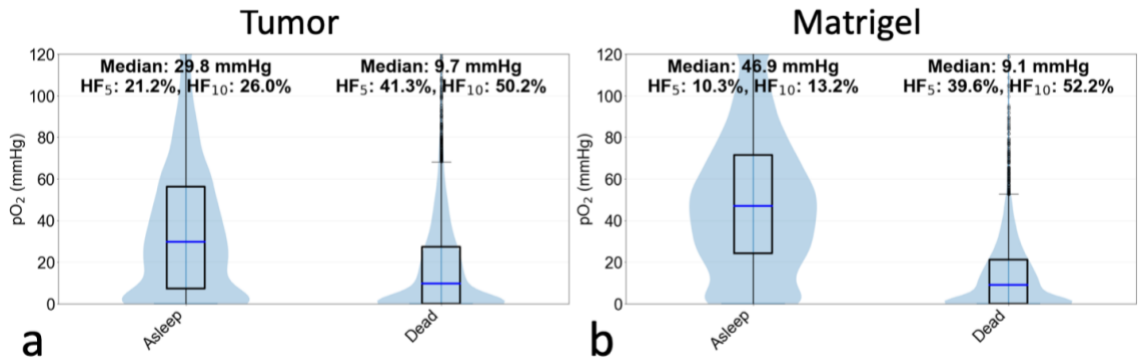


Figure 8.3-5: A box and violin plot showing all the estimated pO<sub>2</sub> values for direct tumoral injections of Oxyphor 2P (N=3 Mice) (a) and for Matrigel injections of Oxyphor 2P (N=3Mice) (b)

To further demonstrate the ability to detect temporal trends in pO<sub>2</sub> changes and as a metric of system reliability, 2-3 image stacks were acquired both before and after sacrifice. The median pO<sub>2</sub> value of each inclusion as the result of a 2Gy dose are plotted in relation to the time of initial injection and time of sacrifice. These cases show the general trend of Matrigel inclusions having slightly higher pO<sub>2</sub> than tumors. It can also be observed the second acquisition after sacrifice reports lower median pO<sub>2</sub> values.

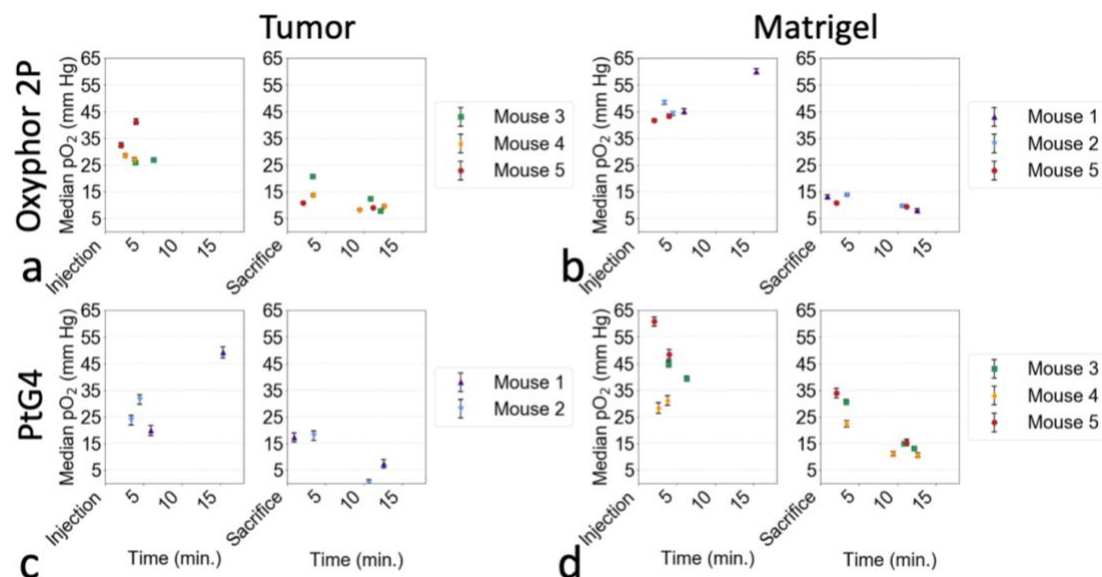


Figure 8.3-6: Multiple 2Gy dose fractions were delivered to each mouse before and after sacrifice. The median  $pO_2$  is shown relative to either injection time or sacrifice for Oxyphor 2P in either tumor (a) or Matrigel (b), PtG4 in either tumor (c) or Matrigel (d). All estimates were determined from a 4x4 median pixel binning and 8 summed frames.

An analysis of the signal to noise ratio (SNR) was conducted by using a constant pulse delay over a full 2Gy dose fraction, similar to our previously published methods. Three delays were used, and a sacrifice mouse was imaged for a total of 6Gy. A total of 170 frames were collected for each dose fraction. The frames were summed in increasing group sizes and the SNR was calculated for each summed frame by taking the ratio of the mean intensity of the inclusion region and the background standard deviation. This produces an SNR measurement which can be related to the delivered dose. By defining a minimum SNR threshold of 1, the limits of detection can be determined based on compound, delay time and dose, as shown in Table 8.3-1. The limiting factor in lifetime and resulting  $pO_2$  estimates are accurate measurements at all time delays.

Table 8.3-1: The measured *in vivo* minimum dose required for detection for 50uM PtG4 or Oxyphor 2P based SNR>1 for given delays

	<b><i>PtG4</i></b>	<b><i>Oxyphor 2P</i></b>	<b><i>Oxyphor 2P</i></b>
	<b><i>Matrigel</i></b>	<b><i>Matrigel</i></b>	<b><i>Tumor</i></b>
<b><i>5μs delay</i></b>	9cGy	4cGy	5cGy
<b><i>15μs delay</i></b>	12cGy	4cGy	5cGy
<b><i>25μs delay</i></b>	19cGy	7CGy	9cGy

## 8.4 Discussion

Our previous work estimated pO<sub>2</sub> during radiotherapy but required a dose fraction (2Gy) per CEL sequence, thus increasing total dose to 4-10Gy depending on the number of time delays acquired, and also required pausing the dose delivery while the camera settings were adjusted. The results were spatially resolved pO<sub>2</sub> estimates but lacked temporal resolution. Through the combination of automatically updating camera acquisition settings and a streamlined analysis workflow, near real-time pO<sub>2</sub> maps at sub millimeter spatial resolution can be acquired at a temporal rate of 0.25 estimates per second, which corresponds to 5 estimates within a single 2Gy dose fraction.

While producing sub-millimeter resolution pO<sub>2</sub> maps every four seconds is not quite real-time, a trade-off can be made between spatial and temporal resolution. The distribution of *in vitro* pO<sub>2</sub> standard deviations (Figure 8.3-3a) provides evidence that by reducing the pixel resolution to approximately 2mm, a temporal resolution of 1-2 pO<sub>2</sub> estimates per second could be achieved. However, in a clinical setting, higher spatial resolution is likely

desired, since Oxygen is known to diffuse only 50-150 $\mu\text{m}$ .<sup>5,11</sup> Conversely, there are spatial limitations to linac collimator delivery, as briefly described in Chapter 6. As such, it can be difficult to define an X-ray beam with dimensions below 1mm.

While up to 5 CEL image sequences can be defined using the modified control software, using only 2 provides the ability for improved temporal resolution. While curve fitting required for (1) is more computationally intensive and requires at least 3 delay measurements, the ratio method of (2) could be used to provide faster pO<sub>2</sub> estimates at higher temporal resolution, since only 2 delay measurements are required. However, filtering noise from these measurements is an important step that will likely reduce the overall number of valid measurements, as was shown in the *in vitro* data in Figure 8.3-2b and c. Under normoxic conditions which have lower luminescent signal this method may be insufficient because it is less robust to low-signal or high noise environments. A combination of the two methods could be used clinically to first quickly estimate using the ratio method, and then at a slower rate verify using the curve-fitting.

It is important to note the timing parameters of the CEL sequences should be optimized to provide sufficient temporal spacing between sequences, while also occurring before the phosphorescence decays below the noise floor. As was shown in the *in vitro* data, a pulse delay of 50 $\mu\text{s}$  is likely too long, so the *in vivo* experiments reduced the delay spacing so the third delay was only 25 $\mu\text{s}$ . The dose-related limits of detection presented in Table 8.3-1 show approximately 9cGy per time delay is required to determine lifetime and pO<sub>2</sub> estimates of Oxyphor 2P in a tumor. This assumes a concentration and volume of 50 $\mu\text{M}$

and 50uL and given camera geometry. This dose value corresponds with the *in vitro* pO<sub>2</sub> standard deviation of approximately <10 mmHg. It is also interesting to note the comparison in dose for the limits of detection of Matrigel. PtG4 required 2.25-3x more dose compared to Oxyphor 2P, which corresponds with the difference in quantum yield.

The current method provides an improvement in the absolute achievable temporal resolution of pO<sub>2</sub> estimation, but over shorter time intervals less dose is deposited, which means less Cherenkov emissions are available to excite PtG4. While intensified camera systems are sensitive to low numbers of photon events, the natural spatial and temporal random distribution of these events make pixel-based lifetime estimates difficult. Temporally summing frames is one method used in the current work. This lowers the lifetime frame rate from approximately 2 frames per second to approximately 0.25 estimates per second. Spatial averaging was used within frames as a way to overcome the sparsity of events. This averaging lowers the resolution by a rate proportional to the kernel size, and in the current system it is decreased from approximately 150μm to 2.4mm.

Further system optimization may be able to provide increased spatial and temporal resolution. Camera placement and lens numerical aperture could be further improved, however care must be taken not to place the camera in the X-ray beam, as such, additional shielding may help protect the electronics and reduce noise. While the bulk of the noise is generated during the X-ray pulse, so while the Cherenkov image is collected, not after the pulse when the CEL sequence is collected, shielding may prove to have limited improvements. Additional signal processing may be able to reduce the background signal and localize the phosphorescence. Additionally, as compounds with higher quantum yields

become available, the complexity of detection and quantification will be reduced. As discussed previously, the improved quantum yield of Oxyphor 2P compared to PtG4 appears to be linearly correlated with limits of detection and shows the ability to improve temporal resolution.

While the current study did not use a secondary method to verify pO<sub>2</sub>, the relative changes observed in both the *in vitro* and *in vivo* datasets provide evidence of a translatable method which could be used clinically to monitor daily changes during fractionated radiotherapy. Further validations of the absolute pO<sub>2</sub> are necessary, however the current method provides estimates of oxygen concentration in extracellular space, whereas most other systems use blood hemoglobin concentration to measure vascular perfusion. Since this method is used during radiation therapy, as opposed to relying on a separate imaging technique like BOLD MRI or <sup>18</sup>F-MISO PET, pO<sub>2</sub> estimates could be used to provide direct clinical feedback. Since hypoxic cells require 2.5-3x more radiation dose for the same cytotoxic effect, the sub-millimeter resolution pO<sub>2</sub> maps collected during a 2Gy dose fraction could be used as a feedback mechanism to modulate dose delivery.

## **8.5 Conclusions**

The current work presents a new method for collecting Cherenkov-excited luminescence images at varied delays, without interrupting radiation dose delivery, which achieves similar spatial resolution and reduces the total acquisition time by 10-20x compared to previous methods. Two techniques were compared to estimate lifetimes, where direct calculation is shown to be approximately 3 orders of magnitude faster than iterative curve

fitting. Due to the low photon counts, there is a demonstrated trade-off between spatial and temporal resolution, while sub-millimeter resolution images have been demonstrated to estimate pO<sub>2</sub> maps at a rate of 0.25 estimates per second, if lower spatial resolution is acceptable then the temporal resolution can be increased to 1-2 estimates per second. Without pixel binning the limit of detection for a delay of 25μs for a direct tumoral injection of Oxyphor 2P is at a dose of 9cGy, and 2.25-3x higher for PtG4, which correlates with differences in quantum yield. Approximately half this dose is needed to detect these phosphorescent compounds immediately after the X-ray pulse. This is approximately 20x less dose than previously demonstrated methods. Further work is needed to verify absolute pO<sub>2</sub> values, but trends are supported by an *in vivo* mouse model.

## 8.6 Acknowledgments

This work was funded by NIH grant R01 EB024498 as well as using shared irradiation resources from the Norris Cotton Cancer Center funded by P30 CA023108. This work is also supported by a National Science Foundation Graduate Research Fellowship

## 8.7 References

1. Bussink, J., Kaanders, J. H. A. M. & van der Kogel, A. J. Tumor hypoxia at the micro-regional level: clinical relevance and predictive value of exogenous and endogenous hypoxic cell markers. *Radiotherapy and Oncology* **67**, 3–15 (2003).
2. Harris, A. L. Hypoxia — a key regulatory factor in tumour growth. *Nature Reviews Cancer* **2**, 38–47 (2002).

3. Brizel, D. M., Sibley, G. S., Prosnitz, L. R., Scher, R. L. & Dewhirst, M. W. Tumor hypoxia adversely affects the prognosis of carcinoma of the head and neck. *International Journal of Radiation Oncology\*Biology\*Physics* **38**, 285–289 (1997).
4. Höckel, M., Schlenger, K., Höckel, S. & Vaupel, P. Hypoxic Cervical Cancers with Low Apoptotic Index Are Highly Aggressive. *Cancer Res* **59**, 4525–4528 (1999).
5. Hockel, M. & Vaupel, P. Tumor Hypoxia: Definitions and Current Clinical, Biologic, and Molecular Aspects. *JNCI Journal of the National Cancer Institute* **93**, 266–276 (2001).
6. Brown, J. M. The Hypoxic Cell: A Target for Selective Cancer Therapy—Eighteenth Bruce F. Cain Memorial Award Lecture. *Cancer Res* **59**, 5863–5870 (1999).
7. Karczmar, G. S. *et al.* Effects of hyperoxia on T<sub>1</sub> and resonance frequency weighted magnetic resonance images of rodent tumours. *NMR in Biomedicine* **7**, 3–11 (1994).
8. Griffiths, J. R. *et al.* The response of human tumors to carbogen breathing, monitored by gradient-recalled echo magnetic resonance imaging. *International Journal of Radiation Oncology\*Biology\*Physics* **39**, 697–701 (1997).
9. Baudelet, C. & Gallez, B. How does blood oxygen level-dependent (BOLD) contrast correlate with oxygen partial pressure (pO<sub>2</sub>) inside tumors? *Magnetic Resonance in Medicine* **48**, 980–986 (2002).
10. Padhani, A. R., Krohn, K. A., Lewis, J. S. & Alber, M. Imaging oxygenation of human tumours. *Eur Radiol* **17**, 861–872 (2007).
11. Vaupel, P., Höckel, M. & Mayer, A. Detection and Characterization of Tumor Hypoxia Using pO<sub>2</sub> Histography. *Antioxidants & Redox Signaling* **9**, 1221–1236 (2007).
12. Holt, R. W. *et al.* Cherenkov excited phosphorescence-based pO<sub>2</sub> estimation during multi-beam radiation therapy: phantom and simulation studies. *Physics in medicine and biology* **59**, 5317–5328 (2014).
13. Zhang, R. *et al.* Cherenkov-excited luminescence scanned imaging. *Optics Letters* **40**, 827–827 (2015).
14. Pogue, B. W. *et al.* Maps of in vivo oxygen pressure with submillimetre resolution and nanomolar sensitivity enabled by Cherenkov-excited luminescence scanned imaging. *Nature Biomedical Engineering* **2**, 254–264 (2018).
15. Čerenkov, P. A. Visible Radiation Produced by Electrons Moving in a Medium with Velocities Exceeding that of Light. *Physical Review* **52**, 378–379 (1937).
16. Frank, I. & Tamm, Ig. Coherent Visible Radiation of Fast Electrons Passing Through Matter. in *Selected Papers* 29–35 (Springer Berlin Heidelberg, 1991). doi:10.1007/978-3-642-74626-0\_2.
17. Popple, R. A., Ove, R. & Shen, S. Tumor control probability for selective boosting of hypoxic subvolumes, including the effect of reoxygenation. *International Journal of Radiation Oncology\*Biology\*Physics* **54**, 921–927 (2002).

18. Rajendran, J. G. *et al.* Hypoxia imaging-directed radiation treatment planning. *Eur J Nucl Med Mol Imaging* **33**, 44–53 (2006).
19. Thorwarth, D. & Alber, M. Implementation of hypoxia imaging into treatment planning and delivery. *Radiotherapy and Oncology* **97**, 172–175 (2010).
20. Halpern, H. J. *et al.* Abstract 1874: First demonstration that hypoxia targeting with radiation improves tumor control in a mammal tumor model. *Cancer Res* **77**, 1874–1874 (2017).
21. LaRochelle, E. P. M., Shell, J. R., Gunn, J. R., Davis, S. C. & Pogue, B. W. Signal intensity analysis and optimization for *in vivo* imaging of Cherenkov and excited luminescence. *Physics in Medicine and Biology* (2018) doi:10.1088/1361-6560/aab83b.
22. Glaser, A. K., Zhang, R., Davis, S. C., Gladstone, D. J. & Pogue, B. W. Time-gated Cherenkov emission spectroscopy from linear accelerator irradiation of tissue phantoms. *Opt. Lett., OL* **37**, 1193–1195 (2012).
23. Shell, J. R. *et al.* Comparison of phosphorescent agents for noninvasive sensing of tumor oxygenation via Cherenkov-excited luminescence imaging. *Journal of Biomedical Optics* **24**, 1–1 (2019).
24. Esipova, T. V. *et al.* Two New “Protected” Oxyphors for Biological Oximetry: Properties and Application in Tumor Imaging. *Analytical Chemistry* **83**, 8756–8765 (2011).
25. Sullender, C. T. *et al.* Imaging of cortical oxygen tension and blood flow following targeted photothrombotic stroke. *Neurophotonics* **5**, 1–1 (2018).
26. Esipova, T. V. *et al.* Oxyphor 2P: A High-Performance Probe for Deep-Tissue Longitudinal Oxygen Imaging. *Cell Metabolism* **29**, 736-744.e7 (2019).
27. van der Walt, S. *et al.* scikit-image: image processing in Python. *PeerJ* **2**, e453–e453 (2014).

# CHAPTER 9

## 9 Conclusions and future work

### 9.1 Overview

The work presented in this thesis addresses four primary aims which are connected through modeling photon-matter interactions. Experimental demonstrations have provided further evidence of a translational path for utilizing broad-spectrum light-tissue interactions for treatment and diagnosis of neoplastic disease. While significant progress has been made in defining a path for clinical translation of these models in the field of Photodynamic Therapy and Radiation Therapy, there are also limitations which could be addressed by future work. A discussion of the advantages, disadvantages, and areas of future work are presented in the following sections.

### 9.2 Modeling

#### 9.2.1 Code modifications

There are a number of methods to improve the execution time required to run Monte Carlo models. Techniques such as multi-threading, GPU-optimization and distributed execution have been discussed in Chapter 2. The distributed execution technique presented in this chapter reduces computation time by  $1/n$ , where  $n$  is the number of independent execution

nodes. This functionality has allowed for numerous models to be created which were discussed in Chapters 3,4 and 6. Other methods could also be beneficial, such as variance reduction techniques that can improve precision without increasing the number of events. One implementation of this technique uses importance sampling is already implemented in GAMOS, but is only applicable to Bremsstrahlung splitting, which commonly occurs in an X-ray source.<sup>1,2</sup> This function can be used to increase the number of scattered secondary gammas in a volume, by 1-3 orders of magnitude, and directional splitting can be used as a filter, killing gammas which are not directed towards a specific plane of interest. Similar functionality could be expanded to the optical plugin to allow uniform or directional splitting of fluorescence or Cherenkov events. While directional splitting may not be suitable for a highly-scattering medium, these two methods could be used to potentially increase the number of detected events, which can be very beneficial when attempting to detect rare events. However, care should be taken when analyzing the resulting simulation to ensure that these techniques do not cause artifactual data.

Over the past decade the Geant4-DNA project has been gaining support through added collaborations and functionality. While photon-matter interactions generally occur on the order of  $<10^{-10}$  seconds, the resulting chemical reactions can occur up to a few seconds after, with biological phases occurring between seconds and days after the original events.<sup>3</sup> The Geant4-DNA project aims to expand the current Geant4 physical modeling capabilities by also considering the chemical reactions induced by ionizing radiation.<sup>4</sup> The model is currently limited to nanoscale interactions in water, but provides the ability to estimate indirect radiation damage through modeling radiolysis.<sup>5,6</sup> This is useful for understanding

the biological dose incurred by radiation events. The chemical reaction of radiolysis of water in ionizing radiation is a very similar reaction to Type 1 Photodynamic Therapy (Figure 1.2-1). As such, it seems possible, with sufficient effort, the Geant4-DNA model could be expanded to estimate photodynamic dose. This could be a valuable tool for PDT community, but also in the burgeoning field of X-PDT, which aims to utilize photosensitizers to boost the efficacy of X-ray therapies. This method could help better localize cell killing, while also removing the depth limitation of conventional optical PDT treatments. The complex interactions at play are difficult to predict, so a Monte Carlo package capable of modeling optical and radiological chemical interaction would be a significant contribution to the scientific community.

### **9.2.2 Infrastructure**

The on-demand distributed cloud infrastructure for executing parallel Monte Carlo simulations presented in Chapter 2 provides a large improvement in execution times, however there are some limitations to the current design. While a packaged virtual machine was provided for local code execution, it is not well-suited for large simulations. When identifiable patient data, such as CT imaging are used as the basis of the simulation, or other large datasets not suitable for network transfer are utilized, a dedicated local server or high-performance computing cluster may be a better solution. Modifications to the container deployment scripts could be implemented to account for the local server solutions, thus allowing for more diverse choices in execution platform. Additionally, other command-line tools could be packaged into the same deployment model. In the realm of Monte Carlo packages, TOPAS and GATE are ideal initial candidates.

## **9.3 Photodynamic Therapy Translation**

### **9.3.1 Light Dose estimates**

The solar irradiance estimates presented in Chapters 3-4 are based on spectral measurements collected at different time-points, where the light fluence model of tissue assumes an average solar spectrum, among other light sources. This averaged solar spectrum is used as a system input in Chapter 4 to compare irradiance with weather reports. While this method has exhibited high correlation between measured irradiance and weather conditions, and has been demonstrated clinically,<sup>7</sup> it does not account for changes in the proportion of UV radiation observed throughout the course of a day. Since indoor treatments were the primary consideration, this is not a major concern to the work presented in Chapter 4, however if outdoor PDT treatments or other forms of photomodulation are desired this may be of larger importance, mainly to prevent erythema and other negative effects.

Spectral models of solar irradiance are well documented,<sup>8,9</sup> and programmatic queries of average total irradiance for a given location are also available.<sup>10</sup> However, while models exist to estimate the spectral changes of sunlight based on location, time and water vapor concentrations, there is currently no way to query the spectral response base on these inputs. Many of these models have been developed for applications in renewable energy, and while the total irradiance is the main importance for photovoltaics, developing easily accessible models with high spectral resolution could be useful well beyond this field. Since many biological processes depend specific wavelengths of activation, models with

higher spectral resolution could be beneficial for applications in both agriculture and health.

The UV-index is a well know standardized index used to predict the duration of sun exposure required to produce a sunburn, and it can be calculated using a measurement of UVA and UVB irradiance. Much like the PpIX-effective spectra discussed in Chapter 3-4, the UVA and UVB measurements are multiplied by an erythema action spectrum and then the effective spectrum is integrated and divided by an index value, resulting in UV-index. With higher spectral resolution measurements, other metrics such as those for rates estimating PpIX activation, Vitamin D production, or photosynthetic output could be tabulated.

While understanding the available spectrally resolved irradiance is one piece of the puzzle in dose planning for daylight PDT, another is estimating irradiance at the treatment field. Patient positioning may drastically alter the received light dose. As such, close clinical monitoring is currently required to record accurate light dose metrics. Future work could address this through technological means by implementing a wearable light dose monitoring system. While wrist-based dosimeters have be used previously, as discussed in Chapter 4, the treatment field is often the scalp, face or chest, and has little correlation with wrist placement. A wearable device would need to be compact and flexible enough to be place near the treatment field, in a form factor similar to a bandage. Light dose could be monitored through UV-sensitive electronics or photochromic pigment. Active light dose monitoring which could be wirelessly transmitted would be an ideal way to notify patients or clinical staff of treatment progression.

The work presented in this thesis has only considered lightly pigmented skin. While pigmentation provides natural protection against UV-induced lesions, it is still possible for those with higher pigmentation to develop neoplasia. Since this model assumes a multi-layer skin geometry, adjusting the melanin concentration in the superficial layers and re-running the simulations would be a fairly trivial task. Another critique of the work presented in Chapters 3-4 is the models are based on optical property estimates for healthy skin. As such, developing models of AKs, superficial SCCs, and nodular BCCs would provide additional insight which may be pertinent to clinical planning. These models would need to estimate both the optical properties and morphology of these lesions.

### **9.3.2 PDD estimates**

The light fluence is only one component in the three contributors to photodynamic dose, which also relies on photosensitizer concentration and oxygen availability. Measuring *in vivo* oxygen levels during PDT treatments is a difficult task. The current work has used the commonly held assumption of fully oxygenated tissue, which is likely accurate for the low fluence-rate activation implemented in daylight PDT. However, to further advance the science and potential clinical applications, a better understanding of oxygen distribution is needed. There are a number of methods to achieve this goal, for example, singlet oxygen produces a weak fluorescence emission at approximately 1270nm, or a contrast agent such as PtG4, discussed in Chapters 5-8, could be used to measure pO<sub>2</sub>. Neither of these applications seem clinically applicable since imaging devices used in NIR detection are currently large and expensive, and adding a second contrast agent which is also a porphyrin would be difficult to translate clinically. One method which could provide a path to clinical

translation is using the concept of delayed fluorescence. In this method the excited photosensitizer is quenched by the presence of oxygen and a portion of the triplet-state photosensitizer undergoes reverse intersystem crossing, resulting in delayed fluorescence on the scale of  $10^{-6}$  -  $10^{-3}$  seconds.<sup>11</sup> This method has been demonstrated *in vivo* using an intensified-CCD and pulsed narrowband light source operating at 2kHz with 50% duty cycle.<sup>11</sup> While this method has been demonstrated in a laboratory setting, incorporating it into existing clinical dosimetry measurements will require further engineering to address system reliability and sensitivity. With hypoxic environments generating longer lifetimes of delayed fluorescence it may be possible to use commonly found CMOS global shutter rates to gate with sufficient time resolution to determine a hypoxic threshold. However, system sensitivity and background rejection may still introduce issues, so an alternative approach might be to use single pixel detection at the cost of lost spatial resolution, where all light is detected by a single detector, and the location of the origin is provided by knowledge of the excitation beam location.

The light activation thresholds used in Chapter 3 are primarily based on *in vitro* studies, so while Chapters 3-4 present minimum treatment times for given depths of activation and irradiance, they have not been clinically verified. Future work using fluorescence dosimetry might help improve these models. Rates of photobleaching, ideally combined with oxygen estimates, would be beneficial for validating the *in vivo* treatment thresholds. While blue-light excitation is well-suited for maximal fluorescence emission of PpIX and is technically easier to image due to its large Stokes shift, it has limited depth sensitivity. While red excitation of the PpIX Q-band at 633nm introduces technical challenges with filtering and

sensitivity, the larger depth sensitivity would provide additional information for estimating the threshold dose of daylight PDT.

## **9.4 Radiation Therapy Translation**

The signal analysis of Cherenkov emissions and Cherenkov-excited luminescence presented in Chapters 5-6 demonstrates the difficulties in detection. This work shows Cherenkov emissions are approximately 100x stronger than Cherenkov-excited luminescence generated by PtG4. While Cherenkov emissions can be imaged under dim room lights using time-gating to reject background illumination, CEL imaging must still be implemented in a completely darkened room. The idea of filtering room light is presented in Chapter 7 and while it proved beneficial to improve the detection of luminescent (and likely scintillating) inks during X-ray delivery, filtering reduced the SNR when imaging phosphorescence after X-ray delivery. It appears Cherenkov imaging resides in the shot-noise limited space, whereas the lower signal and background of Cherenkov-excited luminescence is limited by read-noise. To address this through system acquisition parameters, efforts should be taken to increase exposure time, apply hardware pixel-binning and use a large aperture as close to the subject as possible. From a contrast agent perspective, higher quantum yield compounds, such as Oxyphor 2P presented in Chapter 8 is one mechanism for improving detection.

Expanding beyond solely Cherenkov-excited luminescence, scintillating compounds could be utilized to improve detection. It is likely the UV-sensitive tattoo inks presented in Chapter 7 are excited by both UV-weighted Cherenkov emissions as well as X-ray

scintillation. An initial demonstration of computationally identifying Cherenkov-excited contrast agents was presented in Chapter 6. While fluorescence properties of many compounds are well catalogued,<sup>12,13</sup> and similar data is available for scintillators,<sup>14</sup> neither data sources consider long-lived phosphorescence ( $>10\mu\text{s}$ ) or triplet quantum yield. Further development and standardization of such a database could help identify future contrast agents or X-PDT sensitizers.

Finally, detecting  $\text{pO}_2$  during fractionated radiotherapy was demonstrated in Chapter 8 using a murine model. Over the recent years this project we have transitioned from using approximately 10Gy,<sup>15</sup> to 5Gy,<sup>16</sup> and now Chapter 8 demonstrates detection at cGy levels. With lower doses, a trade-off between temporal resolution and spatial resolution comes into play. The temporal uncertainty due to low dose estimation can be reduced by averaging multiple estimates in time, and effectively increasing the dose used for imaging, or pixel binning can be used to estimate at a lower spatial resolution. Currently, it seems high spatial resolution is more desirable, since it can be used to show the heterogeneity of tumor hypoxia.

## 9.5 References

1. Allison, J. et al. Recent developments in Geant4. Nuclear Instruments and Methods in Physics Research Section A: Accelerators, Spectrometers, Detectors and Associated Equipment **835**, 186–225 (2016).
2. Arce, P. & Lagares, J. I. CPU time optimization and precise adjustment of the Geant4 physics parameters for a VARIAN 2100 C/D gamma radiotherapy linear accelerator simulation using GAMOS. Physics in Medicine & Biology **63**, 035007–035007 (2018).

3. Naqa, I. E., Pater, P. & Seuntjens, J. Monte Carlo role in radiobiological modelling of radiotherapy outcomes. *Phys. Med. Biol.* **57**, R75–R97 (2012).
4. Incerti, S. et al. The geant4-dna project. *Int. J. Model. Simul. Sci. Comput.* **01**, 157–178 (2010).
5. Karamitros, M. et al. Diffusion-controlled reactions modeling in Geant4-DNA. *Journal of Computational Physics* **274**, 841–882 (2014).
6. Incerti, S., Douglass, M., Penfold, S., Guatelli, S. & Bezak, E. Review of Geant4-DNA applications for micro and nanoscale simulations. *Physica Medica* **32**, 1187–1200 (2016).
7. O’Mahoney, P. & Eadie, E. Bring the Sunshine Indoors: Easy Dosimetry for Indoor Daylight Photodynamic Therapy. *Photochemistry and Photobiology* (2019) doi:10.1111/php.13192.
8. Bird, R. E. A simple, solar spectral model for direct-normal and diffuse horizontal irradiance. *Solar Energy* **32**, 461–471 (1984).
9. Paulescu, M. & Schlett, Z. A simplified but accurate spectral solar irradiance model. *Theor Appl Climatol* **75**, 203–212 (2003).
10. Solar Resource Data API | NREL: Developer Network. <https://developer.nrel.gov/docs/solar/solar-resource-v1/>.
11. Scholz, M. et al. pO<sub>2</sub>-weighted imaging in vivo by delayed fluorescence of intracellular Protoporphyrin IX. *Opt. Lett., OL* **45**, 284–287 (2020).
12. Taniguchi, M. & Lindsey, J. S. Database of Absorption and Fluorescence Spectra of >300 Common Compounds for use in PhotochemCAD. *Photochemistry and Photobiology* **94**, 290–327 (2018).
13. Taniguchi, M., Du, H. & Lindsey, J. S. PhotochemCAD 3: Diverse Modules for Photophysical Calculations with Multiple Spectral Databases. *Photochemistry and Photobiology* **94**, 277–289 (2018).
14. Derenzo, S. E. et al. Design and Implementation of a Facility for Discovering New Scintillator Materials. *IEEE Transactions on Nuclear Science* **55**, 1458–1463 (2008).
15. Pogue, B. W. et al. Maps of in vivo oxygen pressure with submillimetre resolution and nanomolar sensitivity enabled by Cherenkov-excited luminescence scanned imaging. *Nature Biomedical Engineering* **2**, 254–264 (2018).
16. Cao, X. et al. Tissue pO<sub>2</sub> distributions in xenograft tumors dynamically imaged by Cherenkov-excited phosphorescence during fractionated radiation therapy. *Nature Communications* **11**, 1–9 (2020).

## 10 Thesis defense video recording

Due to COVID-19 the Dartmouth campus was essentially shut down and began operating in a nearly fully-remote manner by the end of March, 2020. As such, the thesis committee and public participated in a video conference for the thesis defense. A recording of this presentation is available at the following two links:

- [https://youtu.be/\\_0dE6jMvkTs](https://youtu.be/_0dE6jMvkTs)
- [https://dartmouth.zoom.us/rec/play/u8UoIej9qWg3T9WStgSDCqUrW42\\_J62s0CIa8\\_tfzB3kUHVRMwL3ZLBGNOUB6g6ym7r5iBNLkYKolvOT](https://dartmouth.zoom.us/rec/play/u8UoIej9qWg3T9WStgSDCqUrW42_J62s0CIa8_tfzB3kUHVRMwL3ZLBGNOUB6g6ym7r5iBNLkYKolvOT)